Author:
James, Oliver N

Title:
Miniaturisation and Efficiency in Compact and Electrically Small Tuneable UHF Antennas

UNIVERSITY OF BRISTOL

Miniaturisation and Efficiency in Compact and Electrically Small Tuneable UHF Antennas

Oliver Norman JAMES

A thesis submitted in fulfilment of the requirements
for the degree of Doctor of Philosophy

in the

Communications Systems and Networks Group
Department of Electrical and Electronic Engineering

September 2018

Declaration of Authorship

I, Oliver Norman JAMES, declare that this thesis titled, "Miniaturisation and Efficiency in Compact and Electrically Small Tuneable UHF Antennas" and the work presented in it are my own. I confirm that:

- This work was done wholly or mainly while in candidature for a research degree at this University.
- Where any part of this report has previously been submitted for a degree or any other qualification at this University or any other institution, this has been clearly stated.
- Where I have consulted the published work of others, this is always clearly attributed.
- Where I have quoted from the work of others, the source is always given. With the exception of such quotations, this report is entirely my own work.
- I have acknowledged all main sources of help.
- Where the report is based on work done by myself jointly with others, I have made clear exactly what was done by others and what I have contributed myself.

Oliver Norman James

12^{th} September 2018

Abstract

Many wireless communications systems require access to multiple frequency bands in compact form factors. The capability of an antenna to achieve high efficiency and wide bandwidth is linked to its physical size. Efficient wide-band antennas can be too large for compact multi-band systems in the low UHF range (300-1000 MHz). Electrically small antennas (ESAs) can work around the spectrum requirements if they are frequency agile, but efficiency degradation associated with the tuning mechanism is often overlooked. There is also no consistent approach to reporting the performance enhancement over an integrated bandwidth from the efficiency perspective, upon which the user experience ultimately depends. Three topical tuning mechanisms have been investigated in the UHF band, each underpinned by identification of candidate technologies from the literature, design of a frequency agile demonstrator antenna, and measurement of the input response, 3D radiation pattern and realised efficiency.

First, the ability of an RF-MEMS reconfigurable impedance matching network to preserve system efficiency has been challenged. Improved impedance matching in both free-space tuning and hand effect detuning scenarios was achieved, but the radiation performance of the whole system highlighted that previously undocumented losses given by emerging RF MEMS capacitors should not be overlooked when assessing tuner deployment in communication systems.

Second, a Co_2Z magneto-dielectric substrate material was found to offer profound miniaturisation (novel material achieved frequency reduction of $6.4\times$ compared to Duroid RT5880) and susceptibility to magnetic biasing (frequency tuning 32% for S_{11} < -3 dB). The measured efficiency was found to be around 1% for this iteration of the material. Nonetheless, the miniaturisation and tuneability aspects warrant ongoing review for use in applications that are miniaturisation-critical, since the novel material offers significant board area savings as well as radiation pattern stability.

Third, an improved novel approach to quantifying 'tuneability' in compact narrow band antennas (including electrically small antennas) has been formulated, emphasising the perspective of combined realised efficiency and frequency agility. Favouring efficiency aspects in the new approach increases relevance to power consumption, battery life, data rates and carbon emissions at the network level. Metrics for bandwidth of assured efficiency, average efficiency and integrated efficiency-bandwidth product have been given, reducing the commonplace over-reliance on tuneable S_{11} in isolation as a predictor of tuning performance. Demonstration of the approach has been given by application to a set of fixed-frequency/varactor-tuneable loop ESAs. The improved approach provides a platform for objective, quantified performance grading of a diverse range of antenna tuning technologies in future work, alleviating the problem of identification and grouping of tuning technologies by application. This in turn could reduce wasted design effort as well as promoting efficiency as a design concern in tuneable antenna solutions.

Publications

- O. J. Norman, G. Hilton, and M. Beach, "Measurement of efficiency degradation due to external detuning of a tunable patch antenna," in *2016 IEEE International Symposium on Antennas and Propagation* (APSURSI). IEEE June 2016, pp. 2145–2146. DOI: 10.1109/APS.2016.7696779.

- O. James, G. Hilton, and M. Beach, "Radiation efficiency analysis of balanced-impedance hexaferrite substrate for antenna miniaturisation," in *The Loughborough Antennas & Propagation Conference 2017* (LAPC). IET November 2017, pp. 1–5. DOI:10.1049/cp.2017.0235.

- O. N. James, G. Hilton, and M. Beach, "Hexaferrite substrate versus impedance matching for tuneable patch antenna miniaturisation," in *2018 12th European Conference on Antennas and Propagation* (EuCAP 2018). IEEE April 2018.

- Oliver James and Geoff Hilton and Mark Beach, "Efficiency-based approach to quantifying 'tuneability' metrics for frequency-agile narrowband antennas," accepted for publication in *IET Microwaves, Antennas and Propagation Journal*, 2019.

Acknowledgements

This project was supported by the Engineering and Physical Sciences Research Council (EP/I028153/1), the University of Bristol and industrial partners of the University of Bristol Centre for Doctoral Training in Communications. I would like to thank my academic supervisors Dr. Geoff Hilton and Professor Mark Beach for their dedication and the insights they brought to this work when I needed some directing.

Various aspects of the project were supported by the loan of technical equipment. I would like to thank Keysight Technologies for the loan of an E4991B impedance analyser, and DBD Communications for the loan of a pair of OpticalZonu RF-over-fibre transducer units.

This project involved creation of a hand phantom with permittivity properties similar to human tissue. This work was conducted in close discussion with Dr. Tommy Henriksson, then of the University of Bristol. I would like to thank Dr. Henriksson for his insightful discussions on phantom fabrication and his hands-on support in assisting with the phantom fabrication technique.

In addition to the support I have received with the technical aspects of this project, completing a PhD is something of a personal journey. Life carries on around the important mission of debugging code, punching the screen when the simulator crashes, and wincing when one inadvertently burns one's fingers on a soldering iron for the n^{th} week running. In this regard I could not have completed this project without support from my family, my friends and the good people who uploaded countless hours of organ and chiptune music onto the Internet.

Most of this thesis was written while working away from the University campus. I am indebted to the library of the University of Exeter (Penryn Campus, Cornwall), Filton Library and the Thirsty Scholar pub (Penryn, Cornwall) for providing space to write up this thesis. Reader, please don't take your local library for granted. If it's under threat of closure, please consider lending your voice to supporting it: http://www.voicesforthelibrary.org.uk/campaigns/what-can-you-do/.

Finally, I would like to acknowledge the contribution made by the university's two flying societies (Bristol University Hot Air Ballooning Society and Bristol University Gliding Club), both of which helped me gain an interesting sense of perspective at times—the University looks altogether quite a lot smaller when you're flying 1000 feet over it, away from it, and into the great unknown.

Oliver Norman James, September 2018

Contents

List of Figures

List of Tables

Physical Constants

Speed of light in vacuum	c	=	$299\ 792\ 458$	$\mathrm{m\,s^{-1}}$	(exact)
Imaginary unit	j	=	$\sqrt{-1}$		
Permittivity of free space	ε_0	=	8.854×10^{-12}	$\mathrm{F\,m^{-1}}$	
Permeability of free space	μ_0	=	$4\pi \times 10^{-7}$	$\mathrm{H\,m^{-1}}$	
Wave impedance of light in free space	Z_0	=	377	Ω	(approximate)

Symbols

a	Radius of Wheeler radiansphere	m
BW	Bandwidth	Hz
C	Capacitance	F
D	Antenna directivity (linear)	Dimensionless
E_θ	Electric far-field (θ polarisation)	$\mathrm{V\,m^{-1}}$
E_ϕ	Electric far-field (ϕ polarisation)	$\mathrm{V\,m^{-1}}$
f	Frequency	Hz
G	Antenna gain (linear)	Dimensionless
k	Free space angular wavenumber	$\mathrm{rad\,m^{-1}}$
L	Inductance	H
n	Refractive index	Dimensionless
P	Power	W ($\mathrm{J\,s^{-1}}$)
Q	Quality factor	Dimensionless
R	Resistance	Ω
RL	Return loss	dB
$\mathrm{S_{ji}}$	Scattering (S)-parameter into port j from port i	Dimensionless
Z	Impedance	Ω

$\tan\delta_\varepsilon$	Loss tangent due to dielectric effects	Dimensionless
$\tan\delta_\mu$	Loss tangent due to magnetic effects	Dimensionless
ε_r	Electric permittivity relative to ε_0	Dimensionless
η_loss	Ohmic conductor and dielectric loss in antenna	Dimensionless
η_m	Impedance matching efficiency	Dimensionless
η_rad	Antenna radiation efficiency	Dimensionless
λ_0	Wavelength in free space	m
μ_r	Magnetic permeability relative to μ_0	Dimensionless
ρ	Correlation between two radiation patterns	Dimensionless
ω	Angular frequency	$\mathrm{rad^{-1}}$

Acronyms

AUT antenna under test

BST barium strontium titanate

CMOS complementary metal-oxide semiconductor

ESA electrically small antenna

ESR equivalent series resistance

FMR ferromagnetic resonance

HXF hexagonal ferrite

IoT Internet of Things

LTE Long Term Evolution

MD magneto-dielectric

OTA over-the-air

PCB printed circuit board

RF radio frequency

RF MEMS RF microelectromechanical system

RFID radio-frequency identification

SRF self-resonant frequency

TMN tuneable matching network

UAV unmanned aerial vehicle

UHF ultra-high frequency

UWB ultra wide band

VHF very high frequency

VNA vector network analyser

For Kristy, my humble navigator

Chapter 1

Introduction

1.1 Motivation: the trend towards a greater number of bands

Since the turn of the millenium, consumers have increasingly come to expect that communications capability in electronic products will be delivered wirelessly. The rise in the numbers of active cellular phone subscriptions has been well documented [1–3]. Moreover, being able to access the Internet from portable devices is more important than ever before. In 2018, the UK public generally accessed the Internet from their smartphones. On average, among adults 62% of time spent on the Internet was conducted using a smartphone, consuming a total of 1.9 GB of data per month over cellular networks [3] (Figure 1.1). The same report from ten years earlier in 2008 [1] noted only a fledgling number of new connections to mobile broadband communications services in relative terms (about 500,000 using 3G cards and dongles). It is notable that the iPhone 3G edition launched in July 2008, and access to mobile Internet has in some senses become a "standard expectation" of the masses ever since. The growth in total number of subscriptions has been modest (+4.4% growth in subscriptions [3] against population growth of +3.6% from 2012–2017 [4]), while mobile data consumption has ballooned by comparison (+950% in the same period [3]).

In the present day, the nature of the communicating devices is perceived to be changing. Whereas the primary driver of wireless communication subscription numbers was once was assumed to be computers and telephones enabling communications between humans [5], increasingly it is devices communicating with other devices that are forecast to drive growth. The "things" in Internet of Things (IoT) can be taken to mean almost any noun. One could consider the likely deployment scenarios for IoT devices to be nearly any type of resource management, from smart street lighting to improving the timeliness of crop irrigation. Case studies for wireless communications increasingly include platforms that would once have been considered somewhat non-conventional. A shift beyond delivering wireless Internet service to only smartphones is

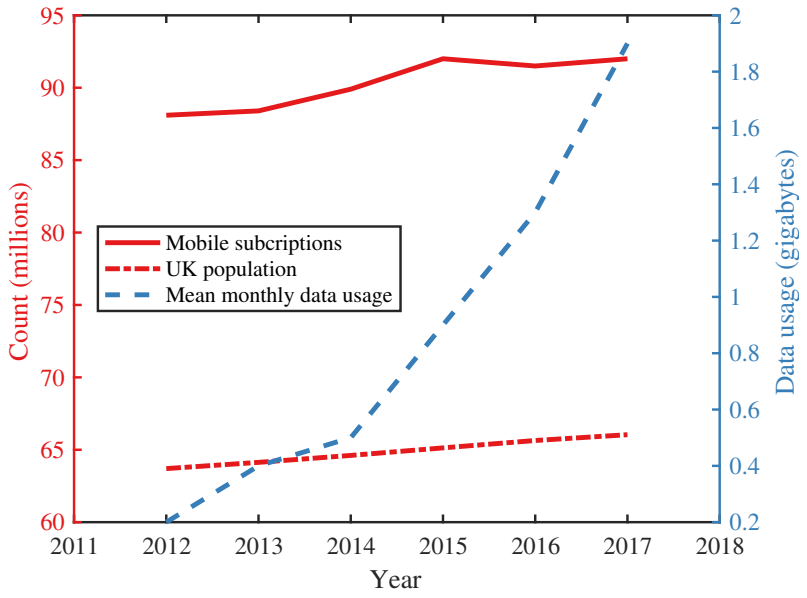

FIGURE 1.1: Comparison of growth in number of mobile data subscriptions against growth in data consumed. Subscription, usage data: [2, 3]. Population data: [4].

coming: connected vehicles, wireless health monitoring, smart utilities and even city-scale wireless infrastructure such as lamp post-mounted devices used for urban monitoring in "smart cities" [6, 7] are all purported as current or future technologies of interest [6, 8]. Any of these applications could benefit from compact antennas that may relieve physical weight burdens on users, or improve sensor acceptance rates amongst the public if IoT packages can be discreetly installed amongst existing infrastructure. The impact of these devices on spectrum consumption is likely to be significant: devices connected to the IoT are forecast to outnumber people by a factor of at least 2:1 by 2020 [9]. Estimated device numbers vary greatly, with forecasts ranging anywhere from 20–30 billion [9, 10] to 200 billion devices by 2020 [8]. The expectation that everything will communicate wirelessly is growing, and the spectrum is getting busier.

To meet the growing needs of more and more wirelessly communicating devices in increasingly congested spectrum, mobile communication devices are expected to be able provide service on multiple frequencies in a single compact physical form factor. The trend for an increasing number of frequencies to be supported in one device has been showcased by the evolution of cellular communications, with the nine principal bands specified for GSM [11] expanding to more than 50 to date in the LTE-A specifications correct to January 2017 [12] (Figure 1.2).

To address the overall spectrum congestion, national regulators have acted to recycle segments of the spectrum formerly occupied by now obsolete services. For example, broadcast analogue television services have been retired to make way for new ultra-high frequency (UHF)-band services[1]. The availability of UHF spectrum in the region 400–800 MHz is highly sought after

[1]The International Telecommunication definition of the UHF band is from 300–3000 MHz [13].

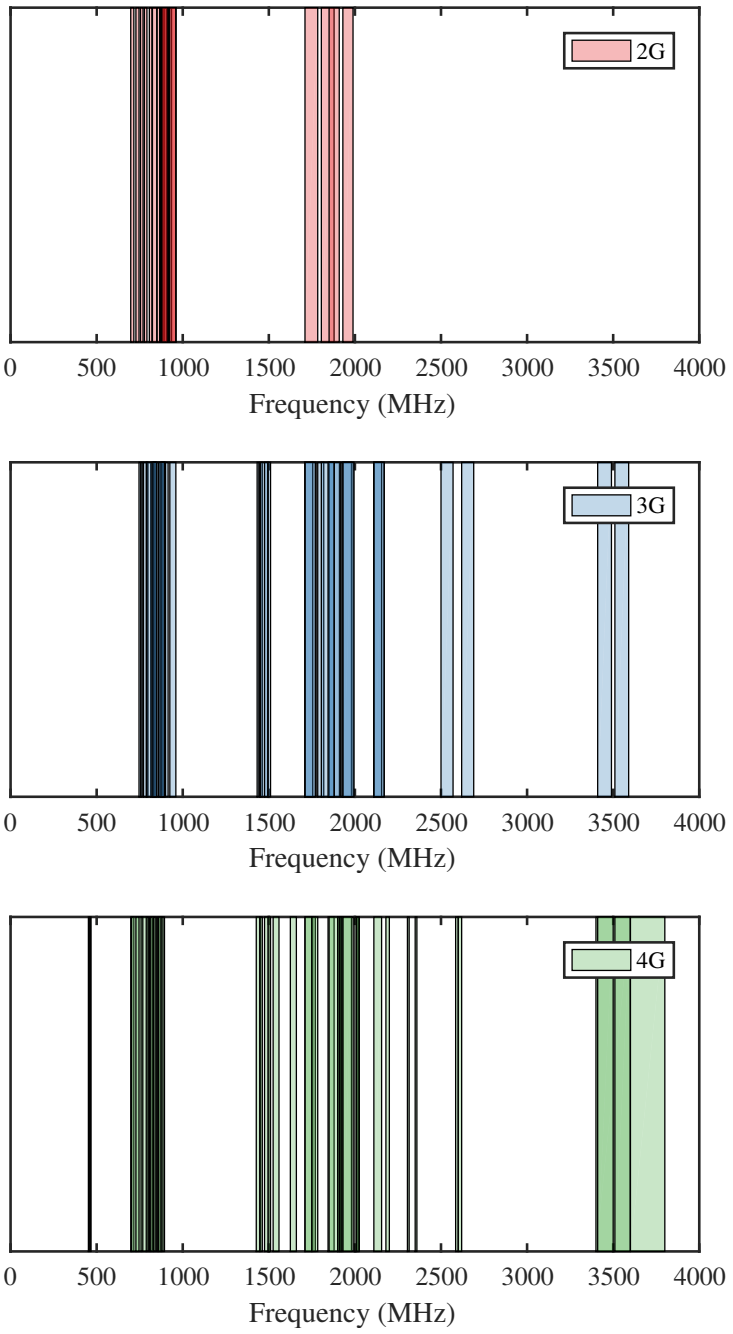

FIGURE 1.2: Growing number of cellular bands to support per generation [11, 12] (band allocations correct to January 2017).

for its perceived favourable propagation characteristics, particularly penetration of foliage and common building materials. Thus, UHF frequencies are suited to services with lower data rates than those associated with 3–6 GHz bands or even the emerging high-capacity links offered in the bands above 30 GHz. The absolute data rates associated with the UHF band may not be world-beating in terms of ability to support gigabit wireless links, but UHF frequency bands will nonetheless play a vital role in allowing devices to communicate effectively given the finite amount of available spectrum and the requirement for in-building penetration. Applications in the

UHF band can include control plane communications in fifth-generation (5G) communications, "TV whitespace" cognitive radio deployments making opportunistic use of available channels (e.g. [14] for provision of Internet services over a wide area), as well as existing mission-critical applications such as emergency services use (e.g. TETRA, 390–460 MHz in the UK [15]).

Thus there is a continuing trend for mobile communications platforms to require service on a number of channels in one compact terminal, which will increasingly include devices serving the lower UHF-band as well as the upper UHF bands depicted in Figure 1.2. However, enabling efficient service on many different frequencies becomes difficult at various points in the RF chain (amplifiers, filters, matching networks and antennas). The requirement to serve multiple frequency bands becomes especially problematic in the low UHF band, since the operating wavelengths can become much longer than the space afforded to the antenna itself (Figure 1.3).

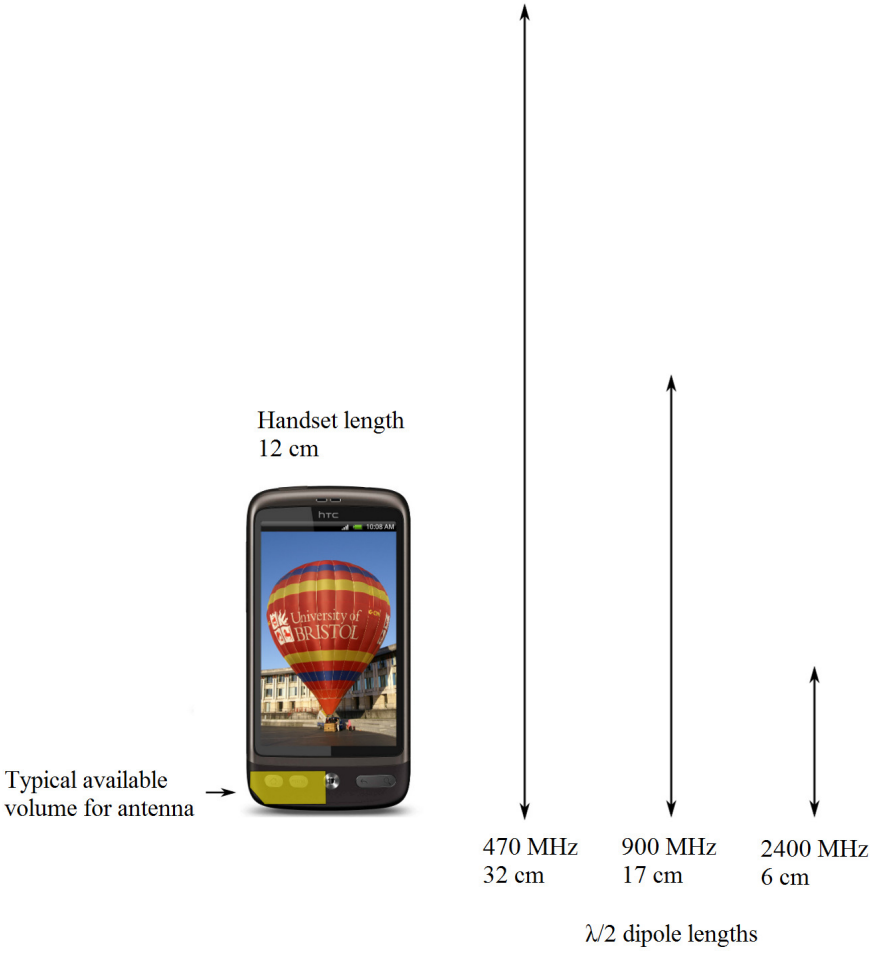

FIGURE 1.3: Comparison of typical operating wavelengths to size of mobile communication terminal. Lengths are depicted to scale.

Antennas are fundamentally not able to simultaneously exhibit wide bandwidth and highly efficient radiation when the antenna has dimensions significantly shorter than the free space wavelength (Section 2.1). The convenient option of deploying small, highly efficient, very wide

band antennas in portable communications terminals transpires to be strongly discouraged by physics. An alternative solution is required.

1.2 Opportunity: tuneable electrically small antennas

At UHF frequencies, tuneable narrow band electrically small antennas (ESAs) provide a solution to the band accessibility challenge. An electrically small antenna has dimensions significantly shorter than the free space wavelength, permitting low frequency band service in a compact terminal. The instantaneous bandwidth is sacrificed in exchange for higher instantaneous efficiency than would be possible given a wider bandwidth. To address each of the bands needed, a tuneable element is included in the antenna structure to allow its operating frequency to be reconfigured over time.

Roaming between cellular base stations provides one such scenario where channel availability changes over time. Antennas deployed in fixed locations maintaining one frequency for significant periods of time might also be required to function in this way, such as in TV whitespace devices where channels are opportunistically allocated and re-assigned over time. Opportunistic access to spectrum and co-existence with adjacent blocking signals in the contested spectrum would indicate that narrow band tuneable antennas will have relevance in such applications, with channel availability varying by geographical region. Regulators such as the United States' Federal Communications Commission have observed a need for devices which "have the flexibility and agility to locate and operate on the unused channels, no matter where the devices are located" [16].

While considering the frequency agility of such compact antennas, an opportunity to address the realised efficiency of such systems exists. Development of wireless communication systems must be considered in conjunction with the broader societal impact of deploying such large numbers of communicating devices in future networks. In light of the planet warming due to the activities of mankind [17, 18], serious efforts must be made to increase the energy efficiency of the entire communications chain—a process that ought to start with being frank about the inefficiencies associated with the present techniques.

The work presented in this thesis is therefore concerned with techniques to miniaturise UHF antennas, techniques to provide frequency reconfiguration in UHF antennas, and the efficiencies associated with these methods. The overall challenge associated with ESA design is broadly summarised as the search for methods to draw an "acceptable" compromise between power efficiency and bandwidth. While the limits on electrically small antenna Q preclude simultaneous wide band and efficient antenna performance, the bandwidth limit can be circumvented using a tuneable antenna. Such an antenna includes a reconfigurable element somewhere in its design

that can tune the instantaneously narrow band frequency response associated with the ESA over a broader integrated range. While the instantaneous narrow band behaviour of the ESA is still dictated by the Wheeler limit on Q [19], it may become possible to serve an appropriate frequency range to serve multiple different channels at different times.

1.3 Research objectives and key contributions

Given the large array of available tuning techniques, it is a challenge to identify which techniques should be used for what purposes. There are reported antenna designs describing antenna frequency reconfigurability, antenna miniaturisation, or both. The frequency agility and miniaturisation offered by various designs are usually communicated relatively clearly. However, regular literature surveys conducted throughout the course of this work found a repeated tendency toward a shortage of works simultaneously addressing antenna smallness and tuning while also documenting the realised radiative efficiency of the system.

The most recent of these surveys, presented in [20], suggested that the tuneability assessment is supported by a stated range of measured tuneable input responses in essentially all cases. Unfortunately, this makes no assessment of the radiation efficiency offered over the tuned range, reporting of which over a tuneable range was found to be much less widespread. That survey found that in nearly half of cases no efficiency data were given, while in others values were given but the method used to measure them was not declared. Of the papers found to have reported both efficiency values and the method by which these values were obtained (only 40% of those surveyed), none were found to have attempted to distil an efficiency-based approach to recording metrics of frequency agility. Hence, information from which antenna designers can draw conclusions on likely tuneable radiation behaviour for a given technique is often restricted. Moreover, a standardised benchmark method did not exist exist in the open literature for recording the frequency agility of tuneable narrow band antennas from the perspective of combined total efficiency and agility, until the one proposed in Chapter 5 and [20] was presented. Such a situation is problematic considering the tendency of ESAs to exhibit low radiation resistance (increasing their sensitivity to losses) and the known losses induced by the various tuning mechanisms (variously caused by dielectric losses in the substrate $\tan\delta_\varepsilon$, losses in lumped components r_{loss}, or both).

To attempt to determine which of the available tuning techniques could be candidates for combined frequency agility and preservation of efficiency under miniaturisation, the following approach was adopted. Literature surveys were conducted periodically throughout the course of the research. These surveys aimed to determine which of the techniques gaining topical[2] attention could offer

[2]Here, predominantly meaning the period 2014-2016.

highly agile tuning with low loss[3]. Tuneable antenna demonstrators were designed, fabricated and characterised for certain down-selected techniques. Study of these antennas and gaps in the literature was directed towards addressing the questions below:

- What tuning techniques are available or emerging, that can potentially offer simultaneous antenna miniaturisation (i.e. reduction of operating frequency) and tuning (frequency agility)?
- Of these techniques, can any be retro-fitted to non-tuneable antennas? If so, what is the frequency agility and realised efficiency associated with such an approach?
- Are there antenna miniaturisation techniques offering (a) greater frequency reduction than the retro-fit approach, (b) preservation of the efficiency under miniaturisation, (c) tuning? If so, what is the frequency agility and realised efficiency associated with such an approach?
- Could these miniaturisation/efficiency values be equalled or surpassed using a more convenient tuning technology, considering that a more convenient/less costly tuning demonstrator permits a broader study of the tuning concept overall?
- Given everything that has been learned from this research and literature survey about the state of the art in recording antenna "tuneability", is the common approach to reporting tuneability helpful in predicting performance of narrow band antennas under tuning? If the common approach is insufficient, what would a revised approach look like and how does it provide benefit?

The main contributions made by the research presented in this thesis are summarised thus:

- Tuneable matching networks were identified as a conveniently integrated tuning solution. A study on such a network tuned with emerging RF MEMS capacitors analysed the performance of a designed and fabricated example. Frequency agility in free space and successful impedance matching recovery under a hand-effect detuning scenario were achieved. The difference between assumed performance enhancement (improvement in S_{11}) and realised performance enhancement (measured insertion loss / realised insertion gain) was quantified in both cases and used to establish the required insertion loss improvement needed to realise more general system efficiency gains. The typical realised insertion loss of an RF MEMS-equipped network had not been reported at the time of the study, and has now been published in [21].

[3] "Low loss" is a relative term in the context of electrically small antennas, given that the maximum available efficiency is severely constrained by the electrical size. The antenna can be made more efficient just by making it larger relative to the wavelength, hence, for general application of a tuning technique it makes more sense conceptually to seek "low loss".

- Magneto-dielectric Co_2Z engineered ferrite materials were identified as a candidate for significant antenna miniaturisation with efficiency preservation in cases where $\varepsilon_r = \mu_r$. The capacity for tuning in the materials was intriguing, but the agility and efficiency had been widely overlooked. A ferrite was identified, sourced, characterised, and deployed in a tuneable patch antenna design. Miniaturisation was achieved with a frequency reduction factor of up to $6.4\times$ in a ferrite antenna compared to a RT5880 antenna. Impedance tuning range of up to 32% (S_{11} <-3 dB) was attained with a stable radiation pattern [22]. Discussion of the low realised efficiency remains absent from much of the literature regarding such materials, but some of these gaps have started to be filled in [22, 23].

- The common approach to reporting tuneability was found to present significant limitations in predicting performance of narrow band antennas under tuning, and particularly in preventing like-for-like comparisons of tuneable antenna designs. Despite the low efficiencies associated with many tuneable narrowband antennas e.g. electrically small antennas, reference methods to quantify tuneability in terms of tuned range of realised antenna efficiency, average efficiency in the band and integrated efficiency-bandwidth product did not exist and thus had not been widely adopted. An improved approach to quantifying antenna tuneability incorporating these metrics has been formulated and published in [20]. Application to a set of fixed-frequency/varactor-tuned ESAs in the UHF frequency band is demonstrated in Chapter 5. The new approach clearly communicates the discrepancy in tuning range of 10% or 25% realised efficiency compared to S_{11}-derived equivalent measures, justifying a shift to efficiency reporting to understand the impact of tuning on system-level network planning, power consumption and user experience. The new approach provides a platform for future performance grading of a diverse range of antenna tuning technologies, which would help to alleviate the problem of efficient and effective identification of the optimum tuning technology for different antenna applications.

1.4 Thesis structure

The thesis proceeds as follows. Chapter 2 introduces the problem being addressed in defining electrically small antennas and the challenges in their design. Methods of frequency reconfiguration are introduced which are intended to overcome the bandwidth limitations intrinsic to compact and electrically small antennas. Given the mutually incompatible requirements for efficient radiation performance and wide band frequency accessibility in an ESA, many techniques for antenna miniaturisation and antenna tuning have been proposed. The review in Chapter 2 considers a selection of these with regard to the ability to simultaneously provide miniaturisation and tuning to realise the tuneable ESA concept in the low UHF band (300–1000 MHz). From the multitude

of techniques available, a down-selection is made to cover those three main themes selected for further study documented in Chapters 3–5 in more detail.

Subsequently, Chapters 3–5 document the new technical work performed in the course of this research. Chapter 3 presents an initial practical study into frequency-reconfigurable antennas through the use of a tuneable matching network (TMN) emplaced between the feed line and a patch antenna. The performance of the TMN was examined in two scenarios. The first was frequency-tuning of the antenna via reconfigurable impedance matching in free space. The second was fixed-frequency recovery from detuning of the antenna in a user-effect detuning scenario. In each case the realised pattern and efficiency of the tuned system were used as indicators for the propriety of the TMN as a candidate for efficient frequency tuning.

Chapter 4 introduces a magneto-dielectric (MD) hexagonal ferrite material as a candidate for miniaturisation of a microstrip patch antenna. The material offered antenna miniaturisation due to the $\varepsilon_{\mathrm{r}}, \mu_{\mathrm{r}}$ properties combining to give a refractive index greater than 1, compressing the wavelength inside the substrate material. The realised radiation pattern and efficiency of a set of MD patch antennas was compared and contrasted with the same degree of miniaturisation afforded to a geometrically similar patch antenna on conventional dielectric substrate, miniaturised to the same extent using only lumped element impedance matching. In addition, the MD material demonstrated susceptibility to magnetic field biasing (i.e. the permeability μ changes in the presence of a magnetic field). The frequency reconfigurability of the MD patch antennas was documented in the presence of magnetic fields of varying strengths to study the viability of the material as a candidate for delivering practical, efficient tuneable ESAs.

Chapter 5 considers the performance metrics generally used for characterisation of performance of tuneable ESAs. Tuneable return loss derived from the scattering parameter S_{11} is commonly reported in publications concerning tuneable antennas. However, S_{11} in isolation is insufficient to establish the utility of an ESA given the risk of low radiation efficiency associated with losses in the miniaturisation and tuning mechanisms as well as the instrinsic electrical smallness. Hence, a revised approach to efficiency-based assessment of reconfigurable tuning performance is proposed, advancing metrics such as integrated efficiency-bandwidth product. A case study of the use of the new is given for a set of tuneable- and non-tuneable ESAs.

The main findings of the work presented in this thesis are summarised in Chapter 6, with recommendations given for future extensions.

Chapter 2

Review of antenna miniaturisation and tuning

This chapter introduces the limiting factors on the achievable technical performance of a small antenna (i.e. one which is small relative to the operating wavelength). One such limitation is the inevitable reduction in operating impedance bandwidth as the electrical size is reduced, motivating a search for techniques to overcome the bandwidth problem. Thus, a review of antenna tuning techniques is given in general terms, including more detailed review of those that were selected for further study in Chapters 3, 4 and 5. The operating concepts of microstrip patch antennas and small loop antennas are introduced, which are used as candidates for demonstrations of miniaturisation and/or tuning technology in this research.

Electrically small antenna operation not only causes narrow instantaneous bandwidth, but also risks low antenna efficiency. The low initial efficiency of the structure is invariably degraded further by any tuning mechanism introduced, therefore for a tuning study to be considered "complete" a characterisation of the radiating behvaiour (efficiency and radiation pattern) are required. Methods to measure efficiency are discussed, and the method used throughout the research (with minor modifications where appropriate) is described.

2.1 Performance degradation in electrically small antennas

Deployment of a single reconfigurable antenna is inherently a compromised position. The optimal solution for efficient wide band service over a large number of frequency bands would deploy a dedicated naturally resonant antenna for each band, with a switching mechanism to enact band selectivity. The benefits of such a solution would be high efficiencies and broad bandwidth, both of which enable the realisation of high data rates and/or low battery usage. Such a solution

would however be impractical to deploy in many mobile communications terminals, due to the large amount of space required. In addition to needing a large amount of space to accommodate the multitude of antennas, the antennas themselves could become impracticably large in the low ultra-high frequency (UHF) band, bearing in mind that a $\lambda/2$ dipole at 300 MHz would be approximately 50 cm in length. Such an approach is therefore incompatible with user expectations of size and weight for various mobile communication devices.

Physically compact tuneable antennas can address the problem of serving multiple bands in a small space, but there are performance penalties associated with using a non-naturally resonant antenna in terms of bandwidth and efficiency. Any discussion of reconfigurable antennas for mobile applications is therefore incomplete without considering the limits imposed by antenna system compactness, to understand why the poor non-tuneable performance of electrically small antennas (ESAs) cannot simply be tolerated in the first instance for many applications. To motivate the challenges associated with ESA adoption, a definition of bandwidth and efficiency is given here, followed by a description of how reducing the electrical size of the antenna impacts on these parameters.

The antenna is a transducer device tasked with the transmission and reception of radio waves over the transmission medium (here, dry air). While maximum system efficiency is desirable for conversion between electrical signals and radio waves, physics limits the instantaneous bandwidth over which efficient transfer of the signal into the antenna occurs. Furthermore, the antenna system designer must specify the desired general shape of the radiation beam. For some applications such as mobile phone connectivity, it is desirable to be able to receive signals from any direction. For other applications such as digital terrestrial broadcast TV reception, use of an antenna with a beam pointing in one principal direction (i.e. towards the transmitter) is sufficient. Formal measures for these performance criteria are defined below, with methods given for their measurement.

2.1.1 Return loss, impedance bandwidth and matching efficiency

An antenna can be modelled in circuit representation by a reactive load, $Z(f) = R(f) + jX(f)$. The antenna input resistance term $R(f)$ is the sum of the radiation resistance term r_{rad} and loss resistance terms r_{loss} [24, Chapter 2]. Radiation resistance r_{rad} of the antenna records the ability of the antenna to dissipate power through radiation via the Poynting vector $\mathbf{S} = \mathbf{E} \times \mathbf{H}$ [25], while power lost to heating mechanisms in the antenna itself is grouped under loss resistance terms r_{loss}. The tendency of the antenna to reactively store energy through inductive or capacitive mechanisms at radio frequencies gives rise to the antenna input reactance term, $X(f)$.

Resonance occurs at the frequency for which $X(f) = 0$. Resonances are therefore naturally bandwidth-limited, since $X(f)$ can only be small over a certain frequency range. In this case,

the frequency range over which efficient power transfer from the transmission line into the antenna occurs is limited by the impedance mismatch between the characteristic impedance of the transmission line (usually 50 Ω) and the antenna input resistance. The frequency dependence of this behaviour can be measured through use of a vector network analyser (VNA) measurement of the scattering parameter, S_{11} [26, Chapter 4]. S_{11} can be interpreted as a return loss value over a bandwidth, as depicted in Figure 2.1.

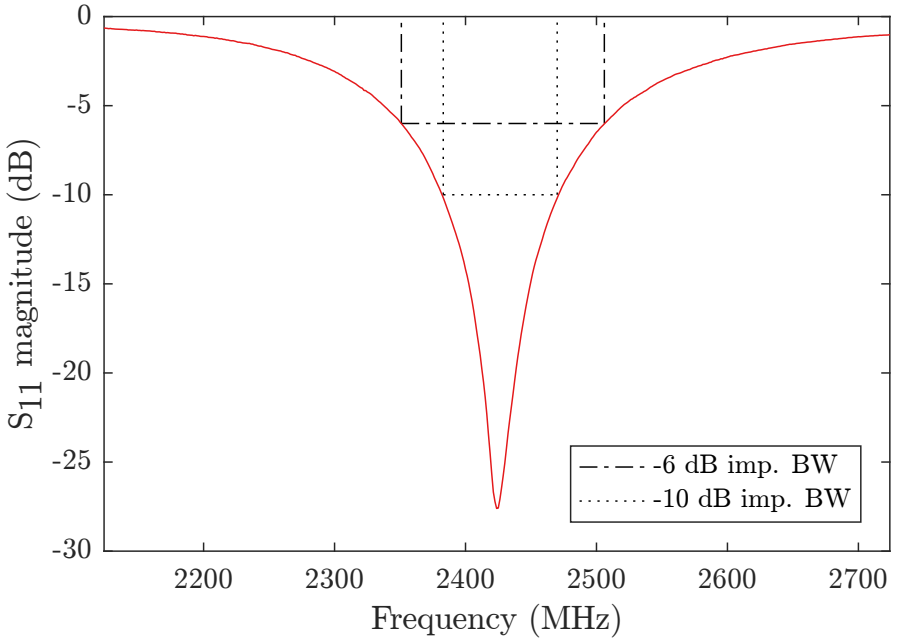

FIGURE 2.1: Impedance bandwidth definitions from measured S_{11}.

The magnitude of S_{11} (usually presented in decibels) is a measure of the fraction of available signal generator power not accepted by the antenna due to the impedance mismatch causing wave reflection [26, Chapter 2]. The magnitude of S_{11} can be measured using a VNA and is related to the magnitude of the voltage of the reflected wave by:

$$|S_{11}| = -20 \log |\Gamma| \text{ (dB)} \tag{2.1}$$

where Γ is the voltage reflection coefficient at the interface between the transmission line of impedance Z_0 and the antenna of input impedance Z:

$$\Gamma = \frac{Z - Z_0}{Z + Z_0} \tag{2.2}$$

For the S_{11} response depicted in Figure 2.1, S_{11} = -27.6 dB is measured at the resonance frequency, 2424 MHz. The impedance bandwidth over which the -10 dB limit is exceeded is 87 MHz, measured between 2383–2470 MHz. Expressed as a percentage of the frequency in the centre of the band, the antenna can be said to have a normalised impedance bandwidth of

3.6%. Alternatively, if the antenna is electrically small and poorly matched, a -10 dB impedance matching range may not be defineable. In that case, a -6 dB impedance bandwidth can be defined instead[1], or *in extremis*, a -3 dB limit can be applied. For the antenna S_{11} measurement given in Figure 2.1, the -6 dB impedance bandwidth is 155 MHz, or 6.4% of the centre frequency.

The measurement of S_{11} permits a measurement of the (linear) impedance matching efficiency to be made. The efficiency with which an antenna accepts power is given by the matching efficiency η_{m}:

$$\eta_{\mathrm{m}} = 1 - \Gamma^2 \tag{2.3}$$

The matching efficiency in Equation (2.3) accounts only for the power loss associated with wave reflection at the junction between the transmission line and the antenna input port due to impedance mismatch. The matching efficiency value does not give an indication of losses in any matching network used, nor the efficiency with which the power accepted by the antenna is converted into radiation. To assess these efficiencies, radiative measurement can be used. A summary and down-selection of efficiency measurement techniques is given in Section 2.4.1.

2.1.2 Definition of antenna smallness factor, ka

A method of quantifying the electrical smallness of an antenna is required. The initial definition of an electrically small antenna was given by Wheeler [19]. Consider a dipole antenna fully enclosed by a sphere of radius a. This sphere is the so-called Wheeler radiansphere, the smallest sphere that can contain the antenna and its feed tracks within its limits. For the antenna to be considered electrically small, the sphere is defined by Wheeler to have a diameter no bigger than one radianlength, $\lambda_0/2\pi$. The radiansphere occupancy of an antenna is commonly recorded through the calculation of the smallness factor ka, where the wavenumber $k = 2\pi/\lambda_0$:

$$ka = \frac{2\pi a}{\lambda_0} \tag{2.4}$$

The dipole fully occupying the radiansphere considered by Wheeler [19] had a length of exactly $l = \lambda_0/2\pi$. Given that the radius of a sphere swept out by this antenna is half of this length, $a = \lambda_0/4\pi$ and the ka factor of Wheeler's hypothesised dipole would be:

$$ka = \frac{2\pi}{\lambda_0} \times \frac{\lambda_0}{4\pi} = 0.5 \tag{2.5}$$

[1] Although an impedance bandwidth of -10 dB is commonly quoted for many antennas, for compact antennas and ESAs less stringent limits have been observed in the literature depending on the application. A required return loss of at least -6 dB is sometimes observed for cellular applications e.g. [27].

Hence, for antennas to satisfy Wheeler's definition of an ESA, the smallness factor must satisfy $ka \leq 0.5$. As a brief example, a naturally resonant dipole of length $\lambda/2$ does not qualify as an electrically small antenna ($ka = 1.57$), while the "small dipole" of total length $l \leq \lambda/10$ such as that analysed in Balanis' popular textbook [24, Chapter 4] would qualify as electrically small, with $ka = 0.314$.

2.1.3 Effect of ka on antenna Q and bandwidth

The value of ka is not a measure of degraded antenna performance in its own right. However, low ka does indicate that the antenna is liable to exhibit electrically small behaviours such as low efficiency and narrow bandwidth. The narrow bandwidth behaviour of ESAs in particular can be highlighted by use of ka, which has been used by various authors to give estimated lower bounds of antenna Q (notably Chu [28], but also McLean [29], Thal [30]). The Q factor of an ESA is a measure of its energy storage behaviour at resonance ($X = 0$), given initially by Chu [28]:

$$Q = \frac{\omega \text{ (average energy stored in resonant circuit)}}{\text{(average energy dissipated per second)}} \tag{2.6}$$

$$Q \approx \frac{\omega \, \mathrm{d}X/\mathrm{d}\omega}{2R} \tag{2.7}$$

Thus, an ESA tuned into resonance by setting $X(f) = 0$ at a sub-resonant frequency is bandwidth-limited by the rapidly changing reactance $\mathrm{d}X/\mathrm{d}\omega$ on either side of the resonance frequency. The high reactance of ESAs below their natural resonance frequencies implies limited impedance bandwidth. A relationship between ka and Q for a lossless antenna was given by Chu [28]:

$$Q \geq \frac{1}{k^3 a^3} + \frac{1}{ka} \tag{2.8}$$

Since it is electrically small, the antenna is not self-resonant at the operating frequency, thus it is assumed that the antenna is tuned into resonance with an ideal (lossless) matching circuit to give purely real input impedance [29]. Though the description of Q given in Equation (2.8) by Chu is the most widely cited, more recent extensions to the modelling of Q have stated improvements in the modelling of the lower limit on Q (e.g. McLean [29], Thal [30]).

The specific differences between Q limits offered by [28–30] are less important for the work conducted in this research than what they have in common: every one of the works quoted contains the cubic dependence on ka, $Q \propto 1/(ka)^3$. Thus, the engineering impact of this theme is that as the physical size of any ESA is reduced, its bandwidth narrows rapidly. For the purpose of this research, the exact Q limits are given less importance than the recognition that the Q can

be broadened by the introduction of losses incurred in construction of a practical antenna. Using additional sources of loss (increased R) can broaden the measured bandwidth but this in turn implies reduced radiated efficiency, as noted by Best [31]:

$$Q = \eta_{\text{rad}} \left(\frac{1}{k^3 a^3} + \frac{1}{ka} \right) \tag{2.9}$$

However, as a strategy the broadening of Q through the inclusion of additional loss is only likely to be successful in scenarios where there is already sufficient radiation efficiency margin that deliberate reduction of efficiency can be tolerated. Unfortunately, ESAs do not provide such a scenario.

2.1.4 Reduced radiation efficiency

Further to the problem of narrow bandwidth, it can be observed that the Q of an ESA can be broadened by introducing sources of loss. However, as the electrical size of the antenna reduces, its reducing physical aperture leads to a corresponding reduction in the radiation resistance r_{rad}. Hence, for an otherwise fixed value of loss resistance r_{loss} comprised of conductor and substrate losses, it can be seen that the overall radiation efficiency η_{rad} is reduced:

$$\eta_{\text{rad}} = \frac{P_{\text{radiated}}}{P_{\text{dissipated}}} = \frac{r_{\text{rad}}}{r_{\text{rad}} + r_{\text{loss}}} \tag{2.10}$$

Thus, methods to broaden the bandwidth of an ESA by means of the introduction of lossy materials are frustrated in practical antennas by the low initial radiation efficiency, even before the inclusion of additional loss sources to decrease the antenna Q are considered. To maintain high efficiency, ESAs benefit from construction using the lowest-loss components and substrates available. Nonetheless, the miniaturisation process itself must be enacted using as many components as are necessary to achieve the required miniaturisation, given that the ESAs are not naturally self-resonant. Considering the high risk of the radiation efficiency of an ESA being low, radiation efficiency measurement is far more critical for an ESA than it might be for say, a metallic horn antenna where radiation efficiencies near 100% might be assumed without measurement.

2.2 Overview of antenna tuning techniques

Given the challenges outlined above, a tuning technique designed to overcome the problems associated with ESAs usage needs to achieve two principal objectives. The first is to introduce a reconfigurable element in the antenna design that allows a greater range of frequencies to be

accessed (by definition, not all at once). The second is to achieve the frequency agility derived from the tuneable element without serious degradation of the limited available efficiency. There is a diverse range of antenna tuning techniques described in the literature, not all of which apply to every frequency band nor communications problem. A selection are described here, which informed the views taken by the author throughout the conduct of this research.

2.2.1 Overall tuning concept

The concept of tuning a narrow band antenna over a broader integrated band is not new, with one example being the voltage-controlled tuning of a microstrip patch antenna using varactor diodes proposed as early as 1982 by Bhartia and Bahl [32]. The authors of that paper declared that by including tuneable capacitance (the varactor) in the antenna aperture, the 1–2% impedance bandwidth typically associated with the patch was broadened to 30% total bandwidth. Thus, from an impedance tuning perspective, the patch antenna was found to be highly tuneable. Since that time, many other techniques have been presented which yield tuneable[2] narrow band compact or electrically small antennas. As a top-level grouping, these techniques include:

- Mechanical antenna reconfiguration (bending or extending the conducting path using spring-like conductors or microfluidic tuning).
- Reconfigurable narrow band impedance matching, or non-Foster matching (i.e. use of negative impedance circuits to cancel the increasing reactance of an antenna with frequency).
- Substrate reconfiguration (changing permittivity ε_r, permeability μ_r or conductivity σ of an antenna substrate material), often with high values of ε_r or μ_r.
- Loading the aperture with tuneable capacitance (using varactor diodes or RF microelectromechanical system (RF MEMS) capacitors).

In general, antenna feed lines have historically been considered to have a fixed impedance of 50 Ω or 75 Ω over the operating frequency range of a radio system, due to the selection of these line impedances as a convention. The matching networks placed between transmission/reception amplifiers and the antenna also present 50 Ω impedance by convention[3]. The complex antenna impedance $Z(f) = R(f) + jX(f)$ however is frequency-dependent. Although the antenna can be designed to provide an input impedance match to the 50 Ω feed line, the rate at which the input impedance varies with frequency limits the operating bandwidth of the antenna.

[2] "Tuneable" in this thesis is taken to mean "frequency reconfigurable" without exception. Pattern-reconfigurable and polarisation-reconfigurable antennas can be constructed but are explicitly not the topic being considered in this thesis.

[3] Exceptions do exist, e.g. [33] which eliminated the 50 Ω "tunnel" and matched the antenna impedance directly to a non-50 Ω impedance presented by an RF front end chip.

Antenna tuning techniques offer the opportunity to construct a "workaround" solution to avoid the core limitation of the Bode-Fano bandwidth theorem, i.e. the instantaneous bandwidth limitation. In brief, the Bode-Fano criterion states that matching a purely resistive feed line to a load of frequency-dependent reactance can only be perfectly reflectionless at one frequency for which $\Gamma(f) = 0$. For all other frequencies, there exists a trade-off between achievable voltage reflection coefficient Γ and the instantaneous bandwidth. Narrow instantaneous bandwidths permit higher performance (less reflective) impedance matching to a frequency-dependent reactive load, as is the case when matching a feed line to an antenna. This is particularly problematic for compact or electrically small antennas, which are typically more reactive than (typically larger) travelling wave or naturally resonant types. The Bode-Fano criterion is defined more fully in Appendix A.

If the intended application permits instantaneous narrow band behaviour over a tuneable frequency range, reduced voltage reflection coefficient can be achieved. This can in turn yield enhanced matching efficiency compared to the scenario requiring instantaneous wide band impedance bandwidth. This concept is illustrated in Figure 2.2, wherein narrow band versus wide band matching solutions are depicted for a hypothetical compact narrow band antenna. How each of the different groupings of tuning techniques functions to achieve this tuning concept is now summarised.

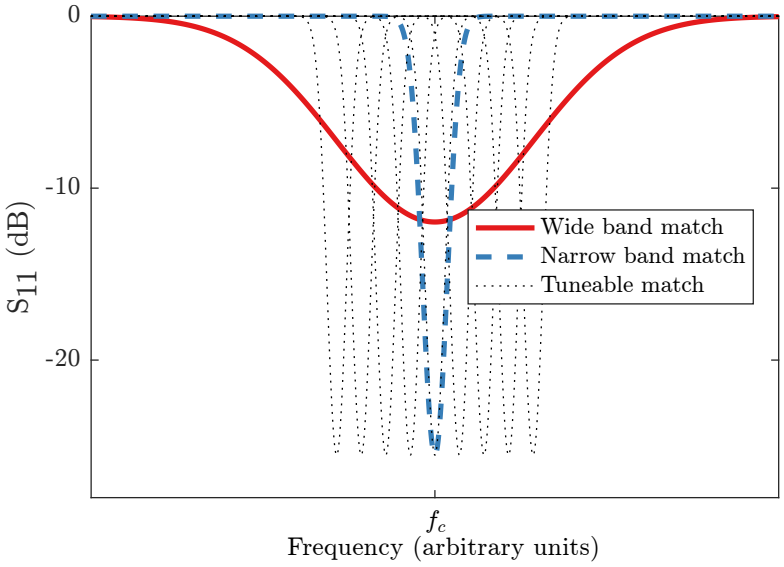

FIGURE 2.2: Conceptual improvement in system performance offered by tuneable narrow band impedance matching network.

2.2.2 Mechanical reconfiguration

Mechanical tuning can be achieved by physically bending or extending the conducting path of the antenna. Such approaches can make use of a motor or solenoid to provide electronically controllable reconfigurable behaviour. Examples include [34] that described a spring-like foldable

helix antenna using paper as a substrate for a copper tape-based conducting path. The length of the helix could be adjusted using a motor, thereby offering electronic control of the antenna behaviour. The example given is representative of a trend with mechanically tuneable antennas: continuous frequency tuning was available, but without any degree of antenna miniaturisation. Without loading the conductor with lumped elements or using tuneable matching, the tuneable UHF antenna in this instance did not confer any size reduction advantage.

Microfluidic tuning can be interpreted as a variant on mechanical reconfiguration of the conducting current path. Antenna substrates can be designed using 3D printing techniques that allow channels to be formed in the substrate. Controlling the presence of liquid metals such as eutetic gallium-indium compounds ("Galinstan") in these channels allows the antenna designer to bend, extend or shorten the current path of the antenna. Hence, changing the radiation pattern or resonant frequency is achieved in a manner not dissimilar to manipulating lengths of wire. A survey of the literature suggests that the use of microfluidics is a topic of present research interest (e.g. [35, 36]), although electrical smallness as a theme does not appear to be under active consideration. The substrate properties are typically constrained by what can be achieved through 3D printing processes, hence high refractive index materials associated with antenna miniaturisation do not seem to feature in microfluidics research. One noteable exception in [36] did report a relatively small top-loaded monopole, wherein the monopole length could be changed to achieve a simulated radiation efficiency of over 50% with a frequency tuning range between 1.8–2.6 GHz but unfortunately the work was not extended to the presentation of measured radiation efficiency data.

Similarly, a microfluidically tuneable antenna was described in [37], with a reported tuneable frequency range of 3.5–3.8 GHz for which the return loss exceeded -30 dB. The antenna itself was a patch antenna microfluidically loaded with varying quantities of different dielectric fluids. These fluids had loss tangents well in excess of $\tan\delta_\varepsilon > 0.5$ and in one case exceeded $\tan\delta_\varepsilon > 1$. Such values are well in excess of the loss tangents associated with substrate materials such as FR-4 ($\tan\delta_\varepsilon = 0.02$). It is quite possible, though as yet unproven, that the tuneable return loss reported in the paper did not translate into an efficient tuneable transmission response. The absence of reported efficiency data leaves that question unanswered.

Since mechanical reconfiguration have not been found to be widely adopted for introducing both tuneability and miniaturisation of the type required for the research (i.e. to implement very compact / electrically small antennas), such techniques are not considered further.

2.2.3 Tuneable impedance matching

It is possible to create an antenna with frequency-reconfigurable performance by placing a tuneable matching network (TMN) in the feed ([38] presents a good introduction). Statically-defined, lumped-element matching networks comprised of L and C components generally offer a means to increase the instantaneous impedance bandwidth of antenna. However, they do so by trading off instantaneous bandwidth against transducer efficiency[4]. Implementation of a TMN with a reconfigurable narrow band frequency response offers the possibility of preserved antenna efficiency across the broader band. Studies to this effect have been given using similar tuneable lumped components to that of the aperture-tuning case, using switches, RF MEMS and varactors. As with claims relating to aperture-tuneable antenna performance, claims relating to suggested efficiency enhancement over a particular integrated bandwidth must be reinforced by measured system efficiency data. A demonstration of improved impedance matching given by increased return loss does not guarantee improved system efficiency once the transducer efficiency (i.e. losses) have been taken into account.

Tuneable narrow band matching concepts for achieving results such as that depicted in Figure 2.2 have been demonstrated in various publications for enhancement of integrated impedance bandwidth [33, 39–44]. Analysis of these revealed a tendency towards omission of radiative characterisation of the realised total system efficiency in a practical implementation, e.g. [33, 40, 41, 43, 44]. Measures of system performance such as the maximum *available* insertion gain can be calculated from the improvement in impedance matching alone described by S_{11}. However, *realised* insertion gain cannot be inferred from S_{11} in isolation due to the effect of losses in the matching network. Such an effect has been noted elsewhere in e.g. [45, 46], but at the time of this study (i.e. contemporaneous with the work conducted in Chapter 3), such loss effects had not been well-documented for practical TMNs in general. An exception exists for [42] which documented the tuning performance of aperture- versus impedance-tuning of an antenna in terms of return loss and radiated efficiency. In some parts of the tuneable frequency range, the return loss of the impedance tuning approach was greater than the aperture-tuned approach. Nonetheless, the measured radiated efficiency of the impedance-tuning system was lower. The authors of that publication noted the impact of losses in the tuning components in arriving at this result.

The necessity to note the impact of losses on realised radiated efficiency is directly relevant to assessing the suitability of commercially available discrete tuning components claiming to address antenna tuning, for example cellular applications, in the light of the increasing number of bands to support in modern cellular handsets (4G/5G and beyond). The shortage of documented radiated efficiencies at the time of the study (2014) was even more pronounced when the search was narrowed to the then "latest technology" for capacitive tuning, i.e. RF MEMS capacitors. At the time of the study, claims were put forward by companies invested in RF MEMS that

[4]Formally, this exchange is described by the Bode-Fano bandwidth limits described in Appendix A.

capacitors based on such technology were preferable to barium strontium titanate (BST) thin film capacitors or semiconductor varactor diodes for matching applications due to their high Q and high linearity characteristics. Quoted efficiency enhancement data were unavailable in the open literature at that time, but capacitor Q values were compared qualitatively in [47]. A quantitative comparison of suitability of each of these technologies would depend on characterisation for the intended application, but by way of indication a comparison of the data sheets for the WiSpry 1050 RF MEMS capacitor bank [48] and the Infineon BB833 varactor diode [49] was made. The MEMS capacitor bank was reported to offer $Q = 200$ at 800 MHz, while the varactor was found by measurement to have a Q factor between 10–50 at 800 MHz depending on the applied bias voltage[5]. Such reported high Q for the RF MEMS capacitors was sufficient to trigger a radiative measurement study to resolve the matter of the realised insertion gain offered by use of an RF MEMS-based TMN for broadening the impedance bandwidth of a compact antenna. This study is described in Chapter 3 as an initial investigation of the potential of a readily integrated tuning technique.

2.2.3.1 Reactive detuning of compact narrow band antennas

In the initial study of the impedance-bandwidth broadening behaviour of the TMN and its transducer efficiency across different frequencies, the antenna itself was considered to exist independently of the environment surrounding it. In practice, environmental effects should be considered in characterisation of the antenna in a commercially realistic deployment scenario within a handset. Deployed antennas in compact terminals can be placed in a compact volume at the edge of the terminal, which exposes them to reactive detuning effects. A commonly cited example is the effect of human tissue (e.g. head, hand, leg) on the antenna, which can detune and shift the resonance [50] and affect the antenna pattern [46]. The extent of this effect has been documented to varying degrees, in terms of signal absorption effects [51] and measured [46, 52] or inferred [53, 54] reduced overall radiated system efficiency due to the impedance shifts away from the well-matched 50 Ω feed line, 50 Ω antenna scenario. Strategies to adaptively match time-varying impedance of the antenna in an automated manner have also been proposed in the presence of various detuning sources: these have included human tissue [55], metallic sheets [56] or even more complex scenarios such as the combined effect of moving human tissue and sea water [57].

The adaptability of TMNs in addressing the matching two arbitrary (potentially time-varying) impedances serves as the basis for much of the demonstrable research interest. To this end, various previous publications have commented on the suitability of TMNs for recovery from user-effect detuning [39, 52, 54, 55, 57]. However, while the potential benefits of reconfigurable impedance matching have been regularly and clearly communicated, the measured impact on total

[5]The measurement procedure is described in Chapter 5.

system efficiency from a transmission efficiency perspective has been far less well documented. Of these noted publications, only one presented measured gain data in the presence of the tuner [39]—the rest relied entirely on reporting of return loss derived from S_{11} for assumed performance enhancement described by S_{11}. Thus, at the time of the study concluded in [21], there was a shortage of openly available measurements of loss in a practical implementation of such TMNs in user-effect detuning scenarios. It was noted in [58] that the power dissipated in matching components is load-dependent and as such, use of a tuning network for impedance mismatch recovery is only justified if the losses associated with implementation do not exceed the compensated mismatch loss.

The contribution of [46] is noteable in highlighting the difference between apparent improvement in system efficiency through increased return loss, and the actual loss of radiative system efficiency associated with a body-effect detuning scenario. A study of user-effect detuning was considered, wherein the radiated efficiency of an ultra wide band antenna operating between 4–9 GHz was measured as a function of the spacing between the antenna and the chest cavity of a human test subject. The authors observed that recording S_{11} was insufficient to predict the loss of radiated efficiency associated with reduced spacing between the antenna and the chest. Measurement of power accepted into the antenna (S_{11}-derived $1 - \Gamma^2$) showed "enhanced" impedance bandwidth, insofar as the -10 dB impedance bandwidth was greatest for a spacing of zero, i.e. with the antenna placed against the chest. However, such a measurement in isolation ignores the effects of radiation coupling into the body and being strongly attenuated. The subsequent radiative characterisation found a 17.6% reduction in realised radiation efficiency. Thus, enhanced impedance bandwidth given by S_{11} was not associated with improved antenna performance in this instance. The studies concluded in [41, 53] reported on the use of TMNs or feed tuners designed for recovery from mismatch between the feed line and the load impedance presented by the antenna, but reporting in these cases was limited to S_{11}-derived performance. The contribution of [46] highlighted the need for radiative assessment of the total realised system performance in user-effect detuning scenarios, but did so in the absence of a tuner. There is a need for a study of realised efficiency enhancement (or lack thereof) in a scenario where user-effect detuning is counteracted by a practical tuner. Thus, in Chapter 3 a study was conducted wherein a hand phantom was fabricated and used to detune an antenna. The realised system efficiency with and without recovery from impedance mismatch using the RF MEMS based TMN was radiatively characterised, as documented in [21].

2.2.3.2 Non-Foster techniques

Considering alternative techniques to broaden the impedance bandwidth for compact antennas and especially ESAs, the non-Foster matching technique had also received attention in the contemporaneous literature (up to 2015), e.g. [59–62], among others. ESAs are recognised to have largely reactive impedances that increase with frequency [19], presenting a challenge for

impedance matching. In commonly deployed passive impedance matching, the reactive part of the impedance is "resonated out" at a single frequency. However, if a circuit can be emplaced creating a negative reactance effect, the increasing reactance could be cancelled over a much greater bandwidth. Such non-Foster circuits aim to achieve this through use of transistor-based negative impedance converter circuits (NICs) which can invert a connected reactance (e.g. $+C$ becomes $-C$). However, this does require a good description of the antenna equivalent circuit, which is generally only accurate over a narrow band. Many papers in the field use curve fitting to find the effective L, C of the antenna at a single resonance e.g. [63, 64]. The sensitivity of the system to getting the right L, C values to invert can be extreme - one still has a problem of increasing sensitivity to component values as the electrical size reduces. Nonetheless, total reactance cancellation leaves only the real antenna impedance to match, which varies much more slowly with frequency. Thus, if negative reactors can be designed to operate efficiently over wide bandwidths, then a match between a highly reactive load and a resistive feed line becomes feasible [59].

The challenges of non-Foster design include addressing the applicable frequency range (many studies appear to be in the low VHF band), network stability considering the presence of transistors, and network efficiency. Various works contemporaneous with the research presented in this thesis (e.g. [65]) noted that measurement of S_{11} in isolation is insufficient to declare performance enhancement at the system level, although that work did go on to suggest that radiation efficiency "above 100% is possible" using non-Foster techniques. Such a claim suggested that a radiative study of the performance of non-Foster technologies would have been a welcome contribution to the domain, especially in comparison to a tuneable matching technique. Regrettably, time constraints prevented such a study being included in this research. Revisiting the state of the literature for non-Foster techniques in 2019 indicates that the lack of efficiency reporting has started to be addressed, but surprisingly is reported in a minority of cases. A brief review of the most recent (2017-2019) results for "non-Foster antenna" on IEEE Xplore found that of the first 50 results, only two [66, 67] mention actual efficiency values (23%, 43% respectively). This is problematic when most papers comment on the efficiency and bandwidth challenges of ESAs as a prime motivation. Some researchers make use of "insertion gain"-like measures but the findings of Chapter 3 will subsequently demonstrate that such measures do not necessarily amount to high efficiency under miniaturisation. A +20 dB insertion gain on a very small antenna can readily transpire to be less than 10% efficient at the radiative level [68].

2.2.4 Substrate reconfiguration

For printed antennas, tuning can be achieved through reconfiguration of the substrate properties. If the permittivity, permeability or conductivity can be controlled, a continuously tuneable antenna can be formed. Use of materials of variable conductivity has been shown in [69], wherein

laser-actuated optical tuning changed the substrate properties of a slot antenna printed on silicon. The authors proposed tuning without the use of varactors or RF MEMS as a means to tune antennas in scenarios requiring greater linearity and power handling than that offered by the use of such discrete components. However, the antenna presented was operated at a significantly higher frequency than those considered in this research (4–6 GHz as opposed to hundreds of MHz). Scaling the technique up in physical dimensions to operate in the UHF band implies the need for a larger physical area of silicon illumination. The authors also acknowledged the need for relatively high power DC supplies for the lasers at that time (2017), but expressed optimism that advances in laser and LED technology will render the optical tuning prospect viable for linearity-critical tuning scenarios such as cellular radio base-station usage in the future.

Moving away from tuneable conductivity, there exist materials that offer tuning of the dielectric permittivity ε_r or magnetic permeability μ_r. Ferrite materials can serve in this role if operated in ferroelectric/ferromagnetic or paraelectric/paramagnetic phase. Ferroelectrics are a subset of materials that have a permittivity dependent on an externally applied **E**-field [70]. One material widely reported upon is BST, which can be designed quite flexibly in RF performance terms, depending on the ratio of barium to strontium used in the composite [71]. BST demonstrates intrinsic tuneability of ε_r under an externally applied electric bias field[6]. BST exhibits very high ε_r which yields physically small components, but its operating region of high tuneability coincides with high dielectric loss [72]. Subsequently, a common complaint relating to the usage of BST components, particularly as substrates, it that the tuneability benefits are severely restricted by the low system efficiency [73].

BST is a particularly popular material of interest at microwave frequencies since its paraelectric and paramagnetic phase transitions occur below room temperature, yielding far higher tuneability than ferroelectric phase materials. The high ε_r offered by these materials suggests a degree of volume minimisation can be achieved by using a high permittivity substrate, although it can be lossy to do so. Tuneable liquid crystal techniques also constitute a modification of the substrate [73], as liquid crystals give molecules within the liquid freedom to move and thus to align with an externally applied field. The varying net orientation of the molecules yields tuneable dielectric constant. However, in common with tuneable ferrites, liquid crystal tuning techniques in the microwave region demonstrate low efficiency. Tuning of approximately 4% normalised frequency range and efficiencies of 20–40% were demonstrated at 5 GHz in [74], but the author is not aware of demonstrations of tuneable liquid crystal antennas applied to the low UHF band.

[6]Perovskites such as BST generally have the structure of $CaTiO_3$, with a cubic structure with oxygen occupying the face centres of the cubes. The tuneability of ε_r stems from the electric dipole generated by off-centre displacement of the transition metal cation under an externally applied electric field bias. The non-zero net effect of dipole moments within the material results in a change to the dielectric permittivity exhibited.

2.2.4.1 Antenna miniaturisation using magneto-dielectric (ε_r, μ_r) substrate

Considering the potential for antenna tuning with ferrite materials, it is noteable that materials offering very high ε_r are not the only way to achieve a high miniaturisation factor. Magneto-dielectric (MD) materials offer both permittivity ε_r and permeability μ_r greater than unity. As such, there are dielectric and magnetic wavelength compression effects. Thus, an antenna can be miniaturised without over-reliance on high values of ε_r. Furthermore, such materials can contain tuneable ferrite compounds, offering a degree of antenna tuning. Such engineered materials, especially those with the property $\varepsilon_r \approx \mu_r$ were the subject of research interest in the materials science literature at the time of initiation of this project (autumn 2014). Reporting of the potential convenience of such materials for antenna use had been noted, but reported results applied to actual antenna designs were in very short supply—even more so when the need for radiative characterisation (i.e. realised efficiency and pattern) were considered.

The physical size of an antenna for a fixed frequency can be reduced by loading the antenna aperture with a substrate having particular properties. Inside a material of refractive index $n = \sqrt{\mu_r \times \varepsilon_r}$, a wave of free space wavelength λ_0 is retarded by a factor up to n. The resulting compression of the wavelength causes electrical lengthening, thus antennas of fixed dimensions incorporating such materials have a tendency to operate on a lower frequency than their physical dimensions would otherwise suggest. Materials exhibiting both $\varepsilon_r > 1$ and $\mu_r > 1$ can be classed as magneto-dielectric (MD) materials. Two available methods for achieving an MD material are the construction of artificial metamaterials [75] and the construction of engineered ferrite materials [76]. In the metamaterial approach, the realised effective ε_r and μ_r values[7] emerge from the periodic nature of an array of unit-cell based resonant structures such as grounded patches or split-ring resonators [78]. In the engineered ferrite approach a compound material can be created by blending ferrite powders in different ratios and sintering them together to yield a compound ferrite block with the required ε_r, μ_r properties. For this research, the engineered ferrite approach was selected based on the combined interest in miniaturisation and tuning. Either approach can in principle be adapted to permit frequency tuning of the antenna: in the case of the structured metamaterial, the underlying unit cell elements could be electrically tuned using, for instance, varactors. However, given the periodic nature of the substrate structure, in practice such tuning may be difficult to achieve, possibly requiring DC biasing control lines to be printed without affecting the RF performance of the structure.

Antenna miniaturisation based on the refractive index properties of the substrate is commonly observed for patch antennas constructed using a purely dielectric substrate of $\varepsilon_r > 1$. Such an

[7] In an artifical metamaterial, these values need not be positive as they are in real materials. ε_{eff}, μ_{eff} or both can be negative [77], introducing a phase behaviour opposite to that of a normal material. The effect is this is that a "quasi-static" resonance behaviour can be created in the material, leading to outcomes such as antennas that have an operating frequency independent of their physical dimensions.

antenna is miniaturised by a factor up to $\sqrt{\varepsilon_{\mathrm{r}}}$ (Section 2.3.1, below). From Equation (2.12), the dependence on n rather than ε_{r} in isolation indicates that linear increases in ε_{r} yield ever-diminishing returns on the maximum achievable miniaturisation factor. The use of an MD substrate permitting control over magnetic permeability μ_{r} in addition to ε_{r} affords the designer a much more rapid potential rate of miniatursation through increasing refractive index n. Alternatively phrased, for a desired antenna miniaturisation factor limited by n, the use of an MD material permits lower values of ε_{r}, μ_{r} to be used for given n than if ε_{r} were to be increased in isolation. In practice, commonly available dielectric materials only exhibit ε_{r} values up to roughly 10 (e.g. materials such as RT6010 [79]). To achieve miniaturisation factors greater than $1/\sqrt{\varepsilon_{\mathrm{r}} = 10}$, the antenna designer could turn to extremely high-valued dielectric substrates such as BST with ε_{r} reported with values over 1000 [80]. BST offers very high ε_{r} and is also paraelectric offering great tuneability, however this regime coincides with large degrees of loss [72], ultimately harming antenna efficiency [73].

The use of a relatively balanced choice of ε_{r} and μ_{r} is reported to provide various benefits compared to use of exceedingly high ε_{r}. The work conducted in [81] indicated that in a loss-free scenario, MD substrates are preferable to extremely high ε_{r} substrates since the reduced ε_{r} associated with increasing $\mu_{\mathrm{r}} > 1$ for given n implies a reduced bandwidth penalty for the same miniaturisation. Arguments presented in the literature also contend that those MD substrates satisfying $\varepsilon_{\mathrm{r}} = \mu_{\mathrm{r}}$ could offer greater antenna efficiency due to improved impedance matching of the antenna substrate to the medium, whereas increasing ε_{r} in isolation reduces impedance matching to the medium [82, 83] or creates difficulty in impedance matching the antenna to the feed due to narrow instantaneous bandwidth [84]. The wave impedance in the substrate is given by [85]:

$$Z = \sqrt{\frac{\mu_{\mathrm{r}}\mu_0}{\varepsilon_{\mathrm{r}}\varepsilon_0}} = \sqrt{\frac{\mu_{\mathrm{r}}}{\varepsilon_{\mathrm{r}}}} \times 377\ \Omega \tag{2.11}$$

From Equation (2.11), it is implicit that increasing ε_{r} in isolation reduces the wave impedance of the material, an effect which has been alternatively described as reducing the characteristic impedance of the antenna [86]. The wave impedance mismatch between the substrate and the medium therefore becomes more pronounced in antennas that have been miniaturised by use of high permittivity substrates. Only MD substrates, offering control over both ε_{r} and μ_{r}, can offer wave impedance matching to the vacuum. This feature has stimulated research into the design of such $\varepsilon_{\mathrm{r}} = \mu_{\mathrm{r}}$ materials [82, 83, 87, 88], with onward application to antennas demonstrated in [89, 90]. However, balanced-impedance material antennas by no means dominate the field of MD antennas, with numerous relevant contributions featuring MD antennas without the objective of satisfying $\varepsilon_{\mathrm{r}} = \mu_{\mathrm{r}}$ [86, 91–96]. The proposed advantages of satisfying the balanced-impedance criterion are reduced electric field confinement leading to increased bandwidth [86, 94] and greater antenna efficiency [70]. The latter point in particular regarding efficiency warrants

testing of the radiated performance of any such antenna given the presence of potentially quite lossy ferrite compounds. However, at the time of the work presented in this thesis being conducted (2015-2017), there remained a shortage of reporting of realised radiation efficiencies for antennas incorporating such materials. A more recent review conducted in 2019 found that it remains the case that most papers do not report all of: the complex ε over the complete frequency range, the complex μ across the complete frequency range, or the methods used to determine simulated/measured efficiency–examples of which include [97–100] among others. This assessment is broadly in line with that given in a recent topical review of trends in antenna miniaturisation [76], which stated that engineered ferrite materials offer profound miniaturisation potential but require more experimental work to be conducted. The work presented in this research [23] aimed to address the shortfall.

2.2.4.2 Hexaferrites as a choice of engineered MD ferrite substrate

An engineered MD ferrite material was sought which approximately satisfied $\varepsilon_\mathrm{r} = \mu_\mathrm{r}$ for a study of antenna miniaturisation and tuneability. Of the many known ferrite compounds, not all are suitable for this purpose since the complex relative permeability μ^* in particular varies greatly as a function of frequency and ferrite type. For example, at UHF frequencies the spinel and Ni-Zn ferrites associated with ferrite bead RF chokes would cause unacceptably high levels of loss [93]. Hexagonal ferrites however transpire to be relevant candidates for the study of $\varepsilon_\mathrm{r} = \mu_\mathrm{r}$ antennas in the lower UHF band. Their ferromagnetic behaviour offers a degree of μ_r tuneability that can be exploited to create a tuneable antenna, while the lossy ferromagnetic resonance effect exhibited in all ferrites is generally considered to occur above 1 GHz.

Hexaferrites are comprised of a compound of barium (Ba), cobalt (Co), iron (Fe) and oxygen (O). Hexaferrites are available in different "material phases," i.e. various ratios of $\mathrm{Ba}_w\mathrm{Co}_x\mathrm{Fe}_y\mathrm{O}_z$ where differing ratios of $\{w, x, y, z\}$ create materials with different electromagnetic properties [85]. Iterative refinement of the starting compounds and processing techniques have yielded materials with approximate $\varepsilon_\mathrm{r} = \mu_\mathrm{r}$ behaviour in the literature, however the loss tangents $\tan\delta_\varepsilon$ and $\tan\delta_\mu$ are artefacts of the processing history of the material. While minimum combined loss tangent is desirable in antenna applications, there is no guarantee that this coincides with the frequency for which $\varepsilon_\mathrm{r} = \mu_\mathrm{r}$. In fact, the frequency associated with minimum loss tangent did not coincide with the frequency for which $\varepsilon_\mathrm{r} = \mu_\mathrm{r}$ in any of the reviewed publications.

For this project a hexaferrite compound was sought which would offer $\varepsilon_\mathrm{r} \approx \mu_\mathrm{r}$ over a relatively large band (hundreds of MHz), within which the antenna behaviour was studied at the frequency of lowest loss tangent. The material identification work is described in Chapter 4.

2.2.4.3 Tuning in hexaferrite materials

The hexagonal ferrite intrinsically offers a degree of frequency tuning due to the presence of ferromagnetic compounds in the substrate. In ferromagnetic tuning, application of a static magnetic field to the substrate reduces the magnetic dipole anisotropy within the material lattice [101]. The alignment of the magnetic dipoles with the field leads to an increase in the material's net magnetisation **M** and a reduction of eddy currents forming in the material, reducing both real and imaginary components of complex μ^*. In principle, a patch antenna should demonstrate increased operating frequency due to lower μ_r (Equation (2.12), while the reduced magnetic loss tangent $\tan\delta_\mu$ offers the prospect of improved antenna efficiency (Equation 2.14). However, while various works have demonstrated tuning in ferrite-based antennas before (e.g. a hexaferrite example in [89]), the impact of the latter point (tuning of $\tan\delta_\mu$) on antenna efficiency is not known to have been assessed through radiative characterisation. This has been addressed through the work described in Chapter 4, as published in [22, 23]. In principle, a ferrite material can also offer ferroelectric tuning under external **E** field biasing. In practice, brief preliminary studies suggested that the tuning effect would be extremely weak compared to magnetic tuning. This finding was consistent with the findings of [102], wherein an electric field bias strength of 5 kV/cm achieved a frequency shift of just 1.3% in the UHF band. Thus, ferroelectric properties of the hexaferrite are not discussed further.

With regard to the balanced-impedance criterion $\varepsilon_\mathrm{r} = \mu_\mathrm{r}$, it is notable that no tuning mechanism is known to simultaneously tune ε_r and μ_r. Hence, the balanced impedance criterion cannot constantly be satisfied under tuning: voltage-biased ferroelectric adjustments would modify ε_r, while magnetically-biased ferromagnetic adjustments would vary μ_r. The use of combined ε_r, μ_r nonetheless offers miniaturisation without reliance on extreme values of ε_r or μ_r.

For completeness, the tuning behaviour of the hexaferrite material should be given with respect to a characterisation of its Curie temperature. The Curie temperature T_C represents temperature above which the material exhibits a regime change from ferromagnetic behaviour to paramagnetic behaviour. In the paramagnetic regime, changes in μ^* per unit of magnetic bias become much more pronounced. BST has a Curie temperature below realistic operating temperatures, leading to high tuneability that drives its popularity as a candidate for electrically-biased tuning applications. The relevance of the Curie temperature to ferromagnetic antenna tuning however appears not to have been matched by widespread interest in the antenna literature. None of the works reviewed for ferrite tuning in general considered the impact of Curie temperature on the tuneability observed in the antenna. Unfortunately, equipment unavailability precluded further examination of the topic during the course of this research.

2.2.4.4 Review of related hexaferrite antenna publications

A selection of relevant antenna designs is summarised here. The selection is limited to works that incorporate hexaferrites in the antenna design, whether the hexaferrites are intended to exhibit the balanced-impedance criterion or not.

Various miniaturised antennas have been reported with hexaferrite elements, including wire-wound conductors on hexaferrite chips serving in applications from very high frequency (VHF) T-DMB applications [90, 103] up to microwave applications at 2.44 GHz for unmanned aerial vehicles (UAVs) [96]. The inverse of this, a conducting rod contained within a hexaferrite cuboid for a similar frequency band was reported in [93]. Patch antenna designs have been reported using solid tile substrates [89, 91], flexible substrates [104] or a lattice of hexaferrite bars [92]. While all of these works reported antenna miniaturisation, varying approaches to performance analysis especially with regard to the treatment of loss tangent and efficiency led to differing conclusions on the applicability of the antenna to various communication problems.

Where high radiation efficiencies have been reported, these appear to be limited to designs using hexaferrite chips as loading elements such as [90, 92, 103], where the miniaturisation is less pronounced than that observed in conventional patch designs due to the lower filling factor. Conventional patch designs often achieve greater miniaturisation [89, 91, 94, 104] but the utility of these designs for common communication problems depends on whether loss tangent and efficiency have been given full consideration. The works of [89, 91] overlook loss tangent, wherein LTE MIMO is proposed as a possible application. Without an analysis of loss tangent, this view may be compromised by low radiation efficiency.

In contrast, works presenting detailed analysis of the loss tangents in hexaferrite patches such as [104] advance the view that hexaferrite patches are mostly applicable to short range communications such as RFID or health monitoring. The low gain of even relatively low-loss hexaferrites makes hexaferrite miniaturisation best suited to cases where miniaturisation is of paramount importance compared to concerns of efficiency, given the form factor requirements.

Considering the body of hexaferrite antenna literature, there exist a variety of designs that either offer efficiency (the wire-wound designs) or pronounced antenna miniaturisation (the patches). None of the observed designs could truly be said to offer both, as the more efficient designs did not approach the upper limit on miniaturisation factor offered by the refractive index (n^{-1}). The relevance of hexaferrites to the UHF band is clearly demonstrated by the application of hexaferrites at frequencies from 198 MHz [90] to 2.44 GHz [96]. While new hexaferrite materials offering various losses and $\varepsilon_{\mathrm{r}}/\mu_{\mathrm{r}}$ ratios continue to be proposed in the materials science literature, there is a general shortage of reported hexaferrite antenna designs offering a characterisation of material loss tangent and the final realised antenna efficiency in the corpus of work.

In addition to the shortage of reported efficiencies, there is a shortage of reported 3D radiation pattern behaviours. Knowledge of the 3D pattern is important for establishing the suitability of an antenna for application to multipath scenarios. The hexaferrite patch antenna examined in this work will be shown in Chapter 4 to preserve the key features of the patch antenna under miniaturisation, namely broad-beam behaviour and a lack of nulls in the majority of the forward hemisphere. Competing approaches to antenna miniaturisation such as impedance matching to a sub-resonant frequency is occasionally advanced as a solution, but the impact of this on changing the antenna pattern and particularly efficiency is generally overlooked (e.g. [105]). A comparative analysis of these approaches is only possible through measurement of the 3D pattern, which is not known to have been conducted elsewhere. Work presented in Chapter 4 and [22] addresses this by comparison of measured 3D patterns for a hexaferrite patch and a sub-resonant impedance matched patch, accompanied by reporting of the efficiency.

Finally, all of the hexaferrite antenna designs presented in the literature should be at least partly tuneable under magnetic bias conditions, given that hexaferrites are intrinsically ferromagnetic. A single example of magnetically biased frequency agility in a hexaferrite patch was observed in [89], but the use of an external Helmholtz-coil type variable-**B** biasing solution would not have easily permitted calculation of the radiated efficiency. Thus, the impact of substrate-enacted tuning of a fabricated hexaferrite antenna is not known to have been examined. An initial assessment of magnetic tuning of a hexaferrite patch antenna is presented in Chapter 4 and [22].

2.2.5 Tuneable aperture loading with capacitance, inductance and switches

Rather than changing the physical length of the conductor as described above for mechanical antenna reconfiguration, the addition of well-placed inductance or capacitance can adjust the effective electrical path length taken by the current flow in the antenna. Recent examples of the aperture tuning approach include use of RF switches [106, 107], varactor diode [108–116], RF MEMS [117] and CMOS [118] tuneable capacitors, PIN diodes [119].

Here, approaches seeking continuous frequency tuning were sought. In practice, the lack of compact tuneable inductors typically limits this discussion to the use of tuneable capacitance. Such an approach was first described for a tuneable patch antenna by [32], turning an otherwise non-tuneable patch antenna into a tuneable copy through the addition of a varactor diode. The aperture-loading technique has been reported elsewhere in various scenarios, with the tuneable capacitor being derived from a technology offering some variation in the parallel-plate capacitor equation, $C = \varepsilon_0 \varepsilon_\mathrm{r} \frac{A}{d}$. A is the plate overlap area and d is the separation between plates. Variable capacitor types such as tuneable BST capacitors and reverse-biased semiconductors (“varactor” diodes) make use of tuneable ε_r. Trimmer capacitors make use of varying mechanically adjusted

plate overlap. RF MEMS capacitors can be constructed from two sprung metal beams, the separation d of which defines the capacitance.

Various antenna designs have been proposed using each of these types of capacitor. Selection of any of these types of capacitor is dependent on compromise between competing factors including the available capacitance values, commercial availability and loss effects in the component. The component Q directly affects the realised antenna efficiency, thus it takes on increased significance in an ESA wherein the tolerance of loss effects is diminished considering the risk of low radiation resistance. Varactor diodes readily offer tuning under voltage control, but with modest component Q and the risk of non-linear effects associated with the use of a biased semi-conductor device during transmission. Trimmer capacitors offer higher component Q [original measurements, Chapter 4] but require user intervention to tune the operating frequency. RF MEMS devices are quoted as having high Q compared to varactors and BST capacitors by companies promoting MEMS technology [47], but such devices could not be readily procured on the open electronics market at the time of writing (2018). As such, performing a like-for-like comparison for an arbitrary antenna design requiring arbitrary values of C was not possible. Therefore, ambitions for practical measurement work involving antennas (as opposed to a simulation-only study) needed to be tempered by component availability. An antenna design based on a capacitively-tuned small loop is discussed further in Chapter 5, a review for which is presented below in Section 5.1. Reported tuning ranges and efficiencies from this work are given for aperture-tuned loop antennas using both trimmer-capacitor and varactor diode capacitors [20].

In addition to the methods described above for continuously tuneable capacitance, it should be noted that it is also possible to achieve frequency reconfiguration by switching between different conductor tracks, each including a different lumped capacitance. Such switching does not constitute continuous tuning according to [120], but has nonetheless been marketed for use in cellular handsets (e.g. Qualcomm market a product that works in this manner [121]). Use of fixed-value capacitors benefits from increased component Q compared to tuneable counterparts, while switching between different conductor tracks can offer multi-band operation without using lumped capacitors at all. However, the former approach does not offer the maximum design flexibility, considering the trend for an increasing number of bands to support in each device. The latter technique does not necessarily lead to antenna miniaturisation. A hybrid solution using both switching of lumped capacitors and a single varactor for fine-tuning has been documented in [122] with some success, giving a reported efficiency of 22–80% over the DVB-H frequency band (470–702 MHz), although the pattern stability over the band is not clear from the results.

2.3 Antennas developed (AUTs)

Popular textbooks on antenna engineering describe a wide array of many different types of antenna for all applications [24, 123]. Of these, a research need for antennas acting in the compact or electrically small regimes led to selection of test antennas to be developed. The antennas designed in this research as devices of interest can be categorised into two types: patch antennas and small loop antennas. This choice was driven by necessity for candidate structures offering both miniaturisation potential and an ability to demonstrate some type of frequency-reconfigurable behaviour under tuning (either feed line tuning or aperture tuning). In this research, patch antennas fitted this description through use of a tuneable matching network or a tuneable magneto-dielectric substrate. Meanwhile, the small loop antennas were both miniaturised and tuned by creating the antenna from a printed tuneable RLC circuit with variable lumped capacitance, C.

A summary of the main operating concepts of these antennas and their construction are given below. Two types of microstrip patch antenna were designed for this project. One was used as a target for impedance tuning in Chapter 3, while the other was a test subject for miniaturisation via increased refractive index of the substrate in Chapter 4. A printed aperture-tuneable small loop was designed and analysed which is presented in Chapter 5.

2.3.1 Microstrip patch antenna

The microstrip patch antenna has been popular since the 1970s in high UHF and microwave frequency applications due to its physically compact form factor and planar profile [24, Chapter 14]. Such properties permit its inclusion in various portable communications terminals as well as in flush-mounted layouts for aerospace and vehicular applications [123, Chapter 3]. The microstrip patch can be fabricated on a copper-clad dielectric substrate by etching with conventional printed circuit board (PCB) production techniques such as laser etching, hence the microstrip patch lends itself to integration with transmission line feeds and matching networks at the PCB production stage, often at minimal additional cost. The patch can be fed using a probe (such as the centre conductor of an SMA connector) or edge-fed by a printed transmission line. Other feed techniques such as slotted feeds existed (e.g. those detailed in [124, Chapter 2]) but were not used in this project. A diagram of the main dimensions and a fabricated patch are shown in Figure 2.3. A more detailed treatment of the patch antenna is given in [123, Chapter 9].

Antenna size reduction is performed most commonly by increasing the dielectric permittivity ε_{r} of the substrate upon which the antenna is fabricated. Commercially available dielectric substrates for varying applications include low cost FR-4 ($\varepsilon_{\mathrm{r}} = 4.3$, [125]) and low-loss Rogers RT5880 ($\varepsilon_{\mathrm{r}} = 2.2$, [126]). The frequency of operation of the lowest $\lambda/2$ resonant mode (i.e. TM_{10} in the

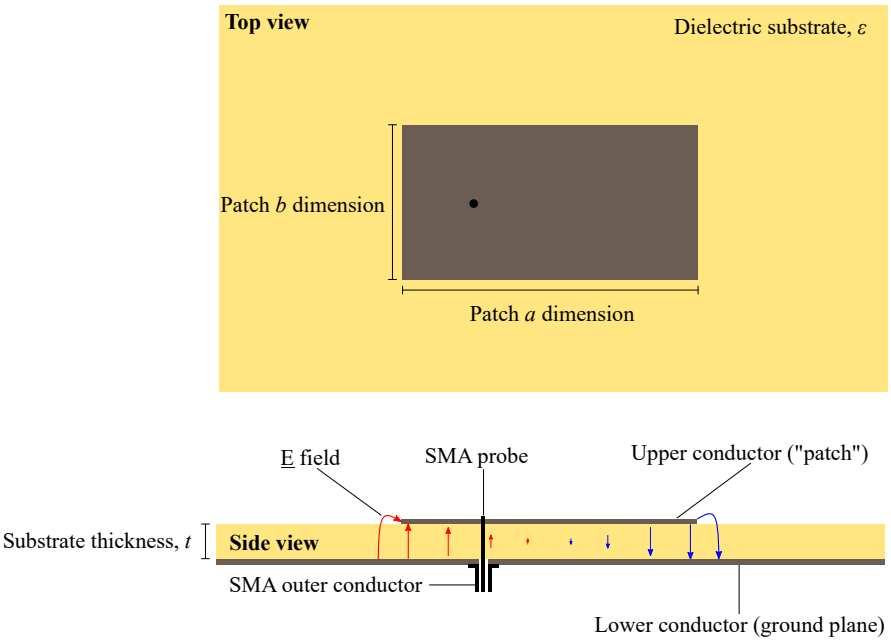

FIGURE 2.3: Patch antenna concept illustration. The radiation derives from the fringing **E**-fields at the patch edges.

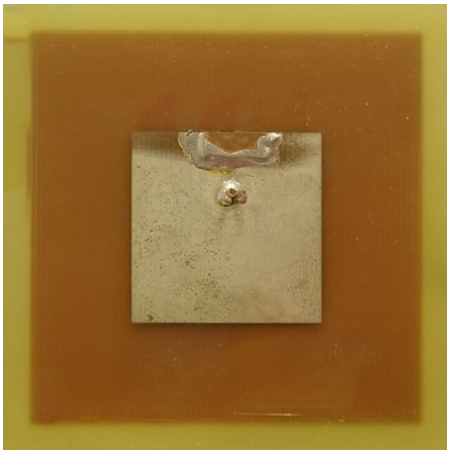

FIGURE 2.4: Fabricated (square) patch antenna.

structure) is given by Equation (2.12), where i, j are mode indices, n is the refractive index of the material and $a_{\text{eff}}, b_{\text{eff}}$ are the effective[8] patch edge lengths:

$$f(\text{TM}_{ij}) \approx \frac{c}{2n}\sqrt{\left(\frac{i}{a_{\text{eff}}}\right)^2 + \left(\frac{j}{b_{\text{eff}}}\right)^2} \tag{2.12}$$

Impedance matching the patch can be achieved by placing a 50-Ω feed pin at a carefully selected position on the patch face. For the $\lambda/2$ mode shown in Figure 2.3, the patch impedance is maximum at the outside edge of the patch ($|Z| = \frac{|E|}{|H|}$, with maximum $|E|$ and zero $|H|$ due

[8]With reference to Figure 2.3, the effective length of the edge of a patch is given by its physical length plus the extensions given by the fringing **E** field.

to the current being zero). The impedance is zero in the patch centre ($|E|$ is zero). Finding an impedance match to 50 Ω is achieved by moving the pin out from the centre of the patch towards one of the edges. This matching technique was used for the patch in Chapter 3 and the feed position to a first approximation is described by:

$$R_{\text{input}} = R_{\text{edge}} \cos^2\left(\frac{\pi x}{a_{\text{eff}}}\right) \tag{2.13}$$

where x is the input position from the centre ($x = 0$ is the outer edge of the patch, $x = a_{\text{eff}}/2$ is the centre giving $R = 0\,\Omega$). The matching technique in Chapter 4 was similar, but since the MD could not be drilled through to allow an SMA male pin to be placed on the patch, an edge-fed approach was used instead. The overall principle is similar. A feed strip was moved out from the centre of the patch towards the outside edge, along the longest edge of the patch. The dependence of the feed position on edge resistance (half the radiation resistance) can be observed for the different substrates in Chapter 4: using substrates with lower loss and lower ε_{r} (giving less miniaturisation and greater electrical size) led to higher radiation resistance and higher edge resistance, requiring the feed to be placed closer to the patch centre.

Patch antennas overall are classified by [123, Chapter 3] as resonant-type, in the same category as $\lambda/4$ wire monopoles and $\lambda/2$ dipoles. Unlike the monopoles and dipoles however, the compression of the electrical size induced by the substrate leads the patch to be a narrow band device. The bandwidth is noted to reduce as the miniaturisation is increased by increasing ε_{r} [81]. The ideal substrate for acceptable bandwidth and high efficiency is therefore a relatively thick substrate with the lowest possible losses and low ε_{r} [24, Chapter 14]. These expectations of the candidate substrate are compatible with operation in the microwave bands but tends to preclude patch antenna deployment at the low UHF bands, where the increasing wavelength not only makes the planar dimensions of a resonant patch quite large in terms of planar area, but also reduces the electrical thickness of the substrate. The latter problem makes construction of a viable patch antenna at lower frequencies e.g. 300 MHz with longer wavelengths difficult to achieve—unless a material of suitably high refractive index can be obtained. The magneto-dielectric patch antenna described in Chapter 4 was constructed from such a material.

2.3.2 Small loop antenna

Small loop antennas can be used in applications requiring a planar, near-omnidirectional antenna in a compact format. Providing that narrow instantaneous bandwidth performance is permissible, the small loop offers a route to omni-directional antenna fabrication in a compact form factor using conventional techniques and materials such as microstrip printing on conventional dielectric substrates.

The small loop has a dipole radiation pattern derived from the alternating current direction on the surface of the conductor. A common modelling approximation is to assume that for cases where the loop circumference is much smaller than the freespace wavelength λ_0, the current magnitude I can be modelled as equal anywhere on the loop. In Figure 2.5, this scenario is shown for a counter-clockwise current on a square loop simulated using CST Microwave Studio [127].

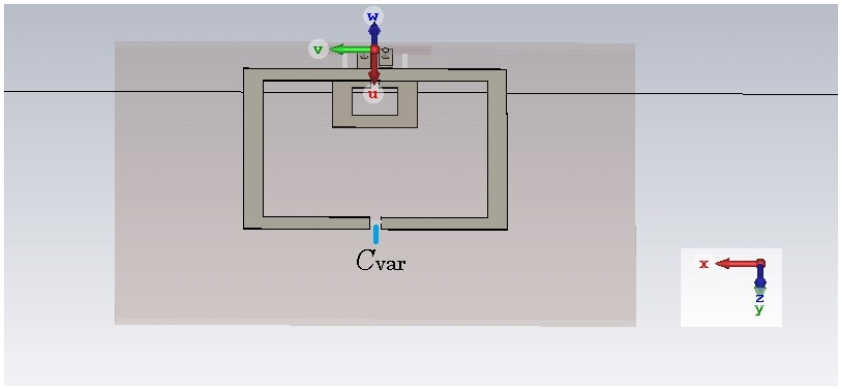

Square loop conductor with feed loop.

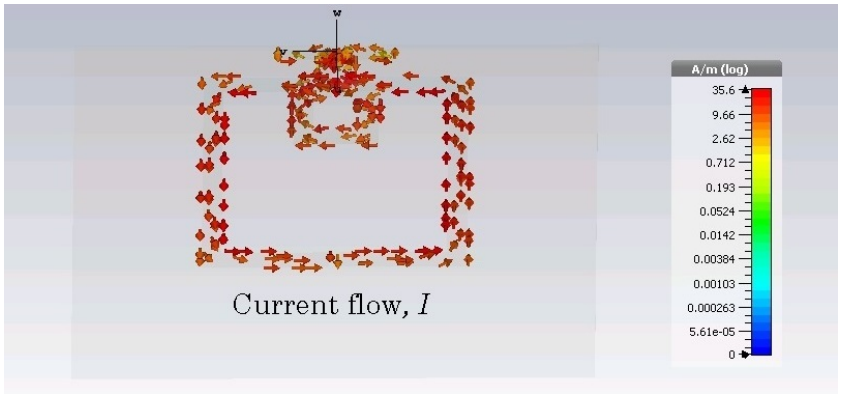

Counter-clockwise surface current on main loop.

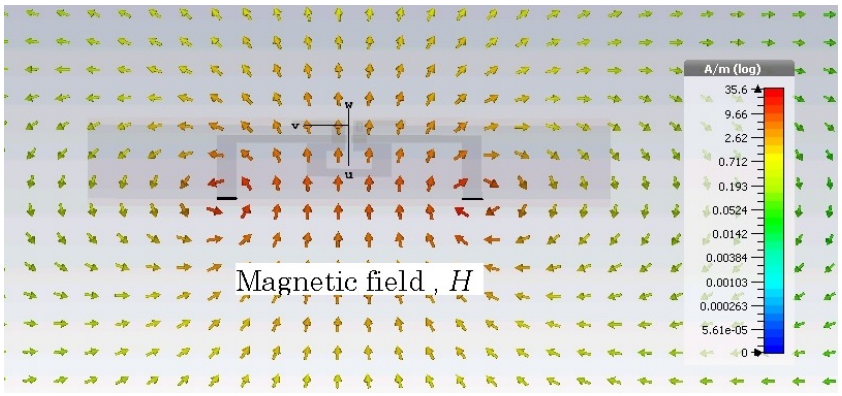

Resulting H-field (xz-plane cut). Constant current causes constructive H field creation.

FIGURE 2.5: Small loop antenna operating concept. Current flow around a loop creates an alternating "magnetic dipole" M_y.

The resultant magnetic fields caused by the current flows in Figure 2.5 summate constructively, with the net magnetic field pointing upwards in the y-axis at the centre of the loop. The alternating current direction in time therefore causes an effective alternating "magnetic current" source $\mathbf{M}_\mathrm{y}$ which is y-directed. Such a loop radiates with a dipole-like pattern with the main beam aligned in the xz-plane. The approximation of equal current around the loop only truly applies to an infinitesimally small loop, thus practical limitations on the approximation exist. Guidance on the breakdown point of the approximation varies: one textbook suggests that the loop should be required to have a longest edge no greater than $\lambda/10$ [123], while another asserts that the loop circumference must be shorter than $\lambda/3$ [128]. The loop antennas designed for this project (Chapter 5) satisfy both conditions, as well as satisfying a more general electrical smallness condition ($ka < 0.5$), the definition for which is given in Section 2.1.2.

Given the lack of resonant dimensions, the small loop is not a naturally resonant structure in terms of the stimulated current path length summating to λ along the circumference (it is commonly considered to have uniform current along its length). Thus, the operating frequency of a non-naturally resonant loop antenna must be derived by another route. In practice, at RF frequencies the loop is an inductive structure. The self-inductance L[9] of the loop can be cancelled against an emplaced series capacitance C in the loop[10].

In this structure there exists a driven resonance frequency $f = 1/2\pi\sqrt{LC}$ for which the reactances cancel, leaving only resistance. At this frequency the structure will radiate despite not having naturally resonant physical dimensions. This strategy achieves two outcomes: first, the loop structure can be made arbitrarily small with respect to λ_0 and still resonate. Second, the operating frequency exhibits a heavy dependence on the value of the series capacitance, C. As such, the small loop is highly susceptible to tuning the behaviour of the current path and it is thus an aperture-tuneable antenna. The capacitive tuning can be implemented through the use of RF switches, PIN diodes, MEMS capacitors and varactors, where smaller values of C yield higher operating frequency. Antennas designs based on this concept are presented in Chapter 5. The loops are fed using the loop-coupled-loop concept first presented by [129]. The loops were designed for a study on the development of efficiency-based tuneability metrics. As such, the loop antenna design was selected for its inherent support for continuous frequency tuning and radiation pattern stability[11] due to being an aperture-tuned design. Additionally, the operating frequency is mostly dependent on the available capacitance values rather than the physical dimensions.

[9] An initial approximation of L can be given by $L = \mu_0 b(\ln \frac{8b}{a} - 2.08)$ (assuming an annular loop of major radius b and minor radius a). This is not accurate enough for a complete design to be based on the approximation, but was found to give predicted frequency of operation to within about 120% of the actual value once the impedance matching loop had been optimised.

[10] The smaller feed loop used here gives an impedance ratio that, roughly, scales with $\sqrt{d/D}$ where d is the feed loop diameter and D is the main radiating loop diameter. The total tuning range is described entirely by the cancellation of C against the inductance of the larger loop L, while the centering of the best impedance match is given by increasing or decreasing the diameter of the feed loop. A larger feed loop favours lower frequency.

[11] Pattern stability is discussed further in section 2.4.2.3.

As such it was possible to design a loop antenna guaranteed to be electrically small across the available tuning range[12].

2.3.2.1 Related tuneable loop antenna designs

To support the development of performance metrics for tuneable ESAs, a set of readily-tuneable ESAs was required. An aperture-tuneable design was desired in order to permit studies of radiation pattern stability as this had been observed to be a desirable feature of the tuneable patch antennas described in Chapter 4. In addition, reasonably high efficiencies approaching 50% and a convenient tuning mechanism were sought.

Numerous tuneable ESAs have been described in the literature. In this work, the review became focussed on tuneable compact loops for their space-saving planar form and the capacity for capacitive tuning, which can be implemented through the use of a number of devices such as RF switches, PIN diodes, MEMS capacitors and varactors. Although MEMS capacitors can potentially offer simpler DC biasing schemes and higher component Q than varactors, varactors continue to be more popular in this role due to their low power consumption and particularly their high commercial availability compared to MEMS capacitors [130]. While small loops are intrinsically narrow band due to their small size with respect to the wavelength, the instantaneous bandwidth relaxes the constraints on efficiency implied by Wheeler's limit on antenna Q while the tuneable element permits a large integrated band to be accessed.

The ESAs developed in this work were capacitively-loaded loop-coupled loops of the class first proposed in [129], targetting the UHF band. Of the relevant planar tuneable UHF designs, other designs observed to yield frequency reconfigurability through the deployment of varactors included meandered-line loops [107, 115] and slot loop designs [130–132], which offer the advantage of uniplanar fabrication. The ESA loops described in this thesis were developed independently of a visually similar square loop described in [116]. Despite visual similarities, the design and operating concept differs. The design given in that work was a naturally resonant design wherein the loop circumference equalled an even-multipled division of the wavelength at the each frequency, tuned using a varactor across an inductor to yield tuneable inductance. The antennas described in Chapter 5 demonstrated electrically small behaviour, having a Wheeler ka factor no greater than 0.36. There are also some design differences such as the varactor being used solely as a tuneable capacitance in tuning the aperture and the differing feed mechanism.

The publications listed here all describe tuneable loop antennas but not in the detail required to generate the required tuneability metrics from their results, especially with regards to requiring radiatively characterised efficiency data. As such, the route toward developing new performance metrics required fabrication of tuneable antennas for use within the Bristol laboratory. The needs

[12] Electrical smallness is introduced in Section 2.1.2.

of increased antenna efficiency, wide tuneable bandwidth and a convenient tuning mechanism led to selection of a capacitively-tuned small loop antenna topology. A combination of trimmer-type and varactor diode capacitors were used to effect the tuning. The antenna design is detailed further in Chapter 5, with simulated and measured results used to support the development of efficiency-based tuning metrics. The antennas were designed to be electrically small by three independent definitions and exhibited continuous tuneability. The antennas were characterised across the available tuning range in terms of measured efficiency and radiation pattern, the values of which were used to support the development of the efficiency-based tuning metrics applicable to tuneable ESAs.

2.4 Efficiency and pattern measurement method

The most flexible antennas in terms of frequency agility can achieve large S_{11} tuning ranges at the expense of radiated efficiency in some or all of the bands served. Since the intention of deploying tuning is to serve each band with increased overall efficiency than a statically defined multi-band antenna, a discussion of radiated performance in each band is critical to understanding the potential of any candidate tuneable antenna. A few relevant methods to measure antenna efficiency are briefly summarised here, and the method used for tuneable ESAs in this research is described.

2.4.1 Comparison of radiative characterisation methods

Far-field measurement: the measurement takes place on an outdoor range in a relatively empty area (e.g. the countryside, with lower background emissions), or indoor chamber that is fully screened and lined with RF absorbent material. The transmit antenna and receive antenna (the antenna under test (AUT) can be either) are separated by some distance s, such that the separation is larger than the far-field condition $s > \frac{2D^2}{\lambda}$ [133]. D in this context is the maximum antenna aperture dimension. Rotating the antenna under test allows a map to be built up describing the sensitivity as a function of angle (i.e. the radiation pattern) as the link strength between the two antennas is recorded. If an additional calibration measurement is made using an antenna of known efficiency is taken, the radiation efficiency can be derived by comparing the patterns. For ESAs, the far-field condition is readily met using modest chamber dimensions because the value of D is small. For a multi-purpose chamber dealing with more than just measurement of ESAs, the required chamber dimensions can become quite large.

Near-field measurement: the measurement takes place in a similarly screened and absorber-lined indoor chamber to the far-field method. The AUT is separated from a probe by a distance less than $s < \frac{2D^2}{\lambda}$ [134, Chapter 3], but more than about $s > \lambda/2\pi$ so that the probe is in the

radiating near-field rather than the reactive near-field [135]. The required chamber dimensions are subsequently reduced. The probed near-field is then Fourier transformed to convert a planar aperture measurement to a far-field measurement [136]. The probing can be achieved using multiple duplexed transmit/receive antennas to avoid physically moving the probing antennas around the AUT, leading to much faster measurements of radiation pattern than is achieved in a far-field measurement. Such systems are commercially available from [137] among others. As per the far-field method, significant investment in terms of cash and laboratory space is needed.

Reverberation chamber measurement: the measurement takes place in a fully screened chamber which is not absorber-lined. Such chambers are usually associated with electromagnetic compatibility (EMC) measurements but can also be used to determine antenna efficiency. A transmitting and receiving antenna are separated in space within the chamber (again, the AUT can be either). A metallic stirrer plate (or multiples thereof) create numerous multipath components in the received signal. If the motion of the plates is sufficiently random [138], the received signal should have the strength of an antenna placed in a truly random multipath deployment eliminating all directivity from the measurement set up, leaving only chamber loss (the walls are not perfectly reflective) and antenna efficiency as the measurement variables. The method requires a fully screened room and sufficient randomness in the plates. [139] offers some useful images to visualise the concept.

Wheeler cap method: a laboratory measurement method not requiring significant specialist equipment beyond the availability of a VNA and the construction of an enclosing conducting structure (often, a sphere–although in principle other symmetrical structures, e.g. cubes, should work). The method rests on the antenna being treated as a two-port linear circuit element, with radiated energy being described as a load resistance when the antenna is in free space. An S-parameter measurement is taken to determine this resistance. The measurement is repeated when the antenna has been enclosed within a conducting shell of radius $\lambda/2\pi$ shorted to the antenna ground plane. The second measurement is intended to short-circuit the radiation resistance and thus determine remaining resistance present in the antenna, interpreted as loss. The resistance ratio then gives the radiation efficiency (assuming impedance mismatch has been corrected separately) [140].

In this research, a variation of the far-field measurement method was selected and its implementation is described in more detail below. The reason for selection was based partly on the availability of the method (the research group already had a chamber), although some modifications were required to make best use of the chamber for ESA measurement. The main reason not to explore the reverberation chamber and Wheeler cap measurement methods further was that the elimination of directivity from the measurement data means that radiation pattern cannot be measured. The work in Chapters 3, 4 and 5 shows that under tuning, the pattern can exhibit interesting changes over a tuned frequency range - which in some cases amount to a critical loss of performance (e.g. polarisation changes shown in Chapter 4 for a sub-resonant impedance

matching technique). The modern near-field techniques (e.g. Satimo chambers) are interesting, as they potentially offer a game-changing increase in measurement speed over a wide frequency range compared to the Bristol far-field chamber method, which intrinsically hinges on measuring one frequency at a time. However, the costs associated with procurement of such equipment are significant. The level of agreement found between the different methods for measuring efficiency would be a topic of general interest, but would have taken the work down a metrology-focussed strand which was not within scope.

2.4.2 3D anechoic chamber method for radiation pattern and directivity measurement

Use of an anechoic chamber facility permits measurement of the angular dependence of the antenna radiation pattern and transmitted/received signal power levels. In turn, radiation efficiency can be determined.

The radiation pattern of an antenna is a graphical description of the transmission or reception behaviour of the antenna as a function of angle in a 2D or 3D co-ordinate system. Antennas are not capable of producing perfectly isotropic radiation patterns with equal radiation intensity in every possible direction. The level of signal received by an antenna therefore depends on its orientation with respect to an arriving polarised planar RF wave. A plot of the received power as a function of angles θ (azimuth) and ϕ (elevation), normalised to the average received signal power, provides an indication of system performance variation caused by differing angles of arrival (and differing polarisations) for incoming RF waves. Figure 2.6 depicts an anechoic chamber measurement set up for the measurement of radiation patterns in 3D.

In Figure 2.7, a sample radiation pattern is given for a $\lambda/4$ wire monopole of the type used as a reference for radiation efficiency measurements throughout the project. The measurement is repeated for two orthogonal transmitter polarisations in all cases. The monopole pattern in Figure 2.7 clearly highlights a dominant polarisation for the monopole antenna, where the antenna has the greatest receive sensitivity for waves with an **E**-field co-polar with the axis of the wire itself.

The receive sensitivity of the antenna as a function of angular orientation is quantified numerically as the directivity, D. The linear directivity D is defined as the ratio of radiation intensity in a given direction from the antenna to the ratio of radiation intensity averaged in all directions $D(\theta, \phi)$ [24, Chapter 2]. Where directivity is quoted as a single value, this is implicitly the maximum directivity, for which the reported value is the ratio of the maximum received signal level to the average signal level recorded anywhere in the data set. The colour scales in Figure 2.7 denote directivity $D(\theta, \phi)$ in dBi.

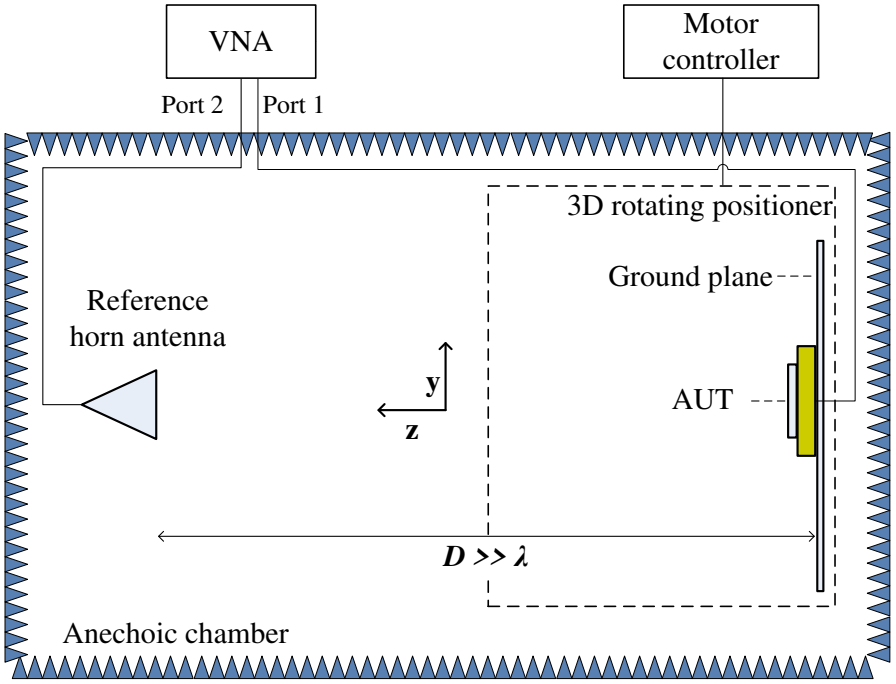

FIGURE 2.6: Radiation pattern measurement setup in anechoic chamber.

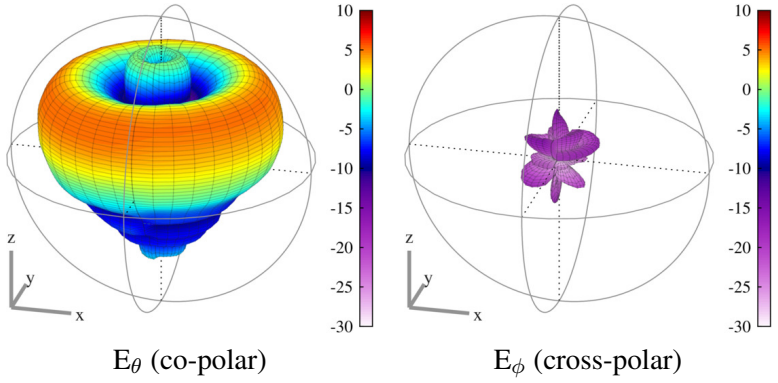

FIGURE 2.7: Typical measured radiation patterns of z-directed $\lambda/4$ wire monopole. The colour scale denotes directivity in dBi.

2.4.2.1 Reference antennas

Throughout the project, the radiatively characterised performance of physically constructed AUTs were measured using one of two reference transmission antennas. These reference antennas were used for determination of the 3D radiation pattern of the AUT. The radiation pattern measurement can be summarised as an expression of relative changes in link strength between two antennas as a function of AUT orientation, normalised to the maximum field strength measured for any orientation [123, Chapter 2]. The reference antennas used for transmission were either horn-type or log-periodic type. Depending on the frequency of interest, the tranmission antenna was any one of: a Flann Microwave DP240 horn antenna offering (switched) dual polarisation from 2.0–18.0 GHz [141], a Flann Microwave 08240 horn antenna offering a single linear polarisation

from 1.72–2.61 GHz [142], or a Teseq (formerly Chase) UPA6109 log-periodic antenna offering a single linear polarisation from 200–1000 MHz [143]. These antennas are depicted in Figure 2.8. The prime function of these antennas was to provide a radiation source over a wide band (compared to the AUTs which are restricted to narrower bandwidths by their small electrical size). These antennas have radiation efficiencies approaching 100% for any given spot-test frequency used within this research (the fact that they are not 100% efficient is calibrated out since the reported levels are all relative). The underlying operating principle of these antennas is given in [128, Chapter 7] for horn antennas and [128, Chapter 6] for log-periodic antennas.

Dual polarised horn antenna

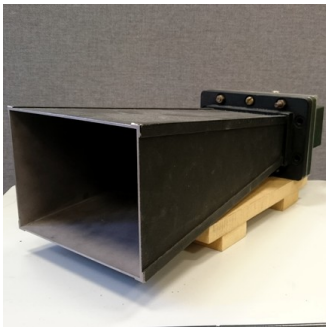

Single polarised horn antenna

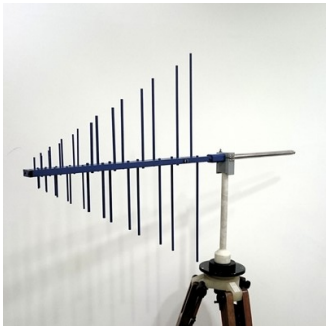

Log periodic antenna

FIGURE 2.8: Reference transmission antennas.

For radiative characterisation of the 3D radiation pattern of an AUT, measurement of relative changes in link strength and phase between the AUT and one of the antennas shown above is sufficient. However, to measure the radiation efficiency of the AUT, an additional reference receive antenna is required. In this research, a new $\lambda_0/4$ wire monopole was constructed for use as the reference receive antenna for every spot frequency f for which radiation efficiencies are reported. The monopole concept is shown in Figure 2.9, showing its construction: each monopole was comprised of a wire or thin brass rod soldered to the centre conductor of an SMA connector. The SMA outer conductor was soldered to a circular metallic plate of diameter at least $\lambda_0/2$.

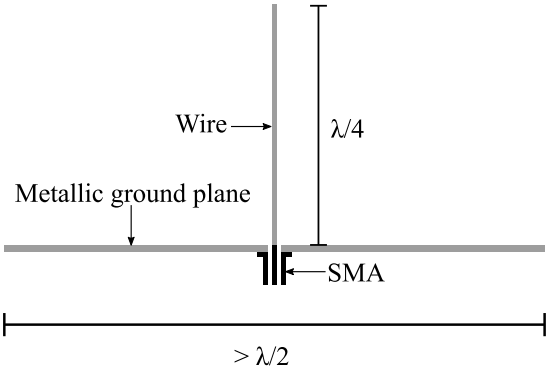

Monopole dimensions

Finished antenna on circular ground plane

FIGURE 2.9: Reference $\lambda/4$ wire monopole antenna.

Thus, all radiation efficiency measurement values quoted throughout this thesis are reported relative to a $\lambda/4$ wire monopole constructed for each reported frequency. While such monopoles have very low loss resistance due to their brass or copper construction, they are not 100% radiation efficient. Use of a reference antenna that has an efficiency calibrated to a national standard would be an option in many strands of antenna research, but given that the frequencies of interest are not known *a priori* when studying tuneable antennas, the ability to use a method dependent on non-calibrated reference antennas was preferred.

2.4.2.2 Calculation of radiation efficiency from radiation pattern

The radiation patterns measured using the configuration in Figure 2.6 permit calculation of the antenna radiation efficiency via a pattern integration method, whereby efficiency is directly calculated from the pattern measured in free space [144]. The overall system efficiency $\eta = \eta_{\text{m}}\eta_{\Omega}$ is given by $G = (\eta_{\text{m}}\eta_{\Omega})D$, where G is the gain, D is the directivity, η_{m} is impedance matching efficiency and η_{Ω} represents total loss in radiation, the conductor and dielectric materials. This loss includes the radiation resistance r_{rad} arising from energy dissipation via the Poynting vector:

$$\eta_{\Omega,\text{AUT}} = \frac{r_{\text{rad}}}{r_{\text{rad}} + r_{\text{loss}}} \tag{2.14}$$

To determine the total efficiency $\eta_{\text{m}}\eta_{\Omega}$, the pattern-derived received power of the AUT was compared to received power of a resonant wire monopole constructed for each frequency. The ratio of overall efficiencies (i.e. including mismatch) $\eta_{\text{AUT}}/\eta_{\text{ref}}$ is given by measurement of the electric field around a surface, S:

$$\frac{\eta_{\text{AUT}}}{\eta_{\text{ref}}} = \frac{\oiint_S |E_{\text{AUT}}|^2 \, \text{dS}}{\oiint_S |E_{\text{ref}}|^2 \, \text{dS}} \tag{2.15}$$

The radiation pattern of a purpose-built $\lambda/4$ wire monopole was measured as a reference antenna pattern. Since the quarter-wave metallic monopole is recognised to be highly efficient [144], for comparison purposes it can be assigned a radiation efficiency value of $\eta_{\Omega,\text{ref}} = 1$:

$$\frac{\eta_{\text{AUT}}}{\eta_{\text{ref}}} = \frac{\eta_{\text{m, AUT}} \cdot \eta_{\Omega,\text{AUT}}}{\eta_{\text{m, ref}} \cdot (\eta_{\Omega,\text{ref}} = 1)} \tag{2.16}$$

Scaling the measured overall efficiency ratio, Equation (2.16) by the S_{11}-derived matching efficiencies η_{m} yields a measure of the radiation efficiency for the AUT, relative to a highly efficient $\lambda/4$ length wire monopole at each frequency:

$$\frac{\eta_{\Omega,\text{AUT}}}{(\eta_{\Omega,\text{ref}}=1)} = \frac{\eta_{\text{AUT}}}{\eta_{\text{ref}}} \cdot \frac{\eta_{\text{m, ref}}}{\eta_{\text{m, AUT}}} \tag{2.17}$$

The radiation efficiency of each candidate antenna was a major performance metric of interest throughout the project. For antennas where the radiation resistance is low, or the loss resistances are high, there is a high risk that the realised radiation efficiency will be low, leading to increased power consumption elsewhere in the RF chain and/or reduced data rates.

2.4.2.3 Pattern correlation

In the absence of any ground planes of fixed dimensions, the radiation pattern of an antenna should be scale invariant. That is, a naturally resonant $\lambda/2$ dipole designed for 1000 MHz will have the same radiation pattern as that of a $\lambda/2$ wire dipole designed for 2000 MHz at the natural resonance frequency, f_0. However, for an antenna of fixed physical dimensions but variable operating frequency, the radiation pattern is subject to change with frequency. The angular position of the nulls, beam maxima and the beam widths can all change. This can be readily seen by observing the radiation pattern of two different modes in a single antenna of fixed dimensions. In Figure 2.10, the power patterns of the TM_{10} and TM_{11} modes of a square patch antenna are shown. The location of the nulls, the maxima and the beam widths have all changed between modes. The transition from one mode to another occurs gradually as the frequency is increased (i.e. there are no discrete changes in mode), with the pattern given for an arbitrary frequency in between modes being a sum of power contributions from modes associated with nearby frequencies.

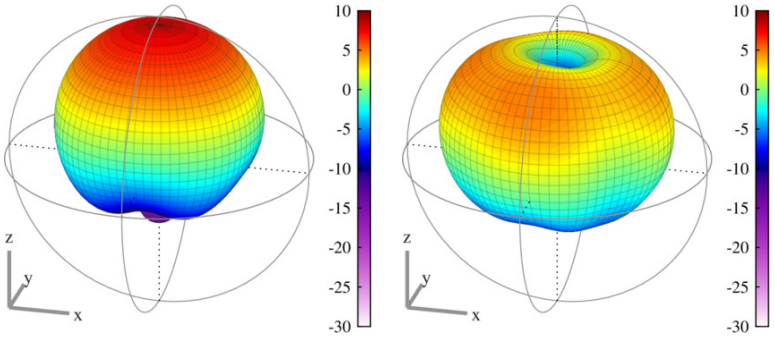

TM_{10} TM_{11}

FIGURE 2.10: Power patterns of non-tuneable square patch antenna.

The concept of frequency dependence in the radiation pattern potentially raises a problem for tuneable antennas. Many tuneable antennas (though not all) have fixed physical dimensions, but operate on different frequency bands due to the changing state of the tuning mechanism. As such, the radiation pattern is susceptible to shifting behaviour under frequency tuning. Measurement of the tuned return loss or efficiency in isolation cannot prove that the radiation patterns obtained

across a tuneable frequency range remains stable. Plots of the 3D radiation pattern over a broad integrated frequency band can provide some indication that the pattern is "sufficiently stable" across a tuned band. In the context of this thesis, "sufficient" is taken to mean that no changes in dominant mode have occurred in the frequency range accessed under tuning. Formal criteria to define the meaning of "sufficient" stability have not been generated for inclusion in this thesis with regards to onward impact on system performance in terms of realised gain or achievable capacity. However, a conceptual measure of pattern similarity at two different frequencies is defined with reference to [145]. Definition of the field correlation performance metric ρ resolves the need for a quantified measurement of similarity between patterns measured for two different tuning states (thus frequencies). The correlated power is given by ρ^2.

The correlation function for two 3D patterns is defined from [145]:

$$\rho = \frac{\oiint_S E_1 E_2 \, \mathrm{dS}}{\sqrt{\oiint_S |E_1| \, \mathrm{dS} \;\; \oiint_S |E_2| \, \mathrm{dS}}} \tag{2.18}$$

Application of Equation (2.18) to the simulated patterns of the two different modes in a patch antenna given in Figure 2.10 yields a power correlation value of $\rho^2 = 0.32$. Such a value indicates that the power patterns have a relatively low degree of overlap. In contrast, the measured patterns of a substrate-tuneable patch antenna detailed in Chapter 4 are given in Figure 2.11. This antenna is naturally resonant at 329 MHz in the absence of a magnetic bias field, but can be tuned to 405 MHz by applying magnets to the substrate. Changing the refractive index of the substrate to achieve the frequency tuning preserves the naturally resonant $\lambda/2$ behaviour of the patch across the tuned frequency range. The resulting stability in the radiation pattern is reflected in the high correlation value calculated for these patterns, $\rho^2 = 0.83$. The correlation of any pattern paired with itself is 1 by definition, thus high correlation values are an indicator that the same mode is stimulated in the antenna throughout the tuning range.

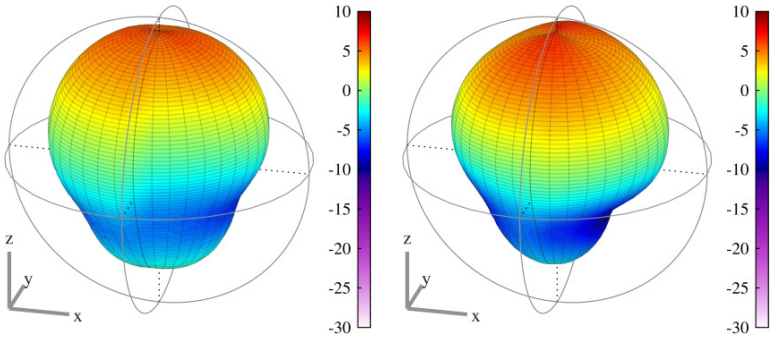

f_{low} (329 MHz) f_{high} (405 MHz)

FIGURE 2.11: Power patterns of substrate-tuneable rectangular patch antenna.

In the context of this thesis, radiation patterns are only measured and compared for spot frequencies. However, the pattern of an antenna is frequency selective and liable to change. Such changes

arise from both the presence of higher order modes in the antenna and the changing electrical size of the ground plane. Thus, over an ultra wide bandwidth (either instantaneously available or tuned), there is no reason that the radiation pattern can be expected to maintain "stability." This was shown in [45], wherein the recorded 3D radiation patterns of a pair of ultra wide band (UWB) antennas operating over the range 3.1–10.6 GHz were found to exhibit multiple mode changes. This matter was raised for UWB antennas but applies equally to tuneable ones. The question of defining a metric for the bandwidth for which a certain pattern correlation threshold value is maintained under tuning has not been addressed in this thesis, but the potential for doing so could be reviewed in future work.

2.5 Summary

In this chapter, the impact of antenna miniaturisation on aspects of performance such as achievable impedance matching and radiation efficiency have been introduced. The instantaneous bandwidth limitation in particular caused by the rapidly rising antenna Q with decreasing Wheeler radiansphere occupancy ka prompts the widespread interest in antenna tuning techniques. The tuning techniques can be used to create a narrow band impedance match in the antenna structure at a given frequency, precluding the need for an instantaneously wide band impedance matching solution, the overall efficiency of which is restricted by the Bode-Fano criterion. Due to the reconfigurable nature of the operating part of the tuning solution, the centre frequency of the impedance match can be varied in time, creating a frequency-agile narrow band antenna.

A representative review of the main categories of narrow band antenna tuning techniques has been given in this chapter. Mechanical tuning methods provide continuous frequency tuning, but do not typically yield highly miniaturised antennas. Tuneable matching networks incorporating fixed inductors and tuneable capacitors have found application for frequency agility, recovery from antenna mismatch induced by a change in the near-field environment surrounding the antenna, and to some extent, miniaturisation. A study of a tuneable matching network for these purposes is presented in Chapter 3 and [21]. Substrate tuning (variable ε_r, μ_r or both) has been found to be a candidate for both antenna miniaturisation and frequency agility. Due to the topical interest in magneto-dielectric materials formed of engineered ferrites, demonstration of material selection, characterisation and incorporation into an electrically small antenna is given in Chapter 4, [23] and [22]. Given that access to tuneable substrate materials remains relatively restricted, aperture tuning of antennas using conventional lumped components remains a popular topic of study. An antenna of this type was created to understand the frequency agility and variable efficiency aspects of such tuning and is presented in Chapter 5. Multiple variants of this antenna (all capacitively tuned) are then used as a demonstrator for the development of improved performance metrics for tuneable antennas: throughout the research, S_{11} was found to be a relatively poor

predictor of realised radiated efficiency under tuning. A radiation pattern measurement technique based on 3D pattern measurement has been described in this chapter, which is used as the basis of all of the efficiency measurements throughout this research. Chapter 5 introduces an improved efficiency-based approach to reporting “tuneability” of narrow band antennas as reported in [20].

Chapter 3

Tuneable impedance matching

In Chapter 1, the motivation for tuneable antennas were discussed. As an initial practical study into frequency-reconfigurable antennas, the use of a tuneable matching network (TMN) is analysed in this chapter. Use of the TMN is demonstrated in conjunction with a naturally resonant patch antenna, the combination of which is characterised in terms of tuneable impedance response and free space boresight gain enhancement for a given tuneable bandwidth in the upper portion of the ultra-high frequency (UHF) band.

Subsequently, use of the TMN is extended to consider recovery from detuning of the patch antenna caused by environmental factors. The impedance detuning effect observed in the patch antenna is recorded, where the detuning is effected using a human hand and a hand phantom of similar permittivity. Following verification of the detuning effect of the phantom, a radiative characterisation of the system power efficiency under reactive detuning with and without the use of the impedance tuner is analysed [21].

3.1 Transducer efficiency

It was noted in Section 2.2.3 that some existing publications describing TMNs documented frequency-reconfigurable behaviour (e.g. [40, 41]). However, in these cases characterisation of the performance of the network under tuning was limited to a description of tuneable S_{11} behaviour. In such a case, the maximum available matching efficiency described by $\eta_{\mathrm{m}} = 1 - \Gamma^2$ can be calculated, but such a performance measure does not account for the resistive loss effects in the matching network. The distinction between reflective (mismatch) loss and resistive loss is given in Figure 3.1.

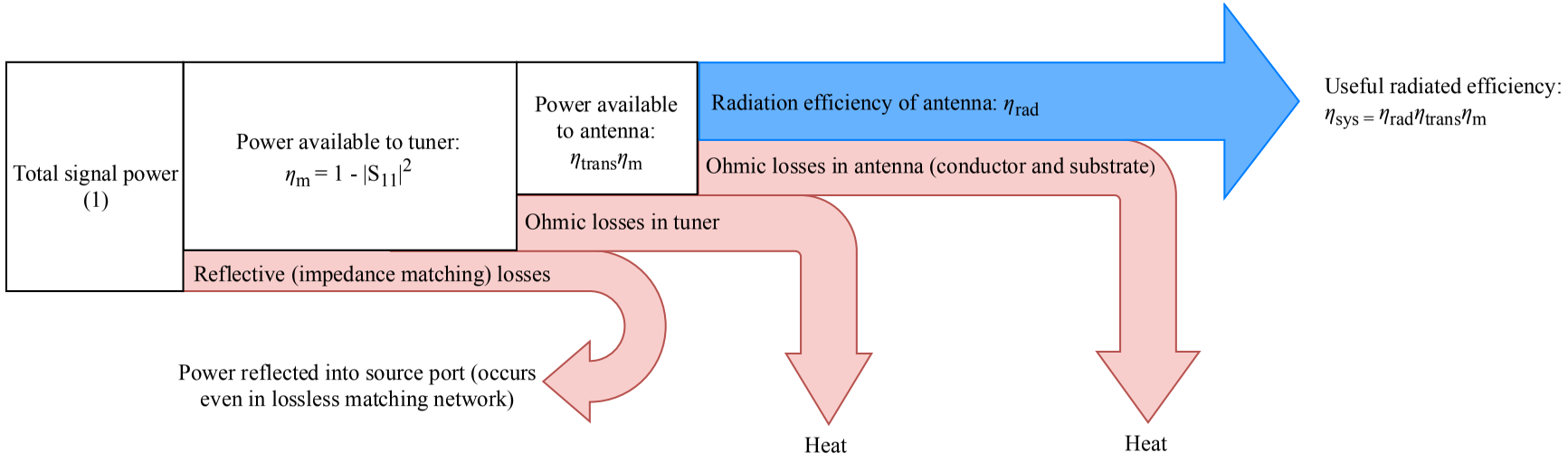

FIGURE 3.1: Sources of inefficiency in tuning antenna using tuneable matching network.

If a perfectly lossless matching network existed, the transducer efficiency would take the value $\eta_{\text{trans}} = 1$ and the maximum available system efficiency enhancement comparing a tuned (T) to non-tuned (U) antenna would be given by Equation (3.1):

$$\text{Max. potential efficiency enhancement} = 10\log_{10}\left(\frac{\eta_{\text{m,T}}}{\eta_{\text{m,U}}}\right) \text{ (dB)} \tag{3.1}$$

It is possible to determine the impact of such losses in the network by comparing the radiated performance with and without the assistance of such a network, once the different impedance matching efficiencies obtained from S_{11} have been removed by scaling. The difference between the two cases is given by losses in the matching network and can be described by the transducer efficiency, η_{trans}.

In practice, use of the TMN for reconfigurable impedance matching may reduce the power lost to impedance mismatch, but will do so incurring some additional resistive loss. S_{11} measurement in isolation is insufficient to determine the extent of these losses. The actual realised system efficiency enhancement can be determined from the ratio of the transmitted system efficiencies with and without the tuner. The realised insertion gain offered by the tuner will be lower than the maximum available given by Equation (3.1), due to the losses in the transducer efficiency. Hence, for practical tuners, $0 < \eta_{\text{trans}} < 1$. The realised efficiency enhancement at the link level is not the one suggested by enhancements in impedance matching efficiency alone. The realised insertion gain can be calculated by comparing the overall transmitted system efficiencies η_{sys} of a tuned (T) and non-tuned (U) antenna:

$$\text{Realised system efficiency enhancement} = 10\log_{10}\left(\frac{\eta_{\text{sys,T}}}{\eta_{\text{sys,U}}}\right) \text{ (dB)} \tag{3.2}$$

The reported system efficiencies are given by Equation (3.3). The impedance matching efficiencies η_{m} in each case were established from measured S_{11}, via $\eta_{\text{m}} = 1 - \Gamma^2$.

$$\eta_{\text{sys,AUT}} = \frac{\eta_{\text{AUT}}}{\eta_{\text{ref}}} = \frac{\eta_{\text{m, AUT}}}{\eta_{\text{m, ref}}} \cdot \frac{\eta_{\Omega,\text{AUT}}}{(\eta_{\Omega,\text{ref}} = 1)} \tag{3.3}$$

The transducer efficiency can be determined from the following argument. The measured system efficiency η_{sys} for an antenna is comprised of its impedance matching efficiency η_{m}, its radiation efficiency η_{rad} and its transducer efficiency η_{trans} (Equation 3.4). Figure 3.1 depicts the splitting of the total system efficiency between different loss mechanisms.

$$\eta_{\text{sys}} = \eta_{\text{m}} \cdot \eta_{\text{rad}} \cdot \eta_{\text{trans}} \tag{3.4}$$

The transducer efficiency can be found by asserting that the radiation efficiency of the antenna under test is a function only of the conductor and dielectric losses and its radiation resistance [144]. Thus, the radiation resistance of the patch antenna is the same whether it it tuned or not, as no changes are made to the antenna structure itself. Furthermore, the untuned antenna does not have a transducer efficiency since there is no tuner in-line with the feed. Hence, the system efficiencies of the tuned and untuned AUTs can be compared to give the transducer efficiency, where the subscripts T, U denote tuned and untuned antennas respectively:

$$\frac{\eta_{\text{sys,T}}}{\eta_{\text{sys,U}}} = \frac{\eta_{\text{match,T}}}{\eta_{\text{match,U}}} \cdot \frac{\eta_{\text{trans,T}}}{(\eta_{\text{trans,U}} = 1)} \cdot \frac{\cancel{\eta_{\text{rad,T}}}}{\cancel{\eta_{\text{rad,U}}}} \tag{3.5}$$

$$\eta_{\text{trans}} = \frac{\eta_{\text{sys,T}}}{\eta_{\text{sys,U}}} \cdot \frac{\eta_{\text{match,U}}}{\eta_{\text{match,T}}} \tag{3.6}$$

The transducer efficiency is thus the difference between the maximum potential efficiency enhancement and the physically measured efficiency enhancement under transmission. Calculation of this value highlights the available margin for improved system efficiency. The remainder of the chapter describes the use of radiative characterisation to calculate transducer efficiency in frequency tuning in free space, and at a single frequency in a reactive user-effect mismatch scenario.

3.2 Matching network design

3.2.1 Topology selection

A matching network topology was initially sought that would offer flexibility to match between two different arbitrary complex loads. Such an infinitely flexible network can be defined in theory using three matching elements in a π matching network topology. In principle, any position on the Smith chart can be matched to with perfect fidelity, but this requires ideal lossless reactances [146]. In reality, the accessible area of the Smith chart is reduced not only by the finite range of component values, but also the extreme sensitivity to component tolerances and board parasitic effects when matching to impedances at the edge of the chart.

The tuneable π network concept is depicted in Figure 3.2 based on the topology presented in [38]. Such π networks have been reported elsewhere as a starting point for more complicated designs e.g. [38, 47], but the three element design given here is sufficiently flexible to match a transmission line to a load regardless of which side of the match presents the higher impedance. Such matching flexibility was desired since the network was created prior to the characterisation of the range of realistic load impedances presented to the TMN under user-effect detuning of the

antenna. The π network would require a tuneable series inductor if it were to be fully tuneable, but the lack of commercially available tuneable inductors led to the addition of a tuneable capacitor placed in parallel with the inductor to provide, in effect, a tuneable inductance. Having identified the tuneable π topology as the preferred candidate TMN, the remaining design work consisted of selecting appropriate capacitors and inductors.

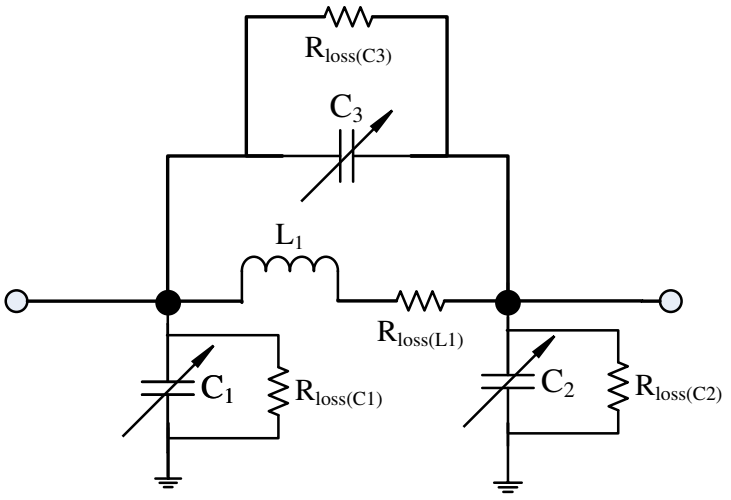

FIGURE 3.2: Tuneable π network concept, showing parasitic losses.

Although a two-element L-section design allows any match to be made in principle, it does so with fixed Q [147]. Use of a low pass π network allows the designer some control over the Q and thus offers the potential for broader instantaneous impedance bandwidth [148]. Moreover, deployment of an L-section design benefits from prior knowledge of which impedance (source or load) will be the greater impedance, such that the shunt element can be placed in parallel with the higher impedance. In the absence of this prior knowledge, construction of a π network allows either the source or the load to be the higher impedance without causing an intractable matching problem.

3.2.2 Component selection

Having specified that the candidate network would have a π topology, selection of L and C components was required. The range of fixed inductors available is much larger than the range of suitable tuneable capacitors, thus the component selection procedure started with capacitor selection, with inductance selection being fitted around the indicated tuneable coverage area offered by the tuneable capacitance. A formal measure of Smith chart coverage area was not sought at the time of the study, although one has been subsequently introduced in the literature [146].

RF microelectromechanical system (RF MEMS) capacitors had already been highlighted as a target technology of interest as part of an initial literature review stage (Section 2.2.5), due to the claimed high linearity and low loss benefits of RF MEMS capacitors over competing tuneable technologies such as semiconducting varactor diode capacitors and barium strontium titanate (BST) thin-film capacitors [47].

At the time of this study, RF MEMS capacitors were not openly available for purchase in the major electronics markets. Component selection was therefore driven by availability via negotiation, rather than a data-sheet comparison of the leading RF MEMS capacitors. On this basis the capacitor bank chosen for the study was a WiSpry WS1050 unit providing three digitally tuneable capacitors of value 0.5–5.9 pF [48].

With the C values given by the WS1050 capacitor bank module, the remaining design requirement was the selection of L. The first design consideration for the selection of L was that the network should be as tuneable as possible, hence the L value selected should give as much Smith chart coverage as possible at the frequency of interest. The second design requirement was for the lowest possible loss in the inductor. To this end, the Coilcraft mini air-core inductor series [149] was selected.

Although the TMN topology offered flexible impedance matching in terms of impedance states covered, there nevertheless remained a requirement to design for a specific frequency. The Smith chart coverage offered by a TMN is dependent not only on its tuneable capacitance values, but necessarily on the operating frequency as well since the reactance of C and L are frequency-dependent.

A patch antenna was selected as the companion antenna for the tuning network in this study to be representative of wider trends in the relevant tuneable antenna literature at the time of the study. At that time, RF MEMS capacitor banks were being proposed and marketed for use in smartphone applications in the upper portion of the UHF band (900–3000 MHz, e.g. [150, 151]). An antenna was therefore designed for use at approximately 2000 MHz to fall into the middle of this range. A patch antenna was used as a target antenna under test (AUT) in this study for its simplicity of design and construction.

The patch antenna was a square patch antenna with conductor edge length 30 mm, constructed on a 1.6 mm thick FR-4 substrate [125]. FR-4 was chosen as the demonstrator substrate because it is representative of typical user equipment. The popularity of FR-4 is driven by cost more than performance: FR-4 is not a particularly "controlled" material compared to high-performance substrates such as Duroid RT5880. In practical S_{11} measurement it was found to be resonant at 2035 MHz (Figure 3.3), i.e. 1.75% higher than the design frequency of 2000 MHz. The discrepancy between the design frequency and the measured frequency is in part caused by variability in the actual ε_r of the substrate (in FR-4, the quoted values of ε_r vary from 4.3–4.5).

An element of the discrepancy in frequency also arises from the slightly imperfect positioning of the feed pin. Nonetheless the frequency given by theory and that given by measurement are in close agreement. The untuned resonant frequency of the antenna for the remainder of this study was therefore 2035 MHz. The -10 dB impedance bandwidth of the untuned patch was 33 MHz (1.6% of the centre frequency). A one-port S-parameter file containing measured S_{11} data for this antenna was used as the load impedance in a subsequent L selection simulation (Figure 3.4).

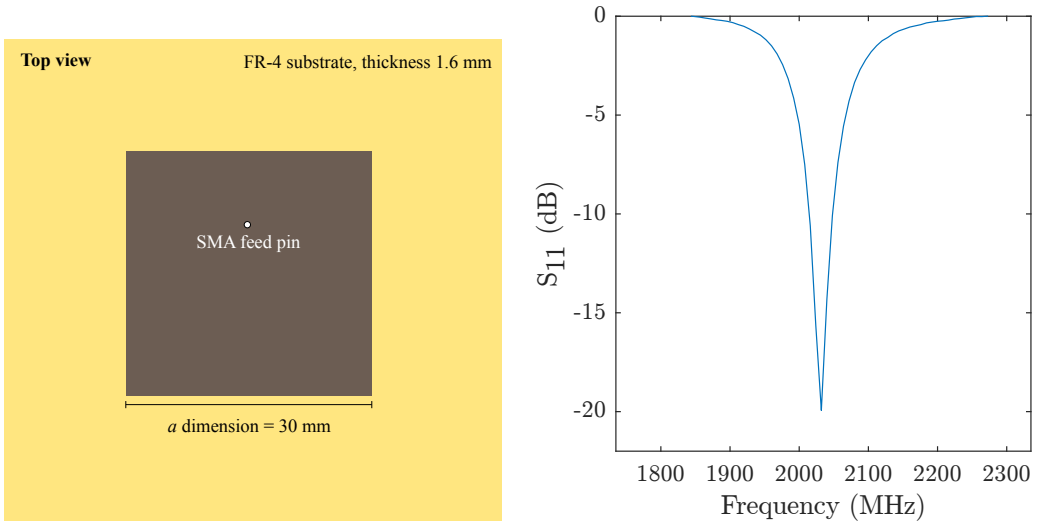

Patch antenna layout Untuned $|S_{11}|$

FIGURE 3.3: Untuned patch antenna layout and input response measurement.

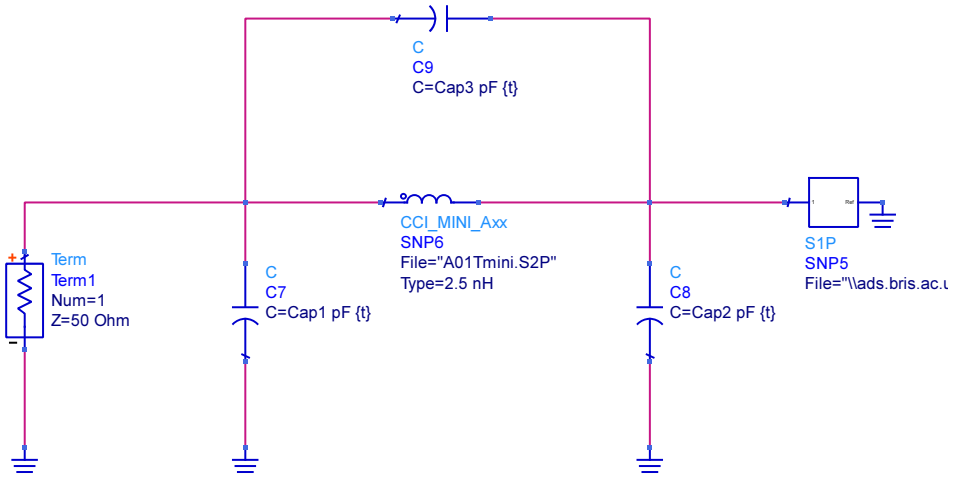

FIGURE 3.4: Keysight ADS simulation for selection of L to maximise Smith chart coverage.

The simulation of Figure 3.4 in Keysight ADS led to selection of a Coilcraft mini air core 2.5 nH inductor [152] as the chosen candidate L. This decision was made based on high inductor Q factor, a self-resonant frequency (SRF) of at least three times the operating frequency and broad coverage area on the Smith chart at 2000 MHz under tuning state $\{C_1, C_2, C_3\}$ sweeping (values 0.5–5.9 pF). The simulated Smith chart coverage is shown for the TMN tuning against a 2035 MHz patch antenna in Figure 3.5. Each marker represents one of 60^3 tuning states $\{C_1, C_2, C_3\}$

in terms of S_{11} at a single frequency of 2000 MHz. The coverage area is comprised of two tuneable shunt C sweeps and one effective series L/C sweep.

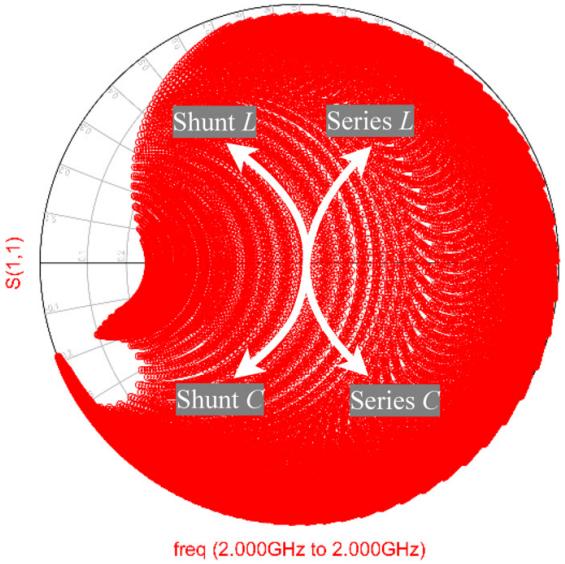

FIGURE 3.5: Simulated Smith chart coverage of candidate tuneable matching network tuning a patch antenna.

3.2.3 Tuning state control

The RF MEMS chips were mounted on bench-testable printed circuit boards (PCBs)[1] as depicted in Figure 3.6. The tuning state $\{C_1, C_2, C_3\}$ could be selected using manufacturer-supplied control software or MATLAB over a USB umbilical cable, with the tuning configuration then being maintained after disconnection from the control PC due to the presence of the CR2032 battery.

The network presented has three degrees of tuning freedom (i.e. the values of $\{C_1, C_2, C_3\}$). This flexibility in matching presents a problem for the optimal selection of tuning states in terms of low complexity of implementation against optimal power transfer. Various works have addressed the tuning state control problem, investigating algorithms to automatically determine the necessary tuning component values [38] and optimisation of the minimum number of processing steps to achieve acceptable matching quickly from a finite set of capacitance values [153].

Such issues are an important consideration for commercial exploitation of a TMN in a dynamically changing impedance scenario such as user-effect detuning in various hand/head usage scenarios, but were explicitly beyond the scope of this investigation that concerned itself only with the power efficiency of the network under frequency reconfiguration and recovery from detuning.

[1] This work was conducted by an electronics contractor (Hexagon PCB Ltd.), with contractor-generated schematics given in Appendix B.

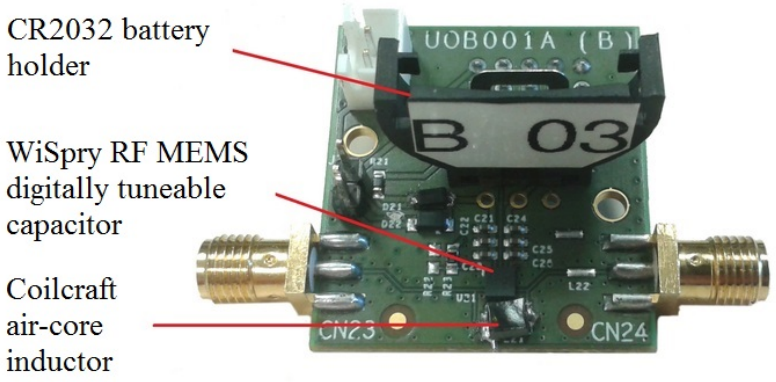

FIGURE 3.6: Physical implementation of tuneable π network.

Hence, advanced tuning state selection methods were not adopted in this work. A near-exhaustive state selection technique was used to characterise an evenly-spread downselection of the 60^3 available capacitance values. The optimal tuning states were determined in post-processing from the strongest transmission response for each tuned frequency, measured using over-the-air (OTA) S_{21}.

3.3 Over-the-air insertion gain

In simulation it was shown that varying the capacitance values caused the TMN to be capable of providing a range of different impedance matches on the Smith chart for a given frequency. Such an approach to demonstrating reconfigurable network flexibility is not uncommon in tuner sales literature, having been demonstrated elsewhere (e.g. [41, 148, 154]). At the time of the study, as a trend formal "Smith chart coverage" metrics were not presented in the antenna literature with authors relying on visual depictions of the Smith chart coverage offered by a sweep of discrete impedance tuning states. Consistent with the trend at the time of the research (2014), this research did not consider formal measures of Smith chart coverage. However, such measures have subsequently been introduced to the literature [146]. In any case, demonstrations of tuning network flexibility through plots of impedance states offered do not completely capture the insertion gain/loss of such a tuner and its transducer efficiency (Figure 3.1). In this section, a radiative characterisation procedure is introduced that determined the insertion gain of the TMN as well as its transducer efficiency.

3.3.1 Bench-top measurement configuration

This section describes an investigation into using the TMN to broaden the useable frequency range of an instantaneously narrow band patch antenna, with the TMN placed in line between the

feed line and the antenna. The investigation included measurement of the input response (S_{11}) as well as the tuned transmission behaviour in terms of received signal strength (OTA S_{21}), with the tuned antenna pointing into a reference horn antenna.

A bench-top measurement of OTA S_{21} was performed for a patch antenna, pointing towards a co-polar reference horn antenna, with and without the impedance tuner. The bench-top measurement configuration is shown in Figure 3.7. OTA S_{21} in this instance is a relative measure of forward scattering into Port 2 from Port 1. The measurement set up contains a pair of antennas which takes the definition of OTA S_{21} here away from the usual "calibrated" S_{21} one would measure for a closed-loop characterisation of a two-port device (e.g. a filter). The concept is similar, but the antennas introduce directivity, inefficiency and frequency/polarisation-dependent path losses. Each of the losses are not straightforward to determine independently of the others on the bench. The approach taken therefore was to treat the S_{21} measurements as a normal S_{21} measurement (including calibrating out the cable phase and losses), and then re-normalise the measured data to the greatest $|S_{21}|$ value measured in the data set for each antenna plus tuner pairing. For repeatability across different measurement sets, the vector network analyser (VNA) was allowed to reach thermal stability by letting it run for approximately two hours before being calibrated at the start of each day. The antennas were mounted on the mounts depicted in Figure 3.7, the heights of which were chosen to align the geometric centres of the antennas. The mounts themselves were aligned to pencil marks on the bench and then not moved throughout the measurement run.

The signal strengths for the tuned and non-tuned cases were compared over a frequency range of 1400–3000 MHz. The capacitor bank sales literature declared an upper rated frequency of 3000 MHz, although closer inspection of the data sheet revealed a minimum SRF of less than 3000 MHz for some tuning states [48]. This in turn could indicate that unintended side-effects could occur in the tuning network for certain tuning states/frequencies, but these effects are not explicitly examined here.

3.3.2 Over-the-air S_{21} versus S_{11} for tuning state selection

Having configured the bench-top measurement set up (Figure 3.7), selection of tuning states to optimise performance at each frequency was addressed. Optimal tuning state selection was conducted in post-processing, having measured the OTA S_{21} for a large number of tuning states $\{C_1, C_2, C_3\}$. From the total data set of all OTA S_{21} values measured over the frequency range 1400–3000 MHz, the best-case tuning state for each frequency was found by means of a linear search script in MATLAB. From the list of best-case tuning states that maximised OTA S_{21} for each discrete frequency in the data set, a look up table was generated for future recovery of that tuning state for subsequent system efficiency characterisation in the anechoic chamber (below,

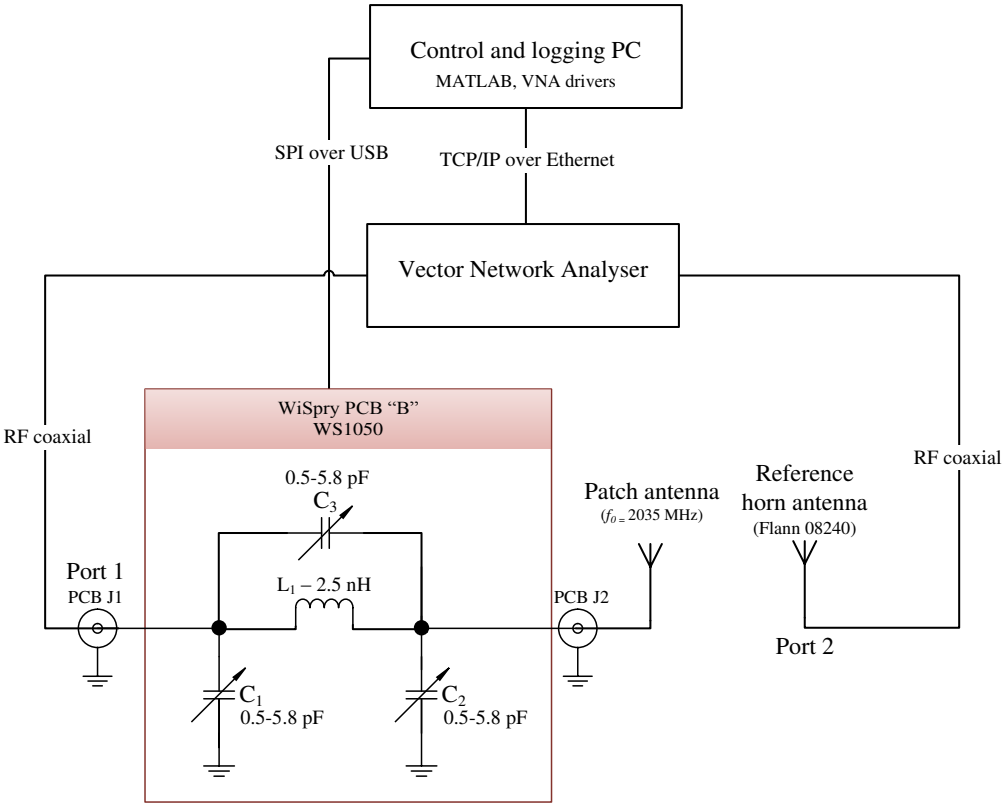

Set up concept.

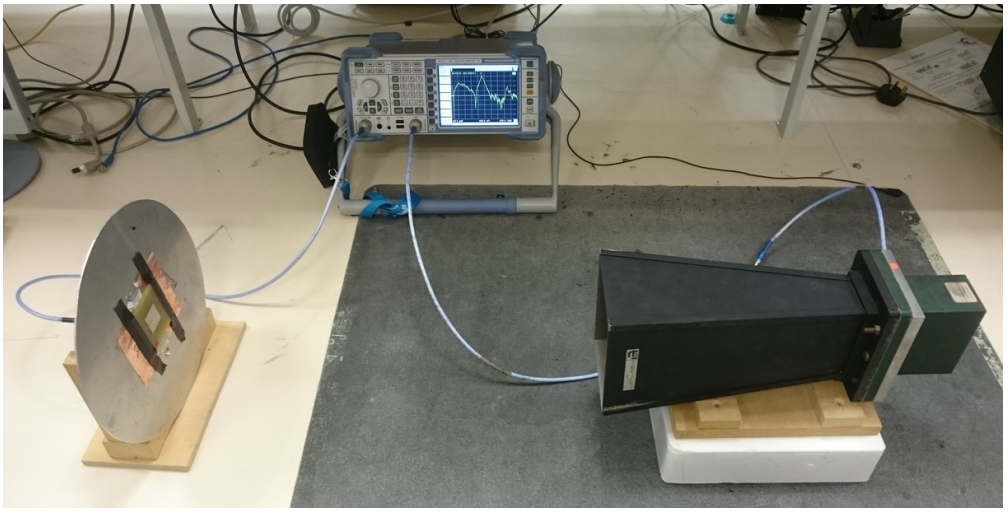

Measurement set up on bench.

FIGURE 3.7: Bench-top set up for boresight over-the-air gain measurement with impedance tuner.

Section 3.3.4). This procedure is depicted in Figure 3.8, where a given tuning state is shown to be the optimum choice for one frequency but not necessarily others.

In the case shown in Figure 3.8, the tuning state optimising OTA S_{21} at 2464 MHz was highlighted for demonstration purposes. This tuning state was chosen because it clearly shows that the matching was optimal at a single frequency, but not others. The tuning state selected delivered

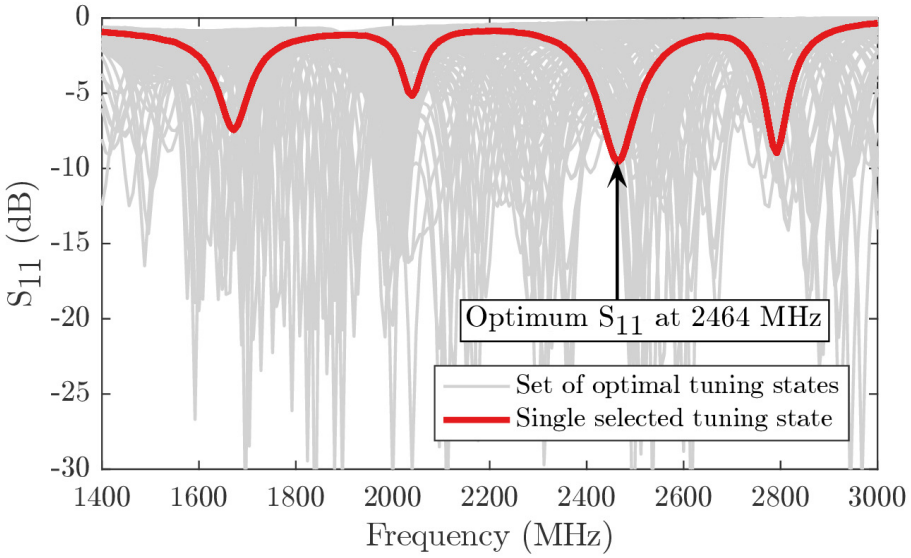

$|S_{11}|$ (gain maximisation goal).

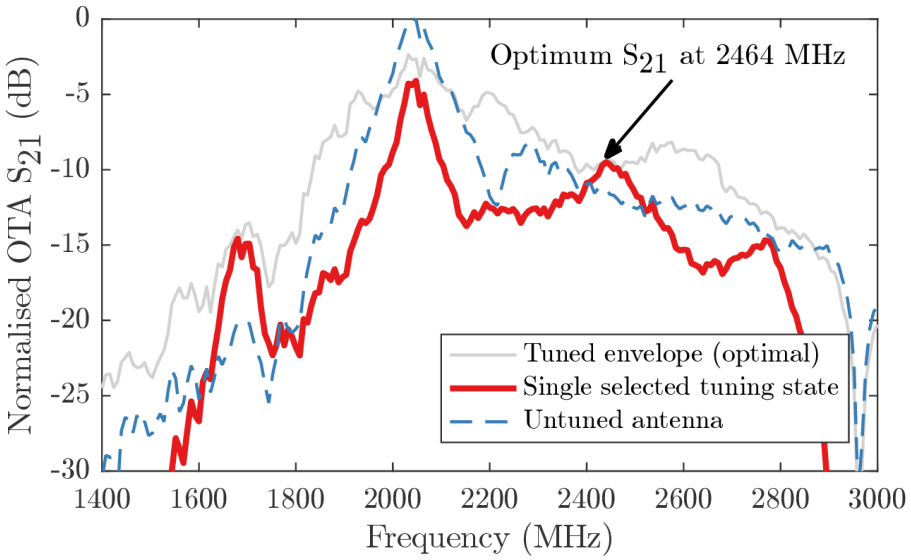

OTA S_{21} (gain maximisation goal).

FIGURE 3.8: Measured $|S_{11}|$ and insertion gain envelopes of TMN-tuned antenna (transmission gain maximisation goal). OTA S_{21} has been normalised to the highest level recorded anywhere in the data set to eliminate the effect of path loss (which occurred for the untuned antenna at 2035 MHz).

insertion gain at 2464 MHz (i.e. net benefit compared to using the untuned patch antenna at 2464 MHz). Each of the troughs in S_{11} arises from resonances in the matching circuit and can be seen to have given rise to a corresponding peak in OTA S_{21}, but it can be seen that this tuning state only optimised OTA S_{21} at the single frequency of 2464 MHz. Searching the data set for tuning states maximising OTA S_{21} for the other frequencies (1400–3000 MHz discretised into 201 frequency points) gave the OTA S_{21} tuned envelope depicted by the grey line for OTA S_{21}.

Taken together, the S_{11} and OTA S_{21} plots given in Figure 3.8 hint at some problems that can arise

from over-reliance on S_{11} as a metric for tuning performance. It is notable that the transmission performance OTA S_{21} was used as the target optimisation metric for tuning state selection. This guaranteed optimal transmission performance, which was not guaranteed by selection of minimal S_{11} as a tuning state selection metric. Figure 3.9 shows the outcome of using tuning states based on those which gave minimal S_{11} instead of maximum OTA S_{21}.

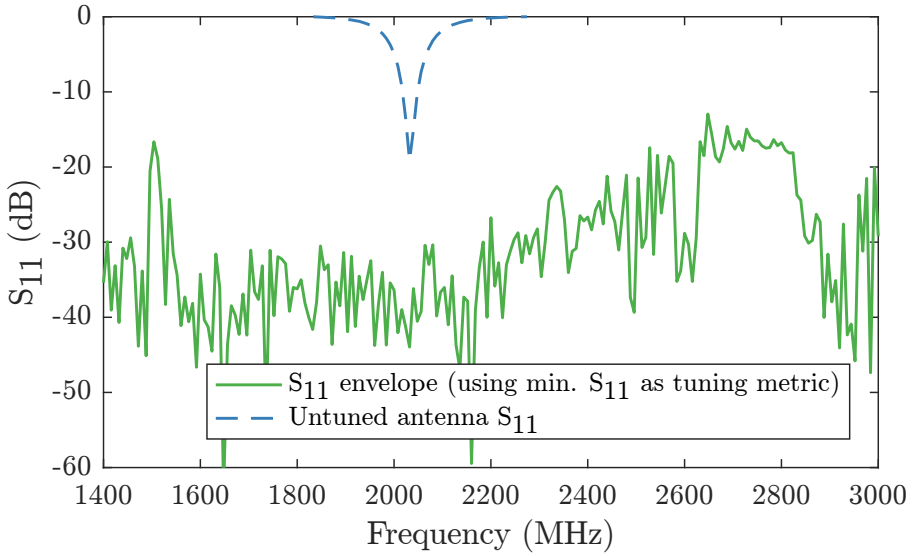

Tuned $|S_{11}|$ (return loss maximisation goal).

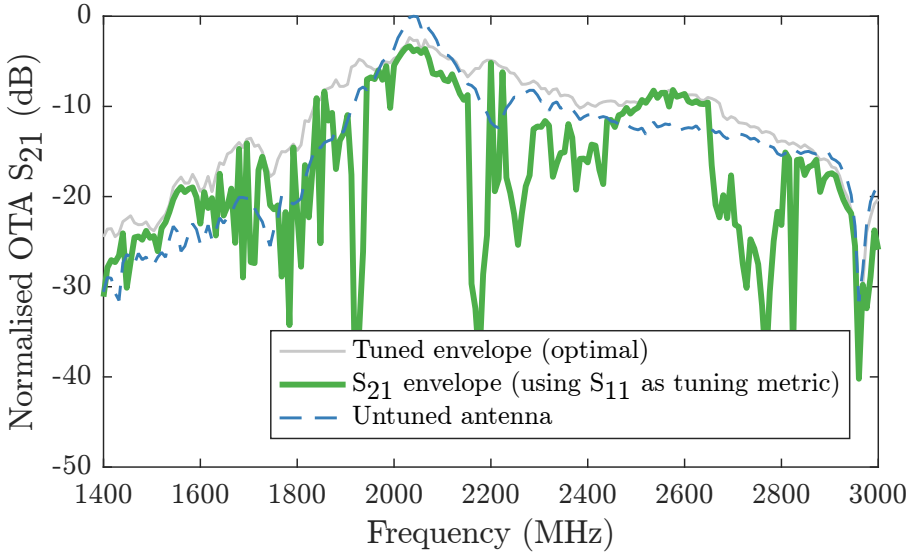

Tuned gain envelope (return loss maximisation goal).

FIGURE 3.9: $|S_{11}|$ and insertion gain envelopes of TMN-tuned antenna (return loss maximisation goal). The OTA S_{21} values share the same normalisation as for Figure 3.8.

With reference to Figure 3.9, tuning state selection based on choosing to minimise S_{11} led to a very wide tuned impedance bandwidth in S_{11}, but did not reliably maximise OTA S_{21}. The TMN had the capability to act as a filter, leading to very low values of S_{11} to being obtained but also yielding poor OTA S_{21} level. Comparing the S_{11} values given in Figure 3.8 (maximum OTA S_{21}

as an optimisation target) and Figure 3.9 (minimum S_{11} as an optimisation target), it is notable that OTA S_{21} gain was in many cases optimised with $|S_{11}|$ less than -10 dB, while much lower values of $|S_{11}|$ available from filtering modes in the TMN provided poor OTA S_{21}. Hence, in this measurement configuration, S_{11} measurement in isolation would not have been a reliable method for determining tuning performance. This finding represents the beginning of a recurring theme throughout this research, that knowledge of S_{11} in isolation is insufficient for determining the "useful" frequency range of a tuned antenna.

More broadly speaking, this finding calls into question the use of total integrated impedance bandwidth as a performance metric of merit for tuneable antenna systems (Section 5.1.1). The tuning range of a tuneable antenna can be reported based on its tuned impedance response, such as a frequency range over which a parameter-swept S_{11} value out-performs a threshold of e.g. $|S_{11}| < -10$ dB.

By this definition, the S_{11} values of the network presented in Figure 3.9 using S_{11} minimisation for tuning state selection would describe a tuning range of at least 72% of the centre frequency in the reported band. This value is valid where the $S_{11} < -10$ dB frequency limits are taken to exist at the boundaries of the 1400–3000 MHz frequency range. It is likely that a greater value for S_{11}-based tuning range could have been quoted, had a wider frequency range been characterised.

Regarding the OTA S_{21} plots given in either Figure 3.8 or 3.9, accompanying S_{11} plots indicate fairly consistent matching linear matching efficiencies across most of the measured band ($\eta_{\mathrm{m}} > 0.9$ at most frequencies). In spite of this, the realised transmission performance was observed to drop as the operating frequency moved away from resonance. With respect to the tuning states providing the best OTA S_{21}, the particular tuning state example given in Figure 3.8 optimised the transmission performance of the overall system while not providing an impedance match better than -10 dB (S_{11} at 2464 MHz was -9.6 dB). From the failure of S_{11} to provide a clear picture of the varying transmission performance across the tuned band, it is clear that an tuning performance metric based on improvements in transmission performance is required. Such a metric is defined for tuneable narrow band antennas in Section 5.5.2 and [20].

3.3.3 Insertion gain on boresight

Initial inspection of the TMN matching flexibility demonstrated by the broad Smith chart coverage (Figure 3.5) and tuneable $S_{11} < -10$ dB range of more than 72% was sufficient to provoke interest in the capabilities of the matching network, but in isolation were not sufficient to describe the range over which effective transmission performance could be maintained. Focussing the discussion of the network performance solely improvements in realised OTAS_{21}, an insertion gain metric can be defined by Equation (3.7), a plot of which is given in Figure 3.10.

$$\text{Insertion gain} = \text{OTA } |S_{21}(\text{tuned})| - \text{OTA } |S_{21}(\text{non-tuned})| \text{ (dB)} \tag{3.7}$$

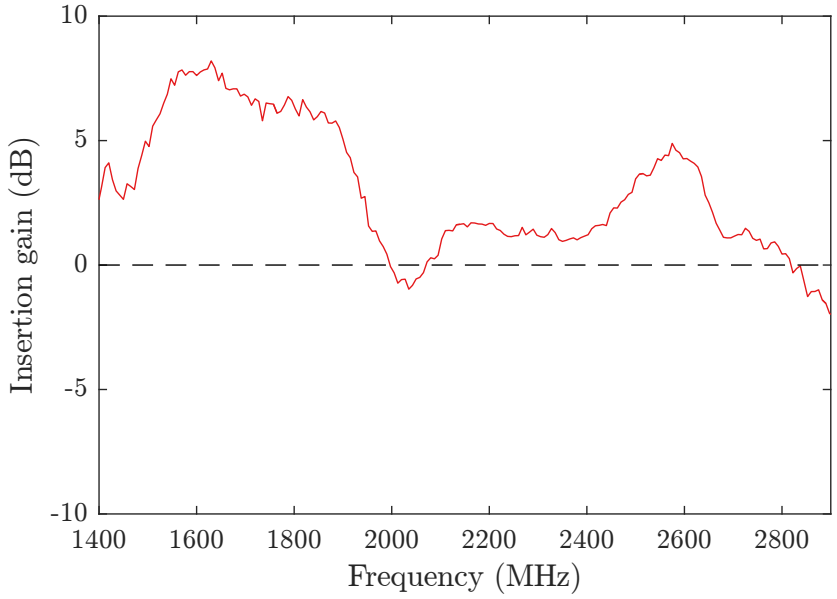

FIGURE 3.10: Insertion gain of tuneable matching network measured on bore sight, normalised to OTA S_{21} level achieved using untuned antenna.

The insertion gain shows a region of enhanced transmission outside the central frequency band around 2035 MHz, where the antenna was well-matched to 50 Ω without the assistance of the impedance tuner. Inclusion of the impedance tuner at frequencies close to 2035 MHz was slightly counter-productive, causing a small degree of power loss while attempting to match a 50 Ω feed line to an already-matched antenna. Moving away from the untuned resonance, the tuner was observed to provide an improvement in OTA S_{21}, demonstrated by the tuned OTA S_{21} envelope showing stronger signal levels than for the untuned case.

The insertion gain values thus recorded an overall performance enhancement when comparing tuned and non-tuned performances of the antenna, yielding a performance advantage in terms of raw signal link strength over a broadened bandwidth. Changing the impedance matching permitted an improvement in power accepted into the antenna and therefore total power radiated at frequencies off-resonance, without tuning the antenna aperture itself.

3.3.4 Total system efficiency in anechoic chamber

In this section, the total system efficiency derived from 3D radiation power patterns is presented to study the expected improvement in system link strength, derived from improved impedance

matching of the antenna at frequencies away from resonance. Subsequently, the transducer efficiency was determined.

To measure the total system efficiency for a small selection of frequencies, the tuned antenna was transferred to the anechoic chamber, wherein 3D radiation patterns and radiation efficiencies relative to a highly efficient $\lambda/4$ metallic monopole constructed for each tested frequency could be derived. The comparison of the tuned/untuned AUTs to the metallic $\lambda/4$ wire monopole showed that the insertion gain plot on boresight was a function of the improved impedance matching, tempered by the varying transducer efficiency.

Using the tuning states determined from the exhaustive selection process in the previous section, the 2035 MHz patch antenna was subjected to efficiency measurement with and without the tuner at frequencies of 1833/1933/2035 MHz. The choice of frequency range was made due to a requirement for a limited number of test frequencies and an interest in frequencies below the natural resonance. The number of frequency points tested was sufficient to establish a general trend for the system losses. Frequencies above natural resonance were explicitly excluded from consideration in this study, as accessing higher frequencies can be achieved by making the initial antenna design smaller. The efficiency testing process started at 2035 MHz and was subsequently stepped down in approximately 100 MHz steps.

The measurement procedure followed the radiation efficiency measurement procedure described in Section 2.4.2.2. In brief, the measured 3D power patterns of the AUT and a highly efficient reference antenna were measured and compared. The anechoic chamber permitted measurement of the 3D radiation pattern for two orthogonal polarisations. These patterns are presented here as power patterns in Figure 3.11 irrespective of polarisation.

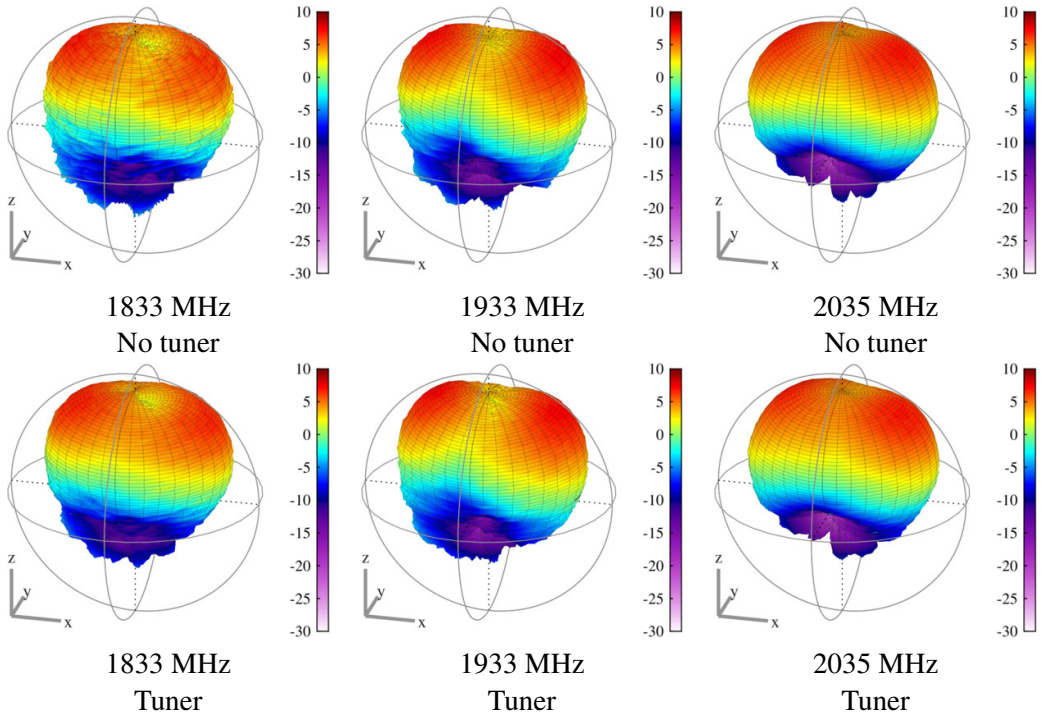

FIGURE 3.11: Total power patterns of patch antenna over 200 MHz frequency range in free space, with and without tuner. Antenna aligned in xy-plane. Colour scale gives directivity in dBi.

Visual inspection of the tuned and non-tuned patterns at 2035 MHz revealed few discernible differences, given that the AUT was well-matched to the feed line with or without the tuner. Moving down in frequency, the pattern was still recognisably representative of the same mode in the antenna (TM_{10}). The pattern similarity metric ρ^2 (correlation, Section 2.4.2.3) exceeded $\rho^2 > 0.96$ for all paired tuned- and non-tuned patterns for each frequency $\{\rho^2(1833\,\text{MHz}) = 0.96; \rho^2(1933\,\text{MHz}) = 0.98; \rho^2(2035\,\text{MHz}) = 0.98\}$.

By comparing the measured radiation patterns of the AUTs and the $\lambda/4$ reference monopole, the system efficiency of the antenna was determined. In the system efficiency results presented here, the measured efficiencies were scaled to remove the effect of imperfect impedance matching of the reference monopole, but not the effect of imperfect matching of the AUTs. Hence, the measured system efficiencies recorded here are reported relative to a perfectly matched, 100% radiation efficient $\lambda/4$ monopole constructed for each test frequency. The impedance matching efficiencies of the tuned/untuned AUTs were not removed from the results, since the performance enhancement from the tuner was expected to be derived entirely from the improvement in impedance matching. The improvements in matching efficiency η_{m} and system efficiency η_{sys} are given in Table 3.1.

With respect to the improvements in system efficiency given in Table 3.1, the improvement in impedance matching efficiency can be observed to have improved the overall system efficiency (i.e. realised transmission link strength) at frequencies away from the naturally resonant frequency.

TABLE 3.1: System transmission efficiencies for patch antenna with and without tuner.

Frequency (MHz)	η_{m} (untuned)	η_{m} (tuned)	η_{sys}, untuned (%)	η_{sys}, tuned (%)
1833	6	99	2	9
1933	21	100	8	11
2035	99	100	38	27

However, the improvement in realised system efficiency can be seen to fall short of the potentially available improvement given by the enhanced impedance matching. Taking the measurements at 1833 MHz as an example, the impedance matching efficiency enhancement suggests that the total system efficiency could have been improved by a factor of $99/6$, or $16.5\times$. In logarithmic terms, the system efficiency enhancement derived from improved impedance matching could have been $10\log_{10}(16.5) = +12.2\,\text{dB}$. Instead, the measured improvement in system efficiency only amounted to a factor of $9/2$, or $10\log_{10}(4.5) = +6.5\,\text{dB}$. The difference in the expected and measured system efficiency enhancements can be ascribed to losses in the implemented matching network itself, which in this work is referred to as the transducer efficiency, η_{trans}.

Applying Equation (3.6) (page 52) to the data in Table 3.1, transducer efficiencies were calculated for each frequency. These are listed in linear and logarithmic form in Table 3.2.

The difference between the maximum potential efficiency improvement, Equation (3.1) and the realised efficiency improvement, Equation (3.2) is accounted for directly by the transducer efficiency presented in Table 3.2. The chamber-derived values for the realised system efficiency improvement agreed with the bench-top boresight-derived values of insertion gain.

TABLE 3.2: Effect of transducer efficiency on realised insertion gain due to tuneable matching network.

Frequency (MHz)	Transducer efficiency (%)	Transducer efficiency (dB)	Max. potential η_{sys} enhancement (dB)	Measured η_{sys} enhancement (dB)
1833	27	-5.6	+12.2	+6.6
1933	29	-5.4	+6.8	+1.4
2035	70	-1.5	< 0.05	-1.5

With regard to Table 3.2, the realised transducer efficiency was low while still providing a net performance enhancement. While the TMN has successfully improved the link strength at frequencies other than the natural resonance frequency as demonstrated by the insertion gain plot (Figure 3.10), the transducer efficiency values demonstrate that over 5 dB of the theoretically available power enhancement was not realised due to construction losses in the process.

Hence, although the TMN can rightly be claimed to deliver a net performance enhancement in delivered signal strength evidenced by the insertion gain alone, the transducer efficiency measure revealed that there was considerable headroom for even greater enhancements in realised

system efficiency. Values for these performance measures were obvious from neither S_{11} nor Smith chart coverage alone. Thus, future work in this area would need to not only report on the realised insertion gain via a transmission measurement as performed here, but also report on the inefficiency of the transducer and seek to reduce this inefficiency. It should be noted that such improvements in transducer efficiency are not trivially easy to accomplish. Performing impedance matching between a 50 Ω source and a load impedance at the edge of the Smith chart is recognised to be a difficult task due to the high rate of change of reactance $X(f)$ associated with the small antenna. The high rate of change of reactance $X(f)$ creates narrow band behaviour [155], which in turn increases the risk of loss of antenna efficiency due to construction losses (i.e. low matching component Q) and tolerances of the matching component values (incorrect reactance cancellation). Examples of both were described and supported with simulation in [156].

For matching networks using fixed-value inductors and capacitors, the inductors are commonly held responsible for the majority of the power loss due to their lower Q factor [157]. A direct, quanitifed comparison between the Q factors of the inductor and tuneable capacitors here are not possible due to the absence of characterised Q data for the inductor and tuneable WS1050 capacitor array at 2000 MHz. However, at 800 MHz there is an overlap in the data offered by the inductor [152] and WS1050 [48] data sheets. In contrast to the common claim that inductors are low-Q devices while the capacitors are comparatively high-Q devices [157], the stated Q factors of the L and C components used here are actually similar at about $Q = 200$. The Q value of the capacitor depends not only on the frequency but also its tuning state, with lower capacitance giving higher Q, but higher capacitance values giving lower Q. There is not enough data in the data sheets to comment on quoted Q values at 2000 MHz, however this finding at 800 MHz does at least suggest that it would be premature to blame all of the transducer inefficiency on the inductor in the absence of additional data. Future work in this area could benefit from measuring the Q factor of the tuneable capacitor bank across the entirety of its tuning state space at the given application frequency, which in turn would help to identify the main source of loss in the transducer inefficiency and hint at which parts of the network to improve.

3.4 Recovery from hand-effect detuning

The study concluded above was an effort to retroactively provide frequency agility in an otherwise non-tuneable narrow band antenna. This is not the only possible application of the TMN described here, however. Instead of seeking frequency reconfigurability with regard to changing the impedance matching of the feed line to a static frequency-dependent impedance, one can consider using the TMN to dynamically recover the impedance matching to a time-varying impedance at a single frequency. User-effect detuning of the antenna provides such a scenario wherein the impedance of the antenna at a single frequency changes in time, as discussed in Section 2.2.3.1.

In this section, the reactive detuning effect in the patch antenna is described, followed by an investigation of whether the TMN successfully improves the overall system efficiency, given that the impedance mismatch caused by detuning can be corrected by re-tuning. The author first detuned the antenna by placing his hand close to the patch face in various positions. The impedance shifts were found to be closely replicated using a hand phantom designed to demonstrate a similar mean permittivity to the hand. The phantom-detuned antenna was then subjected to radiative efficiency characterisation in the anechoic chamber, with and without in-line insertion of the TMN. The results in this section were first presented in [21].

3.4.1 Hand phantom fabrication

The hand phantom detuning object was formed from a mixture of dry powders and water, combined in a ratio to give a similar permittivity ε_{r} to the average behaviour of the human hand (noting that the ε_{r} values of skin, bone, fat and muscle all differ). The approximate permittivities and mixing ratio are given in Table 3.3. The final phantom object was cut down to the approximate dimensions of the author's hand, by placing the hand on top of the phantom mass and cutting around it. The permittivity of the finished phantom was measured using a VNA with a pre-existing open-probe permittivity measurement post-processing script.

TABLE 3.3: Mixing ratio for hand phantom fabrication.

Material	Permittivity ε_{r}	Mass (g)
Water	70	390
TX151 (anhydrous)	2	90
Polythene binder (anhydrous)	Negligible	90
Finished phantom	39 @ 2.5 GHz	540

The phantom was wrapped in a thin layer of cling film to preserve its moisture content, nonetheless it was prone to gradual dehyration. For this reason, the phantom generation, tuning state selection and chamber testing procedures were carried out with the minimum practical time delay between them to minimise the effect of phantom drying causing a change in phantom permittivity.

3.4.2 Impedance shift verification

The 2035 MHz patch antenna was detuned by placing either a hand or the phantom in front of it at various distances. The separation distance d was controlled using an adjustable acrylic mount, and resting the hand or the phantom upon it. The acrylic mount had low permittivity compared to the phantom ($\varepsilon_{\mathrm{r}} \approx 3$ compared to $\varepsilon_{\mathrm{r}} = 39$ for the phantom), and was found not to detune the antenna in the absence of the hand or phantom.

The differences in impedance given by the hand and phantom were found to be small (mean deviation of $0.2\% \pm 3\%$ of $|Z|$), validating the impedance shifting effect of the phantom. A selection of shifted impedance states are depicted in Figure 3.12, displaying the similarity in impedance shifts at various separation distances.

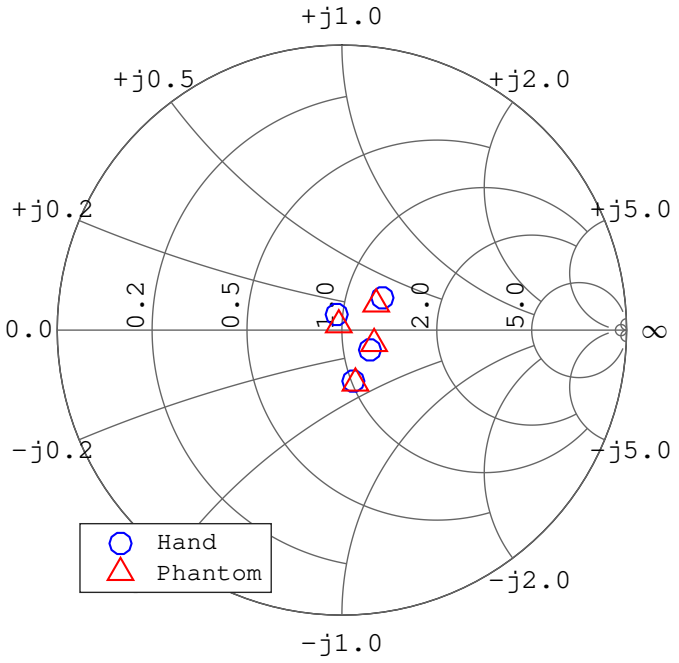

FIGURE 3.12: Impedance shift verification of hand phantom detuning effect at a series of arbitrary positions. Frequency fixed at 2035 MHz.

3.4.3 Efficiency measurements

The patch antenna and phantom were mounted in the chamber (Figure 3.13). The separation distance d between the phantom and patch could be adjusted prior to tuning state selection, and then kept fixed throughout the tuning state selection and anechoic chamber measurement periods. The mount was designed to rotate with the AUT, thereby permitting 3D radiation patterns to be measured with fixed detuning of antenna. As with the boresight insertion gain study, the tuning state selection process was conducted through an exhaustive sweep of tuning states measuring bench-top transmission response OTA S_{21}, followed by an exhaustive search through the data set in post-processing to select the tuning state maximising OTA S_{21}. Immediately following tuning state identification, the phantom detuning assembly was transferred to the chamber and characterised in 3D. Removal of the TMN, leaving the phantom in place, permitted a second chamber measurement to be taken allowing a comparison between the total system efficiencies with and without the re-tuning effect of the TMN.

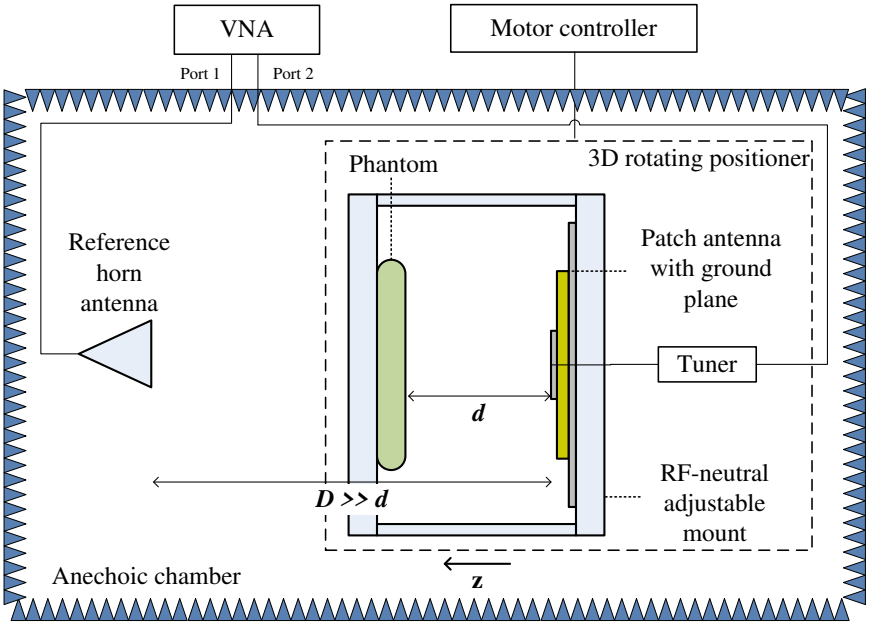

FIGURE 3.13: Anechoic chamber configuration for efficiency measurement under detuning by phantom. Not to scale.

The recorded power patterns at each detuning separation d are given with the impedance tuner in Figure 3.14. The patterns demonstrated clear variation due to the increased blocking of the signal, caused by increasing proximity of the phantom (reduced separation in the z-axis), reading from left to right across the figure. As noted previously for the boresight gain characterisation and subsequent chamber-based efficiency measurements, the main mode in the pattern was unaffected by the use of the tuner and the patterns look nearly identical across the tuner/no-tuner data sets. The pattern correlation metric ρ^2 maintained values in excess of 0.98 across the frequency range for tuned- and non-tuned pairs $\{\rho^2(\text{no detuning}) = 0.98;\ \rho^2(\text{d = 10.5 cm}) = 0.98;\ \rho^2(\text{4.5 cm}) = 0.98\}$.

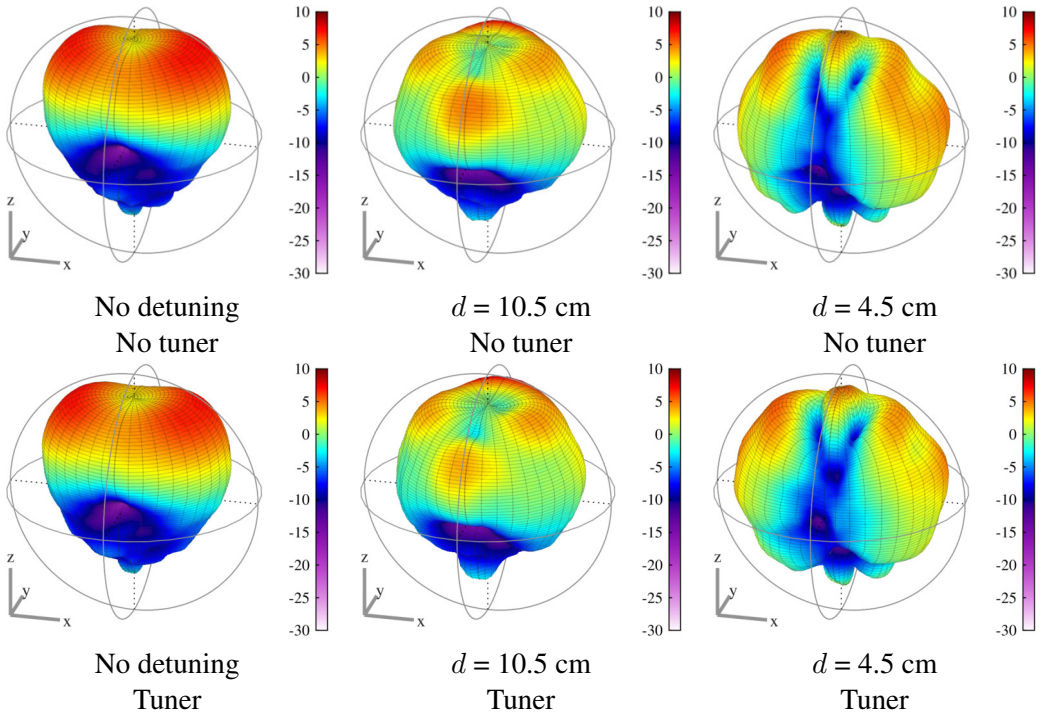

FIGURE 3.14: Total power patterns of detuned patch antenna, with and without tuner. Antenna aligned in xy-plane.

The method for measurement of system efficiency from the recorded patterns with respect to those of an efficient $\lambda/4$ reference monopole remained generally unchanged compared to the previous case of no detuning phantom. The shadowing effect of the phantom provided an additional source of loss, which was incorporated into the measurements by leaving it in place during the reference monopole measurements. Hence, the phantom provided an equal signal blocking/absorption effect for each AUT and the reference antenna for each separation distance d, allowing its effect to be cancelled from the system efficiency calculation. The relative tuned and untuned system efficiencies were therefore given by Equation (3.8), where T and U denote tuned and untuned configurations:

$$\frac{\eta_{\text{sys(T)}}}{\eta_{\text{sys(U)}}} = \frac{\eta_{\text{match(T)}} \cdot \eta_{\text{trans(T)}} \cdot \cancel{\eta_{\text{rad (T)}}} \cdot \cancel{\eta_{\text{phantom}}}}{\eta_{\text{match(U)}} \cdot \eta_{\text{trans(U)}} \cdot \cancel{\eta_{\text{rad (U)}}} \cdot \cancel{\eta_{\text{phantom}}}} \tag{3.8}$$

$$\eta_{\text{trans(T)}} = \frac{\eta_{\text{sys(T)}} \cdot \eta_{\text{match(U)}}}{\eta_{\text{sys(U)}} \cdot \eta_{\text{match(T)}}} \tag{3.9}$$

The system efficiencies, Equation (3.8) and derived transducer efficiencies, Equation (3.9) are reported in Table 3.4 for the separation distances $d = 4.5$ cm, $d = 10.5$ cm and the case of no phantom.

TABLE 3.4: Transducer efficiency of matching network under detuning.

Case	Matching efficiency (%)	Transducer efficiency (%)	Transducer efficiency (dB)
d = 4.5 cm, no tuner	93	-	-
d = 4.5 cm tuner	97	72	-1.4
d = 10.5 cm, no tuner	96	-	-
d = 10.5 cm, tuner	98	67	-1.8
No phantom, no tuner	98	-	-
No phantom, tuner	89	67	-1.7

The measured system efficiencies reduced in both detuning cases compared to the free space scenario due to the combined increase in phantom loss and detuning. The transducer efficiency was observed to be relatively constant with a mean value of -1.6 dB (69%, Table 3.4), nonetheless the tuner did not provide a system efficiency improvement in the example given.

Thus, for the case of detuning using the phantom described above, future work in this domain would need to seek to reduce the transducer losses, in accordance with the findings of the bore-sight and chamber-based TMN insertion gain studies. However, at the detuning distances considered here, the detuning effects demonstrated could be argued not to have been particularly extreme examples. Without the assistance of the tuner, the patch antenna appeared to remain well matched with an S_{11}-derived matching efficiency better than $\eta_{\text{m}} > 90\%$. The detuning examples considered here were sufficient for more efficient matching to be demonstrated through use of the tuner, but not sufficiently extreme for the efficiency lost due to the increased mismatch to be effectively compensated by the recovered impedance tuning offered by the tuner, given the transducer losses associated with retuning.

3.4.4 Potential for performance enhancement under more severe detuning

More extreme detuning was not attempted via reduction of the detuning distance in the original detuning study discussed above, since reduction of the detuning distance would have caused the phantom and $\lambda/4$ monopole to collide (the $\lambda/4$ monopole having a nominal length of 3.75 cm at 2000 MHz). Reviewing the experimental design further, characterisation at reduced separation distances with the potential for more extreme detuning would have been possible if the requirement for system efficiency comparison to the reference monopole had been relaxed, permitting separation distances below 4 cm. At such distances, the results would have not allowed for system power efficiency comparison to the monopole, but would have allowed an insertion gain-type performance measure to have been established.

From the mean transducer efficiency of $\eta_{\text{trans}} = -1.6\,\text{dB}$, an initial estimate can be made of the scale of detuning required to derive a performance enhancement at the system level (i.e. despite

losses in the network). Bearing in mind that the mean transducer loss in the scenario described above was $\eta_{\text{trans}} = -1.6\,\text{dB}$, it can be shown that the break-even point at which the network would become worth deploying would occur for mismatches causing $|S_{11}|$ to degrade to a value no better than $|S_{11}|$ -5.1 dB[2]. If a detuning scenario were created where the $|S_{11}|$ were no better than -5.1 dB, the network could be worth deploying and a net performance benefit in terms of system efficiency might be observed under radiative testing. One caveat to this is that the network efficiency is load-dependent, hence all subsequent calculations are speculative. Nonetheless, the radiative testing method described here shows how such an improvement might be demonstrated in future work.

With regard to the typical impedance shifts demonstrated by the hand phantom (and hand) at various distances in the Smith chart given in Figure 3.12, the required detuning threshold ($\Gamma > 0.55$) was unlikely to ever occur. If the requirement for chamber characterisation and time-consuming tuning state selection were to be relaxed, a quicker test can be used to show that such detuning of an antenna can occur in an alternative scenario where direct contact with the antenna is prevented only by a thin plastic spacer (thickness 1.59 mm).

For the detuning scenarios depicted in Figure 3.15, a metal ruler or a thumb almost in direct contact with a patch antenna can be shown to have caused a much greater impedance shift on the Smith chart (Figure 3.16) than those shown in the initial phantom verification study (Figure 3.12). These impedance shifts of increased severity detuned the antenna with sufficient extremity for the detuning threshold to have been exceeded as evidenced by the S_{11} values given in Figure 3.17.

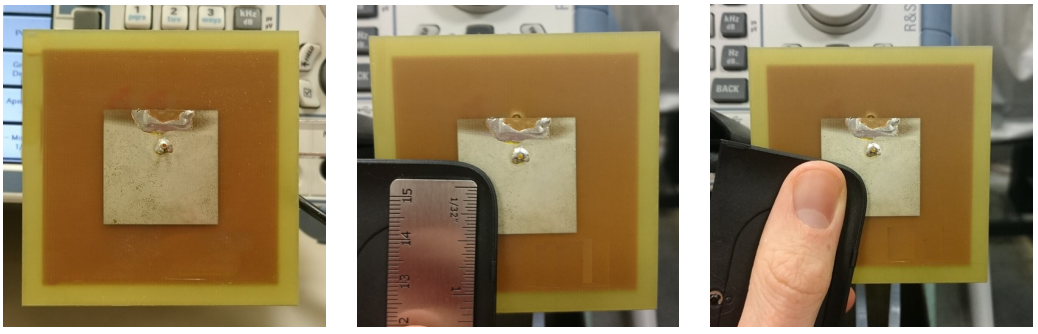

No detuning Metal ruler detuning Thumb detuning

FIGURE 3.15: Demonstration of more extreme detuning scenarios. These states give a voltage reflection coefficient exceeding $\Gamma > 0.583$, which would justify the use of the tuneable impedance matching network with mean transducer loss of -1.6 dB.

[2]Given a transducer efficiency of -1.6 dB, the equivalent power loss purely from mismatch implies an impedance matching efficiency of 69%. This is satisfied by a $|S_{11}|$ value of -5.1 dB.

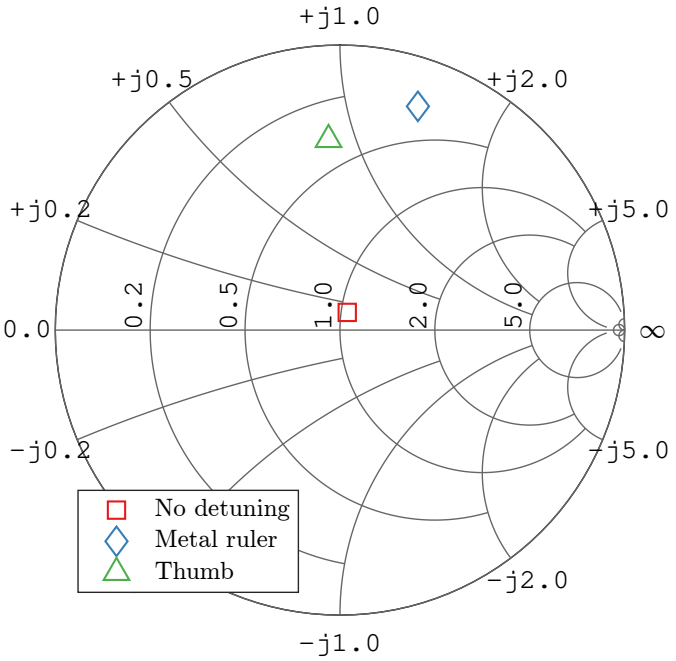

FIGURE 3.16: Impedance shifts under patch antenna detuning caused by metal ruler or thumb close to antenna (Smith chart representation at 2.44 GHz).

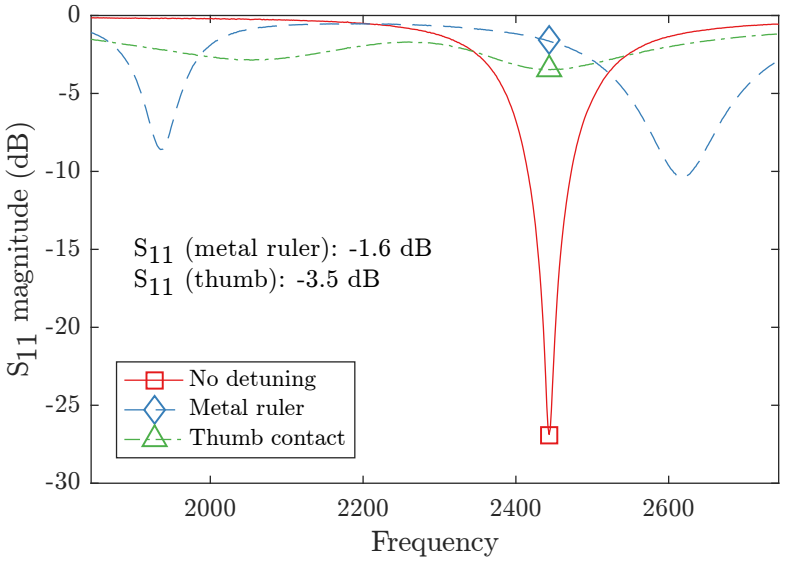

FIGURE 3.17: Impedance shifts under patch antenna detuning caused by metal ruler or thumb close to antenna (S_{11} dB representation).

Hence, although the transducer efficiency was too high for system performance to be enhanced in the relatively benign tuning study conducted using the phantom in the chamber, Figures 3.15–3.17 show that more extreme detuning scenarios can occur wherein the tuner would provide benefit, assuming its transducer efficiency were still limited to -1.6 dB. It is also noteable that the untuned patch antenna in free space offers far superior impedance matching ($|S_{11}|$ = -27 dB) than that offered by many cellular handset antennas, where matching limits of -6 dB are not uncommon.

3.5 Conclusions

In this chapter, the concept of introducing frequency reconfigurability into an otherwise non-tuneable antenna has been addressed. A tuneable impedance matching network was designed and fabricated to achieve impedance bandwidth broadening when connected to a narrow band patch antenna. The network was also used in a study examining recovery of system efficiency in the event of user-effect detuning caused by a hand phantom.

In the impedance bandwidth broadening study, the frequency-reconfigurable behaviour of the network permitted the impedance matching of the antenna to be re-tuned in a narrow band manner over a broader integrated bandwidth. The tuned input response envelope was found to give a -10 dB impedance bandwidth spanning the frequency range 1400–3000 MHz (72% of centre frequency), however, this did not translate into maintenance of high total system efficiency across the same band. The tuneable transmission response was limited by the fixed properties of the non-tuneable antenna aperture, leading to a reduction in system link strength at frequencies away from the natural resonance frequency. While the overall reduction in signal level at frequencies away from resonance could not be prevented through impedance tuning, the tuneable matching network nonetheless demonstrated an insertion gain effect in terms of measured OTA S_{21}. Such a finding is consistent with suggestions elsewhere that realisation of efficient frequency-agility requires the use of aperture-tuneable antennas [154, 158, 159].

Regarding the performance of the tuneable matching network in recovery from a reactive impedance mismatch scenario, the experiment conducted here found that despite efforts to improve the impedance matching and maximise insertion gain of the network, the overall system efficiency was not guaranteed to be improved by the presence of the tuner despite the superior impedance matching efficiency offered.

An assumption of improved system efficiency due to reconfigurable matching leading to improved OTA S_{21} was not upheld in the case of antenna detuning in the chamber using a phantom, despite the use of tuning states optimising the transmission response OTA S_{21} of the system with a transducer efficiency of 69%. It is notable that there are few known published results declaring how much reactive loading a user actually causes for a given antenna, in terms of shifted impedance values. The author concluded in [21] that such detuning scenarios might be found where the tuneable matching network would deliver a performance benefit. This was confirmed by means of a brief demonstration of the detuning given by almost direct finger or metal contact with a patch antenna, sufficiently degrading the impedance matching that a transducer efficiency of 69% would be an acceptable loss and still provide a net performance enhancement. Hence, the work presented in this chapter shows that an understanding of transducer efficiency, derived through radiative measurement, is critical in finding use cases in which the tuner improves system efficiency.

Chapter 4

Hexagonal ferrite materials

In this chapter, a magneto-dielectric (MD) hexagonal ferrite (HXF) material is introduced as a candidate for miniaturisation of a microstrip patch antenna. Use of such a material was motivated by the potential for profound antenna miniaturisation due to the relatively high refractive indices on offer, coinciding with claims of enhanced antenna efficiency and bandwidth compared to other miniaturisation strategies due to the $\varepsilon_{\mathrm{r}} = \mu_{\mathrm{r}}$ criterion (Chapter 2, Section 2.2.4.1). Engineered ferrite MD materials offer not only miniaturisation but also a degree of frequency tuning in the presence of a magnetic bias field. Thus, such materials are relevant candidates for inclusion in the search for effective techniques for tuneable electrically small antennas (ESAs) in the UHF band. However, there has been a shortage of works describing the realised efficiency of tuneable ESAs incorporating engineered ferrites into the design. The work described in this chapter challenges the assumption of high antenna efficiency through a campaign of tuneable HXF ESA construction and measurement, the results of which were published in [22, 23].

A hexaferrite material was specified for manufacture, and the delivered material characterised in terms of complex ε and μ. The radiation efficiency and pattern given by a patch antenna demonstrating hexaferrite substrate-induced miniaturisation were compared to the miniaturisation and efficiency offered by conventional dielectric substrates (FR-4 and Rogers RT5880) [23]. Subsequently, a comparison of the hexaferrite miniaturisation technique to a sub-resonant impedance matching approach was considered, whereby a patch antenna normally resonant at a high frequency constructed upon a dielectric material substrate was miniaturised to that given by the hexaferrite substrate in [23]. The impedance matched sub-resonant patch on dielectric substrate material was compared to a hexaferrite-miniaturised patch in terms of realised efficiency and radiation pattern in [22]. The magnetically-effected tuning range of the patch on hexaferrite material was also discussed [22], with study of the radiation pattern over the tuned frequency range showing pattern stability (i.e. maintenance of the same radiating $\lambda/2$ mode throughout).

4.1 Selection of candidate hexagonal ferrite

4.1.1 Desired features of hexaferrite antenna miniaturisation compound

Initial identification of suitable compounds to pursue for fabrication was conducted by literature review (Section 2.2.4.1). From the known MD materials, engineered ferrites and in particular hexagonal ferrites (or "hexaferrites") were considered. Within the overall class of hexaferrites, a further down-selection was made to consider only the cobalt-substituted Z-type (Co_2Z) hexaferrites. The Co_2Z hexaferrites are given particular attention for the following electromagnetic properties at UHF frequencies:

- Dielectric permittivity ε_r values between 1 and 20 for wavelength compression in the substrate, leading to antenna miniaturisation.
- Magnetic permeability μ_r values approximately equal to ε_r across the frequency range to meet the balanced impedance criterion and provide a large component of the miniaturisation. Hexagonal ferrites commonly display μ_r in the range 10–20 [84], which can be balanced against the ε_r value by formation of a compound material.
- Low loss tangents $\tan\delta_\varepsilon$, $\tan\delta_\mu$ in the frequency range up to 1000 MHz compared to other types of ferrite such as spinel ferrites (though not compared to purely dielectric materials) [93].
- Price of manufacture limited by processing costs rather than cost of underlying compounds. For this work it is assumed that processing costs could be reduced by fabricating the substrate in larger production batches, while the base cost of potentially unusual or high-value elements is perceived to scale less favourably.

4.1.2 Selection of hexaferrite compound from literature

The development of hexaferrite materials with favourable UHF characteristics is a matter of present research interest within materials science [82, 83, 85, 87, 92, 95, 101, 160]. Understanding which hexaferrite materials would be appropriate targets for antenna miniaturisation in this work first required an understanding of material fabrication procedures to be developed.

The hexaferrite materials examined are created through ceramic composition processes, wherein the electromagnetic properties of the final product are dependent not only on the ratio of underlying compounds, but also the material processing history [83, 87]. The powder development method, processing temperatures and pressures are different for each work published, but the major common production steps in producing the solid ceramic products can be summarised as the following [161]:

- Obtain the constituent elements in pure form (often as a solid puck) in the required ratio of molecular weights.
- Grind the pucks in a high power ball mill for several hours (e.g. three hours).
- Compress the resulting powder at high pressure (e.g. 100 kg/cm^2) and sinter at high temperature (e.g. 1100°C) for several hours (e.g. eight to twenty-four hours).
- It should be noted that yield is lower than 100% when following this process. The sintered product acquired for this research had a yield of only 43% by mass compared to the base powdered ferrites.

Detailed variants on this process are given in [85] with procedures described for attempts to achieve single material phases or reduced grain sizes, both of which are held to reduce material loss tangent [85]. The intrinsic pattern of sourcing raw materials and processing them through a high-temperature pressing stage into a solid object remains recognisable throughout the differing variants.

The materials science works relating to hexaferrite development and characterisation at UHF frequencies follow a common theme of adapting the core compounds and processing procedure outlined above, followed by a characterisation of the material properties using an impedance analyser. While the ceramic production methods proved to be too complex to be produced in comparatively large physical dimensions required for this research within the university, it was possible to source such sintered products from Trans-Tech Incorporated (USA).

Of the hexaferrite materials described and published in the literature, the Co_2Z-type hexaferrite described in [83] was chosen as a target material for antenna development. The reasons for the selection of this material can briefly be stated as suitability for the study in electromagnetic terms in terms of ε_r and μ_r, successful realisation of a material matching the balanced impedance criterion (or close to it) across the relevant frequency band, and cost. Specifically, the material designated "Z75" in [83] was a combined Co_2Z,Co_2Y composite, with a ratio of 75% $Ba_3Co_2Fe_{24}O_{41}$ (Z-phase hexaferrite) to 25% $Ba_2Co_2Fe_{12}O_{22}$ (Y-phase hexaferrite)[1]. The production procedure was noted in sufficient detail in the reference [83] to permit an external supplier to attempt to reproduce the material characteristics. The Z75 material is an evolution of a previously published material by the same authors in [87], removing a dependency on iridium that had been introduced in the original design to provide the desired ε_r characteristics and low loss, but with greatly increased cost. The iridium component more generally would be incompatible with broad scale deployments of antennas based on published compound [87].

The main electromagnetic properties of the Z75 material are noted in Table 4.1.

[1]With reference to Section 2.2.4.2: a "material phase" defines the various ratios of $Ba_wCo_xFe_yO_z$ found in different hexaferrites [85].

TABLE 4.1: Electromagnetic dispersion properties of selected hexaferrites

Material	ε_r	$\tan\delta_\varepsilon$	μ_r	$\tan\delta_\mu$	Reference
"Sample C" Co_2Z hexaferrite (with iridium)	7.25	0.07	7.37	0.17	[87]
"Z75" Co_2Z hexaferrite (no iridium)	13.5	0.04	12.3	0.25	[83]

4.1.3 Material acquisition

The source reference [83] was supplied to Trans-Tech Inc., with a briefing to repeat the material synthesis and fabrication procedures as closely as possible to give the greatest chance of repeating the electromagnetic dispersion properties given for the material in [83]. The electromagnetic properties of a ceramic depend not only on the initial compounds but also on the material processing history. Hence, minor deviations between the reference material and the acquired material were expected having been made by separate manufacturers.

Having specified the usage of a given hexaferrite material, the form factor of the delivered samples and the realistic potential for antenna designs based on these samples required consideration. The delivered hexaferrite compound needed to be specified as a powder or a solid sintered tile for delivery. For the purposes of this work the tile form factor was selected. The ceramic production procedure involved a high-pressure compression of the hexaferrite in a stainless steel die at high temperature. The availability of suitable dies and high-temperature ovens limited the tile form factors that could be specified. In discussion with Trans-Tech it was established that the largest single tile size possible would be $50\,\mathrm{mm} \times 50\,\mathrm{mm} \times 2\,\mathrm{mm}$. While hexaferrite tiles of any size may be specified in a simulator, the requirement for practical fabrication restricted the lower frequency limit of any realised antenna design based on the maximum dimensions of the hexaferrite sample. In addition to the square tiles, a small number of discs and toroids were acquired in dimensions compatible with the dielectric and magnetic test fixtures of the Keysight E4991B.

The acquired hexaferrite material samples are depicted in Figure 4.1.

4.2 Material characterisation

4.2.1 Characterisation method

The material dispersion properties were characterised using a Keysight E4991B impedance analyser [162]. The use of this analyser represented a balanced choice between measurement convenience, reduced time to complete measurements and consistency of measurement technique with relevant materials analysis works presented elsewhere [82, 88, 95, 160, 163]. In particular, this type of impedance analyser was used to characterise the reference hexaferrite material [83].

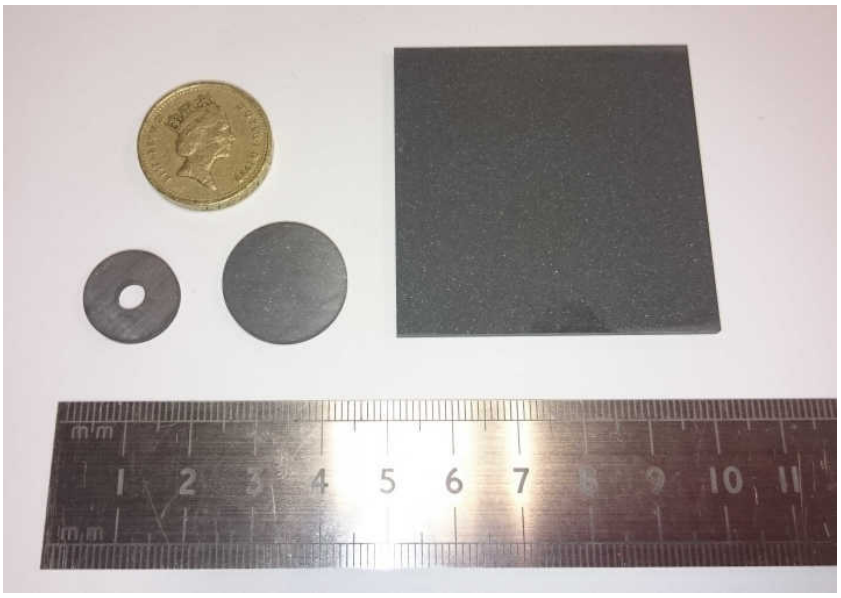

FIGURE 4.1: Hexaferrite tile, disc and toroid samples.

Thus, differences between the material measured here and the properties declared in [83] can be said to be differences in the material rather than differences in the measurement technique, provided that the characterisation was performed at a similar temperature in each case.

Various alternative measurement solutions for the characterisation of $\varepsilon_{\mathrm{r}}, \mu_{\mathrm{r}}$ exist but would have been less suitable considering the frequency of interest and cost concerns. The antenna operating frequencies examined in this work were relatively low compared to the expected ferromagnetic resonance (FMR) above 1 GHz [84]. The large wavelength associated with the low ultra-high frequency (UHF) band rendered alternative techniques such as quasi-optical reflectivity measurements inappropriate since the required sample sizes at 300 MHz (wavelength $\lambda_0 = 1\,\mathrm{m}$) would have been much larger than the 50 mm $\times$ 50 mm tiles available. Similarly, customised waveguide fixtures would have required both precision metalworking and precision ceramics processing not readily available for the project.

The Keysight E4991B operates in a similar manner to a vector network analyser of the type used for general radio frequency (RF) measurements. A dielectric or magnetic test fixture was affixed and calibrated. The dielectric measurement fixture took the form of a pair of electrodes held apart by the material disc sample that acted as a capacitor. Similarly, the magnetic measurement fixture took the form of a short-circuited transmission line with the material toroid sample acting as an inductor. The E4991B firmware converted the measured loss and phase differences into frequency-dependent measurements of complex ε and μ, which permitted frequency-dependent calculation of $\varepsilon_{\mathrm{r}}, \mu_{\mathrm{r}}, \tan\delta_{\varepsilon}$ and $\tan\delta_{\mu}$.

The Keysight E4991B impedance analyser and the associated test fixtures are shown in use in Figure 4.2.

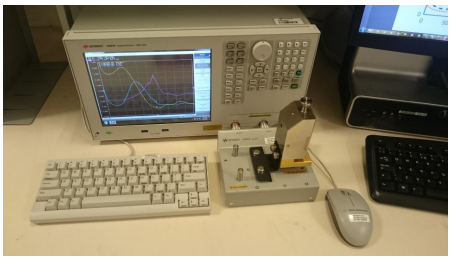

Analyser overview

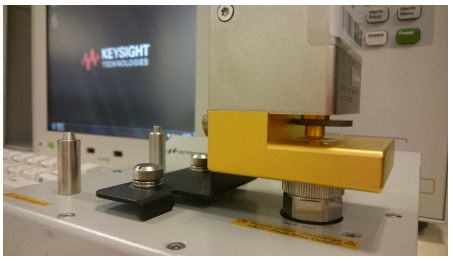

Dielectric permittivity test fixture

Magnetic permeability fixture (during set-up)

Magnetic permeability fixture (during test)

FIGURE 4.2: Keysight E4991B impedance analyser.

4.2.2 Hexaferrite and dielectric material electromagnetic dispersion properties

The electromagnetic dispersion properties of the hexaferrite sample are shown as function of frequency in Figure 4.3 below, with common dielectric materials included for comparison. These materials include Rogers RT5880, FR-4 and Rogers RT6010. The hexaferrite electromagnetic dispersion properties are temperature dependent, hence these results can only be considered valid at approximately room temperature (taken to be 293 K). The Curie temperature of the hexaferrite sample is assumed to be suitably far above the measurement temperature that the material can be considered to be in ferromagnetic phase rather than paramagnetic phase, which would significantly change the tuning behaviours of the material under external bias conditions (Section 2.2.4.3).

The dispersion properties (permittivity ε_r, permeability μ_r and the corresponding loss tangents $\tan\delta_\varepsilon, \tan\delta_\mu$) of the hexaferrite material and selected dielectric materials are given in Figure 4.3. The dielectric permittivity real values $\varepsilon_\mathrm{r}(f)$ were benchmarked against a reference PTFE tile as part of the calibration procedure. The dielectric measurements are therefore all benchmarked against a defined value of ε_r for PTFE, which is given as $\varepsilon_\mathrm{r} \coloneqq 2.1$ from 1–1000 MHz in the instrument operating manual [162]. The magnetic calibration procedure contains no external reference to any material and is inferred entirely from the reactance within the fixture transmission line calibration and the user-defined dimensions of the toroid sample.

The dispersion properties of the hexaferrite sample are given compared to the same properties of the reference "Z75" material published in [83]. The losses in both dielectric and magnetic

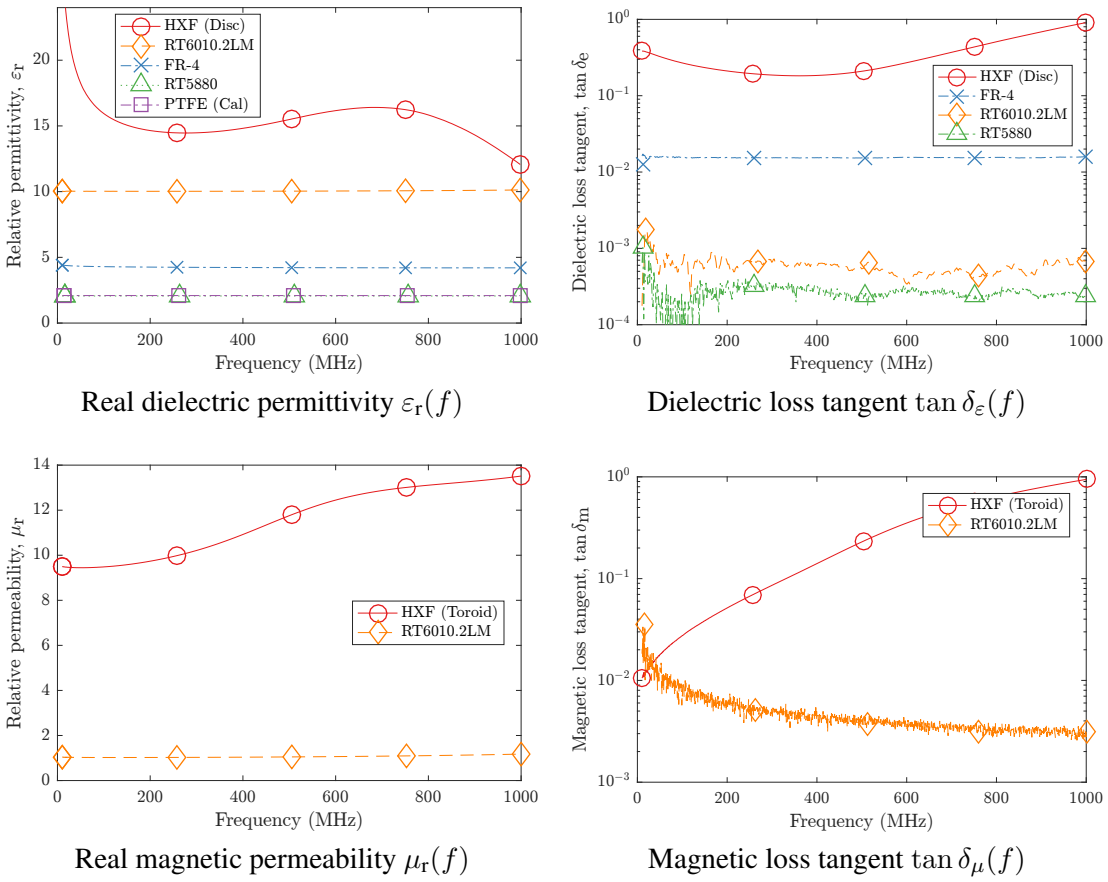

FIGURE 4.3: Dispersion properties of hexaferrite and dielectric material samples.

terms were noted to be higher in the characterised hexaferrite than in the reference hexaferrite across the majority of the frequency range (Table 4.2). By the radiation efficiency definition $\eta_{\text{rad}} = r_{\text{rad}}/(r_{\text{rad}} + r_{\text{loss}})$, the increased ohmic loss $r_{\text{loss (substrate)}}$ suggests that the radiation efficiency of any antenna fabricated on the candidate hexaferrite would be lower than that given in simulation by the reference hexaferrite.

TABLE 4.2: Hexaferrite electromagnetic dispersion properties at selected UHF frequencies.

Material	Frequency (MHz)	ε_r	μ_r	$\tan\delta_\varepsilon$	$\tan\delta_\mu$
HXF	329	14.5	10.4	0.18	0.10
HXF	450	15.1	11.3	0.19	0.18
HXF	650	16.3	12.7	0.32	0.42
“Z75” [83]	650	13.5	12.3	0.04	0.25

As noted in various sources the hexaferrite tile is a type of ceramic [85], hence its characteristics are dependent upon its processing history. The losses in the material can be increased by the presence of unintended material phases, with impurities in the form of unwanted hexaferrite phases increasing loss [85]. The loss in the material is also increased by air gaps increasing the porosity of the material as well as the grain size of the ferrite precipitate that is an effect of the

sintering parameters [85]. Iterative material design is explicitly beyond the scope of this work, which concerns itself mainly with antenna design and analysis. However, it can be said that a re-design of the hexaferrite with the intention of reducing loss would need to examine iterative enhancements to the sintering process and high purity material phase control to reduce the dielectric and magnetic loss tangents. However, the development of well-controlled ferrites from a material phase perspective is reported to be notoriously hard. Quoting from [85], "the formation of hexagonal ferrites is an extremely complicated process, and the mechanisms involved are not fully understood despite having been investigated by many researchers for over 50 years."

Regarding the characterisation of the dielectric materials, from the data sheets [79, 125, 126] it was expected that the dielectric materials would exhibit no useful magnetic properties in terms of antenna miniaturisation. This was confirmed with measured $\mu_\mathrm{r} = 1$ and magnetic loss measured in the noise floor for each of these materials. The dielectric permittivities of the dielectric substrate materials were generally a few per cent of the declared values given in the data sheets in Table 4.3. A comparison of the measured dielectric loss tangents to measured values is given in Table 4.4. Since the data sheets for these materials normally only state the material characteristics at a small number of spot frequencies (e.g. 1 MHz and 10 GHz [126]), the permittivity values measured using the E4991B are taken to be the true values for antenna designs in the UHF frequency range between 300 MHz and 700 MHz for this thesis as well as published works arising from this research [20, 22, 23]. The only major observed difference between measured and data sheet ε_r was found for FR-4, with the measured value being approximately 10% lower than the stated value. This finding broadly agrees with a general awareness amongst RF designers that the dielectric permittivity of FR-4 varies by batch and by supplier, being popular for its low cost rather than tight RF tolerances. The declared data sheet value of FR-4 depends on which source is being referenced, with commonly used values ranging anywhere from $\varepsilon_\mathrm{r} = 4.3$ [127] to 4.7 [125].

TABLE 4.3: Measured ε_r values of selected dielectric substrate materials.

Material	ε_r, data sheet	ε_r, measured
RT5880 [126]	2.2 ± 0.2 @ 1 MHz, 2.2 ± 0.2 @ 10 GHz	2.1 @ 500 MHz
FR-4 [125]	4.7 @ 1 MHz	4.2 @ 500 MHz
RT6010.2LM [79]	10.2 ± 0.25 @ 10 GHz	10.0 @ 500 MHz

TABLE 4.4: Measured $\tan\delta_\varepsilon$ values of selected dielectric substrate materials.

Material	$\tan\delta_\varepsilon$, data sheet	$\tan\delta_\varepsilon$, measured
RT5880 [126]	0.004 @ 1 MHz, 0.009 @ 10 GHz	0.0002 @ 500 MHz
FR-4 [125]	0.014 @ 1 MHz	0.015 @ 500 MHz
RT6010.2LM [79]	0.0023 @ 10 GHz	0.0005 @ 500 MHz

Thus, the dielectric material characterisation showed that the measured values did not differ significantly from those declared in the corresponding data sheets, which in turn built trust in the validity of the E4991B impedance analyser as a method of ε_{r} measurement for the hexaferrite material at RF frequencies. The measured $\tan\delta_{\varepsilon}$ values in the dielectric substrates were considerably lower than those found in the hexaferrite. Again, the definition of radiation efficiency suggests that the increased loss tangent of hexaferrite relative to conventional dielectrics may negatively impact on radiation efficiency.

From the characterised HXF and dielectric material data, an initial assessment of the potential capacity for miniaturisation can be made. Taking a $\lambda/2$ square patch antenna to be miniaturised by a factor n^{-1} where the refractive index $n = \sqrt{\varepsilon_{\mathrm{r}}\mu_{\mathrm{r}}}$, patch antenna area reduction can be achieved as depicted in Figure 4.4. This approximate assessment does not account for a few important factors. These include: the effective length extension associated with the **E**-field, the effective ε_{r} and the effective μ_{r}. The fringing **E**-field causes patch length a to be described by a larger dimension a_{eff} (an extension usually no more than a few per cent of a). Effective filling factors for ε_{r} and μ_{r} have a greater impact on the achieved miniaturisation, particularly the achieved μ_{eff}, since more of the current is "exposed" to the vaccum than is the case for the **E**-field which is mostly contained within the substrate. However, μ_{eff} cannot reliably be determined given the lack of good analytical descriptions of μ_{eff} in such MD patches. Thus, the miniaturisation in Figure 4.4 is intended as a loose guide for motivation, highlighting the profound miniaturisation on offer with use of the HXF material. Experimental demonstration (full-wave simulation or fabrication and measurement) are required to determine practically achieved miniaturisation.

Having characterised the material, the remainder of this chapter establishes the realised radiation efficiency of a pair of hexaferrite patch antennas with respect to identically-sized dielectric-substrate based counterparts (FR-4 and RT5880) [23], followed by an examination of whether the efficiency of the hexaferrite patch antenna could have been surpassed using an RT5880 patch with impedance matching to achieve the required miniaturisation [22]. The frequency agility of the patch is also examined under magnetic tuning [22], with a demonstration of preservation of the radiation pattern across the tuned band.

4.3 Hexaferrite patch antenna design and performance

In this section, small patch antennas fabricated on hexaferrite substrates are considered in three stages. In the first discussion, a set of patch antennas of fixed dimensions with no frequency tuning are examined when fabricated on three different substrates: hexaferrite, FR-4 and Rogers RT5880. By keeping the dimensions fixed while changing the substrate, different operating frequencies were realised for each antenna included in the study due to the varying wavelength compression offered by the different refractive indices. Simulation, measured input responses

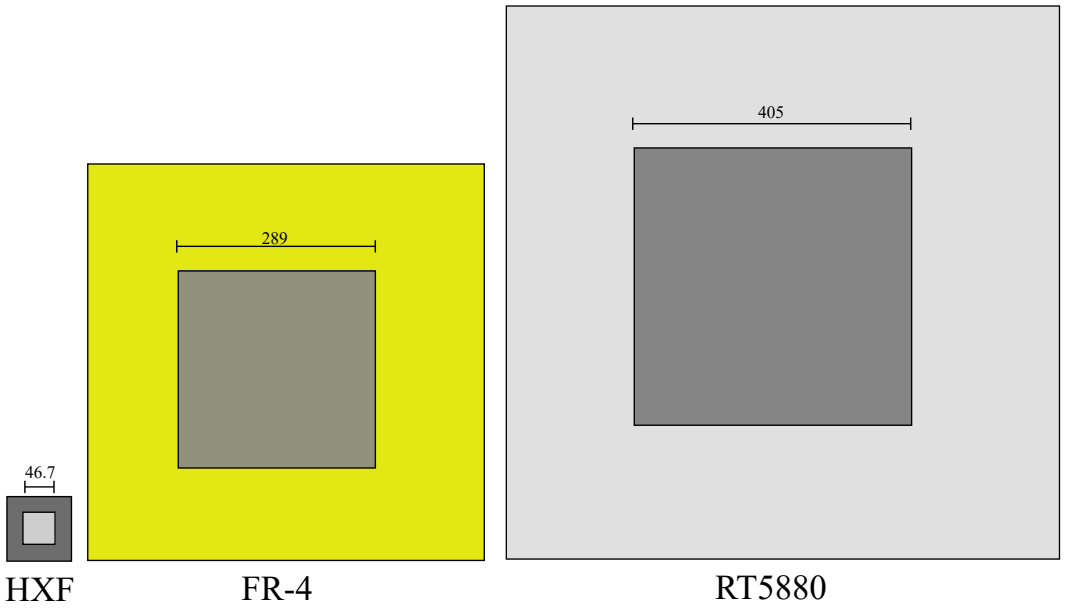

FIGURE 4.4: Board area saved by using high refractive index magneto-dielectric substrate material ($\varepsilon_\mathrm{r} = 15$, $\mu_\mathrm{r} = 11$) rather than conventional FR-4 ($\varepsilon_\mathrm{r} = 4.3$, $\mu_\mathrm{r} = 1$) or Rogers RT5880 ($\varepsilon_\mathrm{r} = 2.2$, $\mu_\mathrm{r} = 1$) substrates. Patches with these dimensions (given in mm) would have nominal operation at 500 MHz (ignoring aspects such as length extension due to **E**-field fringing, or filling factors associated with effective ε and μ). The FR-4 patch depicted here has approximately $38\times$ greater area than the HXF patch, while the RT5880 patch occupies $75\times$ more board area.

and radiative characterisation in an anechoic chamber were used to support an analysis of the radiation efficiency and 3D patterns of each of the antennas, as published in [23].

The second stage of the study examined an effort to miniaturise a RT5880 patch antenna to the same extent as offered by the hexaferrite, without actual use of the hexaferrite. This was achieved by using a matching network designed to operate the RT5880 antenna at a sub-resonant frequency. The impact of the matching approach on efficiency and radiation pattern were published in [22].

Finally, the capability of the hexaferrite substrate to exhibit frequency tuning under magnetic bias conditions was examined. Under magnetic bias conditions, the possibility exists that the operating frequency of the patch antenna can be increased due to the net reduction of real permeability μ_r in the substrate [84]. The efficiencies and radiation patterns are demonstrated under such a biasing scheme as documented in [22], particularly highlighting maintenance of the same radiating mode ($\lambda/2$, TM_{10} mode) across the tuning range.

4.3.1 Non-biased patch antennas of fixed dimensions

4.3.1.1 Antenna design

A set of hexaferrite patch antennas were designed and simulated in CST Microwave Studio [127] with the layouts given in Figure 4.5.

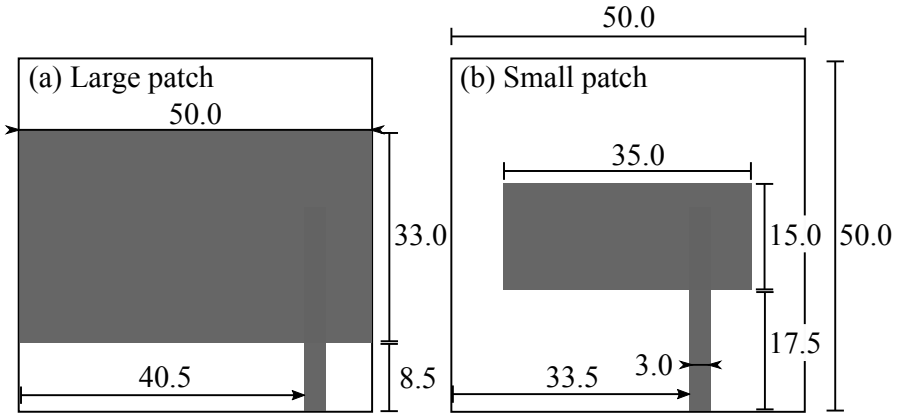

FIGURE 4.5: Hexaferrite patch antenna layout. Dimensions in mm.

The two patch widths, 50.0 mm and 35.0 mm, were selected to target two frequencies: the lowest frequency available (subsequently measured to be 329 MHz), and 433 MHz (ISM band). Since the operating frequency was substrate dependent, to differentiate the two patch layouts the larger design (329 MHz) is referred to as the "large patch," while the smaller layout is referred to as the "small patch." The patch lengths (33.0, 15.0 mm) and track positions were selected to provide impedance matching to a 50 Ω coaxial line. The hexaferrite tiles were limited to maximum dimensions of 50 mm × 50 mm × 2 mm by the manufacturing process.

The copper layout was performed using adhesive-backed copper tape. The fabricated hexaferrite antennas are shown in Figure 4.6. The study centred on an analysis of antenna miniaturisation through change in the substrate properties in isolation. Hence, additional antennas with identical dimensions were fabricated on Rogers RT5880 and FR-4 using laser etching of double-sided copper-clad dielectric substrates. The substrate thickness of the dielectric patch antennas was 1.27 mm. The feed position was adjusted in each of these antennas in order to optimise impedance matching to the feed line.

Since the hexaferrite patch was intended to operate in an electrically small regime ($ka < 0.5$, defined by Equation (2.4) in Section 2.1.2), a measure of electrical smallness is required. The quantity a describing the radius of the smallest sphere completely containing the antenna and feed tracks can be determined from application of Pythagoras' theorem to the dimensions given in Figure 4.7. The blue circle in Figure 4.7 shows the radius a required for a sphere that fully

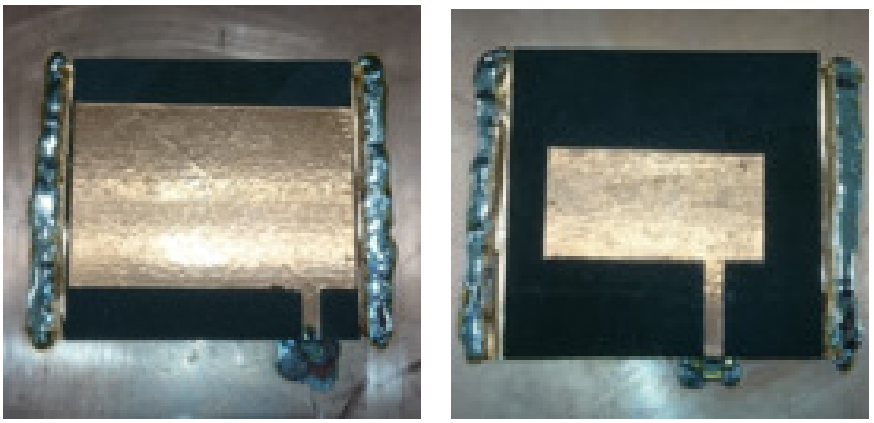

(a) Large patch (329 MHz) (b) Small patch (450 MHz)

FIGURE 4.6: Fabricated hexaferrite patch antennas.

encloses the antenna within its limits[2]. The radius a therefore has a length no greater than 30.0 mm for the large patch and 19.0 mm for the small patch antennas subsequently described, which in turns ensures that the condition $ka < 0.5$ is satisfied at frequencies up to at least 797 MHz for the large patch antenna and 1254 MHz for the small patch antenna.

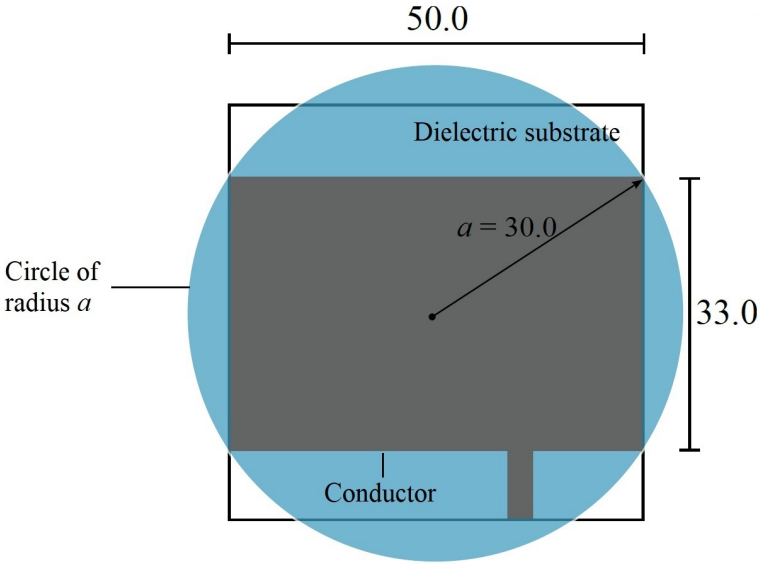

FIGURE 4.7: Calculation of radiansphere of radius a, the smallest sphere which completely encloses the main antenna features (the feed and the patch) in its limits. For consistent ka comparions between antennas using different substrates, the substrate has not been included in the ka calculation in this chapter.

[2]The substrate dimensions have not been included in the ka calculation in this instance because most of the substrate is ineffectual in changing the radiating properties of the antenna. The fringing **E**-field from the patch edges in a dielectric substrate are confined to the area immediately adjacent to the patch and a small extension beyond (typically an extra 1-2% of the patch length). The length extension associated with the fringing **E**-field has not been calculated here, since this extension is usually empirically determined for a dielectric substrate. For magneto-dielectric substrates, empirical calculation of the length extension is complicated by the additional lack of an accurate analytical model for effective μ_r in patches. Hence, the most consistent approach across all substrates is simply to assume that ka is defined solely by the patch dimensions in this study.

4.3.1.2 Input response

Antenna input responses were simulated in CST Microwave Studio [127] and measured using a Rohde & Schwarz vector network analyser (VNA) calibrated using a conventional Open-Short-Match (OSM) technique. The simulated and measured input responses (S_{11}) are shown in Figure 4.8, demonstrating the frequency reduction caused by the increased effective refractive index of the hexaferrite material compared to conventional dielectric substrates. The simulated dispersion data for the hexaferrite material was defined in CST using an ASCII file directly copying the data for every frequency point shown in Figure 4.3. The simulation was able to give an approximate prediction of the frequency associated with the first resonant mode. However, despite repeated simulations with different solver types and boundary condition configurations, CST appeared unable to mimic the strong attenuation observed in the return loss associated with real measured data for the hexaferrite. Similarly, the simulator made overly optimistic predictions of the achievable return loss due to impedance matching in each radiating mode.

The frequency reduction factor is given relative to the measured frequency of the RT5880 antenna in each case by $\frac{f(\text{RT5880})}{f(\text{meas})}$ in Table 4.5. The electrical smallness factor $ka = 2\pi a/\lambda_0$ was calculated as defined in Section 2.1.2 (page 14). Antennas with ka factors smaller than 0.5 may be classed as electrically small [19] and are susceptible to exhibiting low radiation resistance r_{rad}, that may subsequently lead to low radiation efficiency [123]. For comparison, a $\lambda/2$ dipole has ka factor of 1.57.

TABLE 4.5: Frequency reduction and electrical smallness ka of patch antennas.

Antenna	Frequency (MHz)	λ_0 (m)	Frequency reduction factor	ka
HXF large	329	0.91	6.2	0.21
FR-4 large	1514	0.20	1.3	0.94
RT5880 large	2042	0.15	(1, by normalisation)	1.28
HXF small	450	0.67	6.4	0.18
FR-4 small	2110	0.14	1.4	0.85
RT5880 small	2872	0.10	(1, by normalisation)	1.14

The reduction in operating frequency expressed through the frequency reduction factor clearly demonstrates that the antenna is greatly miniaturised by use of a high refractive index MD substrate in the form of the hexaferrite. Neither the FR-4 nor the RT5880 antennas satisfied the electrical smallness criterion of $ka < 0.5$ in their naturally-resonant states, whereas the hexaferrite patches both demonstrate $ka < 0.5$. In this regard, the hexaferrite substrate can successfully be used to achieve pronounced antenna miniaturisation, at least as far as operating frequency is concerned.

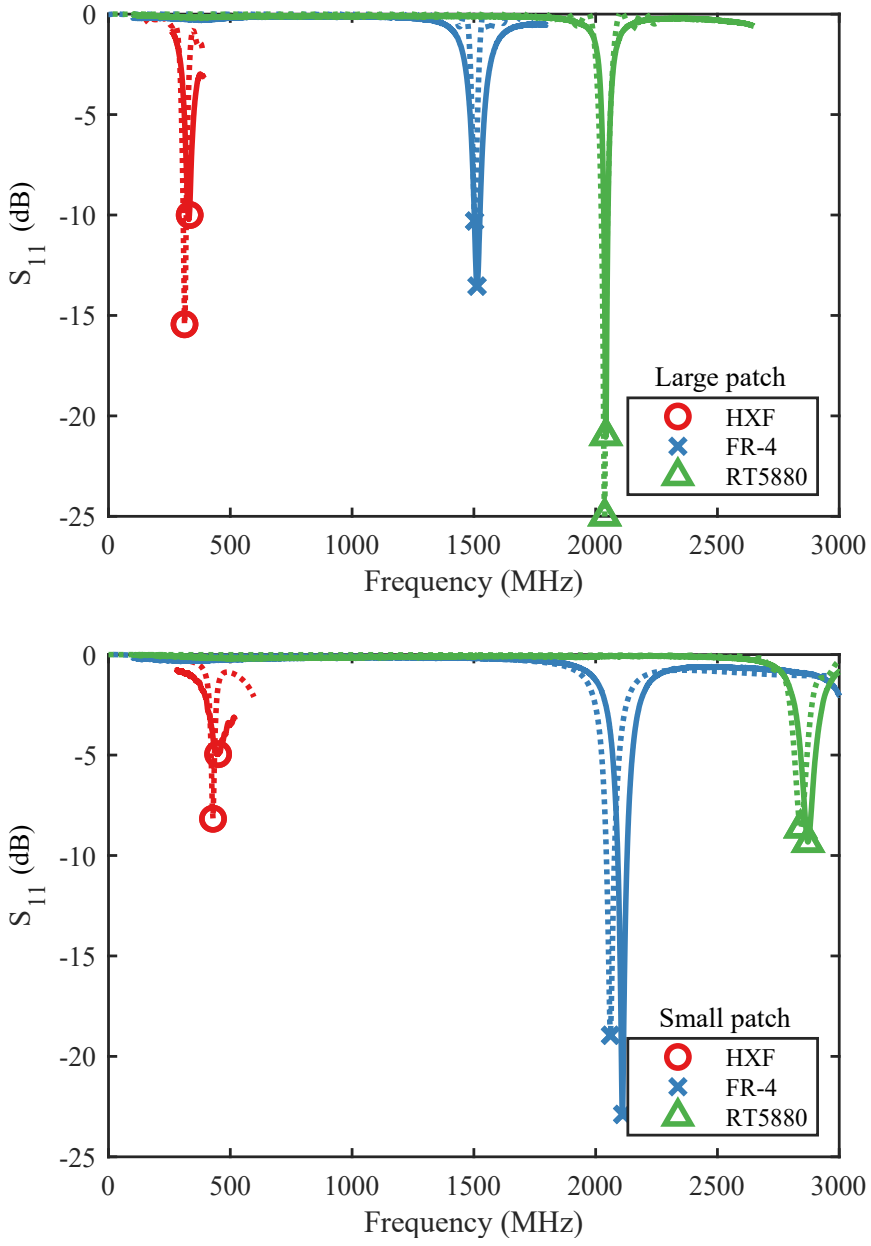

FIGURE 4.8: Measured and simulated $|S_{11}|$ of non-biased patch antennas. Solid lines denote measured results, dashed lines denote simulated results.

4.3.1.3 Radiation patterns

3D radiation patterns were recorded using the anechoic chamber configuration depicted in Chapter 2 (page 41). Selected power patterns (E_{total}) measured at the resonant frequencies of each antenna are compared to simulated patterns in Figures 4.9 and 4.10. The patterns were consistent with the TM_{10} mode, with the pattern similarity across the frequency range indicating that the radiating mode did not change (correlation $\rho^2 = 0.73$ between patterns of HXF and RT5880 large antennas; $\rho^2 = 0.64$ between patterns of HXF and RT5880 small antennas). The increase in directivity with

increasing frequency was an artefact of the increasing electrical size of the fixed ground plane (diameter 400 mm) with respect to the decreasing operating wavelength, reducing diffraction into the $-z$ hemisphere.

It is notable that the hexaferrite antennas while exhibiting electrically small ka factors maintained recognisably broad beam radiation patterns commonly associated with patch antennas. Miniaturisation of the antenna through use of the high refractive index material therefore did not adversely affect the radiation pattern. This feature of miniaturisation through hexaferrite substrate usage was contrasted with the pattern recorded for a sub-resonant impedance matched RT5880 antenna in [22], which is described further in subsection 4.3.2 (page 94).

4.3.1.4 Radiation efficiency

The radiation efficiency of each AUT as a function of frequency is given in Figure 4.11. The radiation efficiency was calculated from Equation (4.1), first introduced in Section 2.4.2.2. The radiation efficiency in this measurement configuration is established from comparison of the integrated received signal levels η_{AUT} given by the antenna under test (AUT) and η_{ref} given by a highly-efficient $\lambda/4$ wire monopole, scaled by the impedance matching efficiency η_{m} of the antennas to a 50 Ω feed line:

$$\frac{\eta_{\Omega,\text{AUT}}}{(\eta_{\Omega,\text{ref}}=1)} = \frac{\eta_{\text{AUT}}}{\eta_{\text{ref}}} \cdot \frac{\eta_{\text{m, ref}}}{\eta_{\text{m, AUT}}} \tag{4.1}$$

The RT5880 substrates delivered greater radiation efficiency than the FR-4 substrate, which in turn was much more efficient than the hexaferrite substrate. This can be understood as a combined effect of increased loss tangent of hexaferrite and FR-4 compared to RT5880 and falling radiation resistance as the electrical size of the antenna decreases. The radiation efficiency is the ratio of radiation resistance to total resistance including heating losses in the the substrate and conductor:

$$\eta_{\Omega,\text{AUT}} = \frac{r_{\text{rad}}}{r_{\text{rad}} + r_{\text{loss (conductor)}} + r_{\text{loss (substrate)}}} \tag{4.2}$$

In the context of a electrically small hexaferrite antenna formed on a lossy substrate, decreasing r_{rad} and increasing $r_{\text{loss (substrate)}}$ conspire to seriously degrade the realised radiation efficiency. The electrical size of either of the hexaferrite patch antennas recorded through the smallness measure ka reveals the patch to be electrically small. Electrically small antennas are known to suffer from low radiation resistance [123], limiting the available radiation efficiency even in the hypothetical scenario of constant loss tangent across all of the measured materials.

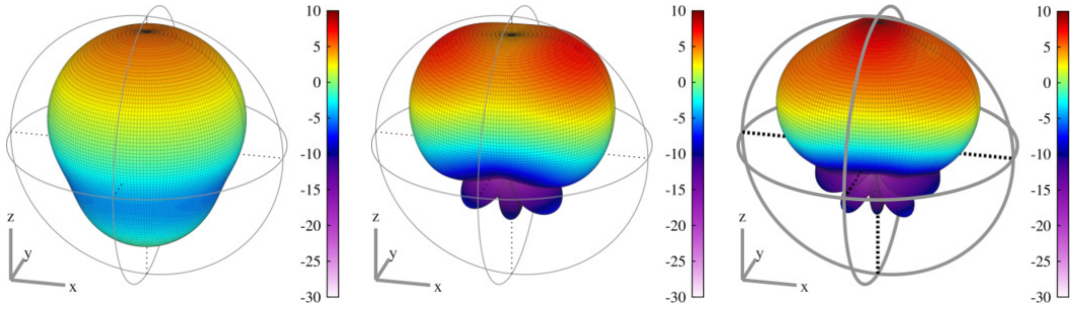

Sim. (HXF, 304 MHz) Sim. (FR-4, 1460 MHz) Sim. (RT5880, 2014 MHz)

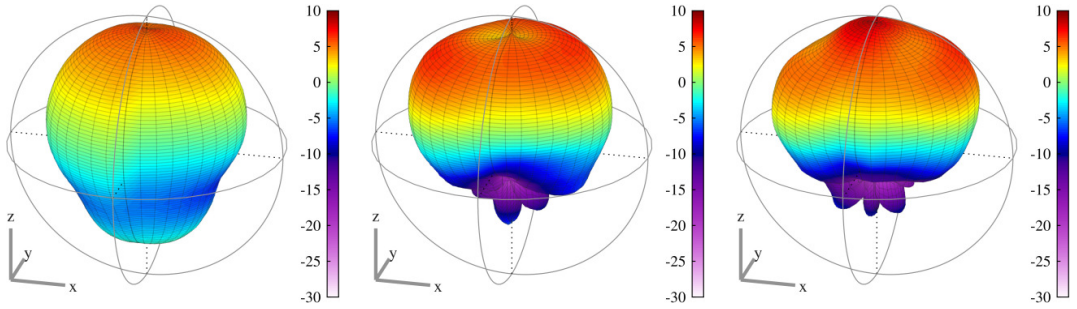

Meas. (HXF, 329 MHz) Meas. (FR-4, 1514 MHz) Meas. (RT5880, 2042 MHz)

FIGURE 4.9: Simulated and measured E_{total} patterns for "large" patch antennas. Colour scale gives directivity in dBi.

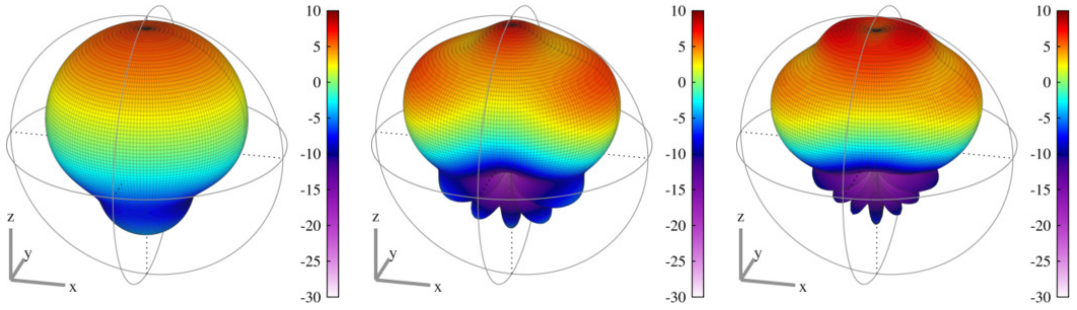

Sim. (HXF, 433 MHz) Sim. (FR-4, 2040 MHz) Sim. (RT5880, 2823 MHz)

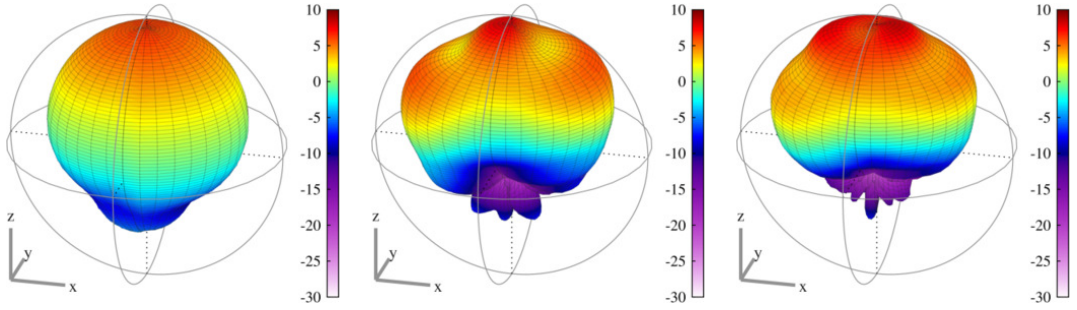

Meas. (HXF, 450 MHz) Meas. (FR-4, 2110 MHz) Meas. (RT5880, 2872 MHz)

FIGURE 4.10: Simulated and measured E_{total} patterns for "small" patch antennas Colour scale gives directivity in dBi.

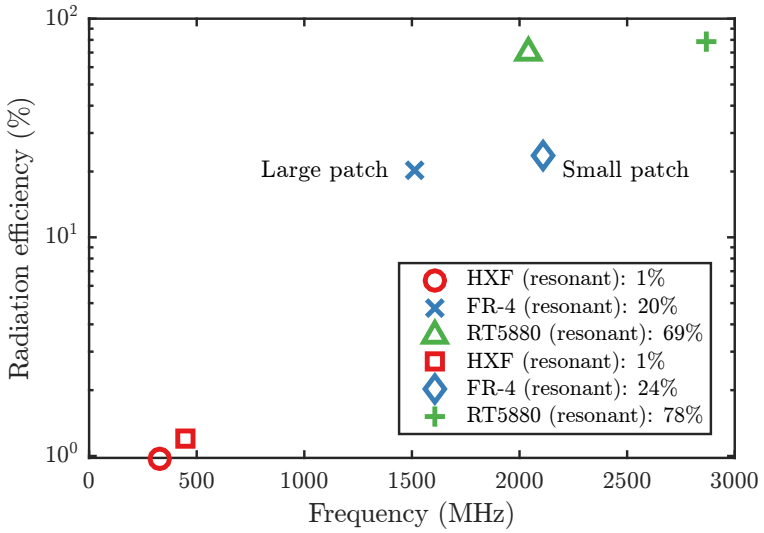

FIGURE 4.11: Radiation efficiency of hexaferrite, RT5880 and FR-4 patch antennas measured in receive configuration.

To compound the problem of low r_{rad}, the loss tangent of the materials increases as one selects materials to achieve greater miniaturisation: if modest miniaturisation compared to RT5880 is required, then an FR-4 substrate can be deployed and the dielectric loss tangent increases compared to that of RT5880 (Table 4.4 on page 84). However if greater antenna miniaturisation than that offered by FR-4 is required, the hexaferrite substrate should be selected. In this case however, the dielectric loss tangent $\tan\delta_\varepsilon$ is a factor of 13 times higher ($\tan\delta_\varepsilon = 0.19$ at 450 MHz), while $\tan\delta_\mu$ increases from a near-zero value to 0.18 at 450 MHz. This occurs while r_{rad} is simultaneously reduced as a result of the high refractive index causing the still-resonant patch to occupy a smaller physical volume.

It is therefore observed that while the loss tangents of hexaferrite materials in development might be considered "low" with respect to other ferrites in the UHF band by material scientists [83], the loss tangents need to be reduced much more aggressively to cope with the reduced r_{rad} coincident with the enhanced miniaturisation offered by MD substrates. The low efficiency available from present-generation commercially available hexaferrite materials likely precludes the use of hexaferrites in long range communications applications such as the suggested Long Term Evolution (LTE) application in [91]. On the balance of the challenges of efficiency versus miniaturisation, the study performed here supports the findings of [104] that hexaferrite patch antennas are best suited to miniaturisation-critical applications such as short range antennas for wearable or radio-frequency identification (RFID) applications, or compact receivers where the received signal strength is already low. The fact that the hexaferrite antenna substrate was well-matched to the medium did not guarantee high antenna efficiency on its own when combined with high material loss tangent [23]. It should be noted that the radiation efficiencies recorded here are all measured in the receive configuration only. Issues associated with non-reciprocity

(e.g. non-linearity of a ferrite antenna in transmission use cases) have not been examined here as they were out of scope for the assessment of the potential of the material in maintaining efficiency under miniaturisation and tuning.

4.3.2 Impedance matched, sub-resonant patch antenna

In the initial study given above, the patch antenna dimensions were fixed while the substrate material was changed to give different operating frequencies. The study demonstrated that the use of the hexaferrite material gave much greater antenna miniaturisation than FR-4 substrate when compared to a benchmark Rogers RT5880 substrate.

Antenna miniaturisation could alternatively have been achieved by impedance matching the patches constructed on conventional dielectric substrates to the 50 Ω feed line at lower frequencies. Since the patch antennas each have their own resonant frequencies closely related to the half-wavelength in the substrate, operation at frequencies lower than this frequency necessarily means that the boundary conditions of the lowest non-DC mode (TM_{10}) are not satisfied in terms of natural resonances. Thus the patches in this scenario can be said to be operating at a sub-resonant frequency.

In addition to comparison of the realised radiation efficiency under this miniaturisation scenario, changes in the radiation pattern must be noted, i.e. when the antenna has a strong power contribution from the "uniform field" TM_{00} mode [164]. In general, patch antennas operating in the lowest-order naturally resonant $\lambda/2$ mode (TM_{10} or TM_{01}) have an **E**-field distribution similar to that depicted in Figure 2.3 (Section 2.3.1). However, there exists a "uniform field" mode at frequencies below the TM_{10} resonance, with the total radiation pattern given by addition of power contributions from the two modes [165, Chapter 3]. Such an effect on the **E**-field distribution is subsequently depicted in Figure 4.15.

For proof-of-concept purposes, the efficiency and pattern effects of matching a single patch at a sub-resonant frequency were examined. The small RT5880 patch antenna was used for this purpose as described in [22]. The impedance matching techniques involved could be similarly applied to any of the FR-4 or RT5880 patches examined up to this point.

4.3.2.1 Impedance matching network design

The patch dimensions of the small RT5880 antenna remained unchanged from the dimensions given in Figure 4.5 (page 87). The natural $\lambda/2$ resonance frequency of the small RT5880 antenna without additional impedance matching was 2872 MHz. Thus, antenna miniaturisation via impedance matching was a process of designing and fabricating a matching network that

transformed the non-50 Ω input impedance of the antenna at 2872 MHz to the 50 Ω feed line at a target frequency of 450 MHz (i.e. the same miniaturisation as offered by the hexaferrite substrate).

The matching network design approach is given in Appendix C (page 155), resulting in a three-stage series of L-section elements. The three-stage solution was chosen over a single-stage solution since the input resistance of the patch was low at 450 MHz, requiring a relatively large impedance transformation from 0.25-j24.6 Ω to 50 Ω. The impedance matching network and fabricated antenna are depicted in Figure 4.12. Note that the dimensions of the antenna are generally unchanged, barring the extensions to the feed track.

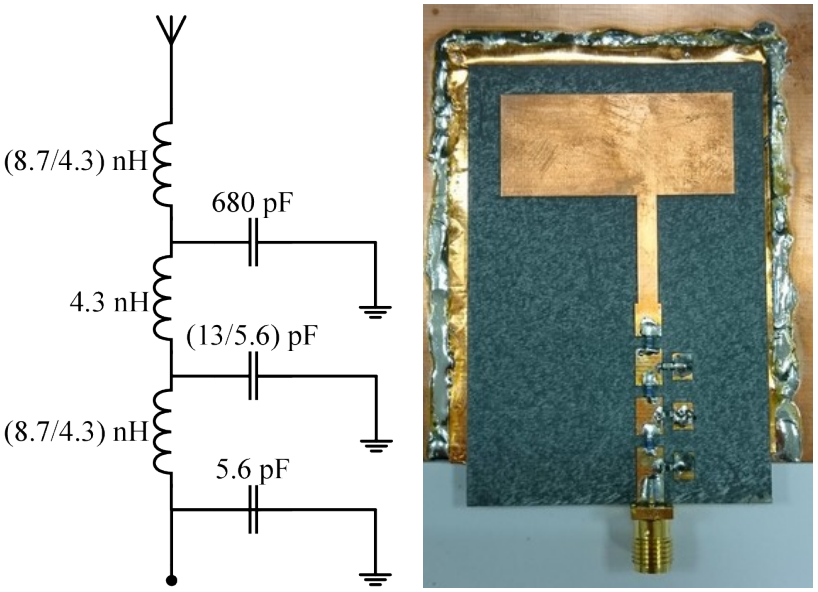

Matching network with (simulation/fabricated) values.

Fabricated matched patch.

FIGURE 4.12: Sub-resonant RT5880 patch antenna matching network.

From simulation and physical measurement, the input response measurements for the matched antenna are given in Figures 4.13 and 4.14. The Smith chart shows the unmatched target value of Z simulated in CST at the single frequency of 450 MHz, while the matched responses are given for a ± 5 MHz arc around the best-matched frequency (410 MHz in ADS, 402 MHz measured).

While the realised frequency of 402 MHz is lower than the target frequency of 450 MHz (Figure 4.14), the objective of the study was to examine the change in pattern and efficiency under significant miniaturisation through matching alone, rather than achieving a perfect match. Achieving high-quality matching (e.g. $|S_{11}|$ better than -20 dB) is possible in simulation, yet in practice the practical implementation of the high Q structure led the author to conclude that matching to within 10% of the target frequency would appropriately demonstrate the overall pattern and efficiency impacts of using a matching-only miniaturisation solution. The design

progression from an idealistic network of lossless components to realistic network of loss-inducing preferred-value components is described in Appendix C.

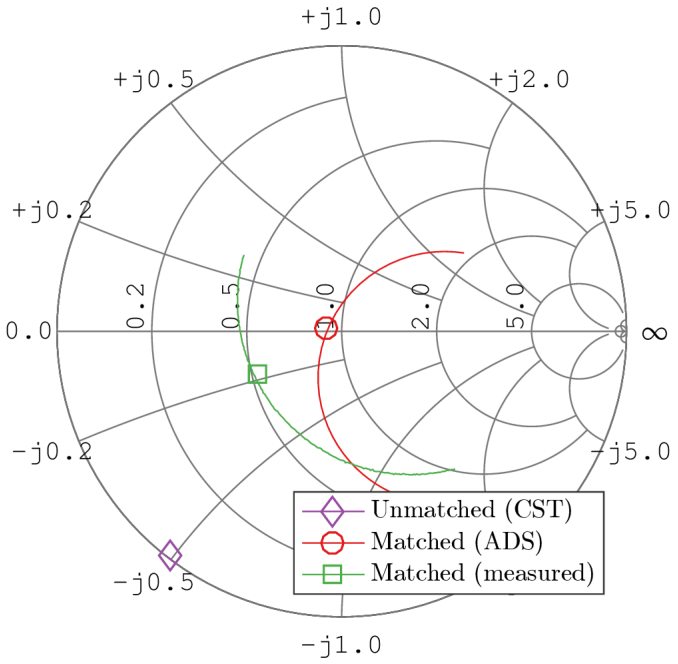

FIGURE 4.13: Smith chart representation of Z_{input} with and without matching network.

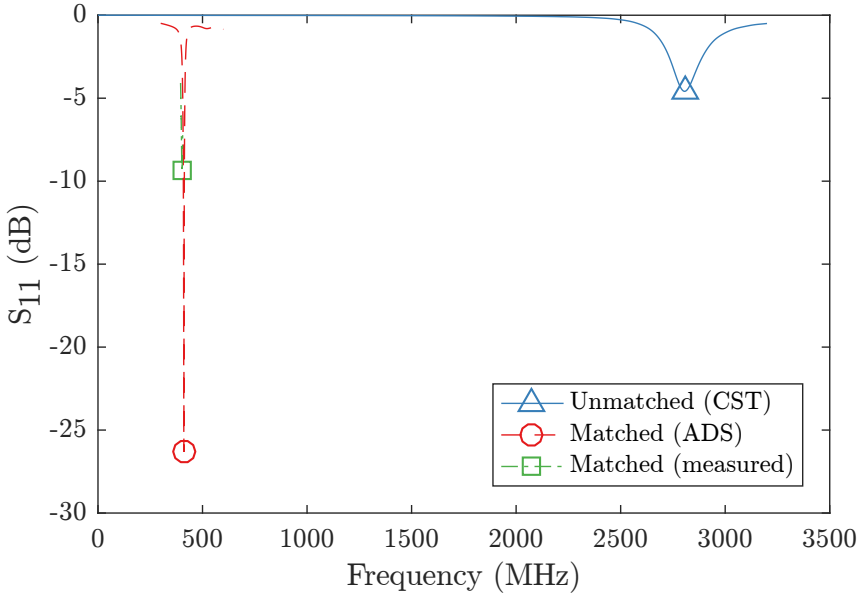

FIGURE 4.14: Reflection coefficient representation of Figure 4.13.

A measure of the power lost due to reflection is given by the matching efficiency, η_{m}, where Γ is the reflection coefficient magnitude:

$$\eta_{\mathrm{m}} = 1 - \Gamma^2 \tag{4.3}$$

$$\Gamma = 10^{\frac{\mathrm{S}_{11}(\mathrm{dB})}{20}} \tag{4.4}$$

In terms of impedance matching efficiency given by measured η_{m} (Equation 4.3), the network provides a matching efficiency of 88% at 402 MHz (S_{11} = -9.2 dB). While this is an improvement compared to the unmatched case (unmatched $S_{11} \approx 0$ dB at 402 MHz), radiative testing is required to confirm the efficiency and pattern behaviours in the sub-resonant regime. S_{11} can only account for power loss caused by reflection at the port looking in to the matching network from the source. It does not record the power available to the antenna at the other side of the matching network (as previously highlighted in Figure 3.1).

4.3.2.2 Sub-resonant radiation patterns

Differences in radiation pattern between the TM_{10} mode and the TM_{00} mode arise from the changing phase relationship of the **E**-field around the perimeter of the patch. In simulation, two patch antennas on different substrates with identical dimensions are shown in Figure 4.15. In (a), the antenna is simulated using a hexaferrite substrate causing it to have a natural resonance frequency of 422 MHz. The **E**-fields at either end of the naturally resonant patch show opposite sign (TM_{10}). That is, there exists a $\lambda/2$ path length difference between the **E**-fields at either end of the patch. In (b), an antenna of the same dimensions on RT5880 substrate is miniaturised entirely through lumped-element impedance matching. Its natural $\lambda/2$ resonance does not occur until the frequency is increased to 2872 MHz. If the frequency is reduced sufficiently far below the resonance of $TM_{10} = 2872$ MHz, the **E**-field between the patch and the ground plane becomes uniform across the entirety of the patch (TM_{00}). At frequencies between DC and the first natural $\lambda/2$ resonance, the total power pattern is a sum of the power contributed from each of these modes. At this frequency, much below the natural $\lambda/2$ operating frequency, the TM_{10} mode in the patch itself is "cut-off". The simulated **E**-fields in Figure 4.15b lead to a current flow largely directed in the vertical direction (y-directed current I) along the feed. The resulting pattern then obtains a skewed vertical polarisation, with the skew caused by the off-centring of the patch relative to the feed line. The changing polarisation with reducing frequency can be observed with help from a simulation in Figure 4.16: the initial TM_{10} mode at 2872 MHz gives horizontal polarisation since the current flow I across the face of the patch is horizontally directed at this frequency. As the operating frequency is reduced by matching, without tuning the antenna aperture, the current flow shifts to being vertically oriented in the direction of the feed line. Thus, at the miniaturised frequency, predominantly vertically polarised operation occurs.

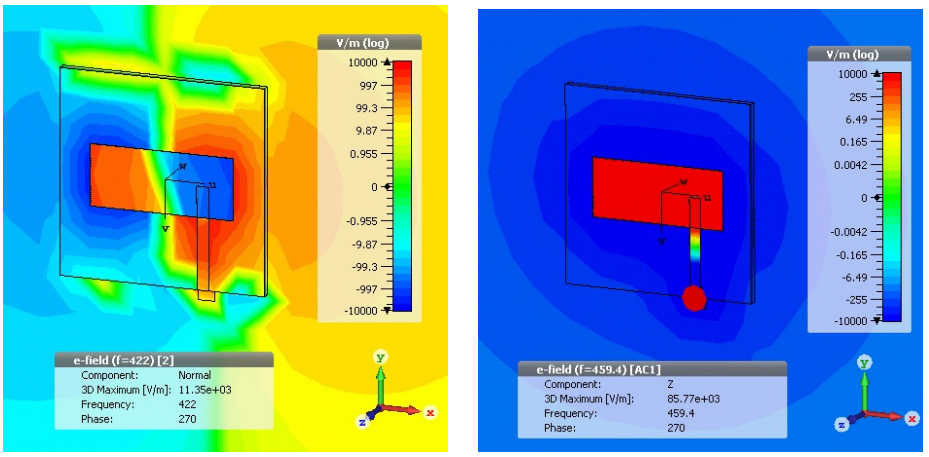

(a) $\lambda/2$ natural resonance (TM_{10}) (b) Sub-resonant (TM_{00})

FIGURE 4.15: Simulated E_z fields of naturally-resonant $\lambda/2$ and sub-resonant patch antennas.

The radiation pattern of the matched sub-resonant RT5880 small patch antenna is given in Figure 4.17 with comparison to simulated sub-resonant pattern and the measured pattern of the equivalent hexaferrite antenna at 450 MHz. The measurement configuration of the anechoic chamber remained unchanged from that given in Figure 2.6, Section 2.4.2. All measurements and simulations included a circular ground plane of 400 mm diameter. While the measured sub-resonant antenna was dependent upon a feed network of real components with fixed values, the CST-simulated pattern was obtained using a feed network of ideal lossless components in arbitrary precision, adjusted to simulate good matching at 402 MHz[3].

The simulated pattern served as a prediction of what kind of radiation pattern should be expected in the highly sub-resonant scenario using ideal matching. The visual similarity between the simulated and measured patterns built trust that the physically measured patterns were truly a function of radiation from the antenna as opposed to any spurious feed cable radiation, given that the simulated antenna contained a SMA connector model but no lengths of cable[4].

[3]For reasons of space, the simulated feed component values and topology are given in Appendix C, Figure C.1.

[4]In principle, the "pattern similarity" statement can be quantified through calculation of the pattern correlation metric ρ^2. Unfortunately, at the time of writing, compatibility issues between measured and simulated data preclude this comparison without incurring considerable additional work.

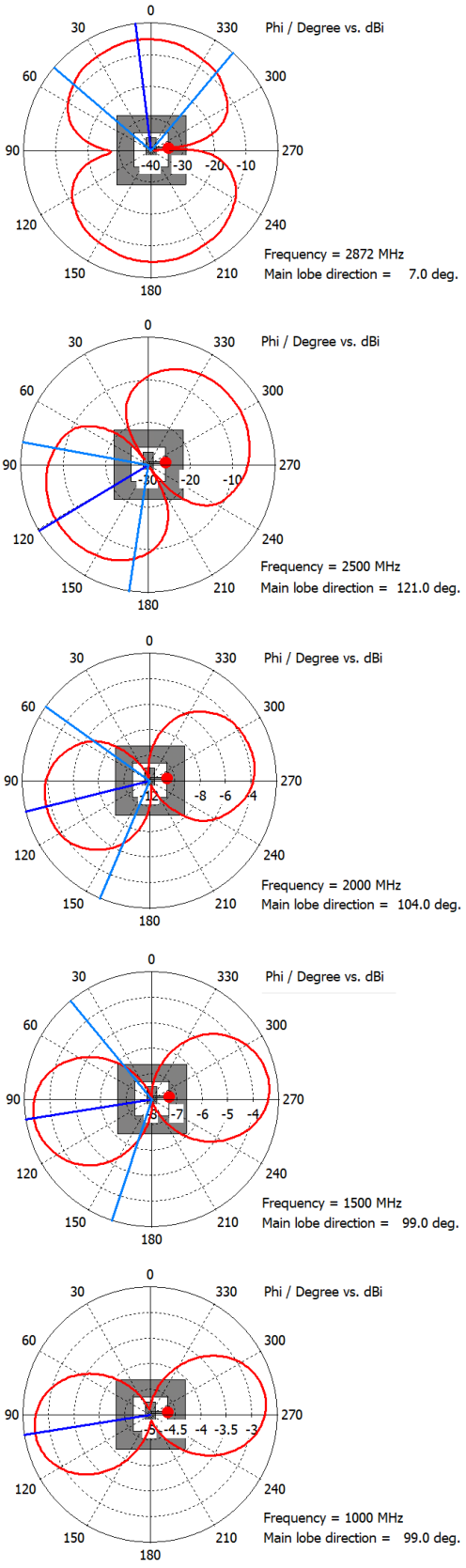

FIGURE 4.16: Shift in polarisation angle under impedance matched (non-resonant) antenna miniaturisation. The polarisation angle changes relatively quickly with reducing frequency to begin with, eventually converging on a polarisation defined entirely by the conductor geometry independent of the $\lambda/2$ mode present at 2872 MHz. The plots are 2D cuts of $\mathbf{E}_\theta$ at constant $\theta = 90°$.

While S_{11} suggested that the RT5880 antenna was not poorly matched to the feed line, with S_{11} better than -9 dB at 402 MHz, the simulated antenna pattern for the RT5880 patch presented reduced levels in the forward hemisphere that the hexaferrite antenna did not. There was reduced correlation between the measured power patterns of the RT5880 antenna at 402 MHz and the HXF antenna at 450 MHz ($\rho^2 = 0.55$) compared to the case where each operated in its TM_{10} mode ($\rho^2 = 0.64$, for patterns presented in Figure 4.10). The sub-resonant pattern of the RT5880 sub-resonant patch exhibited skew and the polarisation patterns revealed nulls in the pattern close to the boresight $+z$ direction. The E_{total} pattern exhibits a deep null in the $-z$ direction (not visible in given 3D pattern, but visible in 2D cuts, Figure 4.18). The position of the main beam is shown to have experienced significant rotation in the elevation angle, i.e. rotation about the z-axis, in the $xy-$plane. The measured radiation pattern is predominantly vertically polarised (y-axis, with skew), whereas the HXF patch at the same frequency operating in a $\lambda/2$ mode operates with horizontal polarisation (x-axis). Miniaturisation via impedance matching alone has therefore incurred an unintended change in operating polarisation, in addition to the low efficiency and sensitivity to component reactances.

4.3.2.3 Sub-resonant radiation efficiencies

The measured radiation efficiencies of the resonant hexaferrite antenna and the sub-resonant tuned RT5880 antenna are given in Table 4.6. As described previously, the radiation efficiencies are given relative to a reference $\lambda/4$ monopole constructed for each frequency (Equation 4.1).

TABLE 4.6: Realised efficiencies of HXF substrate and sub-resonant impedance matched RT5880 patch antennas.

Antenna	Frequency (MHz)	η_m (dB)	η_{tot} (dB)	η_Ω (dB)	Radiation efficiency (%)
HXF	450	-1.9	-20.9	-19.0	1
RT5880 (matched)	402	-0.5	-24.7	-24.2	0.4
RT5880 ($\lambda/2$)	2872	-0.5	-1.6	-1.1	78

Given ideal lossless matching, the CST simulation suggested that an upper limit on the radiation efficiency of the RT5880 sub-resonant patch itself at 402 MHz would be no more than approximately -14 dB (3%). However, that simulation represented an upper limit on efficiency in the absence of losses in the matching components (although conductor and substrate losses in the antenna were modelled). In this sense, it was expected that the measured radiation efficiency could be no higher than 3% due to the sub-resonant nature of the patch, further reduced by the losses in the matching network.

The measured radiation efficiency of the RT5880 patch at 402 MHz was found to be 0.4%. This compared unfavourably to that of the hexaferrite antenna (1%), notwithstanding the observations

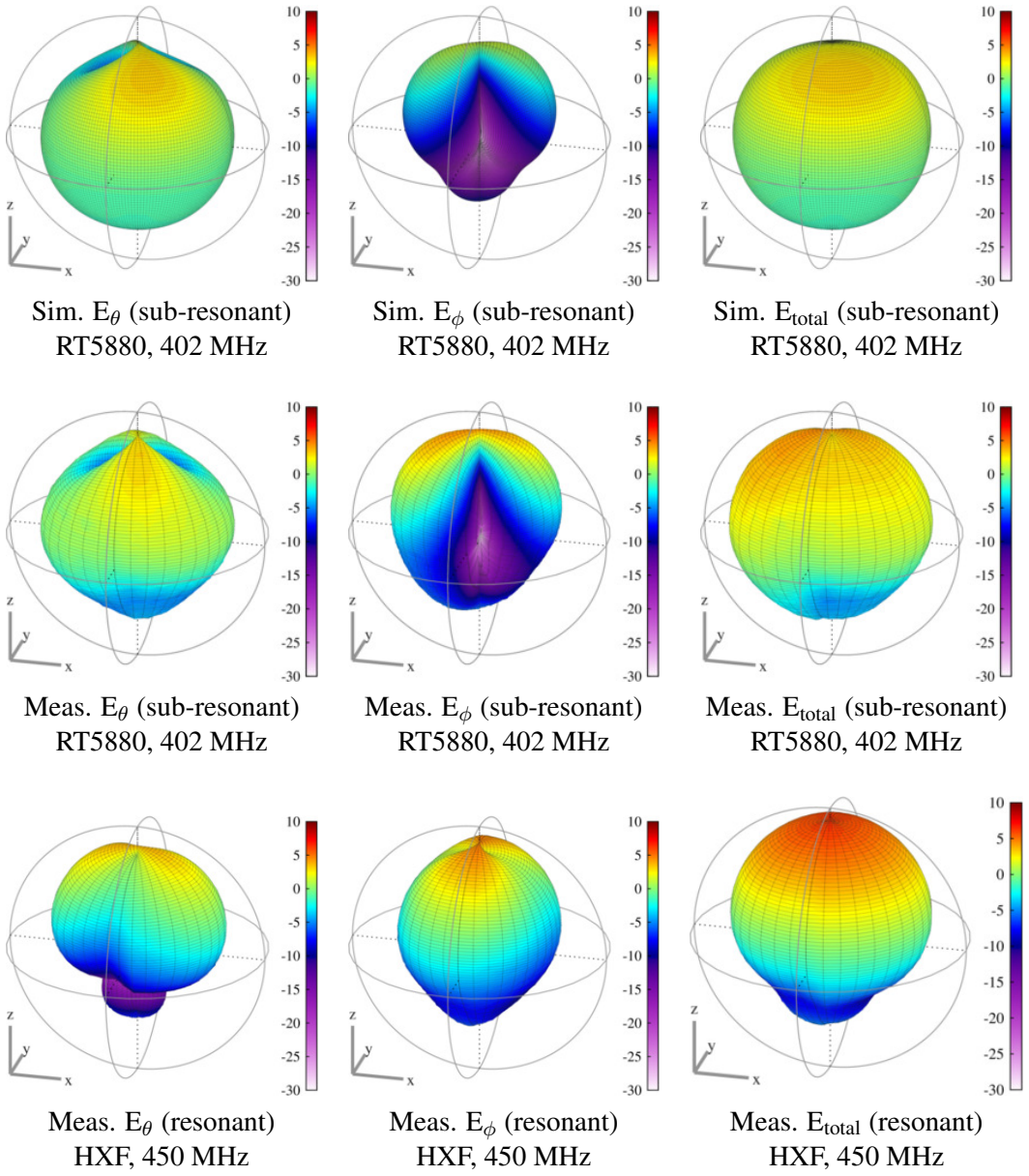

FIGURE 4.17: Simulated and measured radiation patterns for matched sub-resonant RT5880 small patch antenna, compared to HXF antenna naturally resonant at 450 MHz. Colour scale gives directivity in dBi.

already made regarding the changing mode in the pattern. The low efficiency in this context can not be attributed to the high loss tangent $\tan\delta_\varepsilon$ of the RT5880 material compared the combined losses in HXF, since the material losses in RT5880 were already found to be lower by characterisation in the E4991B impedance analyser ($\tan\delta_\varepsilon$ for RT5880 = 0.0003, compared to $\tan\delta_\varepsilon$ = 0.18 and $\tan\delta_\mu$ = 0.19 at 450 MHz for hexaferrite [23]). CST gave a predicted radiation efficiency of 3% for the RT5880 antenna operating under ideal (lossless matching), suggesting that the reduced radiation efficiency was limited in part by reduced radiation resistance associated with poor coupling of the antenna to the far-field at 402 MHz given its lack of a naturally resonant mode at this frequency. This limit on available efficiency was then degraded by loss in the

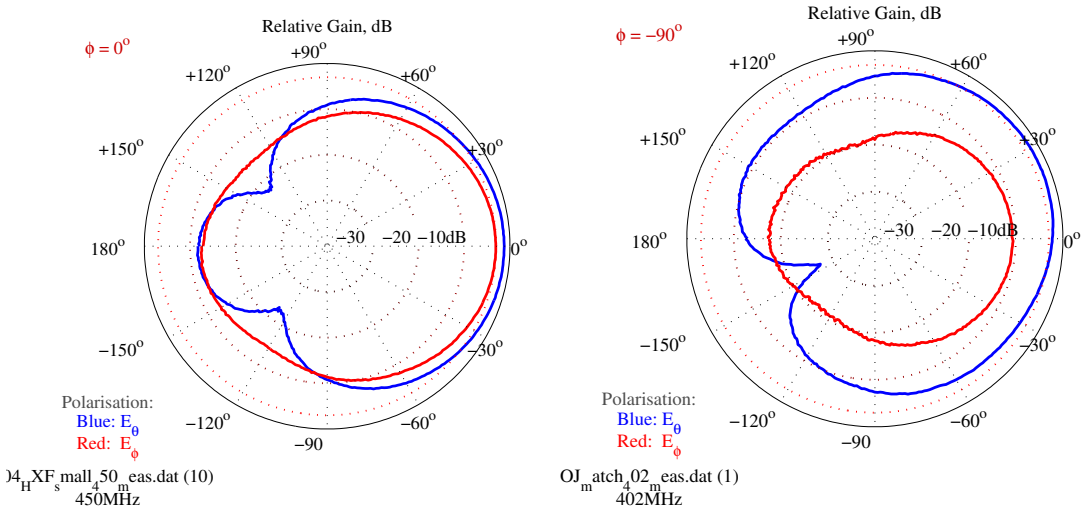

Hexaferrite $\lambda/2$ patch (TM_{10})

RT5880 sub-resonant patch (mixed TM_{10}/TM_{00})

FIGURE 4.18: 2D cuts of patterns presented in Figure 4.17.

matching network components. While the L and C components were selected for nominal high Q, comparison of the data sheets [149, 166] for the chosen components suggested that the inductors were responsible for the majority of the power loss within the matching network (inductor nominal Q 30–50 compared to capacitor nominal $Q > 800$). Thus, lumped-element impedance matching to miniaturise an otherwise efficient, low-loss antenna is not a guaranteed strategy for efficient antenna miniaturisation given the sensitivity to component losses at sub-resonant frequencies.

4.3.3 Ferromagnetic substrate tuning

4.3.3.1 Ferromagnetic tuning overview

It has been shown above that the hexaferrite substrate offers better efficiency than an impedance matched sub-resonant dielectric substrate solution, despite the high substrate losses. Another point of differentiation between hexaferrite and dielectric substrate materials is that the hexaferrite offers the capacity for ferromagnetic tuning. The hexaferrite material demonstrates susceptibility to tuneable μ_r due to its ferromagnetic properties, which in turn affords a degree of tuneability in the resonant frequency of the patch antenna (Equation 2.12, Section 2.3.1). This tuneability is shown in this section to maintain pattern stability under tuning, as presented in [22].

To date, comparable studies of the frequency-reconfiguration of hexaferrite patch antennas have been limited. Tuning through applied voltage was attempted in [102] and found tuneability of less than 2% of the centre frequency. Tuning through magnetic biasing appears only to have been addressed in the work [89], but as with [102] this was not accompanied by a radiative

characterisation of the efficiency or pattern across the tuned band. As such, the overall effect of tuning on radiation efficiency is not known.

Thus, prior to this study, the overall effect of magnetic tuning on patch antenna radiation efficiency was not known to have been reported for a hexagonal ferrite material. For a radiation efficiency ratio $\eta_\Omega = r_{\text{rad}} / (r_{\text{rad}} + r_{\text{losses}})$, the radiation resistance term should increase with increasing frequency due to the antenna's increasing Wheeler radiansphere occupancy coincident with rising ka [167, Chapter 3]. However, it has already been shown from characterisation of the hexaferrite material in its magnetically unbiased state that the material loss tangents are highly frequency dependent, rising with increasing frequency (Figure 4.3). Thus, assumptions of increased realised antenna efficiency based on increased ka alone cannot be guaranteed to be valid, demonstrating that there is a need for substrate-tuneable miniaturised antennas to be radiatively assessed to clarify the impact of tuning on efficiency.

4.3.3.2 Magnetic biasing method

A preliminary study of the actual tuneable μ_{r} of the hexaferrite material would have permitted a prediction of the total available tuning range of the patch antenna in CST Microwave Studio, prior to practical measurements in the laboratory. However, a lack of access to suitable material magnetic characterisation equipment (such as high-strength variable magnetic field generation equipment and vibrating sample magnetometry) prevented the research proceeding in this direction. As such, from the results that follow, it is not clear whether the patch antenna could have been tuned further with a stronger biasing field, or whether the material was in fact already operating near its magnetic saturation point. Similarly, direct measurement of variable μ_{r} was not possible under magnetic biasing using the E4991B impedance analyser, due to the operating constraints of the firmware and fixture geometry. Instead, study of the realised patch antenna tuning range was executed through a direct study of magnetic biasing on one of the hexaferrite patch antennas using high strength magnets.

To enact the tuneable μ_{r} biasing in a patch antenna, a source of variable external bias field **B** is required. This can be effected through the use of magnetic-field generating coils or the application of permanent magnets to the antenna. Since the aim in this work was to examine the tuned antenna behaviour in the anechoic chamber, the permanent magnet biasing method was chosen for ease of mounting on the rotating antenna positioner. Strong neodymium magnets (class N35 2×3 mm magnets, each with nominal remanence value 1.22 T [168]) were applied to the patch conductor face in varying numbers to achieve different magnetic bias field strengths. The magnets were arranged with co-polar magnetic orientation, such that the magnets repelled when pushed toward each other (Figure 4.19). This arrangement maximised the magnetic bias field density in the material.

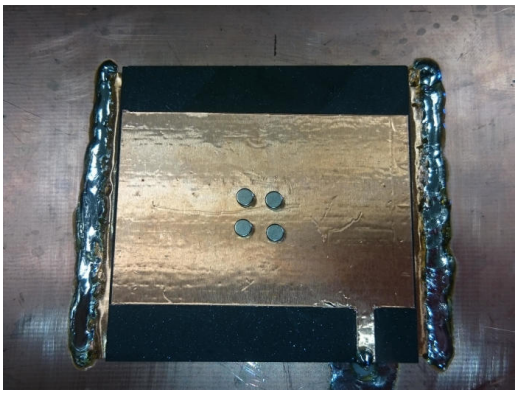

Few magnets: high μ_r, low f.

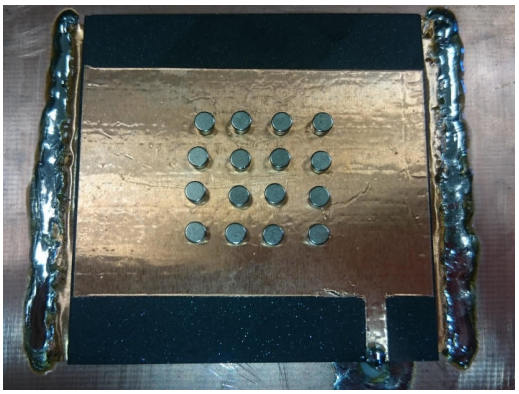

More magnets: reduced μ_r, higher f.

FIGURE 4.19: Magnetically tuned "large" HXF patch antenna.

4.3.3.3 Input response measurement

Each hexaferrite patch antenna was subjected to **B** field biasing using a variable number of magnets (such as in Figure 4.19). The number of magnets was gradually increased from zero to the maximum number that would fit on the patch face, noting that the upper limit on the number of magnets is capped by the repulsion effect of adjacent co-polar magnets. The degree of tuning observed was found to be a function of the number of magnets on the patch face, with no noticeable sensitivity to the spacing between magnets.

The measured reflection coefficients as a function of increasing numbers of magnets are shown in Figure 4.20. The increasing magnetic flux density in the material caused by the increased number of magnets reduces μ_r [101], thereby increasing the patch operating frequency. The percentage tuning bandwidth, $\mathrm{BW}_{\mathrm{tune}}$ for each antenna is calculated in Table 4.7. $\mathrm{BW}_{\mathrm{tune}}$ is calculated using the lowest and highest resonant frequencies observed for the lowest mode in the antenna, normalised by the centre frequency:

$$\mathrm{BW}_{\mathrm{tune}} = \frac{f_{\mathrm{high}} - f_{\mathrm{low}}}{(f_{\mathrm{high}} + f_{\mathrm{low}})/2} \times 100\% \tag{4.5}$$

TABLE 4.7: Accessible frequency range of hexaferrite magnetically-tuned patch antennas.

Antenna	Frequency (MHz)	ka	$\mathrm{BW}_{\mathrm{tune}}$
Large	329 (lowest magnetic bias) 405 (highest magnetic bias)	0.21 0.25	21.7 %
Small	450 (lowest magnetic bias) 622 (highest magnetic bias)	0.17 0.23	32.1 %

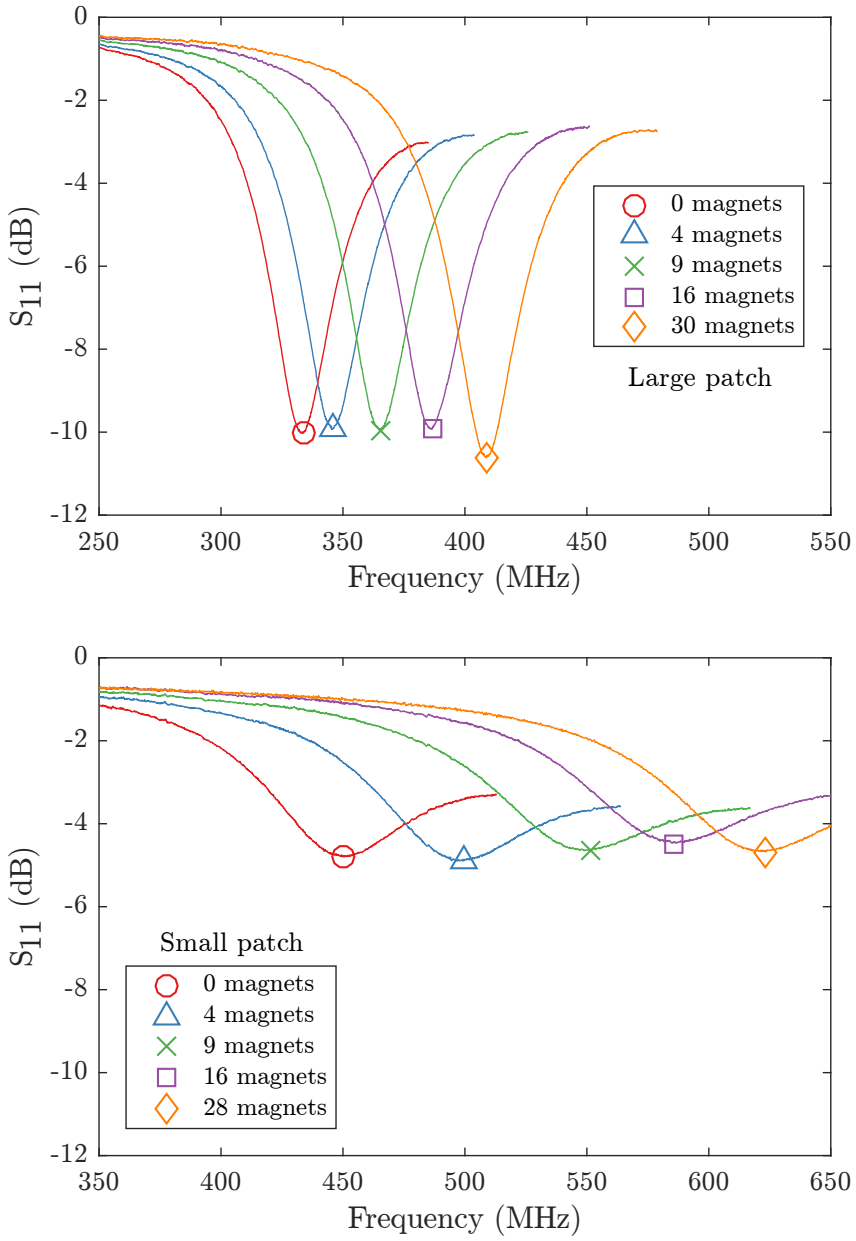

FIGURE 4.20: Magnetically biased hexaferrite patch reflection coefficients.

4.3.3.4 Radiation efficiency

The radiation efficiency (Equation 4.1) was measured using the anechoic chamber procedure depicted in Figure 2.6 (Section 2.4.2.2). The measured efficiencies remained low (Table 4.8). The efficiency remained relatively unchanged, with the caveat that only the extremes of the available band were measured.

Considering that the increase in ka was 19% and 35% for large and small patches respectively, the realised efficiencies may have been expected to increase with frequency due to increased coupling of the antenna to the far-field with increasing radiansphere occupancy ka. While this

behaviour was observed for the "large" antenna tuned from 329 MHz to 405 MHz (+2.0 dB increase in radiation efficiency), the opposite was true for the "small" antenna tuned from 450 MHz to 622 MHz (-0.9 dB reduction in radiation efficiency). With regard to Figure 4.3, the magnetic loss $\tan\delta_\mu$ increased by a factor of $1.46\times$ with frequency while the dielectric loss $\tan\delta_\varepsilon$ exhibited a minimum at 369 MHz and remained relatively unchanged in the band 329–405 MHz. The "small" antenna however suffered a $1.50\times$ increase in $\tan\delta_\varepsilon$ and $2.2\times$ increase in $\tan\delta_\mu$ over the frequency band 450–622 MHz.

TABLE 4.8: Realised efficiencies of magnetically-tuned HXF antennas.

Antenna	Frequency (MHz)	η_Ω (dB)	η_Ω (%)
Large	329 (lowest magnetic bias)	-20.1	1
	405 (highest magnetic bias)	-18.1	2
Small	450 (lowest magnetic bias)	-19.0	1
	622 (highest magnetic bias)	-20.1	1

Considering the known material properties in the absence of a magnetic bias field (Figure 4.3) and the rising ka of the antenna under tuning, it seems that the most probable cause of loss of radiation efficiency under tuning would have been increasing substrate losses as a function of frequency. However, the validity of this statement cannot be verified directly with the data presented here, considering the previously noted limitation that the material properties were not characterised as a function of bias field strength. The measured antenna efficiencies are a function of the electrical size ka (and therefore r_{rad}) and the frequency-dependent losses in the material as a function of magnetic bias strength. In the measurement configuration described, there are more loss variables than control mechanisms and as such a study of independent loss mechanisms is difficult to achieve. An extended investigation into the loss mechanisms in the patch could be performed using two independent routes.

First, a study of substrate losses $\tan\delta_\varepsilon$ and $\tan\delta_\mu$ as a function of frequency *and* **B**-field bias could be performed using a biasing coil arrangement in conjunction with measurements of μ determined from VNA transmission line analysis (given that ε is known from measurement data at $\mathbf{B} = 0$ and is not susceptible to magnetic biasing). Such a measurement campaign to determine $\varepsilon(f, |B|)^*$, $\mu(f, |B|)^*$ would represent a thorough approach to verifying the actual losses as a function of frequency and bias strength (as exhibited in antenna tuning), but represents significant effort in terms of collating the required equipment for variable **B** field generation and subsequent analysis of the data.

A second approach based entirely on simulation of antennas would provide some more insight into the competition between r_{rad} and r_{losses} that exists in the antenna. A simulation campaign studying the available efficiency of a lossless antenna can be envisaged, wherein the changes in

efficiency as a function of electrical size and simulated loss tangents is conducted. One simulation campaign could be conducted for antennas of swept ka (therefore changing r_{rad}), with fixed loss tangents. A second campaign could examine the simulated efficiency with fixed ka, with variable loss tangents. The combined results of both could be used to try to determine the increase in loss needed to negate the increasing r_{rad} presented by a patch antenna tuned upwards in frequency.

While the realised efficiency of all of the hexaferrite antennas tested was low, the work described above would still have value in establishing the threshold to which the losses would have to be reduced to achieve some arbitrary "reasonable efficiency" for a tuneable ESA, e.g. 10%. The existing body of published work on ferrite antenna efficiencies and materials science literature taken together does not converge on this outcome. The measured efficiencies presented here highlight the fact that increasing the operating frequency of the antenna is an insufficient guarantor of increased efficiency in light of increasing ka, and as such all studies of antenna tuning should be accompanied by efficiency testing across the operating band.

4.3.3.5 Radiation pattern

The measured radiation patterns are depicted in Figures 4.21 and 4.22 for the large and small hexaferrite patches respectively. The simulated patterns were obtained for the unbiased (low) frequencies by simulating the patch structures with the material properties given in Figure 4.3. The simulated patterns for the maximally biased patches (largest number of magnets, high frequency) were obtained by conducting a sweep of μ_{r} values, with μ_{r} being reduced until the frequency of the simulated antenna matched that measured. The simulated patterns were used primarily as a "trust indicator" that the measured antenna properties were truly those of the radiating antenna and not disturbed by factors such as the feed cabling, given the very low measured efficiency.

With reference to Figures 4.21 and 4.22, no mode changes were observed in the radiation pattern, with the pattern maintaining broad-beam characteristics similar to the untuned patch patterns. Inspection of the radiation pattern revealed the radiation patterns to be relatively stable across the accessible tuning range, compared to the changes in radiation pattern observed for tuning solutions using tunable impedance matching alone (see Chapter 3). The operating mode remained the TM_{10} mode throughout, with high correlation maintained between the measured power patterns at low and high frequencies (for the large antenna, $\rho^2\{329\text{ MHz},405\text{ MHz}\} = 0.92$, while for the small antenna $\rho^2\{450\text{ MHz},622\text{ MHz}\} = 0.81$). Changes in the radiation pattern were to limited to varying diffraction effects associated with the fixed dimensions of the ground plane with respect to the operating wavelength. Thus, the patterns became more directive in the $+z$ direction due to reduced diffraction into the rear hemisphere. Hence, substrate-based tuning as a

means to exercise frequency-agility can be observed to preserve a stable broad-beam radiation pattern across the frequency range.

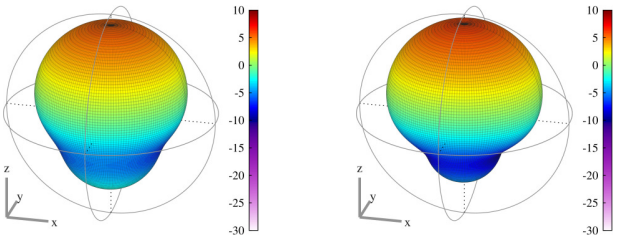

Sim. E_{total}, 329 MHz
Zero bias density, lowest f

Sim. E_{total}, 405 MHz
Max. bias density, highest f

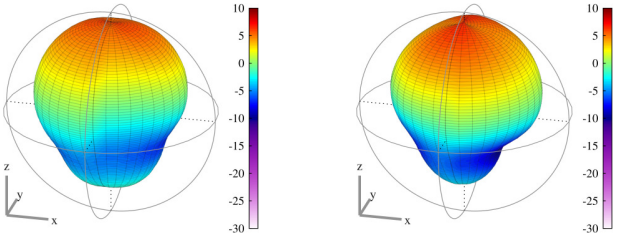

Meas. E_{total}, 329 MHz
Zero bias density, lowest f

Meas. E_{total}, 405 MHz
Max. bias density, highest f

FIGURE 4.21: Magnetically tuned "large" HXF patch antenna patterns. Colour scale gives directivity in dBi.

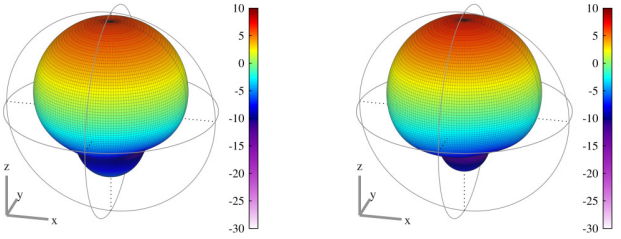

Sim. E_{total}, 450 MHz
Zero bias density, lowest f

Sim. E_{total}, 622 MHz
Max. bias density, highest f

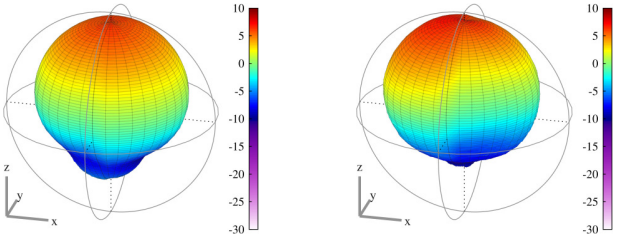

Meas. E_{total}, 450 MHz
Zero bias density, lowest f

Meas. E_{total}, 622 MHz
Max. bias density, highest f

FIGURE 4.22: Magnetically tuned "small" HXF patch antenna patterns. Colour scale gives directivity in dBi.

4.4 Conclusions

In this chapter a magneto-dielectric hexagonal ferrite material was studied as a candidate for preserving efficiency under antenna size reduction. The capacity for ferromagnetic tuning of the substrate also stimulated research interest. The miniaturisation and efficiency performance of an unbiased hexaferrite patch antenna was contrasted against the conventional dielectric substrates FR-4 and Rogers RT5880 as published in [23], followed by an examination of the magnetically-biased tuning range and comparison against the efficiency of a sub-resonant RT5880 patch antenna, impedance matched to an electrically small frequency as published in [22].

From measurements of S_{11}, the frequency of the hexaferrite patch was found to be $6.4\times$ lower than that of an identically-sized RT5880 counterpart. This constitutes a significant saving in board area: square patch antennas comprised of Rogers RT5880 substrate would need to be up to $75\times$ larger than the hexaferrite counterpart to maintain the same operating frequency. Such miniaturised hexaferrite antennas could find application at shorter ranges where miniaturisation could be advantageous (e.g. in array form for automobile to infrastructure communications with low overall transmission power to reduce interference to adjacent users). The antenna size reduction was accompanied by a major loss of radiated efficiency, with the hexaferrite patch efficiencies being recorded in the region of 1% (against 20% in FR-4 and 69% in RT5880). While electrically small, the substrate-based miniaturisation still resulted in a naturally resonant $\lambda/2$ design, with mode stability across the tuned band evidenced through high pattern correlation. This favourable pattern was maintained over an S_{11} < -3 dB magnetic tuning range of 32%. This contrasts strongly with the worse performance (lower efficiency and lack of pattern stability) observed for a sub-resonant patch antenna miniaturised using an alternative technique. Lumped element impedance matching miniaturisation to this extent incurred significant sensitivity to component values and intolerance of realistic feed track effects, and ultimate excitation of a poorly-radiating evanescent mode. Those challenges showed that when miniaturisation to scales of $ka < 0.5$ are considered, MD materials remain a compelling prospect.

Future work should consider the incremental advances being made in hexaferrite material development. Newer materials have been described (e.g. [82], offering the properties $\varepsilon_\mathrm{r} = 6$, $\mu_\mathrm{r} = 6$, $\tan\delta_\varepsilon = 10^{-3}$ and $\tan\delta_\mu < 0.15$ below 500 MHz). The efficiencies obtained under tuning show that the losses need to be reduced significantly to achieve a breakthrough in realised efficiency under miniaturisation. While material characterisation and antenna measurement evidence is to be preferred generally, the complexity, cost and technical barriers to accessing the materials science domain were found here to preclude a broad study on material type vs. increased antenna efficiency. Future work should consider expanded use of simulation, punctuated with measurement evidence to validate the models, to consider whether relaxing the $\varepsilon_\mathrm{r} = \mu_\mathrm{r}$ criterion allows less lossy materials to be selected.

Chapter 5

Efficiency-based performance metrics for tuneable antennas

In Chapter 1, the need for antennas addressing multiple frequency bands was established. From a commercial standpoint, these antennas can be required to operate in a small physical volume that restricts the available efficiency and bandwidth of such an antenna (Section 2.1). Frequency-reconfigurable antennas are proposed in the literature as a means to address the bandwidth problem, however, reports of accessible tuning range are often limited to reported tuneable impedance bandwidth rather than tuneable transmission response, i.e. the changes in efficiency and pattern (Section 5.1). In the presence of low radiation resistance associated with electrical smallness and potentially significant loss mechanisms associated with the miniaturisation and tuning mechanisms, high radiation efficiency in a realistic ESA is by no means guaranteed. As such, tuneable return loss derived from S_{11} in isolation is not a useful indicator of transmission performance under tuning. Hence, metrics tracking tuneable transmission performance for ESAs are required.

In this chapter, efficiency measurements taken from continuously-tuneable ESAs were used as the basis for development of previously unpublished performance metrics intended for comparison of tuneable and non-tuneable ESAs. These metrics emphasise assured levels of minimum and average efficiency across a tuned band, as well as providing a way to distinguish between continuously- and discretely-tuned antennas. To support the metric development work, a set of electrically small loop antennas were constructed for use in the low UHF band (roughly, 300–600 MHz). These antennas were tuned into resonance using either trimmer capacitors (serving as fixed capacitance) or voltage-controlled varactor diodes (variable capacitance).

5.1 Performance metric development for tuneable ESAs

5.1.1 Use of S_{11} as a metric for tuning performance

The measures of antenna performance given in Section 2.1.1 (return loss, impedance bandwidth and matching efficiency) are generally defined for each mode in a non-tuneable antenna. As such, the quoted return loss given from measurement of S_{11} is usually given for a single frequency point at the centre frequency for each mode. Alternatively, impedance bandwidth such as the -10 dB impedance bandwidth is given with respect to a bandwidth either side of the resonance frequency.

For a frequency-reconfigurable antenna, performance metrics are required that capture the range of frequencies that can be accessed under tuning. A relatively common approach is to use return loss derived from S_{11} as the basis of a metric determining whether a tuneable antenna can "access" a certain frequency. Under such an approach, the tuning range is quoted as a total integrated bandwidth over which a tuneable antenna can provide a return loss better than a set threshold e.g. -10 dB (or less if the antenna is electrically small). Tuneable compact and electrically small antennas lend themselves to such characterisation, where the tuning range offered by the ESA is of particular interest due to the general inability of an ESA to simultaneously demonstrate wide bandwidth and high efficiency. Various works have demonstrated this type of characterisation of S_{11}-derived tuning range, including but not limited to [107, 115, 169] which all describe the tuneable input response of the antennas in question, but have not provided a full 3D radiative assessment of the antenna pattern and associated efficiency.

S_{11}-derived tuning metrics serve as a measure of input matching efficiency at each tuned frequency. S_{11} itself is relatively easy to measure, requiring only a VNA. However, the definition of S_{11} does not extend to a prediction of realised transmission efficiency. The implicit suggestion that the transmission efficiency can be estimated from $1 - \Gamma^2$ is especially risky for an electrically small antenna. The radiation efficiency of an ESA is likely to be significantly less than 100% due to low radiation resistance associated with low ka factor, further reduced by potentially high construction losses associated with the tuning mechanism [123]. A tuning metric based on realised transmission performance incorporating both matching efficiency and radiated efficiency would be preferable to one based on S_{11} alone.

5.1.2 Use of gain-bandwidth product as a metric of tuning performance

The performance metric of "gain bandwidth product" relates transmitted performance to instantaneous bandwidth performance. However, it is not straightforwardly applied to ESAs in general. In the general case, calculation of gain bandwidth product can be performed for a single mode

measuring the gain at the resonance frequency. The realised gain can be assumed to be scaled only by the matching efficiency η_{m} over a narrow band, thus one radiative measurement of gain at the resonance frequency and a more finely spaced sampling of S_{11} are sufficient for calculation of gain-bandwidth product. Gain-bandwidth product has been described along these lines for antennas elsewhere e.g. [170–172]. However, no works are known strictly to have addressed metrics for tuneable ESA performance. Publications examining gain-bandwidth product have variously been limited to single-mode performance [170–172], not given a comprehensive descriptions of the efficiency/gain measurement method to be used [170], or dealt with electrically large antennas that cannot be considered suitable comparison for development of metrics useful for ESAs [172]. The latter work was claimed to be compact in its operating context, but not electrically small given its recorded gain of over 20 dBi and a radiation efficiency of 94%. Thus, no known works have considered the modifications required to make the gain bandwidth product concept more applicable to tuneable ESAs.

In a tuneable ESA, the measured gain may not be relied on to exceed the common -3 dB threshold of calculation due to the low radiation resistances associated with ESAs. This is readily rectified by setting a less stringent limit on the realised transmission efficiency more appropriate to ESAs, such as -10 dB. However, the issue of how to address the total accessible bandwidth in a tuneable system remains. Using S_{11} as an indicator for frequency accessibility is not intrinsically flawed, and makes a reasonable basis for the accessibility metric provided it is accompanied by radiatively measured data. The realised transmission efficiency can vary greatly depending on the electrical smallness of the antenna and the nature of the tuning component. As such, somewhat regularly spaced radiative measurements of the efficiency across the available integrated band area are required. A single efficiency measurement in the centre of the available band for a tuneable ESA is unlikely to capture the frequency-dependent changes in efficiency. Thus, the issue of defining transmission-bandwidth metrics for tuneable ESAs remains an open problem, particularly for the case of comparing continuously-tuned and discretely-reconfigured ESAs where gain-bandwidth product would otherwise be quite useful.

5.1.3 Pattern-measurement basis for new efficiency-based tuning metrics

From the limitations of existing gain-bandwidth studies, it can be seen that there is room for an initial study to be made on methods to give metrics that are applicable specifically to tuneable ESAs. For reasons relating to potential changes in the antenna pattern, it is advisable that such metrics are based on 3D radiation patterns rather than 2D cuts. The work of [45] documents why this is preferable to the use of 2D cuts. That work considered characterisation of radiative performance of a pair of ultra wide band antennas over a frequency range 3.1–10.1 GHz, a normalised frequency range of 109% of f_{c}. That work compared a discone antenna to a printed slotted bow tie antenna. While S_{11} measurement of the bowtie demonstrated superior impedance

matching compared to the discone over the total frequency range, the bowtie design exhibited much greater changes in its radiation pattern. The bowtie presented a dominant polarisation at lower frequencies that was lost as higher order modes emerged at higher frequencies. The discone meanwhile maintained a clearly dominant polarisation across the frequency range with 9:1 polarisation purity, albeit with increasing directivity due to the changing electrical size. Hence, the author of [45] highlighted the disconnect between measurements of S_{11} and the impact of pattern changes associated with the emergence of higher order modes. The position taken by the author of [45] was that recording only two cuts of the radiation pattern for the principal E- and H-planes ignores most of the radiation around the structure and implicitly suggests that the most important pattern features are likely to occur in these planes. Similarly, studying only the boresight gain assumes that the position of the main beam does not change by a significant margin, but this is intrinsically not a reliable assumption to make over a frequency range which allows for higher order modes to emerge. Therefore, identification of changes in the radiation pattern over a wide frequency range which may be deleterious to the intended application is best supported by 3D pattern measurement.

The arguments given by [45] were made for an ultra wide band case where the radiating mode was found to change over the characterised frequency band. These arguments are equally applicable to an antenna with fixed dimensions providing service over a wide tuneable frequency range. Thus, in developing transmission-based performance metrics for tuneable antennas, use of 3D patterns provides the most complete insight into system performance.

In this chapter, a method is proposed for the comparison of tuneable and non-tuneable ESAs based on radiatively characterised performance data. The measured total transmission efficiency established from measured radiation patterns is used as a baseline performance measure for the calculation of three novel metrics: -10 dB transmission efficiency bandwidth, integrated area covered by the efficiency curve between the -10 dB limits, and average realised efficiency. Basing these metrics on measurements of combined transmission response and input response is intended to assist RF system designers with the direct comparison of tuneable and non-tuneable ESA candidates, handling such issues as minimum/average efficiencies in the band and comparison of channel availability within the integrated band, as well as the ability to inspect the underlying 3D pattern of the antenna to confirm suitable coverage for use at arbitrary orientations in multipath channel.

5.2 Antenna design

For this work, a set of planar microstrip loop antennas were designed in CST Microwave Studio and subsequently fabricated. The operating concept of an electrically small loop is described in Chapter 2, Section 2.3.2. Since the objective of the study was to examine antenna performance

in an exclusively electrically small regime, antenna dimensions and component values were chosen to satisfy various defined criteria for electrical smallness (Section 5.2.1). Selection of the loop over any other topology was based on a desire to conduct the tuning metric study using an antenna structure that was highly susceptible to tuning under voltage control, with predictable pattern stability across the band.

5.2.1 Selection of loop dimensions

The loop circumference was selected to satisfy various definitions of electrical smallness required to ensure that the resulting antenna would be strictly limited to the electrically small regime in all tuned states. The loop circumference was chosen to give an antenna satisfying three different recognised conditions for loop ESAs:

1. None of the loop dimensions should exceed $\lambda_0/10$ [123].
2. The total loop circumference should not exceed $\lambda_0/3$ [128].
3. The given loop dimensions do not exceed the limit $ka < 0.5$ for the highest frequencies accessed (Table 5.1). The blue circle in Figure 5.1 shows the radius a required for a sphere that fully encloses the antenna within its limits. The substrate has not been included in the ka calculation in this instance because the substrate is largely just a carrier for the printed conductor in this antenna design. The board could have been cut down to be slightly larger than the conductor loop without having significantly affected the radiating properties of the loop.

A square loop-coupled-loop of the type first proposed by [129] is used throughout all subsequent discussion. The tuneable loop dimensions were fixed as per Figure 5.1 to satisfy the above three conditions. The loop is tuned into resonance by cutting a section from the loop and emplacing a lumped tuneable capacitance, C_{var}, which is tuned against the self-inductance of the loop.

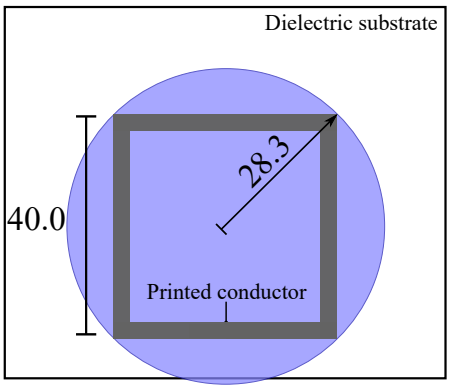

Calculation of ka for loop ESA. Dimensions in mm.

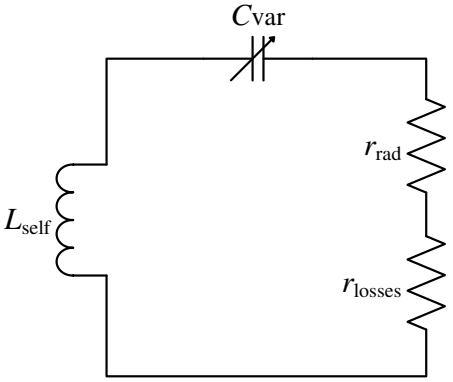

Tuneable RLC antenna concept.

FIGURE 5.1: Dimension limits and operating concept for tuneable loop ESA.

TABLE 5.1: Electrical smallness factor ka of tuneable loop ESA.

Frequency (MHz)	Free space wavelength λ_0 (m)	ka
350	0.86	0.21
400	0.75	0.24
450	0.67	0.27
500	0.60	0.30
520	0.58	0.31
550	0.55	0.33
600	0.50	0.36

The smallness factor ka has the definition $ka = 2\pi a/\lambda_0$, where λ_0 is the free space wavelength and a is the radius of the smallest sphere inscribing the antenna conductor and feed tracks as described in Chapter 2, Section 2.1.2. From Figure 5.1, a can be seen to have a length of 28.3 mm[1].

Table 5.1 shows ka to never exceed 0.5 up to 600 MHz, thereby satisying Condition 1. The longest single dimension of any part of the loop conductor is 4 cm, while the smallest value of $\lambda_0/10$ occurs 5 cm at 600 MHz, thereby satisfying Condition 2. The loop circumference of 16 cm against a limit of 16.67 cm for Condition 3 is also satisfied. The electrical smallness limits placed an upper limit on permissible length of the main conductor loop (16 cm). The remaining dimensions were chosen to satisfy various practical concerns, for example: the track width of the main radiating loop was chosen to allow mounting of a range of trimmer capacitors prior to final selection of a given trimmer package. The feed tracks for the smaller feed loop were chosen to accommodate connection of an SMA male connector during construction. Thus, an antenna of

[1]For the dielectric substrates given, simulation of the loop antenna structure in CST for range of board areas showed the operating frequency to be almost completely independent of substrate size in terms of lateral extent. Simulating board areas between 75% and 200% of the board area described in Figure 5.2 showed the operating frequency to change by less than 0.2%. Thus, the horizontal extents of the board are ignored for definition of ka in this scenario.

the dimensions given in Figure 5.2 permits a programme of performance metric development exclusively targeting ESAs to proceed, provided an operating frequency limit of 600 MHz is not exceeded. The dimensions and layout given in Figure 5.2 are those of a loop-coupled-loop tuned into resonance using a trimmer capacitor, which does not require any supporting components. An additional antenna structure was created to be tuned using a varactor diode, the layout for which is given in Figure 5.3.

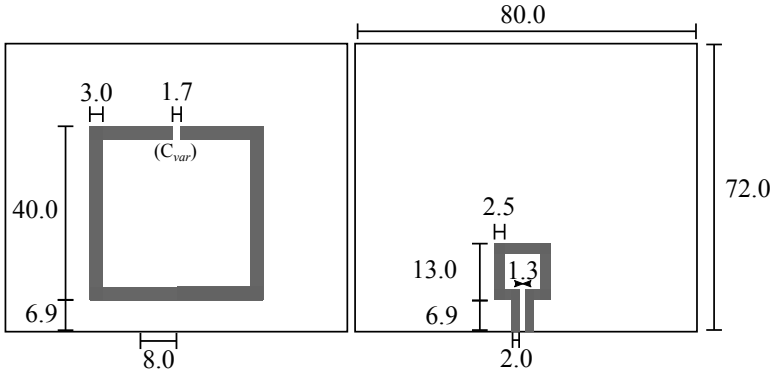

FIGURE 5.2: Trimmer antenna layout: (a) tuneable loop side, (b) feed loop side. Dimensions in mm.

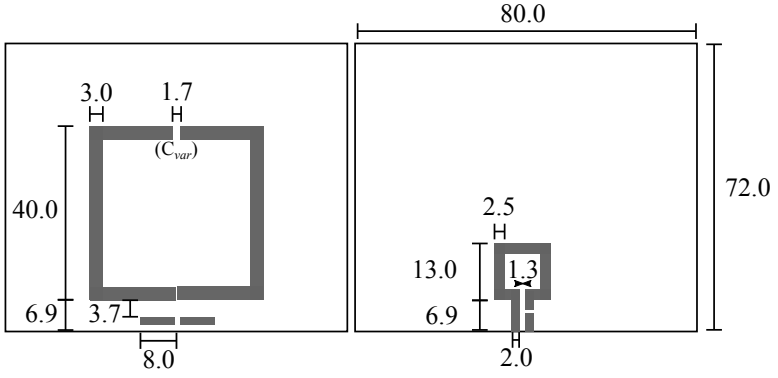

FIGURE 5.3: Varactor antenna layout: (a) tuneable loop side, (b) feed loop side. Dimensions in mm.

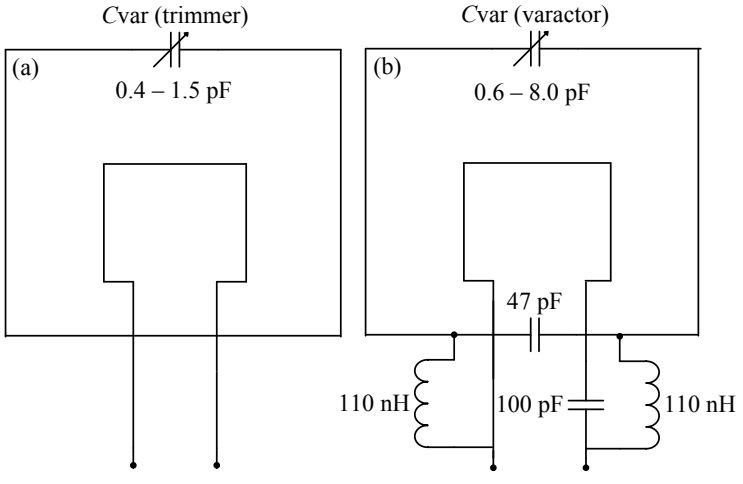

FIGURE 5.4: Antenna circuit diagram: (a) trimmer layout, (b) varactor layout.

5.2.2 Selection of discrete component values

The self-inductance of the main loop was set by the fixed dimensions of the loop layout (Figure 5.1). The dominant tuning behaviour of the antenna was therefore established through careful selection of the variable capacitance C_{var} and any supporting components required to enable tuning. Use of mechanically-adjusted trimmer capacitors did not require any additional supporting components, while the use of voltage-controlled varactor diodes required additional lumped components to support DC biasing in the structure.

Selection of C_{var} was conducted as an exercise in seeking capacitors that offered a balance between minimum available capacitance and a tuning range sufficient to cover an impedance bandwidth of at least a few hundred MHz, where minimisation of C_{var} yielded the highest frequency of operation[2]. Two candidate capacitors were sought (one trimmer, one varactor) with low values of capacitance that would at least partially overlap with each other in terms of tuning range, to permit a direct comparison of the impact of capacitor type on antenna efficiency. The selected capacitors were a Murata trimmer capacitor [173] and an Infineon varactor BB833 diode [49] with the main performance parameters listed in Table 5.2. Prior to efficiency measurement of the antennas it was noted that the two different capacitor types provided significantly different component Q (implying different degrees of loss). Thus, it was anticipated that each would yield different realised efficiencies.

TABLE 5.2: Variable capacitor major performance parameters.

Type	Typical capacitance range (pF) @ 1 MHz	Required biasing voltage (V)	Measured max. in-band Q
Trimmer [173]	0.4–1.5	N/A	~ 1000
Varactor diode [49]	0.75–9.3	0–28	~ 120

Use of the varactor diode required additional components to provide a DC bias mechanism for the varactor. The value of the DC blocking capacitor was found in simulation not to be critical, provided that the pass band impedance at RF was low and the self-resonant frequency exceeded the upper operating limit frequency by a suitable margin. From a review of the data sheets self-resonant frequency (SRF) was found to decrease with increasing values of C, but high C generally implies reduced pass band impedance. Hence, a compromise exists between SRF performance and the high C value desired for DC blocking. Similarly, the value of the RF-choke L was drawn as a compromise between sufficient blocking impedance at low frequency while offering the highest available SRF and component Q.

The need for compromise in the selection of component values was addressed by iterative simulation of the trimmer antenna structure (Figure 5.4a), with added DC block / RF block

[2]Graphs showing the achievable tuning range using unrealistically high/low values of capacitance are given in Appendix E.

components (Figure 5.4b). Addition of these bias network components reduced the simulated tuning range due to the presence of additional fixed reactance (both extra fixed L and C were added)[3].

5.2.3 Simulated tuning range (impedance bandwidth)

The tuning range of the trimmer- and varactor-tuned antennas were determined in simulation using CST Microwave Studio during the tuning component selection phase. The operating frequency found from the reflection coefficient S_{11} of the antennas for each simulated capacitance value is given in Table 5.3. The addition of extra tracks and lumped components required for DC biasing of the varactor-tuned antennas can be seen to have marginally reduced the available tuning range.

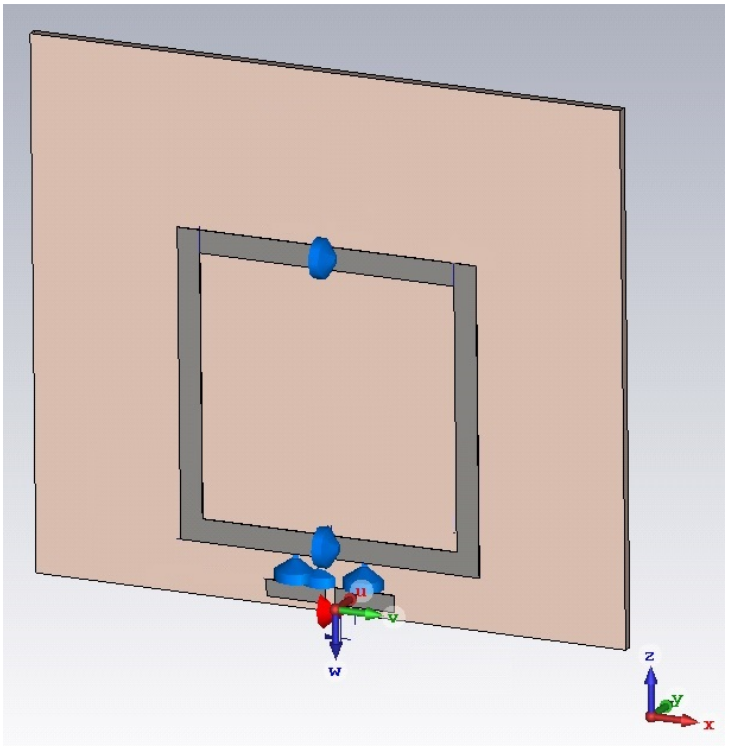

FIGURE 5.5: CST simulation configuration for tuneable loop antenna.
Blue elements represent lumped components.

The available frequency ranges for the antennas to be fabricated (i.e. including DC bias network components for the varactor designs) are depicted in Figure 5.6.

The main features of the simulated S_{11} are described as follows: high capacitance is observed to deliver low operating frequency as required. The FR-4 substrate induced a slight downward

[3]Much later on, it transpired that the DC/RF-block components chosen create a non-tuneable region in the centre of the tuneable band, which was overlooked at the time of the design due to trade-offs made in the exchange of simulation speed versus accuracy. This could have been avoided through a careful re-design of the feed network.

TABLE 5.3: Achievable ESA loop frequency range indicated by CST simulation.

Substrate	Capacitor type	Capacitance range (pF)	Expected frequency range (MHz)	Expected frequency range with DC bias network (MHz)
RT5880	Trimmer	0.4–1.5	397–627	N/A
RT5880	Varactor	0.75–9.3	172–519	190–517
FR-4	Trimmer	0.4–1.5	387–591	N/A
FR-4	Varactor	0.75–9.3	171–488	190–485

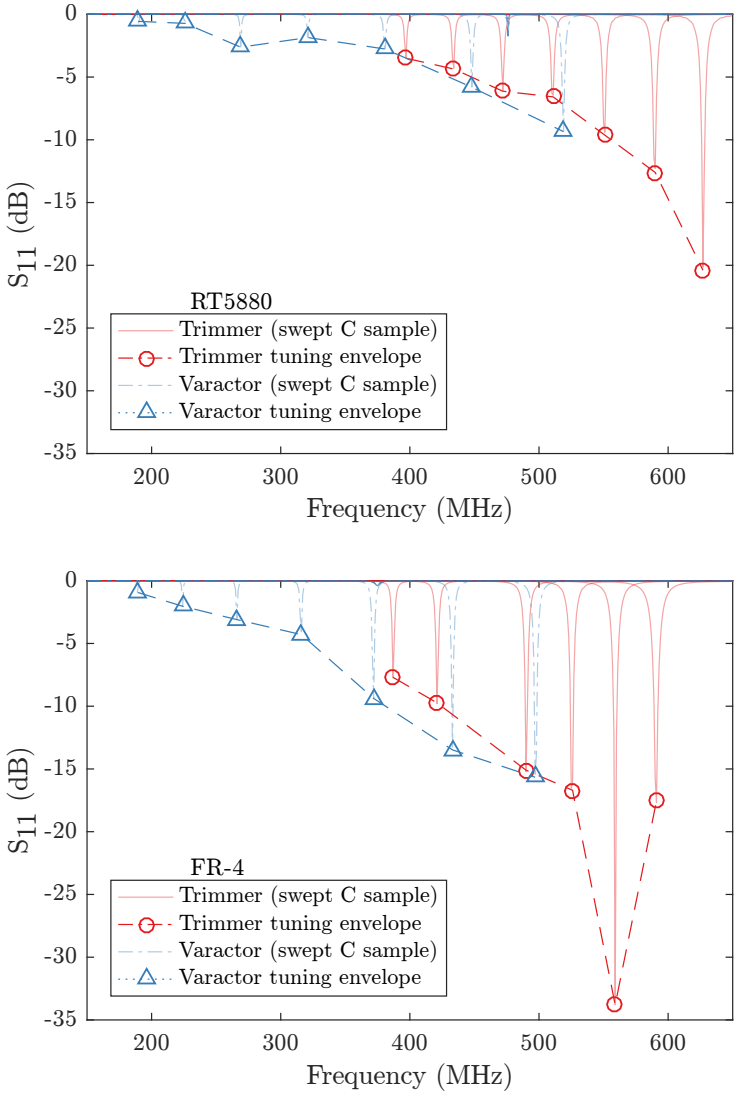

FIGURE 5.6: Simulated return loss for continuously tuneable loop ESAs.

frequency shift (electrical lengthening) associated with the greater dielectric permittivity, but the frequency reduction associated with the permittivity is fairly low since the loop inductance is mainly affected by the magnetic permeability μ_r of the substrate (FR-4 and RT5880 both exhibit $\mu_r = 1$). The impedance matching can be observed to be superior for the FR-4 antenna than that given by the RT5880 antenna, which is an artefact of having designed the FR-4 antenna first, and

having selected feed track dimensions which optimised the feed for an FR-4 substrate. The feed track dimensions were not adjusted for the RT5880 substrate.

5.2.4 Antenna fabrication

A set of four test antennas was constructed on either Rogers RT5880 or FR-4 substrate, using the dimensions and component values given in Figures 5.2 and 5.4. The substrate thicknesses were 1.27 mm for RT5880, 1.6 mm for FR-4 mm substrate. The FR-4 versions of these antennas are displayed in Figure 5.7, with the feed loop on the reverse side of the board visible through the substrate. The layout for the trimmer-capacitor antenna was the same as for the varactor antenna, but without the need for the notches and DC bias pads associated with varactor usage.

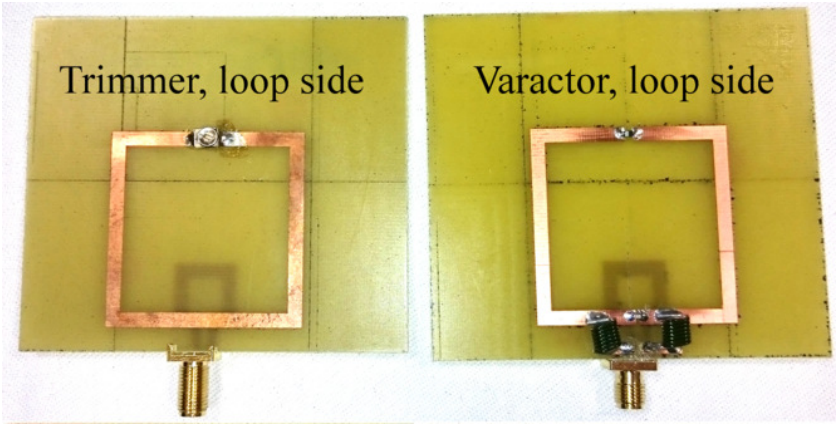

FIGURE 5.7: Constructed FR-4 loop antenna:
(left) Murata trimmer capacitor, (right) Infineon BB833 varactor.

5.2.5 Antenna material and component characterisation

The electromagnetic dispersion properties of the substrate materials and the lumped components used in the antenna design were characterised using a Keysight E4991B impedance analyser. The losses associated with each have an onward impact on the radiation efficiency $\eta_{\Omega,\mathrm{AUT}}$, adding loss terms to the conudctor and substrate loss terms already given in the radiation efficiency definition first presented in Section 2.4.2.2.

$$\eta_{\Omega,\mathrm{AUT}} = \frac{r_{\mathrm{rad}}}{r_{\mathrm{rad}} + r_{\mathrm{substrate}} + r_{\mathrm{conductor}} + r_{\mathrm{components}}} \tag{5.1}$$

5.2.5.1 Substrate characterisation

The use of the E4991B for substrate material characterisation has already been documented in Chapter 4 in relation to the hexaferrite materials work package. The material characterisation method is detailed in Section 4.2.2 with the dielectric substrate properties detailed in Figure 4.3, in Section 4.2.2 for the frequency range 1–1000 MHz.

To review, the Rogers RT5880 sample was found to have the properties $\varepsilon_{\mathrm{r}} = 2.1, \tan\delta_{\varepsilon} = 0.0003$ near the centre of the operting band of the antenna at 450 MHz. The measured sample of FR-4 was found to have the properties $\varepsilon_{\mathrm{r}} = 4.3$, $\tan\delta_{\varepsilon} = 0.015$ at 450 MHz. While loss tangent in FR-4 is commonly understood to vary between manufacturers and production batches, it is inferred from the higher loss tangent of FR-4 that the loop antennas built on FR-4 substrate risks reduced radiation efficiency compared to the same designs on RT5880 substrate due to the higher substrate loss term in the radiation efficiency, Equation (5.1).

5.2.5.2 Capacitor Q characterisation

The justifications for use of the E4991B as a test bench for discrete component characterisation were similar to those for justifying its use in characterising materials, namely the convenience afforded in ease of measurement. The instrument intrinsically acts as a vector network analyser with both physical and firmware amendments designed to relieve the user of the burden of calculating component de-embedding parameters in post-processing. Of particular use was the ability to measure the capacitance and loss behaviours of the BB833 varactor under automatically adjusted DC bias conditions, permitting a large number of swept bias voltage states to be characterised. Use of the E4991B in the device characterisation mode is illustrated in Figure 5.8a.

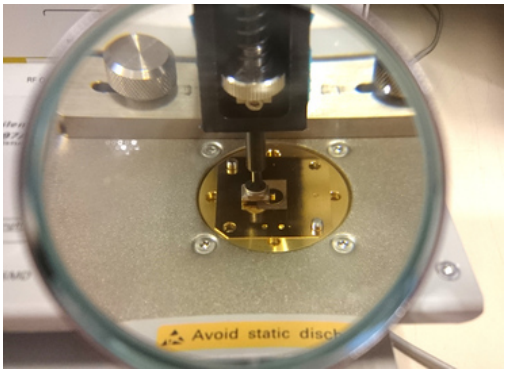

(a) Keysight E4991B impedance analyser operating in device characterisation mode.

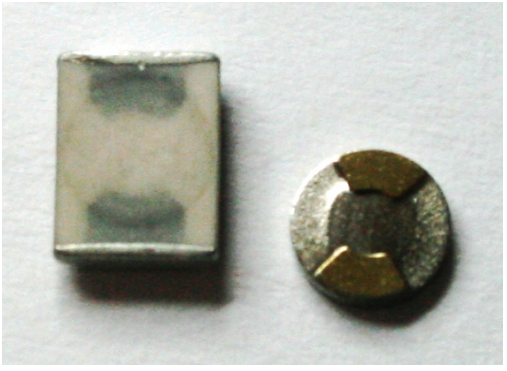

(b) Deconstructed MuRata trimmer capacitor.

FIGURE 5.8: Impedance analyser configuration for capacitor Q_{cap} characterisation.

The quality factors of the trimmer and varactor capacitors were measured in terms of component Q_{cap}. Measurement of Q_{cap} offers a means to compare the energy dissipation of two capacitors

at the same tuned frequency under de-embedded conditions, which is not directly possible from a reading of the component data sheets alone [49, 173]. Q_{cap} in this context is given by the ratio of reactive energy storage to resistive energy dissipation terms:

$$Q(f)_{\text{cap}} = \frac{X_{\text{cap}}(f)}{R_{\text{cap}}(f)} \tag{5.2}$$

The design of the trimmer capacitor was closer to that of the conceptual "ideal" capacitance, being comprised of overlapping metal plates separated using a dielectric chip (deconstructed view given in Figure 5.8b). In contrast, the varactor depends on a reverse voltage-biased semiconducting junction for its variable capacitance. As far as capacitance mechanisms are concerned, it can be shown that the varactor is an inferior capacitor through measurement of Q_{cap}, given its much lower Q at any given frequency or bias state. This is depicted in Figure 5.9 over the frequency range 300–650 MHz.

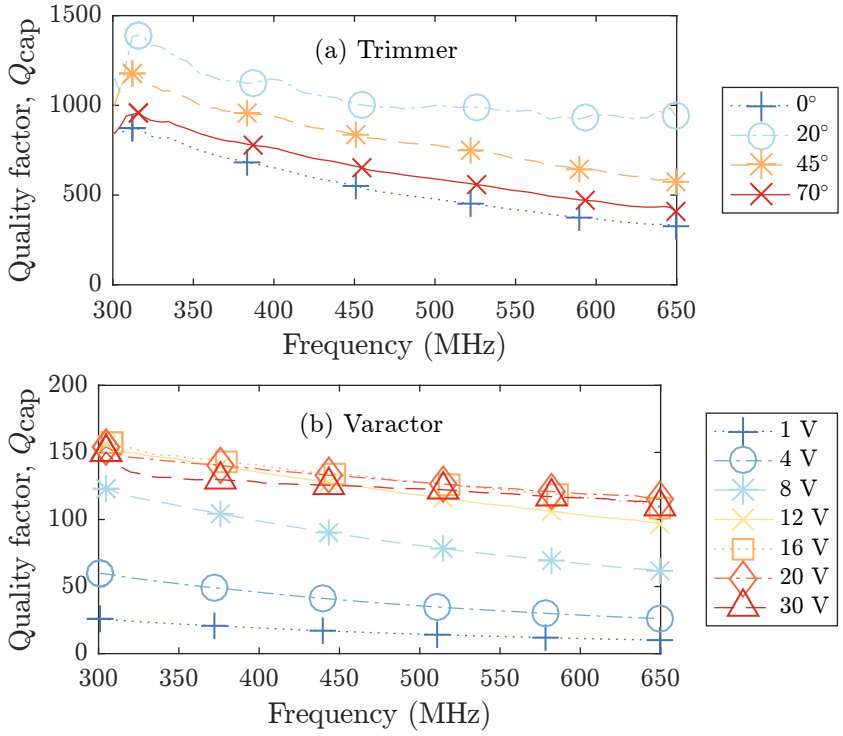

FIGURE 5.9: Measured Q_{cap}: (a) Murata trimmer capacitor, (b) Infineon BB833 varactor diode.

The comparison of measured capacitor Q_{cap} can be interpreted as a relative measurement of loss in each capacitor. For the varactor, Q_{cap} was measured as a function of frequency and bias voltage. The trimmer capacitor however needed to be configured by hand, hence tuning angle was set as the control variable. The full tuning range of capacitance could be accessed through a single quarter-turn (i.e. 0°–90°) of the upper tuning slot of the capacitor. The tuning angle corresponds to varying overlap of a pair of metal plates, with greater overlap yielding higher C and thus lower operating f_0 in the tuned antenna.

From Figure 5.9, generally the trimmer can be seen to possess a much greater Q_{cap} than the varactor regardless of frequency or tuning state. As an approximate guide, the minimum Q_{cap} over the measured tuning states and frequencies for the trimmer capacitor was at least $Q_{\text{cap, trim}} = 500$, ranging up to $Q_{\text{cap, trim}} = 1000$ for tuning angles associated with the middle of the frequency tuning range for the antenna. Not only does the trimmer possess a higher Q_{cap} factor, but it can be used independently of additional biasing components. The additional loss resistances of these components are liable to reduce the radiation efficiency, i.e. the $r_{\text{components}}$ terms are non-zero in Equation (5.1).

While the overall $Q_{\text{cap, varactor}}$ of the varactor was lower, in practical tuning scenarios for the antenna designed here the value of $Q_{\text{cap, varactor}}$ was actually quite flat across the frequency range. Furthermore, it was found to operate in its high $Q_{\text{cap, varactor}}$ region (high DC biasing at the frequencies radiatively tested). In the case of the varactor-tuned antenna, a reliable table of voltage-to-frequency conversion could be generated by measuring S_{11} as a function of applied bias voltage. Subsequently, the $Q_{\text{cap, varactor}}$ value could be judged from the data in Figure 5.9b. Thus, for the frequency range between 400–522 MHz for the RT5880 varactor antenna (bias voltage 8–30 V), the value of $Q_{\text{cap, varactor}}$ varied between 110–120. This is lower than any of the Q values measured for any frequency or tuning state for the trimmer capacitor, pointing towards lower efficiency as a likely outcome as the varactor places higher parasitic equivalent series resistance (ESR) in the current path.

5.3 Antenna measurements

5.3.1 Measured tuning range (impedance bandwidth)

The measured reflection coefficients as a function of swept capacitance are given in Figure 5.10, together with the "tuning envelope" derived from the minimum values of S_{11} in each tuned state. The trimmer capacitor antennas were tuned in approximately 20 MHz steps over the entire available tuning range, while the equivalent varactor antennas were tuned using a series of DC reverse bias steps from 0 V to 30 V. A plot of the required bias voltage to achieve each operating frequency is given in Figure 5.11. The maximum operating frequency of the antenna occurred when the tuning capacitance C_{var} was at its minimum value. For the varactor, this corresponds to the highest DC bias across the semiconductor junction, since the capacitance is controlled by the width of the depletion region across the semiconductor junction [56].

For plotting of Figure 5.10, only states with $S_{11} < -3$ dB were retained, hence the tuning ranges given in Figure 5.10 describe the total range of impedance bandwidth for which $S_{11} < -3$ dB. When setting a bandwidth metric, a reference power level must be defined. In this scenario, -3 dB was chosen for convenience given the poor matching often associated with ESAs (Section 2.1.1).

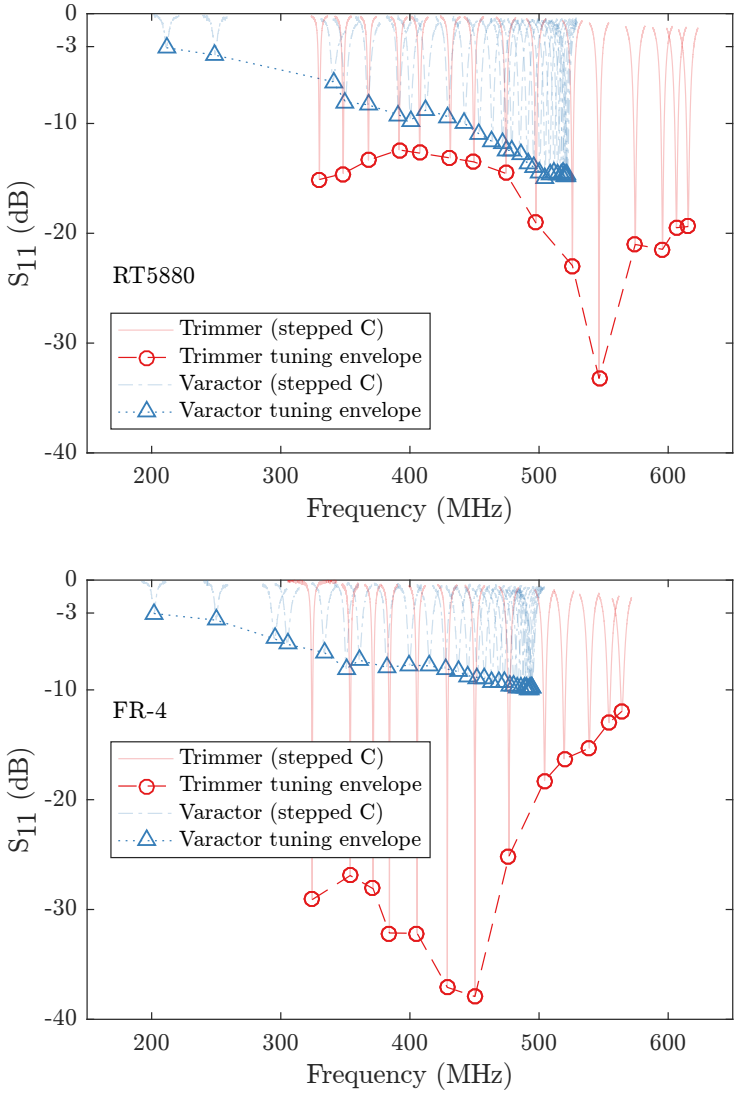

FIGURE 5.10: Measured reflection coefficient S_{11} for tuneable loop antennas. "Tuning envelope" defined by frequency range in which $S_{11} < -3$ dB.

The -3 dB tuning ranges as described by the "tuning envelopes" in Figure 5.10 are listed in Table 5.4 and are also expressed as a percentage bandwidth by:

$$\mathrm{BW}_{\text{-3 dB}} = \frac{f_{\text{high}} + f_{\text{low}}}{f_{\text{high}} - f_{\text{low}}} \tag{5.3}$$

where f_{low} and f_{high} are the limits of the tuned frequency range[4].

Overall, the measured S_{11} data show that the fabricated antennas operate in broadly the same frequency range as that indicated by simulation. The -3 dB tuning ranges differ slightly between

[4]In practice, the upper limit of the -3 dB impedance tuning range was given by the lowest available capacitor values, rather than the antenna dimensions with respect to the wavelength. Appendix E shows plots of the maximum achievable -3 dB impedance tuning range where unrealistically low capacitances can be achieved.

TABLE 5.4: Measured loop tuning range for -3 dB impedance bandwidth.

Substrate	Capacitor type	Frequency range (simulated, MHz)	Frequency range (measured, MHz)	-3 dB impedance bandwidth (%, Eqn. 5.3)
RT5880	Trimmer	397–627	330–616	30.2
RT5880	Varactor	190–517	212–522	42.2
FR-4	Trimmer	387–591	324–564	27.0
FR-4	Varactor	190–485	201–496	42.3

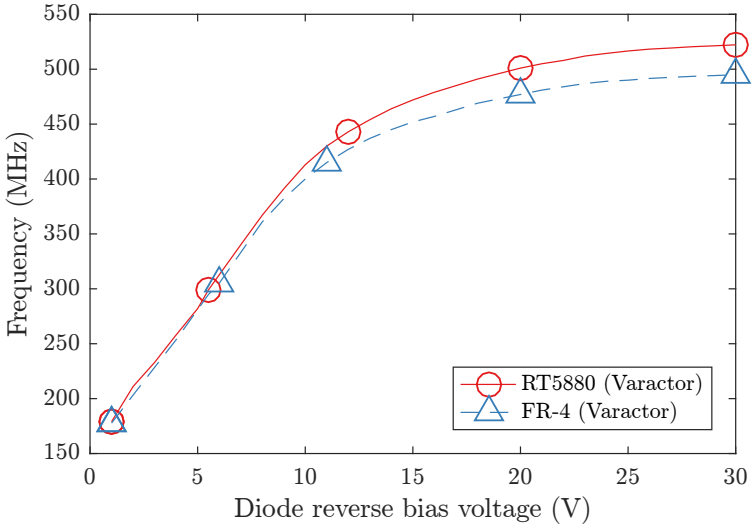

FIGURE 5.11: Tuned varactor antenna frequency as a function of bias voltage.

simulation and measurement (Table 5.4) due to tolerancing in the practical components. Each of the antennas can be seen to exhibit quite a large frequency tuning range of 27–42%.

The objective of the antenna introduced in this chapter was to achieve an antenna design that would offer convenient tuning over a wide enough frequency range to observe variable efficiency due to the influence of changing electrical size (ka). In this regard, the varactor-tuned loop was successful in meeting the design objective of supporting transmission-based performance metric development for tuneable ESAs. Between the varactor and trimmer antenna designs, there is sufficient overlap in accessible frequency range to permit radiative efficiency and pattern measurements in the range approximately between 400–520 MHz. The radiation performance of the trimmer- and varactor-tuned antennas in terms of realised pattern and efficiency is now examined.

5.4 Radiative characterisation

5.4.1 Physical measurement configuration

The radiation pattern measurement configuration is generally similar to the setup first introduced in Section 2.4.2. As before, the measured patterns were recorded for the two orthogonal polarisations E_θ and E_ϕ, with positioner steps of $\Delta\theta = 1^\circ$ and $\Delta\phi = 10^\circ$.

Preliminary work performed for this study considered an antenna that used either long DC biasing lines or a bias tee for voltage control for the varactor. It was discovered that the radiation pattern was excessively disturbed by RF coupling into the long DC feed cabling, an effect also noted in [116]. Secondary testing was conducted using a bias tee, which succcessfully suppressed cabling effects at the higher frequencies but not the lower frequencies. It was found that re-designing the bias system to use the shortest possible DC bias leads and RF-over-fibre feed cabling was conducive to successful 3D pattern measurement. In light of these revisions to the chamber setup, minor alterations to the general setup introduced in Section 2.4.2 are shown in Figure 5.12. These changes are the use of RF-over-fibre cabling and locally mounted DC bias units (i.e. provision of snagless DC power inside the chamber for the RF-over-fibre transmitter unit, and DC bias voltage at the antenna head for the varactor-tuned antennas). The antenna was mounted at the end of an ABS plastic tube with a circular metallic ground plane with a diameter of 400 mm to provide extra room between the AUT, the RF-over-fibre and DC biasing boxes and the rotating motor head (shielded by the ground plane to reduce unpredictable pattern corruption effects). The stand-off distance between the AUT and the ground plane was 25 cm.

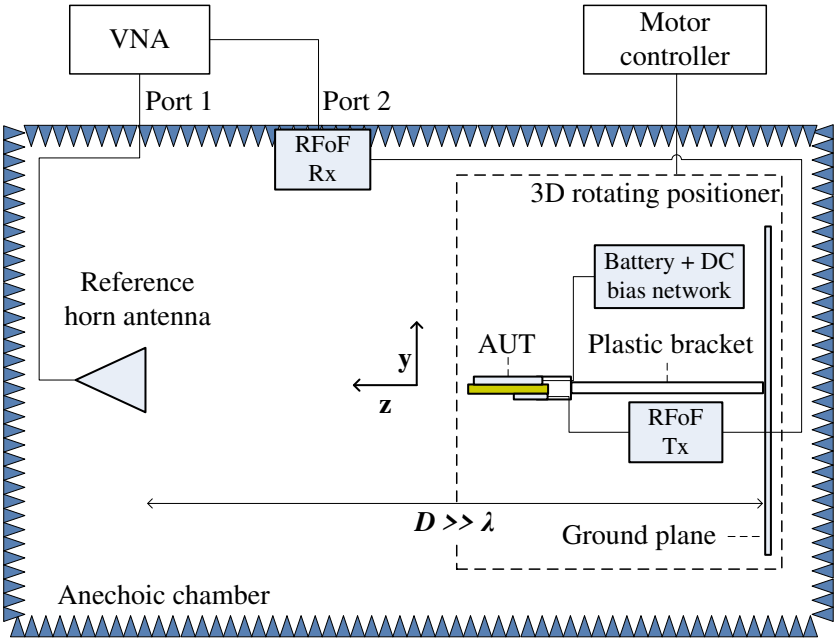

FIGURE 5.12: Radiation pattern measurement setup for tuneable ESA loops (not to scale).

Regarding the selection of measurement frequencies, it has already been demonstrated that the loop antennas offer continuous frequency reconfigurability in the input response. However, the practical consideration of time spent preparing and measuring each tuning state in the anechoic chamber imposed a requirement for a reduced testing set of frequencies for radiative characterisation. Efficiency comparisons between the different antennas were sought in a region of overlap in the achievable frequency range offered by each design. Hence, a subset of tuning states was selected for an approximate frequency range between 350–500 MHz in 50 MHz steps. Additionally, a test at 475 MHz was subsequently included to confirm the efficiency behaviour in a region of rapid change in efficiency, as well as another at 520 MHz that represented the highest frequency available for the RT5880 varactor antenna. A $\lambda/4$ metallic wire monopole was constructed as a reference antenna for efficiency measurement at each frequency as described in Section 2.4.2.1.

Figure 5.13 gives a comparison of simulated and measured patterns for each polarisation at the single frequency of 500 MHz as a demonstration of the similarity between the simulated and measured pattern in the presence of a mounting bracket and ground plane, with the loop mounted parallel to the xz-plane[5].

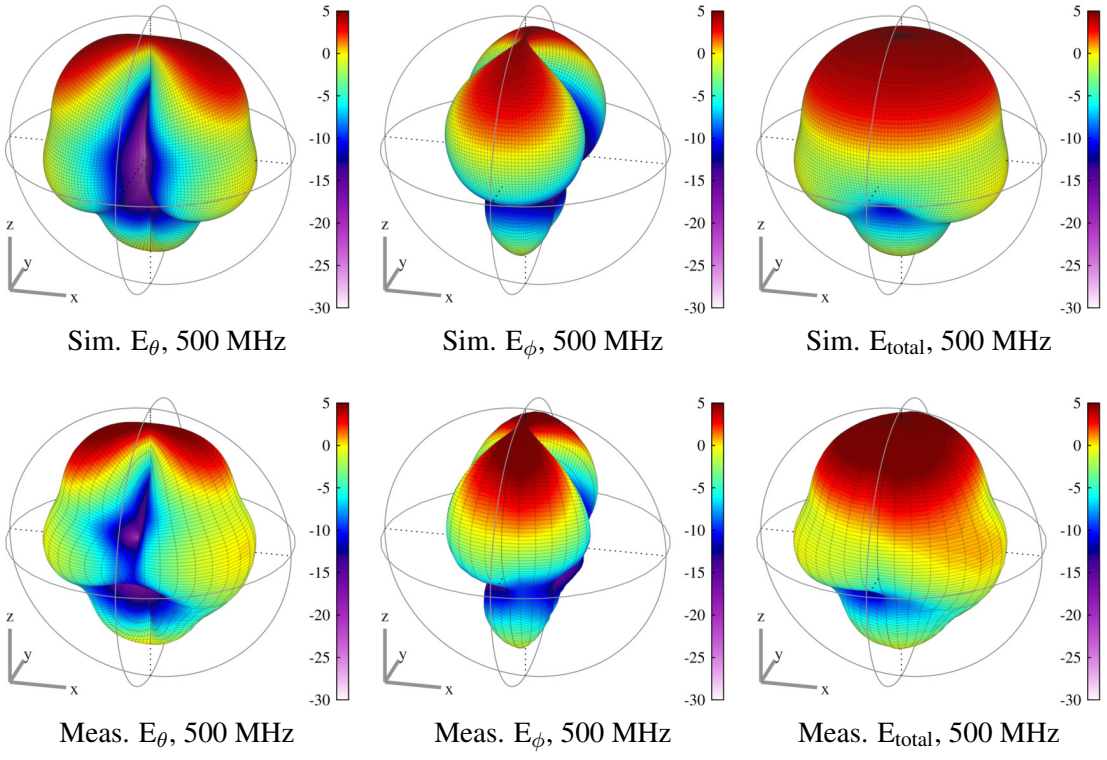

FIGURE 5.13: Simulated and physically measured directivity patterns for RT5880 antenna with ground plane and trimmer capacitor at 500 MHz. Antenna aligned in xz-plane, ground plane aligned in the xy-plane at stand-off distance of 25 cm. Colour scale gives directivity in dBi.

[5]File compatibility issues prevented calculation of the pattern correlation between the measured and simulated patterns in this work.

While the distance between the antenna and the ground plane was fixed at 25 cm, over the frequency range 350–520 MHz this presented a varying phase relationship between the AUT and the ground plane, the electrical length of which varies between 0.44–0.66 λ over the measured band. Similarly, the electrical path length to the ground plane varies between 0.29–0.43 λ over the measured band. Accordingly, the radiation patterns measured in the anechoic chamber were found to exhibit a degree of frequency dependence caused by the ground plane. The mirror symmetry expected in the xy-plane was eliminated, with the patterns becoming more directive in the $+z$ direction. A reduced level of diffracted energy was recorded in the rear hemisphere, permitted by the finite size of the ground plane.

Figure 5.14 depicts the measured and simulated total power patterns for a selection of tuning states spanning the range 350–520 MHz, comparing the trimmer and varactor antennas on RT5880 substrate. The simulated (trimmer antenna) pattern for each frequency highlights that the main frequency-dependent change in directivity of the pattern is a function of the proximity to the ground plane, as opposed to any cabling radiation effects (bearing in mind that the simulated environment contained no cables).

The measured patterns were found to be substantively similar to the simulated patterns for antennas using either trimmer capacitors or varactors, suggesting that the DC biasing elements did not adversely affect the radiation pattern. Under both simulation and measurement, each pattern demonstrated consistency with a dipole pattern associated with a y-directed magnetic current source, $\mathrm{M_y}$, consistent with a small loop antenna aligned in the xz-plane [128, Chapter 2]. Thus, maintenance of the dipole-like radiation pattern indicates that the antenna designed in this work would maintain favourable broad-beam reception characteristics over much of its tuning range and would therefore be suited to signal reception in a multipath channel.

5.4.2 Radiation efficiency

The radiation efficiencies were recorded using the configuration given in Figure 5.12, which permitted calculation of the antenna efficiency via the pattern integration method described in [144] in free space, as first described in Section 2.4.2.2.

The radiation efficiencies recorded for the trimmer- and varactor-tuned antennas are derived from comparison of the measured received signal levels of the AUTs to those of $\lambda/4$ wire monopoles constructed for each tested frequency. Assigning the $\lambda/4$ monopole a relative radiation efficiency of 100%, the radiation efficiency of each AUT at each frequency is then derived from scaling the total receive efficiencies η by the respective impedance matching efficiencies η_{m}. η_{m} is established from the measurement of $\mathrm{S_{11}}$. Thus, the radiation efficiency of each AUT is given by:

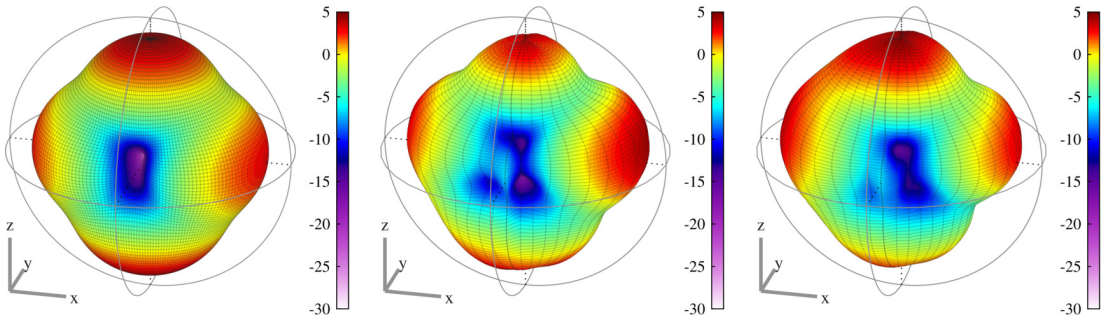

Simulation, 350 MHz
0.29λ to ground plane
0.44λ ground plane width

Trimmer, 350 MHz
0.29λ to ground plane
0.44λ ground plane width

Varactor, 350 MHz
0.29λ to ground plane
0.44λ ground plane width

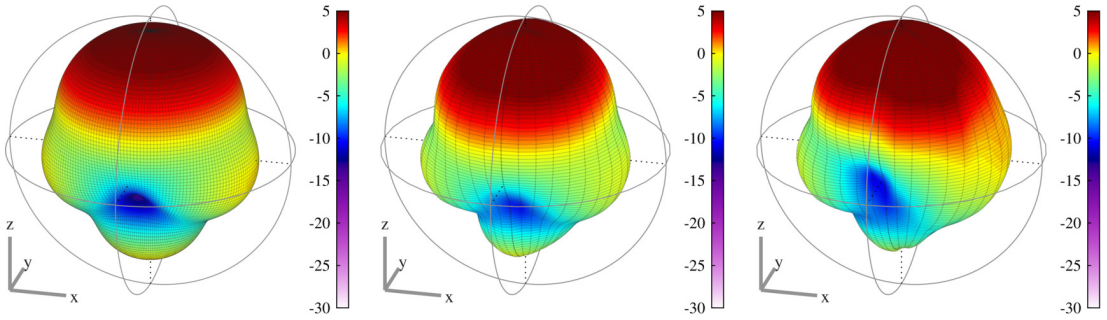

Simulation, 450 MHz
0.38λ to ground plane
0.58λ ground plane width

Trimmer, 450 MHz
0.38λ to ground plane
0.58λ ground plane width

Varactor, 450 MHz
0.38λ to ground plane
0.58λ ground plane width

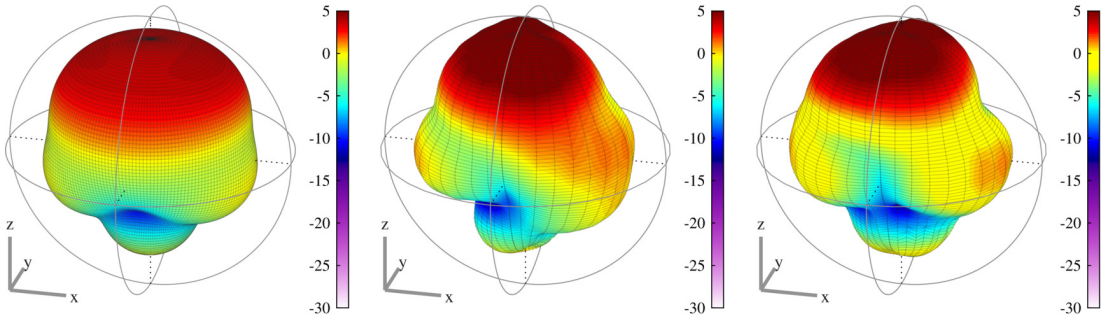

Simulation, 520 MHz
0.43λ to ground plane
0.66λ ground plane width

Trimmer, 520 MHz
0.43λ to ground plane
0.66λ ground plane width

Varactor, 520 MHz
0.43λ to ground plane
0.66λ ground plane width

FIGURE 5.14: Simulated and physically measured power patterns for RT5880 antenna with trimmer capacitor or varactor. Antenna aligned in xz-plane, ground plane aligned in the xy-plane at stand-off distance of 25 cm. Colour scale gives directivity in dBi.

$$\frac{\eta_{\Omega,\text{AUT}}}{(\eta_{\Omega,\text{ref}}=1)} = \frac{\eta_{\text{AUT}}}{\eta_{\text{ref}}} \cdot \frac{\eta_{\text{m, ref}}}{\eta_{\text{m, AUT}}} \tag{5.4}$$

The radiation efficiency of each AUT as a function of frequency calculated from Equation (5.4) is shown in Figure 5.15.

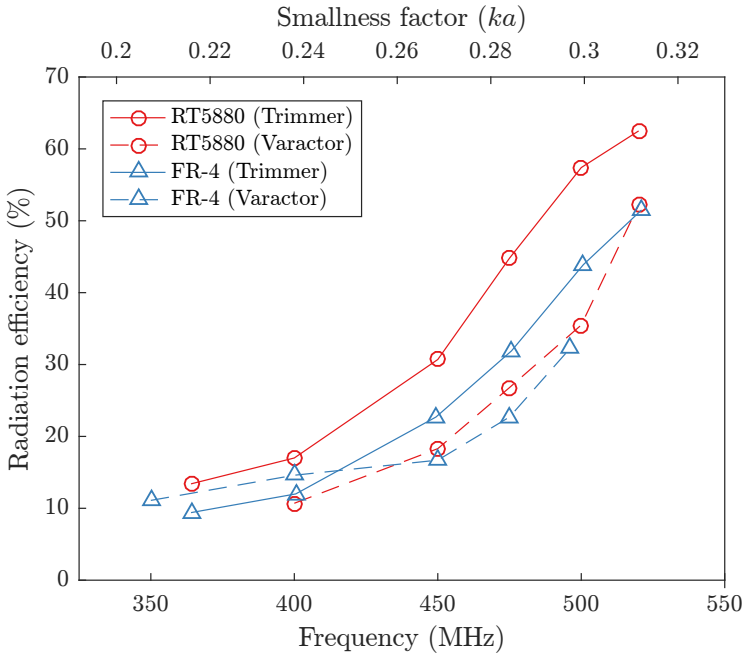

FIGURE 5.15: Radiation efficiency of tuneable loop ESAs.

5.4.2.1 Impact of choice of capacitor

Examining the shape of the radiation efficiency curves overall, it can be seen that the radiation efficiency generally increased with frequency across all AUTs. This can, in part, be ascribed to the increase in ka factor with increasing frequency. In electrical terms, the antenna has a larger effective area with respect to the wavelength at the higher frequencies. The trimmer-capacitor based designs can be seen to be more efficient than the counterpart varactor-based designs at each frequency. This can broadly be attributed to the difference in tuning capacitor Q and the presence of additional series components required to bias the varactor, given that the identical operating frequencies and substrates should yield the same radiation resistance and substrate losses for either capacitor type. The lower Q_{cap} of the varactor compared to the trimmer across the frequency range can be observed in Figure 5.9.

While use of the trimmer yielded greater efficiency, such use remains a commercially unappealing prospect due to the requirement for manual adjustment of the capacitance. High Q RF microelectromechanical system (RF MEMS) capacitors might be capable of providing the balance between high Q and convenient voltage control, but continued poor commercial availability of these devices (Section 2.2.5) precluded inclusion of such devices in this study. Thus, the efficiency of the trimmer-tuned capacitor should be viewed as an upper limit on the achievable efficiency for the given antenna layout, while the varactor design demonstrated a compromise between convenience of use and realised efficiency.

5.4.2.2 Impact of choice of substrate

Turning to consider the choice of substrate, the RT5880 substrate can be observed to deliver greater radiation efficiency than the FR-4 substrate for the most part. This is consistent with the RT5880 substrate having a lower loss tangent than FR-4, as measured using the impedance analyser. However, the use of FR-4 substrate appears to yield greater instantaneous impedance bandwidth. The trade-off between impedance bandwidth and efficiency can be measured by plotting the product of the instantaneous -3 dB impedance bandwidth and the realised radiation efficiency for the trimmer and varactor antennas where overlapping measured efficiency values exist.

As a starting point, the definition of impedance bandwidth in this context is derived from the frequency limits for which $S_{11} < -3$ dB for a given tuning state (not to be confused with the total tuning range over which $S_{11} < -3$ dB, which is much wider). The -3 dB instantaneous impedance bandwidth multiplied by the radiation efficiency at a given frequency determines the (impedance-based) efficiency-bandwidth product, $\mathrm{EBW}(f)$. This approach to creation of an impedance-bandwidth product measure was noted in the literature review section (Section 2.2.3.1), and particularly [46], noting that improved efficiency-bandwidth product is not a guarantor for improved antenna efficiency and in fact suggestions of enhanced performance from improved return loss can be misleading from an efficiency perspective.

$$\mathrm{EBW}(f) = \eta_{\Omega,\,\mathrm{AUT}}(f) \times \mathrm{BW}_{\text{-3 dB, inst.}}(f) \tag{5.5}$$

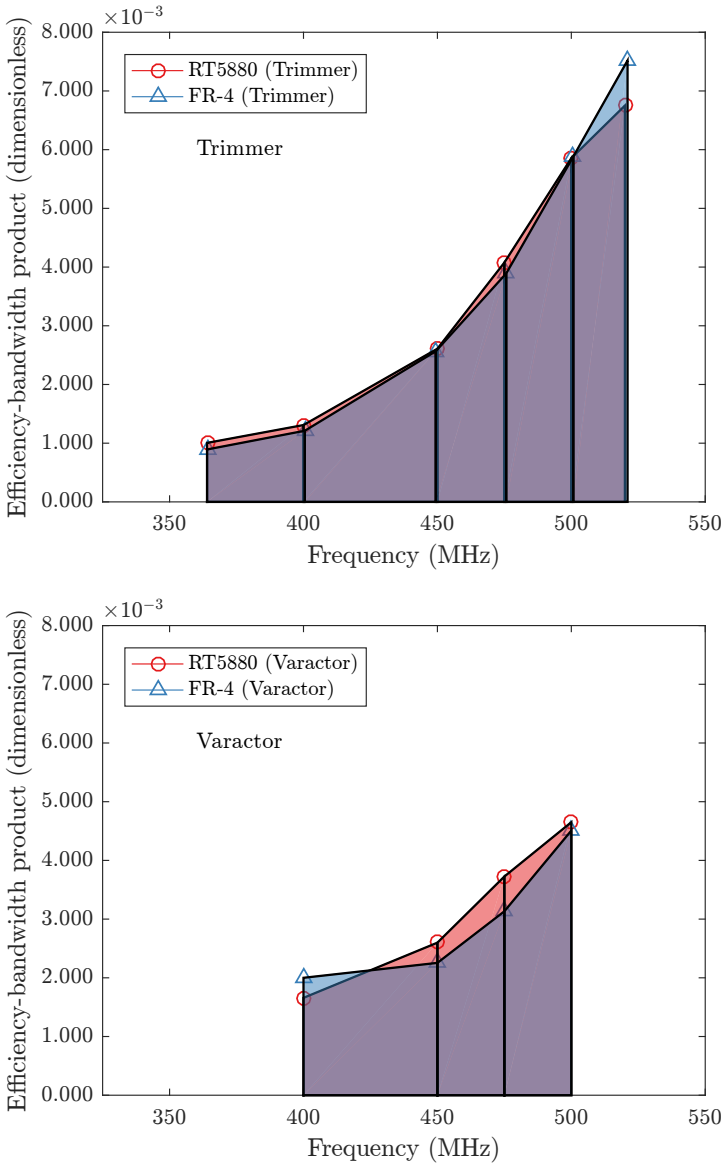

FIGURE 5.16: Comparison of instantaneous efficiency-(impedance) bandwidth product between substrates, Equation (5.5).

Figure 5.16 depicts the efficiency-bandwidth product for the trimmer- and varactor-tuned antennas. For a given choice of tuning capacitor, only the substrate was varied. In initial analysis, the lumped bias network components were expected to have constant performance for a given frequency regardless of substrate, such that the differences in instantaneous EBW would be driven mainly by the substrate.

In the absence of a bias voltage or lumped components for the trimmer capacitor case, this initial analysis is satisfied by the data. The capacitor Q is very similar for either of the substrates for a given frequency, hence the overall difference between the EBW(f) values for each antenna is small. The area under each EBW(f) curve was calculated using a trapezoidal integration

method[6]. Calculation of these integrals provided a similarity measure for the two curves. For the trimmer antennas, the integrated area of the FR-4 EBW(f) curve was found to be within 1% of the integrated area of the RT5880 curve. Thus, to the first level of analysis, it appears that loss of efficiency in FR-4 substrate is compensated by an equivalent increased impedance bandwidth to maintain the overall impedance bandwidth product.

Applying the same analysis to the EBW(f) data for the varactor antennas, the curves and integrated areas were still somewhat similar, with the difference between integrated areas being less than 8% of the area occupied by the RT5880 curve. The initial assumption of identical behaviour in the lumped components on each substrate may not be true, since to achieve a given operating frequency f, different bias voltages were required. In practice, the reactances of all of the lumped components (not just the varactor) are liable to exhibit some dependence on the applied bias voltage, which may complicate the analysis. This analysis is not pursued further due to the lack of contemporaneous Q measurements for each lumped component. Nonetheless, the integrated area covered is similar between both substrates, again implying that exchanging more efficient RT5880 for better impedance bandwidth in FR-4 might be an acceptable trade off.

While the above analyses are logically correct interpretations of the measured data, they highlight a flaw with the definition of EBW as defined by Equation (5.5) as a metric of performance measurement. Namely, the metric of efficiency multiplied by impedance bandwidth is not a useful discriminator. In coming out with similar values of EBW for each substrate, the metric itself fails to highlight that the RT5880 is quite likely to be the superior antenna from a transmission perspective. Since the primary job of the antenna is to launch signals from the transmission line into the air, any metric recording for the performance of two different substrates in performing this task needs to be able to discriminate between substrates. The fact that the EBW definition used above does not discriminate between RT5880 and FR-4 substrates when RT5880 is likely to deliver superior overall transmission performance means that the metric in its present definition fails to deliver useful benefits to antenna system designers.

Thus, a revised metric of performance measurement is required that correctly accounts for variable transmission performance across the measured band. In the case of either substrate and either capacitor type, the antennas were found to exhibit varying radiation efficiency across the available band, with radiation efficiency often below 50%. Hence, the performance metrics developed must be appropriate for the efficiencies commonly encountered in ESAs. The next section introduces a set of transmission-based performance metrics to determine how well the loop antennas satisfy the objective of delivering efficient frequency reconfigurable transmission over the integrated band. In this context, use of the metrics is demonstrated by comparison between a tuneable ESA (the varactor-tuned antenna) and a non-tuneable ESA (the trimmer-capacitor tuned antenna).

[6]The physical meaning of this integral is not examined here as it is superceded by a more useful efficiency-based performance metric in the next section.

5.5 Performance metrics for tuneable ESAs based on realised efficiency under tuning

In Chapters 1 and 2, it was acknowledged that ESA design carries an inherent risk of encountering low realised total efficiencies and narrow instantaneous bandwidths (both in impedance and transmission response terms). A major motivation for the development of tuneable ESAs in this work was to exploit the operating concept of recovery of overall performance by accepting the narrow instantaneous bandwidth, and attempting to tune the frequency response of the antenna over a larger integrated range in order to produce an antenna that can exhibit "reasonable" efficiency over a broad band. Definitions of "reasonable" in this context depend entirely on the application being considered. For instance, mobile phone terminal antennas have a typical efficiencies below 50% [171], while very small narrow band antennas such as car key fobs have realised efficiencies as low as 1% [174]. It is apparent that a range of efficiencies in the region of 1–50% may be comparable to other volume-constrained antenna designs presently in service. However, there is a trend for operating bandwidth to be stated as a function of antenna input response alone, precluding convenient comparison of the wide band performances of tuneable antennas.

In this section, a transmission response-based approach is advanced that has the potential to give antenna designers an objective means of comparison between the transmission performances of differing tuneable ESA designs operating in a given band. The metrics are briefly described as the -10 dB transmission efficiency bandwidth[7], the integrated area given by the efficiency curve over this band (i.e. a measure of efficiency-bandwidth product appropriate to tuneable antennas), and average realised efficiency in the band derived from the integrated area.

Advantages of these metrics over use of S_{11} for defining antenna performance over a frequency range include assured levels of minimum and average realised efficiency, while the integrated area coverage metric permits comparison between continuous and discretely-tuned antenna, where the former offer greater system flexibility. Practical use of these metrics is demonstrated through application to the same pair of varactor-tuned and trimmer-tuned antennas as before, with the trimmer-tuned antenna re-interpreted to serve as a fixed-frequency, non-tuneable ESA. This work was also presented in [20].

5.5.1 Comparing tuneable ESA to non-tuneable and $\lambda_0/2$ counterpart antennas

It has already been established that in terms of radiated efficiency, the varactor-tuned antennas on either substrate were less efficient than their trimmer-tuned equivalents. Given the lack of a convenient tuning mechanism not requiring end-user intervention, the trimmer-tuned antenna

[7]Noting that -3 dB radiation efficiency is an unrealistically high target to be applicable to many ESAs.

can be considered to be a non-tuneable, fixed-frequency ESA in the discussion that follows. Thus, initial consideration of the performance metrics described here considers an examination of the relative transmission efficiency-bandwidth behaviours of the RT5880 loop antenna layout, with the varactor biased to tune the antenna over a frequency range of 400–520 MHz. The trimmer-tuned loop was adjusted to operate on a single frequency approximately in the middle of this range, at 450 MHz.

In addition, a $\lambda/2$ wire dipole was fabricated for operation at 450 MHz. The radiation resistance of the wire $\lambda/2$ is held to be large with respect to that of any truly electrically small antenna. Similarly, the loss resistances of a purely metallic dipole are held to be low [144]. Thus, the performance metrics should emphasise that even though the impedance bandwidth of the large dipole may be surpassed by that offered by a tuneable ESA, comparison of realised transmission efficiencies is still warranted over a broad tuneable band.

The -3 dB impedance bandwidth data used hereafter for performance metric development are those given in Figure 5.17. The values of the -3 dB impedance bandwidths are given in Table 5.5. The required radiation efficiencies of the loop antennas are those given in Figure 5.15 (page 131). The relative radiation efficiency of the $\lambda/2$ dipole antenna in this context is 100%, consistent with the defined radiation efficiency measurement method given in [144].

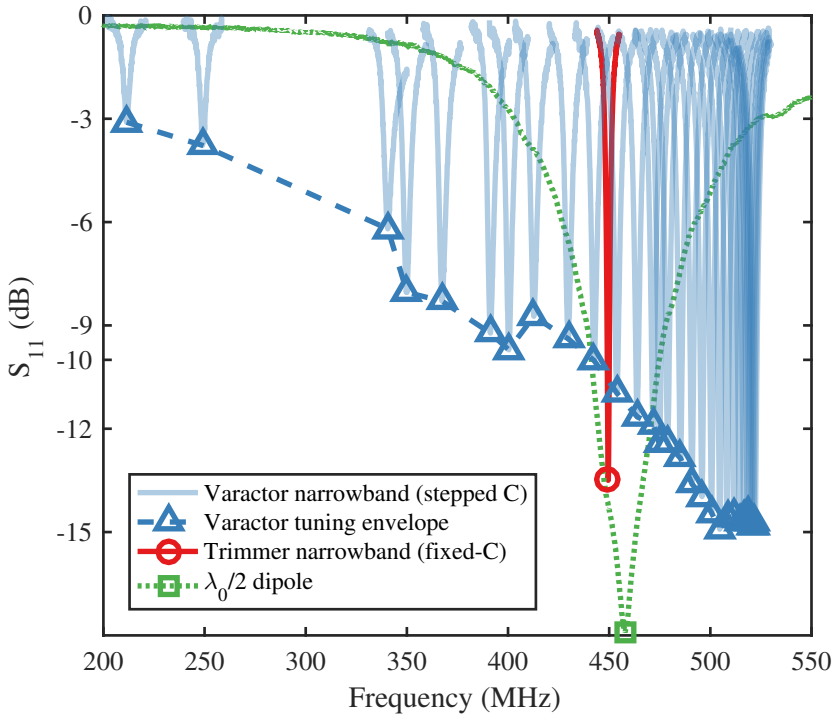

FIGURE 5.17: Tuneable impedance bandwidth measurements for RT5880 fixed-frequency/varactor-tuned antenna for performance metric development.

TABLE 5.5: Impedance bandwidths of RT5880 tuneable/non-tuneable ESAs and $\lambda/2$ dipole at 450 MHz.

Antenna	-3 dB bandwidth (MHz)	Fractional bandwidth (%)
Varactor	212–522	42
Fixed-C	448–452	0.9
$\lambda/2$ dipole	405–529	27

Using the measured input responses and radiation data, the transmission response-based metrics of bandwidth of assured efficiency (e.g. -10 dB), integrated efficiency-bandwidth product and average efficiency in the tuned band can be calculated.

5.5.2 -10 dB transmission efficiency bandwidth

Development of the set of transmission-based performance metrics starts with the requirement for definition of an underlying efficiency value relevant to RF link budget calculation. For this purpose, the realised transmission efficiency η was used ($\eta = \eta_{\mathrm{m}} \cdot \eta_{\Omega}$).

The transmission efficiency values for each of the ESA loops are documented in Figure 5.18, with the $\lambda/2$ dipole assigned a relative radiation efficiency of 100%. This approximation was applicable since the conductor losses of the dipole were expected to be negligible compared to the radiation resistance of its fundamental mode, thus being assumed to have an absolute (though not measured) radiation efficiency within a few percent of 100%. Such an assumption cannot be applied to ESAs such as the loops considered here, since the radiation resistance is generally held to be sufficiently low that the conductor, substrate and tuning component loss resistances form a major contribution to the radiation inefficiency. This statement is justified by measurement: the realised radiation efficiency was generally less than 50% for the varactor-tuned antennas, thus the loss resistances by definition must generally be at least as large as the radiation resistance.

From the plot of total efficiency, determination of a useable tuning bandwidth based on transmission response rather than input response becomes possible. In tuning range measures based on S_{11}, a threshold S_{11} requirement of -10 dB or -3 dB is commonly applied. In this spirit, a threshold value of 10% (-10 dB) for transmission efficiency was applied. Application of a 50% (-3 dB) limit was also considered, but was not favoured in this work since ESAs often have low radiation efficiencies and the metrics would subsequently fail to capture a large range of the tuning behaviour in a performance regime typical of small antennas.

Thus, the lower and upper frequency limits $[f_{\mathrm{l}},\ f_{\mathrm{u}}]$ of the -10 dB transmission efficiency bandwidth for the RT5880 antenna demonstrated here were [400.5, 528.1] MHz for the varactor-tuned loop and [446.8, 452.4] MHz for the fixed-frequency loop. Without conducting further analysis, the tuneable ESA can already be seen to have achieved the objective of delivering useable antenna

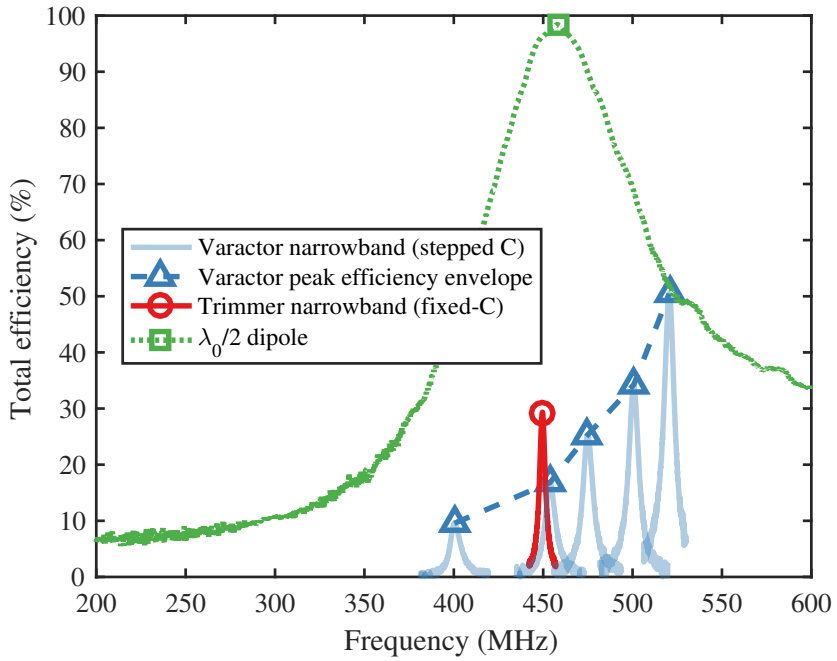

FIGURE 5.18: Total realised transmission efficiency of tuneable vs. non-tuneable antennas.

efficiency over a greater bandwidth than a non-tuneable ESA equivalent. In the given band, the system designer can expect to acheive at least 10% realised total transmission efficiency, and is equipped in some sense with a worst-case estimate of efficiency. Using the -10 dB transmission efficiency bandwidth metric in isolation, a pessimistic value of antenna efficiency can be incorporated into link budget calculation for the frequency range defined by $[f_l,\ f_u]$. Such link budget-ready performance indications are not available from S_{11} alone.

To demonstrate the danger of depending on S_{11} alone for prediction of realised antenna performance, consider a comparison between the impedance bandwidths of the varactor-tuned loop and the $\lambda/2$ dipole (Figure 5.17). The -3 dB tuneable impedance bandwidth of the varactor-tuned antenna (42%) not only exceeded that of the fixed-C loop (1%), but also exceeded that of the electrically large dipole (27%). This finding could mislead antenna system designers into expecting superior realised transmission performance from the varactor-tuned ESA than from the dipole at frequencies where the impedance matching efficiency of the varactor-tuned ESA exceeded that of the dipole (below 441 MHz or above 470 MHz). This concept is shown in Figure 5.19, where the impedance matching efficiencies η_m are shown. Inspection of the total efficiency plot (Figure 5.18) reveals this notion to be false, despite the improved impedance matching of the tuneable ESA. Thus, antenna system designers should continue to select electrically large antennas over electrically small counterparts where possible for greater efficiency and non-tuned bandwidth performance. ESAs remain liable to providing reduced total transmission efficiency, despite the potentially misleading suggestion of superior performance offered by improved S_{11}.

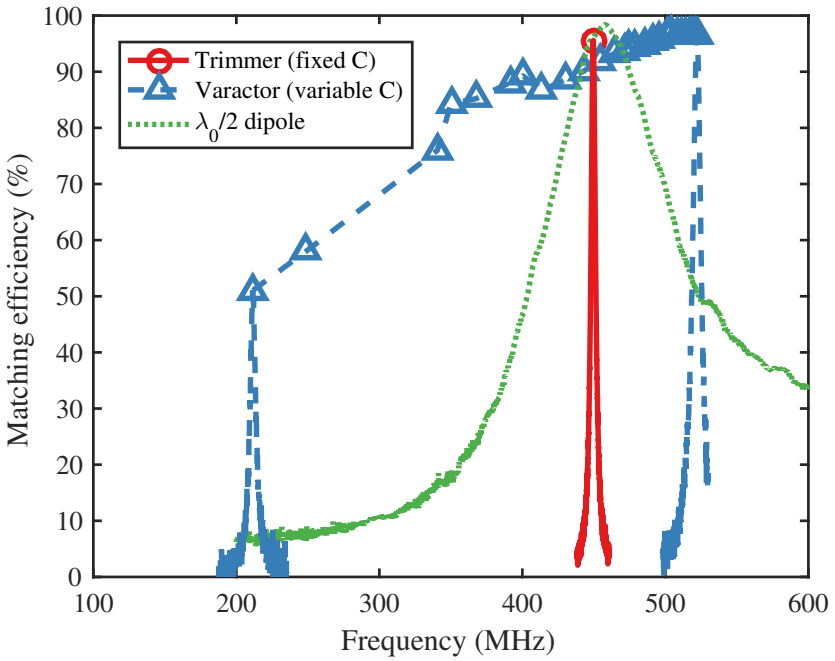

FIGURE 5.19: Matching efficiency η_m of tuneable ESA, non-tuneable ESA and $\lambda/2$ dipole. Below 441 MHz and above 470 MHz, the tuneable ESA has better impedance matching than the $\lambda/2$ dipole, but the realised transmission efficiencies in Figure 5.18 shows the dipole to remain the superior antenna.

5.5.3 Discrete vs. continuous tuning in terms of transmission response

While the -10 dB transmission efficiency bandwidth provides advantages over S_{11} in recording useable tuning bandwidth, extensions are possible that more fully record the varying performance of the antenna over the tuned band. The -10 dB transmission efficiency bandwidth alone does not give any indication as to the efficiency behaviour in the available tuned band, other than to say that it exceeds 10%. Using this metric in isolation, the tuneable loop characterised here over the range $[f_l,\ f_u]$ receives the same performance score as any other antenna offering at least 10% efficiency across the band. This issue with the use of the -10 dB transmission efficiency bandwidth in isolation can be observed by comparing the transmission efficiency bandwidths of a complementary pair of hypothetical antennas in Figure 5.20, one of which offers discrete frequency-reconfigurability (e.g. via switching), while the other demonstrates continuous frequency tuning.

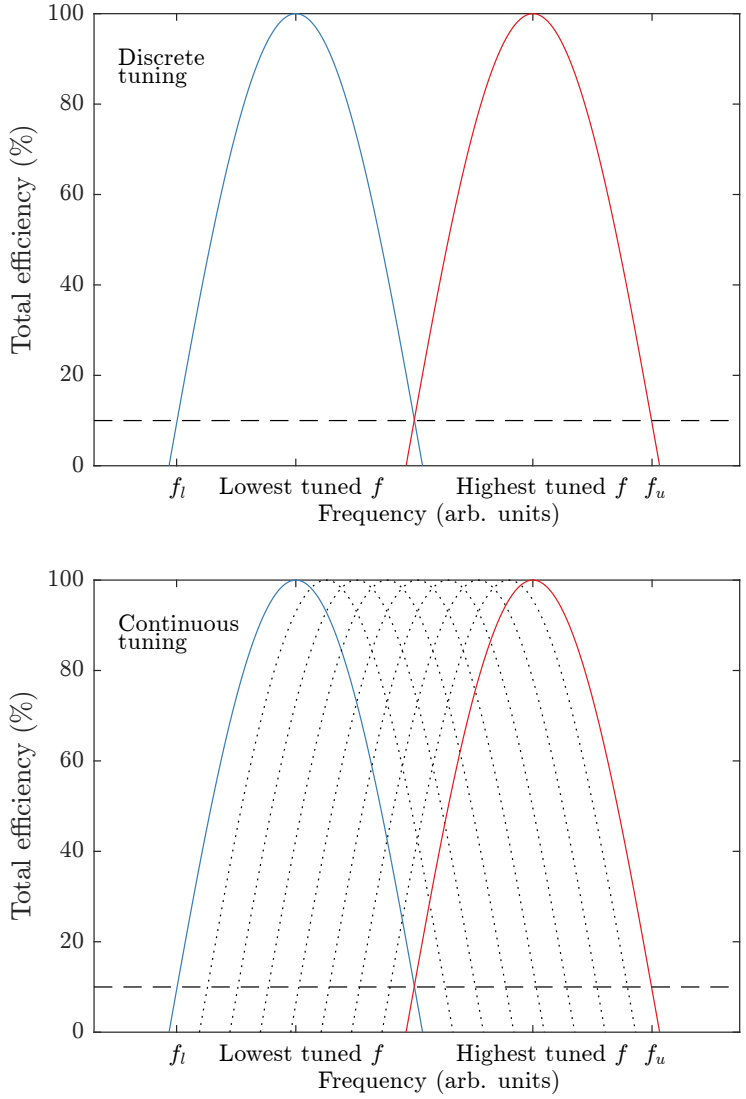

FIGURE 5.20: Demonstration of difference in available efficiency offered by discrete vs. continuous tuning, for two antennas of equal -10 dB efficiency bandwidth. Dashed horizontal line denotes -10 dB transmission efficiency limit.

The transmission efficiencies shown for these two antennas describe the same -10 dB transmission efficiency bandwidth between the frequency limits $[f_\mathrm{l},\ f_\mathrm{u}]$. The antenna offering discrete frequency switching does not, however, offer high efficiency across the entire available band. The continuously tuneable antenna in this example can optimise the tuning state to deliver maximum efficiency on any targetted frequency within the band, which should be captured by transmission-based performance metrics developed as an extension to the -10 dB transmission efficiency bandwidth. Hence, extensions to the metric are developed to record the average realised transmission efficiency in this band, via an integrated efficiency curve coverage method.

5.5.3.1 Integrated efficiency-bandwidth product

Using the frequency limits $[f_{\text{l}}, f_{\text{u}}]$, a "frequency coverage" metric can be established on the total efficiency graph to record the combined efficiency and frequency-access behaviours. Continuously tuneable antennas sweep out a large area on the total efficiency plot, while equally (instantaneously) efficient discretely-tuned antennas receive a lower score, assuming both antennas demonstrate the same -10 dB total efficiency bandwidth, as conceptualised in Figure 5.20.

The integrated area covered on the total efficiency graph is described by:

$$\text{Frequency coverage integrated area} = I = \int_{f_{\text{l}}}^{f_{\text{u}}} \eta(f)\, df \tag{5.6}$$

where $\eta(f)$ is the total transmission efficiency for each radiatively characterised frequency. For the practical reasons previously described, radiative characterisation of a continuously tuneable antenna will often be reduced to a sub-set of the available tuned states. In general, a numerical integration will provide a suitable approximation for the area coverage measure. In this work a trapezoidal integration was used:

$$I \approx \frac{1}{2} \sum_{n=1}^{N} (f_{n+1} - f_n)\left[\eta(f_n) + \eta(f_{n+1})\right] \tag{5.7}$$

This definition of the integrated frequency coverage metric I provides a defence against "gaming" of the performance metric through the development of a discretely-tuned antenna offering a small number of switched highly efficient non-overlapping modes, which could achieve a large -10 dB transmission bandwidth through the use of switched conducting tracks while offering poor channel availability in between (as demonstrated in Figure 5.20). Continuously tuneable antennas therefore receive higher scores under this system than discretely-tuned antennas offering only coarse frequency selection, reflecting their greater flexibility in addressing arbitrary frequency bands. For a particular application such as a limited number of bands to support, the discretely-tuned approach may be perfectly acceptable to meet the required specification. Nonetheless, the metric is defined in such a way as to highlight the superior frequency band access offered by continuous tuning without loss of generality.

The integrated frequency coverage metric using Equation (5.7) was calculated for the varactor-tuned and fixed-frequency loops using the integration limits calculated above ($[f_{\text{l}}, f_{\text{u}}]$ = [400.5, 528.1] MHz for the varactor, and [446.8, 452.4] MHz for the fixed-frequency loop). During integration the transmission efficiency is considered to take values between 0 and 1 and is

dimensionless. The frequency limits are defined in MHz, therefore the integrated area also has units of MHz. The integration areas themselves are depicted by shaded areas under the total efficiency curves in Figure 5.21. The integrated areas were found to be I = 29.8 MHz and I = 1.1 MHz for the varactor-tuned loop and fixed-frequency loop respectively.

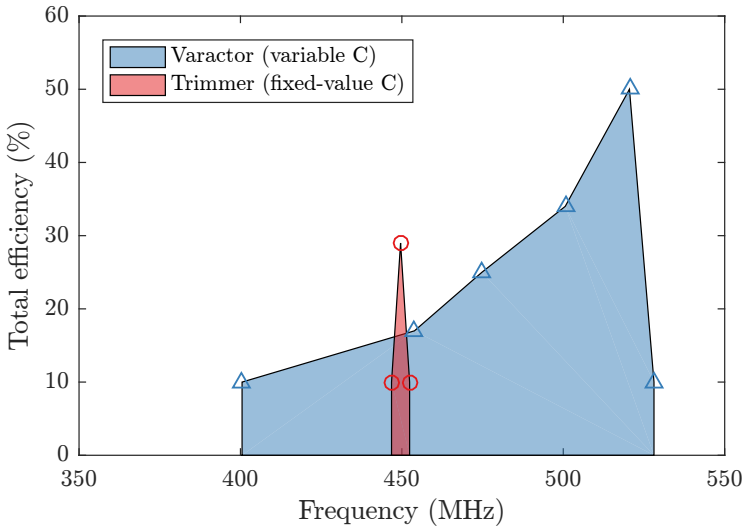

FIGURE 5.21: Numerical integration of transmission efficiency bandwidth envelope (RT5880 substrate).

5.5.3.2 Average value of broad band transmission efficiency via integration

The area coverage measure I captures the combined transmission efficiency and frequency-accessibility behaviour of a tuneable antenna, but does not provide the antenna system designer with a convenient indication of useable antenna efficiency above the 10% value already indicated. The transmission efficiency plot (Figure 5.18) can be used to provide this information as a function of frequency, but as an additional step, the average transmission efficiency can be calculated from the integrated area coverage metric. From the integrated area and frequency limits $[f_\mathrm{l}, f_\mathrm{u}]$ already given, the average efficiency is readily calculated by:

$$\text{Average value of total efficiency} = \frac{1}{f_\mathrm{u} - f_\mathrm{l}} \times I \tag{5.8}$$

From Equation (5.8), the average efficiencies of the RT5880-substrate ESAs across their respective -10 dB total efficiency bandwidths were 23.4% for the varactor-tuned loop and 19.6% for the fixed-frequency loop.

5.5.4 Use of the performance metrics to discriminate between tuneable loops on RT5880/FR-4 substrates

Development of the transmission-based performance metrics of -10 dB transmission efficiency bandwidth, integrated area coverage and average transmission efficiency has to this point only considered the relative performances of the tuneable (varactor) and non-tuneable (trimmer) loop antennas on an RT5880 substrate. Application of the metrics to the antennas constructed on FR-4 substrate yields the values given in Table 5.6, with the integrated -10 dB transmission efficiency bandwidths shown in Figure 5.22.

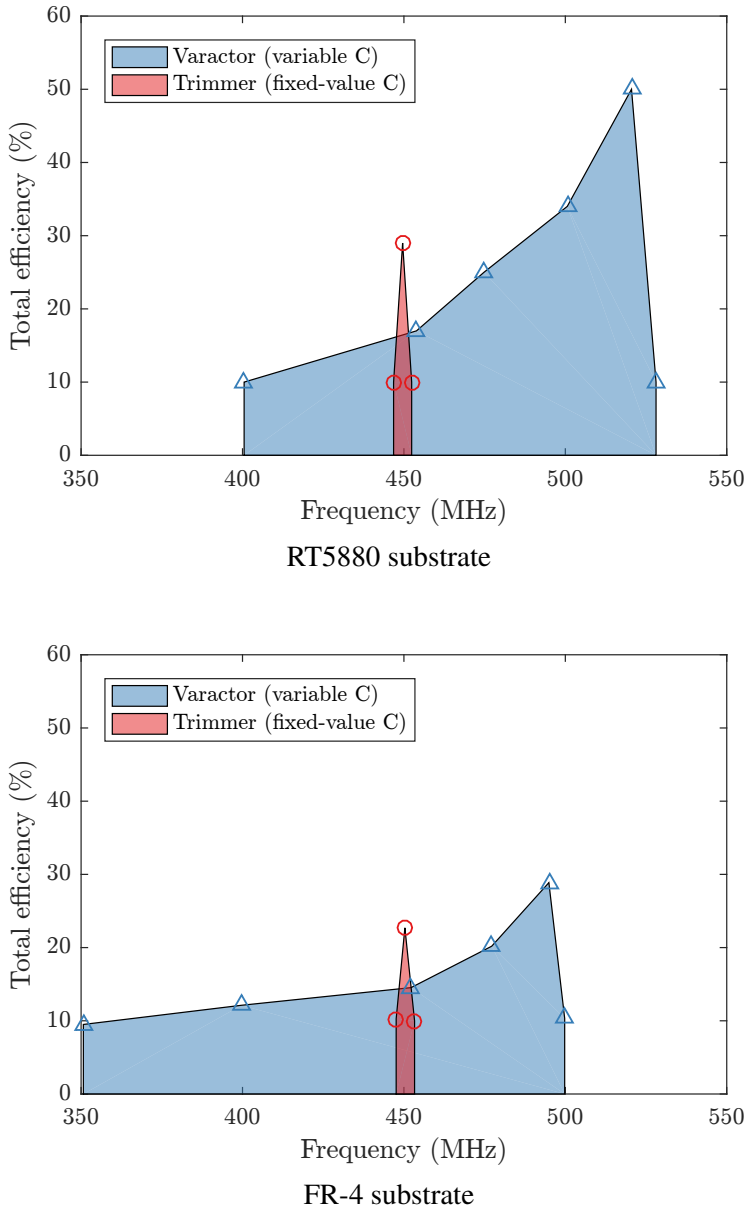

FIGURE 5.22: Integrated -10 dB transmission efficiency bandwidth of tuneable ESAs.

TABLE 5.6: Transmission response-derived performance data for tuneable loop antennas.

Antenna	Substrate	-10 dB BW (MHz)	Integrated efficiency-bandwidth coverage, I (MHz)	Average total efficiency (%)
Fixed-C	RT5880	446.8–452.4	1.1	19.6
Fixed-C	FR-4	447.6–453.5	0.9	15.3
Variable C	RT5880	400.5–528.1	29.8	23.4
Variable C	FR-4	350.7–499.8	21.9	14.7

From the data in Table 5.6, a few trends emerge. The first is both tuneable ESAs satisfy the "successful" tuneable ESA concept, each offering greater integrated efficiency I over a broad frequency range than that offered by a non-tuneable counterpart, despite the loss of instantaneous efficiency for any given frequency. This was true of either substrate. To compare substrates directly, the reduction in efficiency for FR-4 substrate was accompanied by access to lower frequency tuning states exceeding -10 dB total efficiency (lower limit on f_l). However, access to some of the upper tuning states was lost (about 28 MHz of relatively high efficiency area coverage from 500–528 MHz is available from the RT5880 design, which is not available in the FR-4 design). Hence, the additional frequency coverage from 350–400 MHz demonstrated by the FR-4 antenna did not lead to greater integrated efficiency I in this case, despite the greater -10 dB transmission efficiency bandwidth.

How to interpret this finding depends on what the antenna designer is trying to achieve. If the designer sought maximum efficiency from 400–500 MHz, the RT5880 antenna would be the correct choice. If the designer needed to access a tuneable frequency band at frequencies below 400 MHz with a minimum tuneable efficiency of 10% over the band 350–450 MHz, the FR-4 antenna would be the antenna to pick, despite the generally higher efficiency of the RT5880 option. The use of transmission-based performance metrics has highlighted the overall superiority of the RT5880 substrate however: unlike the impedance-based definition of efficiency bandwidth product (EBW, Equation 5.5), the transmission-based counterpart shows that the total efficiency-transmission bandwidth area covered is higher for the RT5880 substrate in the given measurement scenario.

5.5.5 Limitations

There are two principal drawbacks to the system of metrics defined here. The first is that compared to tuneable impedance bandwidth, measurements of tuneable transmission response can be much more time-consuming. Using a vector network analyser and a programmable voltage supply, a set of tuneable S_{11} measurements for the varactor-tuned antennas could in principle be measured in a matter of minutes. In contrast, the far-field radiative measurement setup used throughout this research takes approximately 45 minutes to record a single power pattern. The additional need to

measure the pattern of a reference monopole or dipole for efficiency calculation increases the measurement time per frequency point to approximately two hours once antenna changeover is accounted for. The measurement time could however be reduced using 3D near-field scanning techniques (e.g. Satimo Stargate chamber, among others).

The second limitation of the metrics in general is that in their present form, the metrics are most useful for a comparison between electrically small antennas. Comparison of the total efficiency area coverage of the varactor and $\lambda/2$ dipole antennas can be interpreted visually with respect to Figure 5.18. It can be observed that the dipole offers much greater area coverage and is more efficient at all depicted frequencies, where its transmission efficiency was derived from an assumption of 100% radiation efficiency by definition and efficiency scaled entirely by the impedance matching. An attempt to evaluate the full -10 dB transmission efficiency bandwidth of the $\lambda/2$ antenna is somewhat hampered by the contribution of additional natural modes at higher frequencies. This effect has also been observed elsewhere [170], where it was noted that application of single-mode gain bandwidth product was only conveniently applied to ESAs, with multiple-mode antennas being awkward to define in terms of an exact upper limit on gain-bandwidth product. For an antenna occupying a sizeable fraction of the wavelength (e.g. $\lambda_0/4$, $\lambda_0/2$), a 50% total efficiency limit (-3 dB) on the integration limits could be more appropriate, and was initially trialled as a candidate for performance metric development. However, inspection of Figure 5.18 reveals that the varactor antenna only briefly exceeds 50% total efficiency (at 520 MHz). Calculating the integrated area with respect to the 50% total efficiency would be unreasonably harsh on an ESA, considering that the radiation efficiencies of ESAs are often low due to their low radiansphere occupancy and subsequent low radiation resistances relative to construction losses [123]. This effect was also observed in [171], wherein a study of cell phone antenna efficiencies led the author of that work to settle on a value of -3 dB as a "rough estimate of the average antenna efficiency", which was often found to be much worse than -3 dB under various usage modes (e.g. user browsing rather than free space). Hence, in the context of this thesis, the author submits that numerical use of the set of performance metrics proposed here should be limited to comparison of the performance of ESAs against other ESAs, whether tuneable or not.

Finally, the large quoted -10 dB transmission efficiency bandwidth would take no account of changes in antenna mode observed in this band, causing changes in antenna pattern liable to degrade performance. Such an effect was previously documented regarding mode changes over ultra wide instantaneous impedance bandwidths in [45] (described in Section 5.1.3). That work introduced the pattern correlation ρ for individual pairs of patterns. Extended work could define a metric for maintenance of pattern correlation bandwidth under tuning and relate this to impact on system performance.

5.6 Conclusions

In this chapter, a candidate ESA was required to demonstrate the viability of the tuneable ESA concept defined in Chapters 1 and 2, namely realisation of useable efficiency over a greater band than that available from a non-tuneable ESA counterpart. A set of small loop ESAs were fabricated for this purpose, using either trimmer-capacitor or varactor diodes to tune the antenna.

Through the use of efficiency-based performance metrics developed in this chapter, the varactor-tuned loop antennas were shown to be generally successful in demonstrating the tuneable ESA concept. They offered greater accessible tuned impedance and transmission bandwidths than fixed-frequency ESA designs, but this was accompanied by an efficiency penalty associated with the additional components associated with varactor tuning. The Q factor of the varactor diode was also found to be lower than the Q of the trimmer capacitors used for the fixed-frequency antennas, thereby harming the efficiency.

Considering the tuneable impedance bandwidth with respect to the criterion $S_{11} < -3$ dB, the available tuning ranges were 212–522 MHz and 201–496 MHz for antennas constructed on Rogers RT5880 and FR-4 substrates respectively, yielding normalised percentage tuning bandwidths of 42% each. However, as has been noted throughout this thesis, S_{11} is insufficient as a guarantor for high efficiency particularly for ESAs. To analyse the tuneable transmission performance instead, a -10 dB transmission efficiency bandwidth performance metric was developed in this chapter. The -10 dB transmission bandwidths of the varactor-tuneable and fixed-C trimmer antennas given in Table 5.6 showed the varactor-tuneable antennas to have -10 dB tranmission bandwidths of 400–528 MHz (14.7%) for the RT5880 antenna and 350–500 MHz (15.3%) for the FR-4 antenna. This "useful" tuneable bandwidth is approximately 1/3 of the quoted tuneable impedance bandwidth. Nonetheless, for each varactor-tuned antenna characterised here, the transmission bandwidths exceeded the -10 dB transmission bandwidth of a fixed-frequency trimmer-capacitor tuned loop centred at 450 MHz (approximately 1%). Hence, the tuneable ESA concept advanced in Chapters 1 and 2 is validated by the varactor-tuned antennas, with margin for improvement in the instantaneous efficiency.

Concerning the realised efficiencies for the ESAs in general, while the tuneable ESA was found to out-perform the non-tuneable ESA in terms of overall transmission response, the much larger $\lambda/2$ dipole remained more efficient over an even wider band despite having lower impedance matching efficiency at the outer edges of the measured band. This finding highlights the danger of depending purely on S_{11} as a measure of antenna performance, where realised total efficiency suggests that antenna system designers should continue to opt to consume as much volume as possible for the antenna given the potential to achieve greater efficiency and instantaneous bandwidth performance. ESAs remain liable to providing reduced total transmission efficiency despite the potentially misleading suggestion of superior performance offered by improved S_{11}.

Chapter 6

Conclusions and further work

6.1 Outcomes

Antenna miniaturisation introduces performance degradation in terms of instantaneously achievable bandwidth and radiation efficiency. The latter is degraded by the tuning mechanisms used to recover lost bandwidth performance. Literature review (Chapter 2) identified key contemporary antenna tuning/miniaturisation technologies for further study: matching networks featuring emerging tuneable capacitor technologies; novel magneto-dielectric materials; varactor diode tuning (used to support a study advancing the state of the art in assessment of tuneability). The outcomes of the studies given in Chapters 3-5 and [20–23] are detailed below. Each study incorporated literature review, identification of a candidate solution, design of a demonstrator for the given tuning concept (using simulation where appropriate), prototyping and practical antenna measurements. Throughout, the tuned antenna efficiency was measured and contrasted against the tuning range implicit from S_{11} in isolation. The commonly encountered disparity between S_{11} and efficiency under tuning prompted development of a new efficiency-based approach [20] to measurement of frequency agility in tuneable narrow band antennas.

6.1.1 Tuneability and efficiency of a tuning solution retro-fitted to a non-tuneable narrow band antenna

Chapter 3 considered the use of a tuneable π-section narrow band matching network for enabling efficient tuning in free space and near-field reactive detuning scenarios. The topical interest in RF microelectromechanical system (RF MEMS) tuneable capacitor technology was derived from the perceived low loss and high linearity benefits of RF MEMS compared to predecessor technologies such as complementary metal-oxide semiconductor (CMOS) capacitors. Prior to the work performed here, these claims were supported by little actual measurement data,

however. A demonstrator was designed to maximise Smith chart coverage at 2 GHz when paired with a particular microstrip patch antenna, offering reconfigurable impedance matching at frequencies either side of this. A practical realisation of the tuneable matching network (TMN) was characterised in terms of agility using an over-the-air S_{21} measurement as a function of tuning state. A positive insertion gain was shown over a wide integrated frequency band accessed under tuning. The tuner thus delivered an efficiency enhancement over a wider band than that offered by a non-tuneable antenna, but this was only a relative enhancement: in absolute terms, the overall system efficiency could not be prevented from decaying, hence while comparatively convenient to deploy, the TMN approach to tuning is not well suited to achieving efficient antenna miniaturisation.

Additionally, a hand phantom was constructed which was designed to have similar impedance properties to a real hand. Reactive detuning was induced in the antenna using the phantom, which the tuner was able to correct. In the scenario studied, the detuning was not sufficiently severe for the realised system performance to be improved by the tuner due to its insertion losses. However, these losses were characterised and had more extreme detuning scenarios been demonstrated, a net performance enhancement would be been achievable.

6.1.2 Miniaturisation, efficiency and tuneability of an antenna incorporating a modern magneto-dielectric hexagonal ferrite material as the substrate

Chapter 4 described investigation of claims that a particular class of magneto-dielectric (MD) materials is able to effect antenna miniaturisation while preserving the antenna efficiency. The novel aspect of the work is derived from the use of the modern MD material, where advances continue to be made in the material formulation decreasing the substrate losses. A survey of the literature in the antenna and materials science domains was conducted. A "best obtainable" candidate hexagonal ferrite material was identified and procured. It was characterised in terms of its electromagnetic dispersion properties (complex permittivity ε^* and permeability μ^* at UHF frequencies) using an impedance analyser method up to 1 GHz. A set of antennas was designed using this material, as well as conventional FR-4 and Rogers RT5880 substrate, using a combination of the cavity model of patch antennas and CST simulation. Prototypes were constructed and subjected to input response (VNA) and anechoic chamber measurement. The antenna was successfully miniaturised using the MD material, as demonstrated by a reduction in operating frequency of up to $6.4\times$ lower on the MD material than was achieved using the equivalent RT5880 patch antenna. Alternatively put, for two antennas of the same operating frequency, an RT5880 substrate-based antenna would have to be significantly larger (e.g. up to $75\times$ board area saving for the characterised material).

The material was shown to permit antenna tuning under external magnetic field biasing achieved using neodymium magnets (32% for S_{11} <-3 dB), a capability which had been widely overlooked for such materials at the time of writing. The antenna also maintained a stable, broad-beam radiation pattern under tuning which maintained its dominant polarisation across the tuned range (this has been shown not to be the case for alternative miniaturisation methods which could be made tuneable, e.g. lumped-element impedance matching). The varying efficiency of such a Co_2Z patch antenna had similarly not previously been reported under tuning, and was found to maintain an efficiency of approximately 1% across the tuned band [22, 23]. While the efficiency was low, this is fairly typical of electrically small antennas (ESAs) overall. The finding of very low efficiency makes clear that such materials are best suited to miniaturisation-critical and short range applications. The relative ease of impedance matching the antenna, and its pattern stability over the tuned range, justifies further investigations into newer MD materials.

6.1.3 Improved approach to reporting antenna tuneability, encapsulating realised efficiency as well as agility

Chapter 5 contributed an improved approach to quantifying tuneability in compact narrow band frequency agile antennas. Formulation of this approach is a major contribution of this research and has been published in [20]. Measurements of tuneable input response, 3D pattern and efficiency have been made for a set of tuneable narrow band antennas. These have been used as the basis of metrics of tuneability formulated to concentrate attention on the realised (variable) efficiency of the antennas across a tuned band. Tuneable bandwidth of realised efficiency, integrated efficiency-bandwidth product and average antenna efficiency in the tuned band have been defined and demonstrated for a set of fixed-frequency or varactor-tuneable ESAs. While the tuneable ESAs were validated as addressing larger bands than a fixed-frequency ESA, the extent to which this is the case varies greatly depending on the metrics used. The process followed here to measure and report minimum and average efficiencies in a tuned band is beneficial from the viewpoint of holistic reduction of power consumption in reconfigurable communication systems. The efficiency-based metrics of tuneability formulated here have been shown to be successful in meeting the objective of providing greater insight into realised efficiency across the accessible band, identifying tuning ranges of assured efficiency several times narrower those indicated by e.g. -3 dB tuneable impedance bandwidth. While narrower tuning ranges are likely to be a common result of reporting tuneability from the efficiency perspective, the benefit is that within the quoted tuned range, RF designers can be confident that a certain level of realised performance is obtained. Researchers conducting tuneability studies in compact antenna scenarios are recommended to communicate the range of assured efficiency, average efficiency in the band and integrated efficiency-bandwidth product so that the trade between agility and efficiency may be more readily compared between different designs.

6.2 Future work

From the conclusions and limitations of the work presented, suggestions for expansion of the work have been identified:

- In Chapter 3 it was shown that impedance matching levels better than $S_{11} < -10\,\text{dB}$ or even $S_{11} < -20\,\text{dB}$ were obtained for the TMN but were no guarantor of high transducer efficiency, given the network losses. The search for more efficient tuneable matching networks may benefit from a more general study of varied impedance mismatch scenarios and earlier indication of the detuning impedance shifts likely to be encoutered. The TMN and antenna could then be co-designed with the likely impedance shift in mind, potentially leading to a less complex network with lower associated losses.

- In Chapter 4, the selected MD material was based on criteria requiring $\varepsilon_\text{r} = \mu_\text{r}$, which created a narrow scope for material selection. Broadening the search to allow arbitrary values of $\varepsilon_\text{r}, \mu_\text{r}$ would create freedom to optimise lowest overall loss for a given miniaturisation factor. Claims that $\varepsilon_\text{r} = \mu_\text{r}$ assures high efficiency under miniaturisation continue to be advanced, but it is problematic that materials are being proposed without reporting losses across the whole tuning range. This work shows that these losses are significant and frequency-dependent. Future MD miniaturisation/tuning studies need to involve a similar complex material and radiative antenna characterisation approach to that employed here, to assess performance of a wider set of newer materials in the broader $\varepsilon_\text{r}, \mu_\text{r}$ space.

- An initial aim of this research was to find the most efficient and tuneable narrowband antennas in a particular band (UHF). The present adopted approach to reporting frequency agility (widespread reliance on S_{11}) does not readily support useful comparison of different tuneable antenna designs. Future work should expand utilisation of the approach given in Chapter 5 and [20] to grade a diverse range of tuneable antenna technologies in terms of maximisation of both efficiency and tuneability (thereby maximising the efficiency-bandwidth product). Different tuning technologies could even be grouped for different applications, quantified along the axes of efficiency, agility and cost/complexity (something the existing S_{11}-based approach does not lend itself to). The problem of efficiently identifying tuning technologies for a given application on an objective basis would be significantly alleviated by work to populate such a mapping of tuning technologies to antenna applications.

Appendix A

Bode-Fano bandwidth limits on impedance matching

In Chapter 2, the existence of the Bode-Fano criterion on matching network bandwidth was noted, describing a trade-off between instantaneous impedance bandwidth and the power loss caused by the non-zero voltage reflection coefficient, Γ. The discussion of the Bode-Fano criterion presented in [26] the noted impact of the criterion on the performance of impedance matching networks. For a given load impedance, the impedance bandwidth and voltage reflection coefficient are necessarily traded against each other. It is not considered to be possible to improve one without degrading the other. Additionally, high Q circuits (high reactance) are more difficult to match to than low Q circuits (low reactance). As far as antennas are concerned, reducing their electrical size is generally held to increase their reactance [19], hence the Bode-Fano criterion applied to electrically small antennas (ESAs) implies an increasingly difficult trade off between impedance bandwidth and impedance matching efficiency decribed by Γ as the antenna volume is reduced with respect to the free-space wavelength. Tuneable matching networks (TMNs) are proposed as a means to circumvent the limitations proposed by the Bode-Fano criterion, by accepting narrow band instantaneous network bandwidth in exchange for greater efficiency and subsequently tuning the response in frequency as necessary. For completeness, a brief review of the implications of the Bode-Fano criterion applied to matching problems is given here.

In [26] Chapter 5.9, Pozar presents an application of the Bode-Fano criterion to a lossless network matching a transmission line to an arbitrary complex load. For a non-zero impedance bandwidth, the voltage reflection coefficient at the interface between the transmission line and the load can be improved by insertion of the matching network. However, the match cannot be perfect (reflectionless) over any bandwidth greater than zero. Given that this is the case, the Bode-Fano criterion sets out a limit of trade-off between matching efficiency arising from the

voltage reflection coefficient Γ, and the impedance bandwidth denoted in [26] by $\mathrm{d}\omega$, where the angular frequency $\omega = 2\pi f$.

The Bode-Fano criterion assumes that the load impedance can be represented by a "canonical impedance" type, i.e. it can be described by any one of series RC, parallel RC, series RL or parallel RL over a given frequency range. The Bode-Fano criterion sets a limit on $\Gamma(\omega)$ given in Table A.1, depending on the load impedance type.

TABLE A.1: Bode-Fano criteria for canonical load impedance types.

Impedance type	Bode-Fano criterion
Parallel RC	$\int_0^\infty \ln \frac{1}{\lvert\Gamma(\omega)\rvert}\, \mathrm{d}\omega \leq \frac{\pi}{RC}$
Series RC	$\int_0^\infty \frac{1}{\omega^2} \ln \frac{1}{\lvert\Gamma(\omega)\rvert}\, \mathrm{d}\omega < \pi RC$
Parallel RL	$\int_0^\infty \frac{1}{\omega^2} \ln \frac{1}{\lvert\Gamma(\omega)\rvert}\, \mathrm{d}\omega < \frac{\pi R}{L}$
Series RL	$\int_0^\infty \ln \frac{1}{\lvert\Gamma(\omega)\rvert}\, \mathrm{d}\omega < \frac{\pi R}{L}$

For a given load impedance type in Table A.1, rearranging the applicable Bode-Fano criterion gives a limit on Γ over a bandwidth $\Delta\omega$. As an example, in the case of the parallel RC load, the limit on Γ satisfies $\Delta\omega \ln \frac{1}{\Gamma} \leq \frac{\pi}{RC}$. From this formulation of the limit on Γ, Pozar draws three conclusions [26]. The first is that for a given load (i.e. a fixed RC product), broadening the bandwidth ($\Delta\omega$) can only be allowed if increased reflection coefficient Γ is accepted. Second, perfect reflectionless matching ($\Gamma = 0$) only occurs for an impedance bandwidth of $\Delta\omega = 0$. This condition precludes perfect matching over a continuous finite bandwidth. Finally, increasing the RC product through increasing R or C degrades the quality of the match (either $\Delta\omega$ or $1/\Gamma$). High Q circuits are therefore harder to match than low Q circuits.

As far as small antennas are concerned, the reactance of an antenna is held to increase as the electrical size is reduced [19]. The antenna Q therefore increases with reducing size, which in turn makes efficient impedance matching increasingly difficult as the required instantaneous bandwidth is increased, given the trade-off between bandwidth and voltage reflection coefficient imposed by the Bode-Fano criterion. TMNs have been proposed which can exploit narrow band instantaneous behaviour, relaxing the constraint on Γ and achieving a more efficient match than might be achieved using a wide band passive matching network. Nonetheless, practical limitations on tuning range and realised power throughput efficiency (transducer efficiency) must be considered for any realised tuneable matching network, which is a topic examined in Chapter 3.

Appendix B

Tuneable matching network schematic

The schematic for the tuneable matching network described in Chapter 3 is given here for completeness. The schematic and the board itself was created by Paul Evans of Hexagon PCB Ltd., a local electronics contractor.

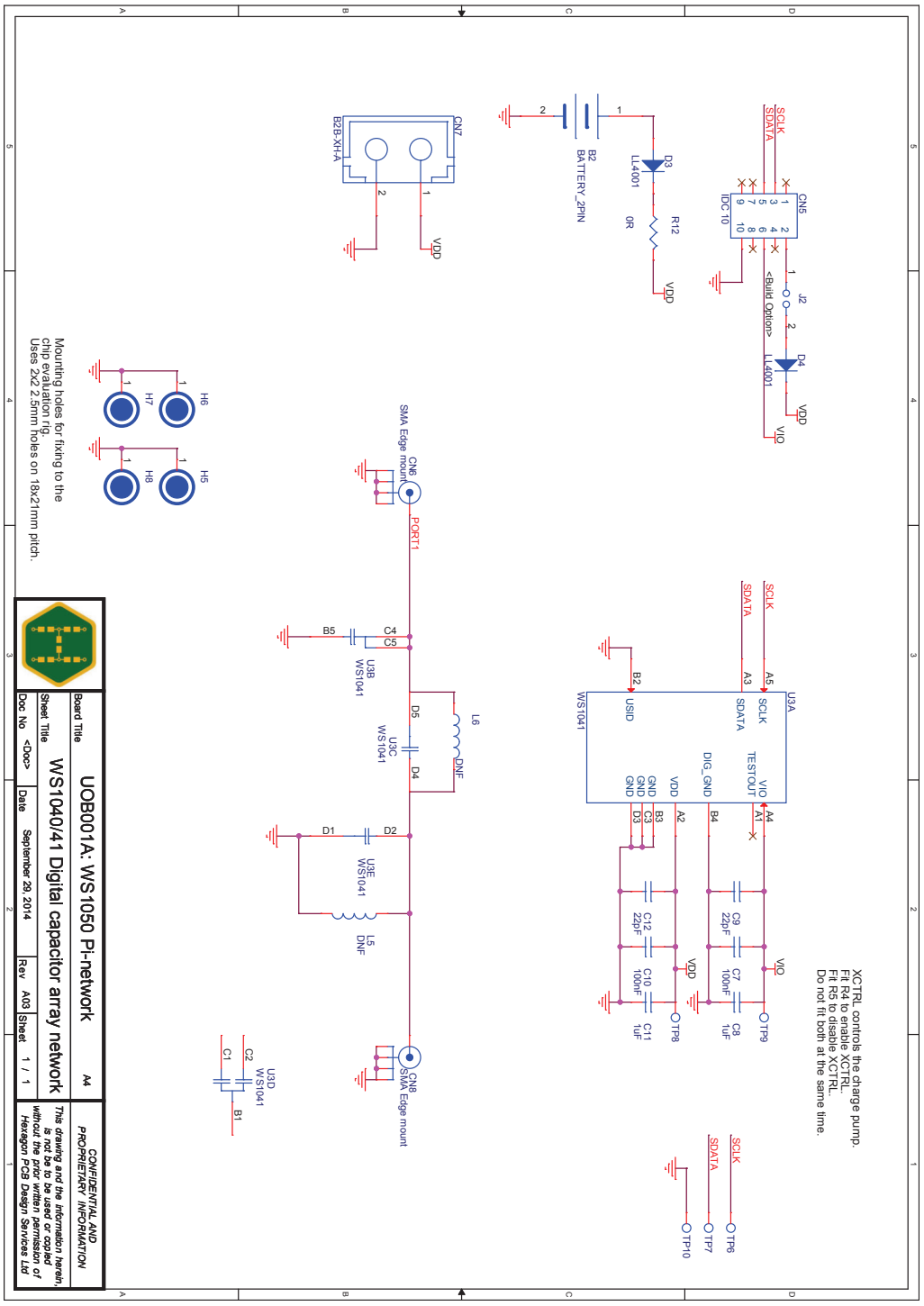

FIGURE B.1: Schematic for tuneable matching network PCB.

Appendix C

Matching network design for sub-resonant patch antenna

This appendix describes the specification of an impedance matching network intended to operate an RT5880 patch antenna at a sub-resonant frequency (lower than TM_{10}) as described in [22]. The operating frequency of the patch was reduced from its natural $\lambda/2$ resonance frequency of 2872 MHz to a sub-resonant frequency of 402 MHz through use of a series of three L-section matching stages.

C.1 Design process

The input responses of the fabricated and measured naturally-resonant RT5880 patch antennas were previously shown to differ in Figure 4.8 (page 90). This presents a question over which value of Z_{input} to use at 450 MHz for the matching network design, since the selection of actual matching components requires an initial stage of ideal-valued component selection to demonstrate the existence of a suitable matching topology, followed by a more thorough circuit-level simulation including components with frequency-dependent Q, parasitic R, L and C, as well as parasitic reactance associated with the microstrip feed tracks. Since iterative simulation was required, adding layers of realism on each pass, it was decided to use the simulated input response for the definition of target Z_{input} to match.

The objective of the study was to observe the general effects of the impedance-matching miniaturisation procedure on the sub-resonant patch antenna, rather than to invest large degrees of development time in precisely tuning the antenna to exactly 450 MHz. If this had been the goal, fine-tuning the matching network could have been achieved through using trimmer capacitor elements or fine adjustment of the copper antenna layout itself (providing its physical size were

never increased, lest the electrical size of the antenna be enlarged). Considering the requirement for the antenna to be tuned to (approximately) 450 MHz for a general comparison to the equivalent hexaferrite patch, frequency deviations of up to 10% were deemed to be acceptable. Thus, the simulated input response of the RT5880 small patch antenna was used to establish Z_{input} at 450 MHz, which was found to be equal to $0.25 - 24.6\text{j}\ \Omega$ with the ambition that the fabricated network would tune the patch antenna to a point inside the frequency range 400–500 MHz.

From the very low real part of the input impedance $Z_{\text{input}} = 0.25 - 24.6\text{j}\ \Omega$, it was judged that a multiple-staged matching network would be necessary. An iterative design process using three stages of single L-section matching networks was assessed to give acceptable results in CST and ADS simulators using ideal components in terms of impedance matching to the band. The design procedure used was to implement two stages of purely real impedance transformation, from 50Ω to 25Ω and then from 25Ω to 12.5Ω. The third stage, where the majority of the capacitance is found, accounts for the final complex match from 12.5Ω to Z_{input} at 450 MHz. No claim is made that this network is optimal in terms of bandwidth or Q constraints, concerning itself mainly with the aggressive real impedance transformation required from 0.25Ω to 50Ω. A design procedure for single L-section design is described in [147].

While design equations are available for lumped-element matching network designs such as L- and π-networks [147], in practice component packaging and printed circuit board (PCB) parasitic effects necessitated network modelling of the complete PCB in an radio frequency (RF) simulator to reach an acceptable solution in terms of matching for a suitable frequency. In this work, Keysight ADS [175] was used to model and design the matching networks. The ADS schematics used for the matching network design are given below. The realised improvement in impedance match for the fabricated network/antenna combination was found at 410 MHz in ADS and 402 MHz in measurement, as demonstrated in Chapter 4.

C.2 Matching network schematics

The schematics used to design the matching network shown in Chapter 2, section 4.3.2, are given here. These schematics were created and simulated using Keysight ADS simulator, with Murata and Coilcraft Incorporated libraries for the C and L elements where available.

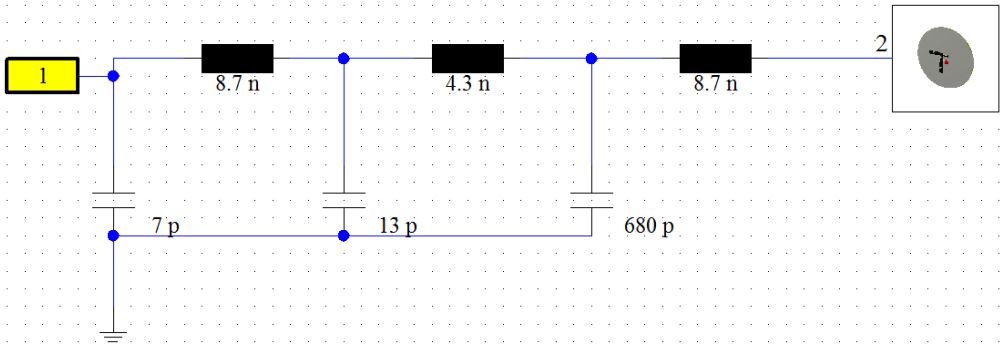

FIGURE C.1: Co-simulation setup for analysis of ideal radiation pattern using ideal matching network.

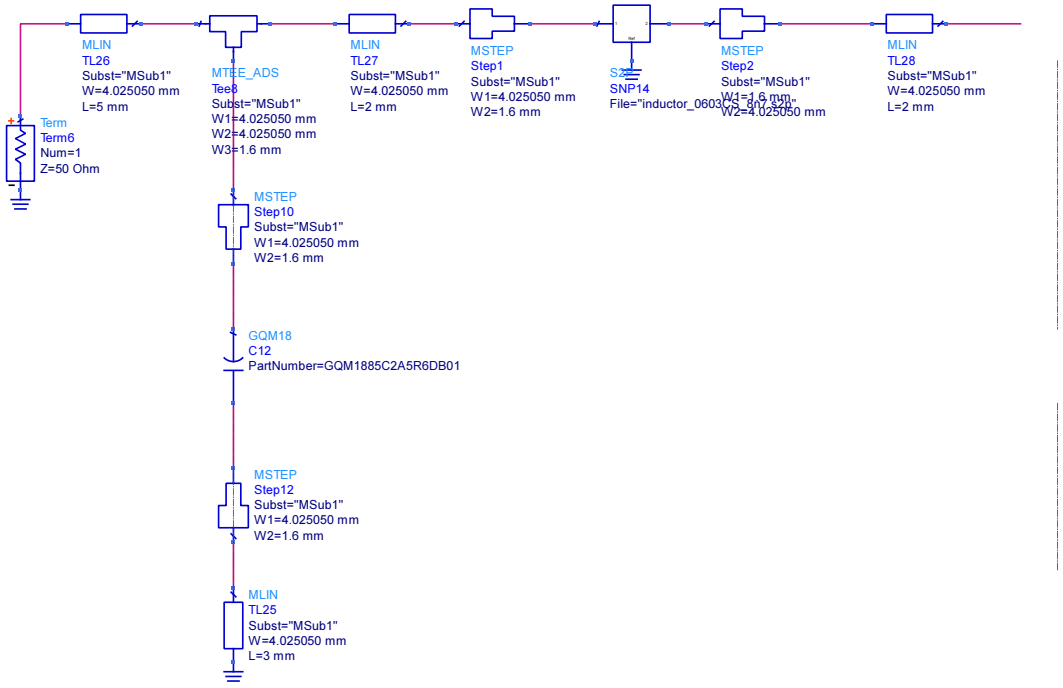

FIGURE C.2: Schematic for selection of practical (preferred) C and L values in ADS, accounting for parasitic effects of microstrip traces over practical PCB substrate: first stage, connected to feed line.

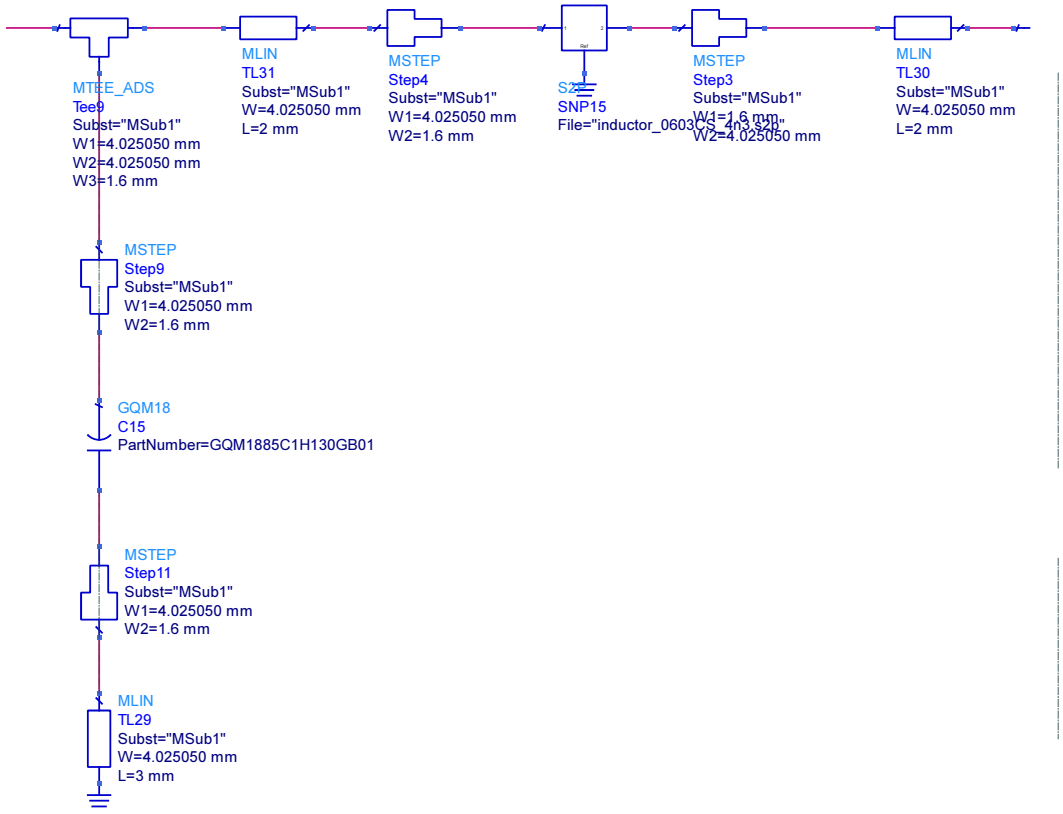

FIGURE C.3: Schematic for selection of practical (preferred) C and L values in ADS, accounting for parasitic effects of microstrip traces over practical PCB substrate: second stage.

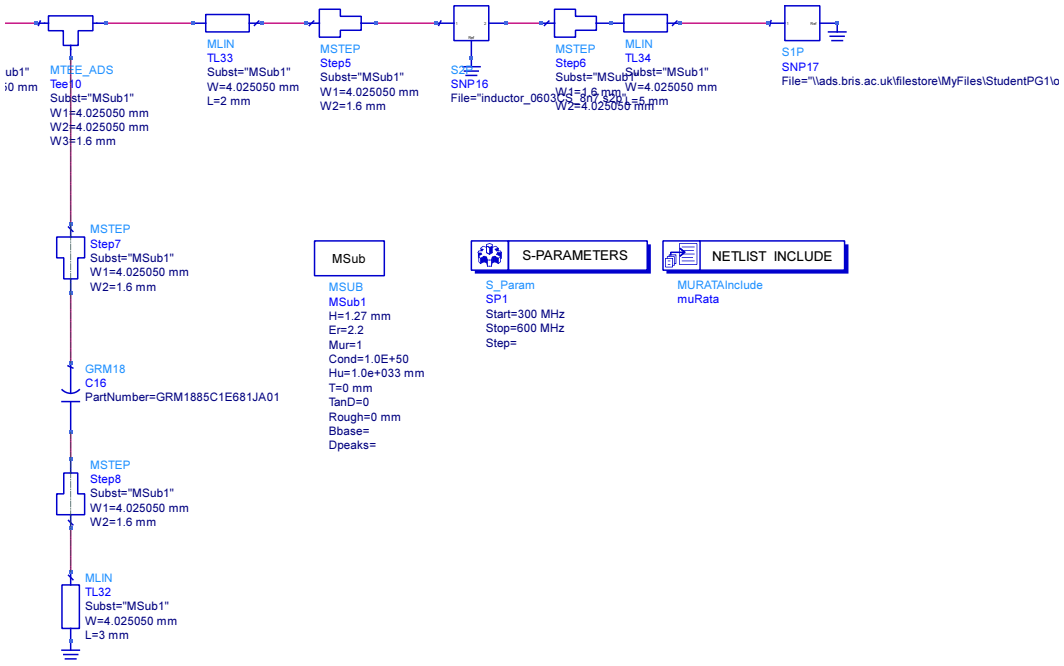

FIGURE C.4: Schematic for selection of practical (preferred) C and L values in ADS, accounting for parasitic effects of microstrip traces over practical PCB substrate: third stage, connected to antenna.

FIGURE C.5: Fabricated impedance-matched sub-resonant RT5880 small patch antenna.

C.3 Search for a more efficient matching network

C.3.1 Theoretical maximally efficient matching network

In the paper [22], the author noted the matching network described above was in no way claimed to be optimal, representing one candidate network out of many possible solutions. Various topologies exist which will match the 50 Ω feed line to the impedance of the RT5880 antenna at the sub-resonant frequency of 450 MHz. If the objective of the match is taken to be maximisation of the efficiency of the matching network in terms of incurring minimum resistive loss in the components, then the method suggested by Han and Perreault [157] can be used as a guide to seeking a more efficient matching network. That work sought to optimise the number of L-section matching networks taking into account the inductor losses described by Q_L.

Efficiency in this context is taken to assume perfect reflectionless impedance matching exists, with voltage reflection coefficient $\Gamma = 0$. Thus, the only power losses occur in ohmic heating of the matching components. Han and Perreault advanced the argument that losses in capacitors are typically far lower than those in inductors due to their higher Q value. The author agrees with this sentiment, noting the quoted Q of these components in various data sheets [149, 166] and also noting the impact of replacing ideal C, L sources with realistic C, L models in simulation. Thus, Han and Perreault proceeded to develop a model of power transfer efficiency for a series of L-section networks, with the power transfer efficiency limited by inductor Q.

They developed an equation for establishing the optimum number of matching stages n to use to match a real resistance R_{source} with a load resistance R_{load}, for a network using inductors all of quality factor Q_L. The power transfer efficiency η is given as a function of n, as:

$$\eta \approx 1 - \frac{n}{Q_L}\sqrt{\left(\frac{R_{\text{source}}}{R_{\text{load}}}\right)^{\frac{1}{n}} - 1} \tag{C.1}$$

The efficiency of such a series of Q_L-limited matching stages can improve if the number of matching stages is increased, particularly when the required voltage transformation ratio is large (as is the case with the load resistance given by the simulated RT5880 antenna at 450 MHz, where $R_{\text{load}} = 0.32\,\Omega$). Increasing the number of matching stages beyond the optimal value incurs unnecessary additional resistive loss, degrading the efficiency.

Applying Equation (C.1) to the case of $R_{\text{source}} = 50\,\Omega$, $R_{\text{load}} = 0.32\,\Omega$, $Q_L = 60$ (from [149] for the 0603CS series inductors used in this project), the optimum number of matching stages is found to be three, with a stated maximum efficiency of 89.5% (Figure C.6). The subsequent discussion is limited to design of a three-stage matching network. The change in load impedance from the published value given in [23] was used since this measurement of the load impedance recorded contemporaneously with the development of the optimal matching code and simulations. In practice, the recorded value of load impedance was found to vary over time, and by equipment configuration. Each one of total measurement bandwidth, number of frequency points, network analyser type and cabling seemed to affect the measured impedance despite following the standard VNA calibration procedure. The target load impedance also varies depending on whether measurement or simulated antennas are being considered: measured values of load impedance found values such as Z_L = 0.25-j26 Ω to 0.32-j13 Ω. Simulation however indicated values such as Z_{ANT} = 0.03-j10 Ω (CST, frequency domain) and 0.03-j26 Ω (CST time domain). Thus, searching for a fixed target impedance for design of the matching network is a challenge in its own right. For the following discussion a target load impedance of 0.32-j13 Ω is assumed and given as a worked example. The technique was also applied to a simulated load impedance of 0.03-j26 Ω (results omitted for brevity), the extremely low load resistance of which produced a requirement for very low inductances of < 0.1 nH, and relatively high capacitances of over 3300 pF[1]. The network also displayed much more extreme sensitivity to feed track parasitic effects. Subsequently, it was subsequently much more difficult to find suitable impedance matching values.

[1] Incidentally, the optimal network for $R_{\text{load}} = 0.03$ requires five stages of matching rather than three. It will be shown shortly that fabrication effects would render successful construction of such a complex network to be, at best, a significant undertaking.

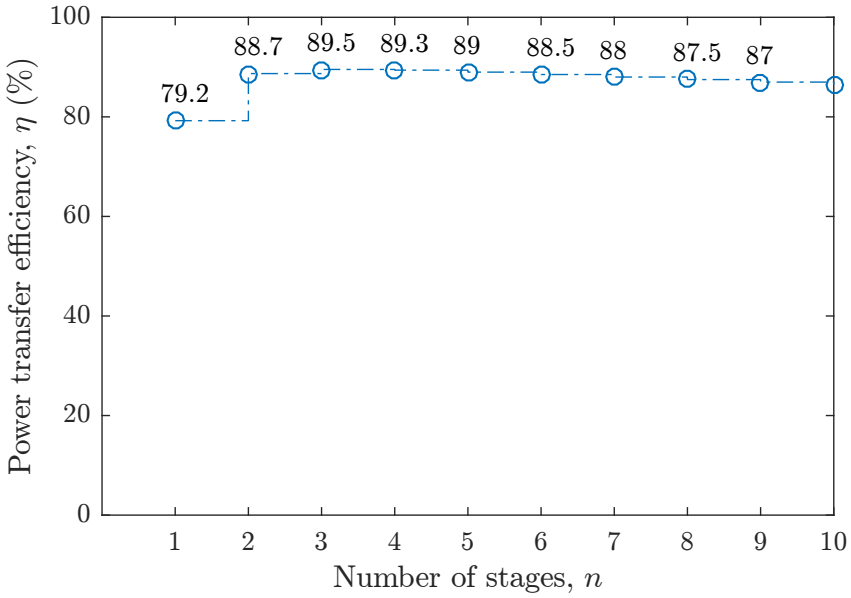

FIGURE C.6: Matching network power transfer efficiency as a function of number of L-section stages of fixed Q.

The maximal power transfer efficiency is achieved when the quality factor Q_i of each stage is equal to the Q of every other stage:

$$Q_i = \sqrt{\left(\frac{R_{\text{source},i}}{R_{\text{load},i}}\right)^{\frac{1}{n}} - 1} \tag{C.2}$$

The input R_{source} of the first stage is 50 Ω. The output R_{load} of the output stage is 0.32 Ω. The intermediate impedance values which achieve ideal matching are given by the Q_i of each stage, from which the reactances of high-pass and low-pass configurations are found using the MATLAB code listing given in Appendix D. Thus, limiting the discussion to a three-stage, low-pass matching network design, a near-optimally efficient matching network described by [157] for matching a resistance of 50 Ω to a resistance of $0.32\,\Omega$ is achieved using the matching network given in Figure C.7.

The low-pass configuration was chosen to address the fact that the RT5880 antenna reactance at 450 MHz has yet to be cancelled out: the three-stage solution provides an inductance value of 0.237 nH for the series inductor in the third stage reading from left to right. However, recalling that the input impedance of the antenna is not just $0.32\,\Omega$ but in fact $0.32 - j13\,\Omega$, increasing the inductance value to 4.827 nH provides the required $+j13\,\Omega$ of reactance at 450 MHz to cancel the reactive component of the antenna mismatch, while the rest of the network provides the real resistance transformation. The simulated S_{11} and S_{21} are given for this network in Figure C.8.

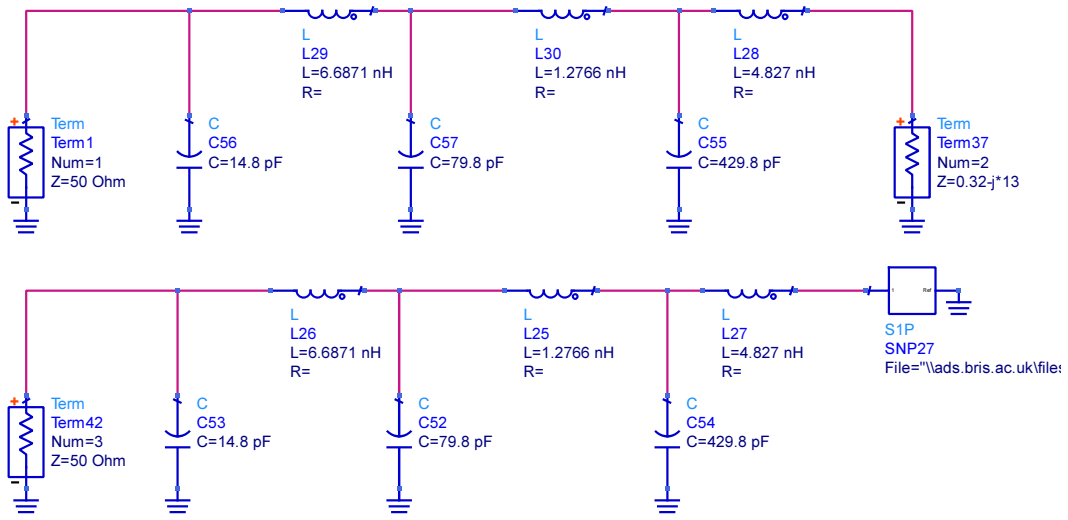

FIGURE C.7: Optimally efficient matching network realised using ideal lossless components in arbitrary precision. Simulation layouts shown for (top) matching into ideal fixed port impedance for convenient estimated S_{21}, and (bottom) matching into measured antenna S-parameter block.

Strictly, the effects of inductor Q_L are not considered in this simulation, hence S_{21} achieves near-perfect efficiency.

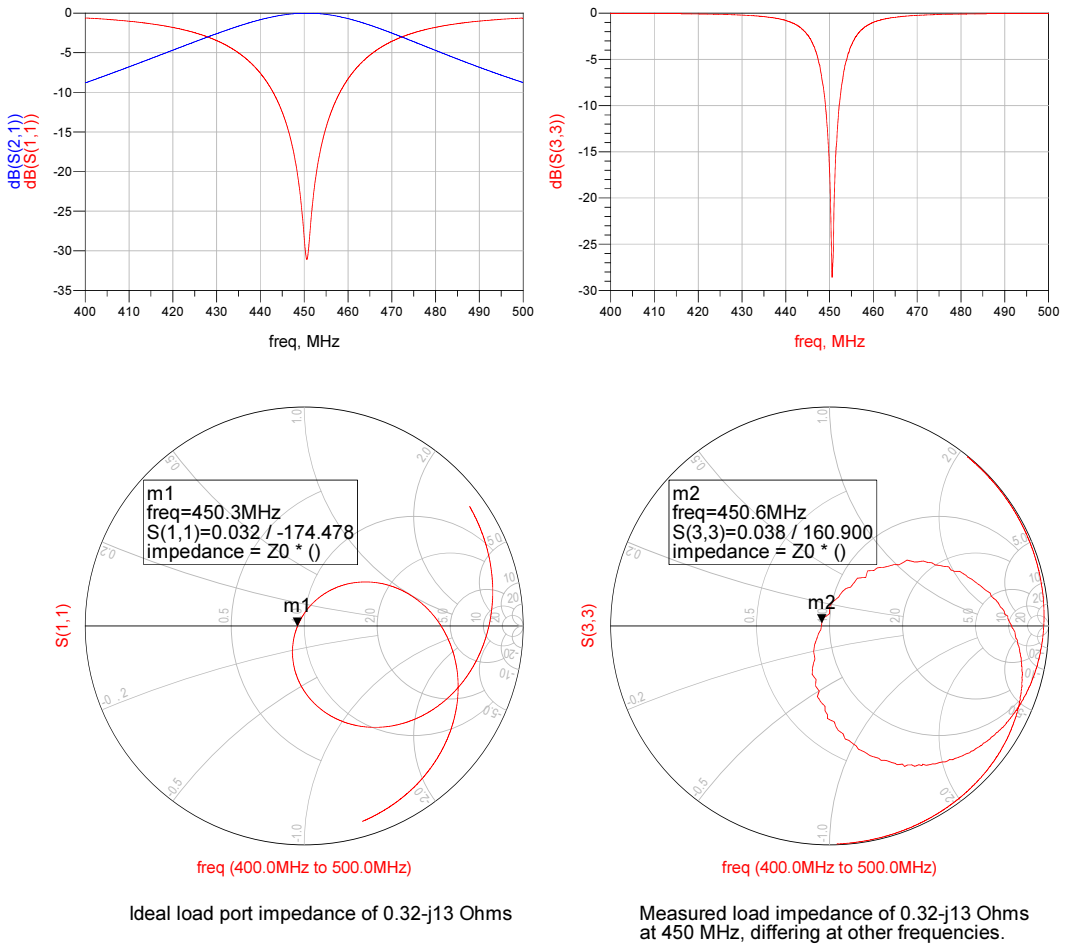

FIGURE C.8: Performance of near-optimal three-stage matching network realised using ideal components. Note that the bandwidth is narrower when matching into the measured S-parameter block of the real antenna (right).

C.3.2 Practical limitations on realisation of efficient, high Q matching network

The previous section presented a method for determining an optimally efficient match between a conventional 50 Ω feed line and a low load resistance of 0.32 Ω. This network was shown to provide excellent matching efficiency using ideal components, however, this assumed that components were available in arbitrary precision. In practice, component values must be selected from those offered by component manufacturers. In addition, eventually feed track effects need to be considered.

Figure C.9 shows the network as before, with arbitrary components switched for the nearest available component values (“preferred” values) in both ideal lossless representation and as manufacturer-provided S-parameter blocks. The performance of the network can be seen to degrade in the absence of components in arbitrary precision (Figure C.10), particularly where S-parameters aare used to represent the lumped components.

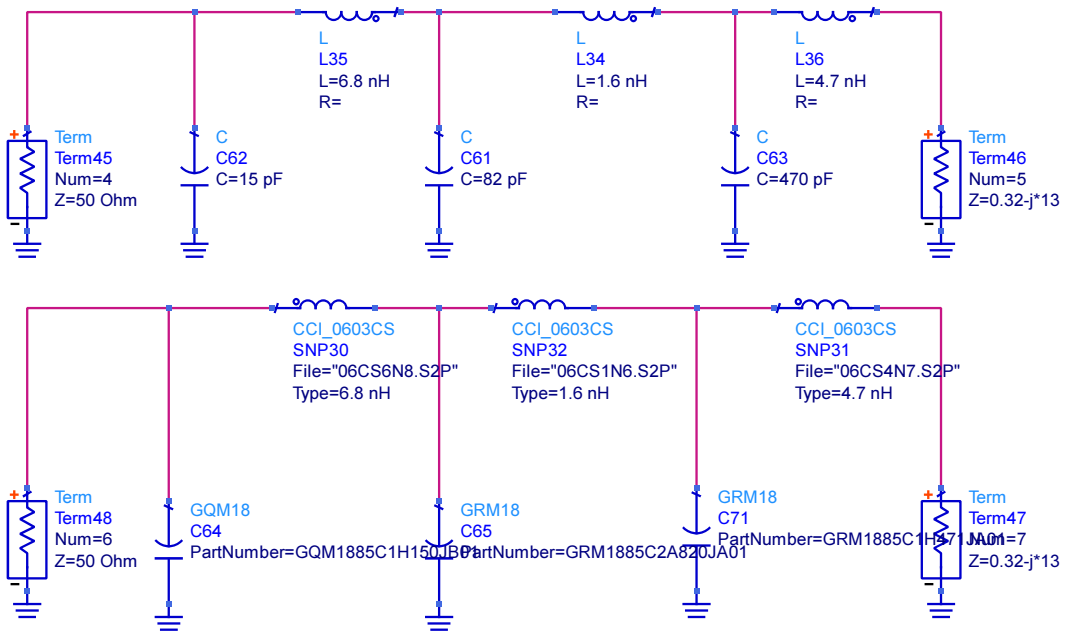

FIGURE C.9: Near-optimally efficient matching network realised using ideal components in nearest-preferred values. Top: ideal components. Bottom: using S-parameter blocks.

Experimentation with switching the values of components revealed two main sources of sensitivity in the matching network. Firstly, changing the value of L3 (third stage series inductor) is directly responsible for the majority of the frequency shifting behaviour in the network. This can be understood from the selection of L3 to cancel the antenna reactance. L3 has an ideal value of 4.827 nH, with only 0.237 nH of this inductance used for real resistance transformation. The sensitivity of the network to the value of L3 could be viewed as a disadvantage in terms of the overall capacity of the network to fail to serve the targeted frequency. On the other hand, the magnitude value of S_{11} was found to be similar regardless of small difference in L3 causing frequency shifting. This indicates that the rest of the network continues to provide real resistance transformation regardless of small deviations in L3, thus the matching network offers future frequency reconfigurability based almost entirely on tuning of L3 alone. However, the sensitivity of the network to the second stage of the network is more problematic. Sensitivity of the matching network to the impedance of the second stage is an unwelcome artefact of the large resistance transformation expected of the matching network.

Finally, realistic feed tracks are considered. The layout given in Figure C.11 uses similarly dimensioned microstrip traces to the network fabricated in Figures C.2–C.4, with the simulated performance given in Figure C.12. As can be seen from the equivalent of S_{21} in Figure C.12, the power throughput of the network in band is low and the reflection coefficient indicates poor matching at the target frequency of 450 MHz. Hence, although the algorithm used to pick starting values for the matching network provided excellent matching under ideal conditions, practical fabrication issues such as parasitic reactance in the components and transmission lines cause

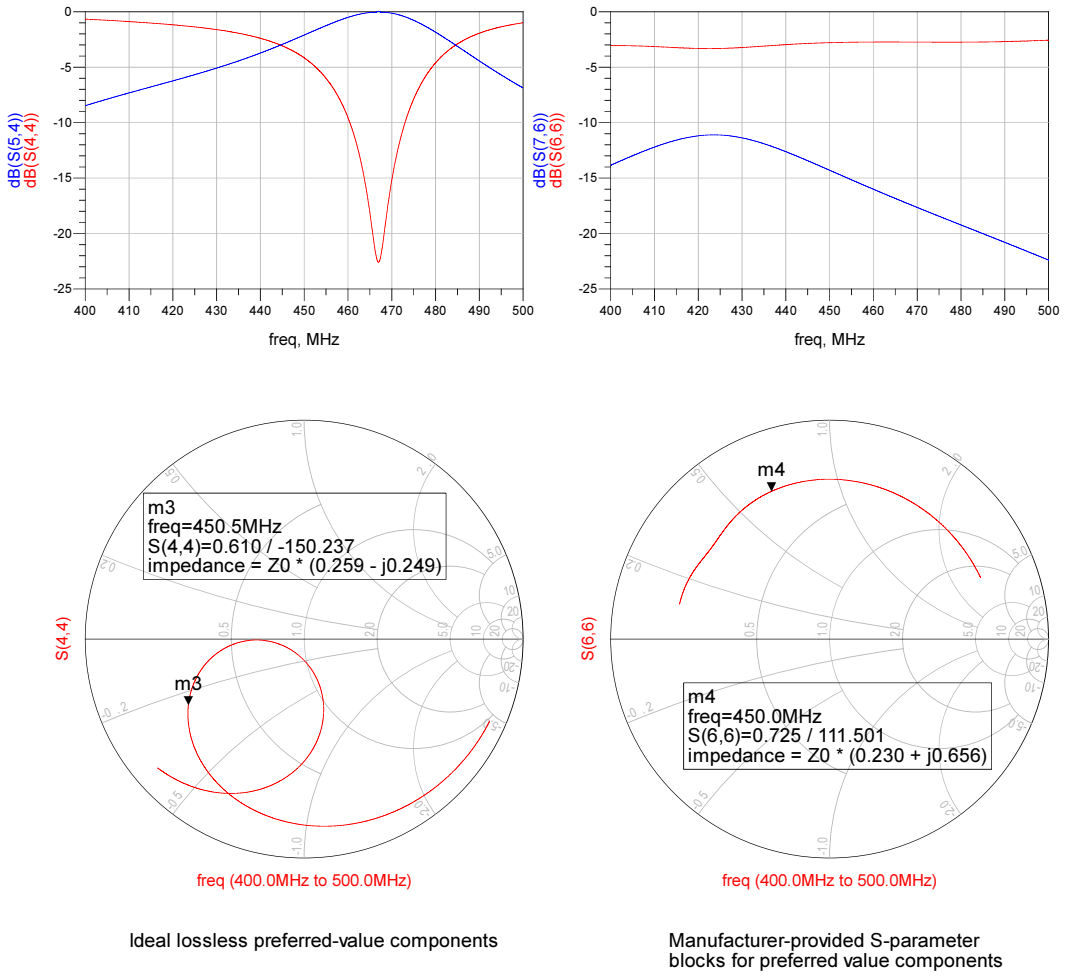

FIGURE C.10: Matching network performance for preferred-value components, using (left) ideal lossless components and (right) S-parameter representations including parasitic effects and losses. Parasitic effects detune the antenna.

further detuning of the network. The feed track effects transpired to be particularly difficult to correct during attempts to remove the additional inductance.

The conclusion of this appendix therefore is that even with algorithms for impedance matching solutions which are optimal in some sense, an antenna in the very electrically small regime far from resonance is extremely difficult to impedance match in practice.

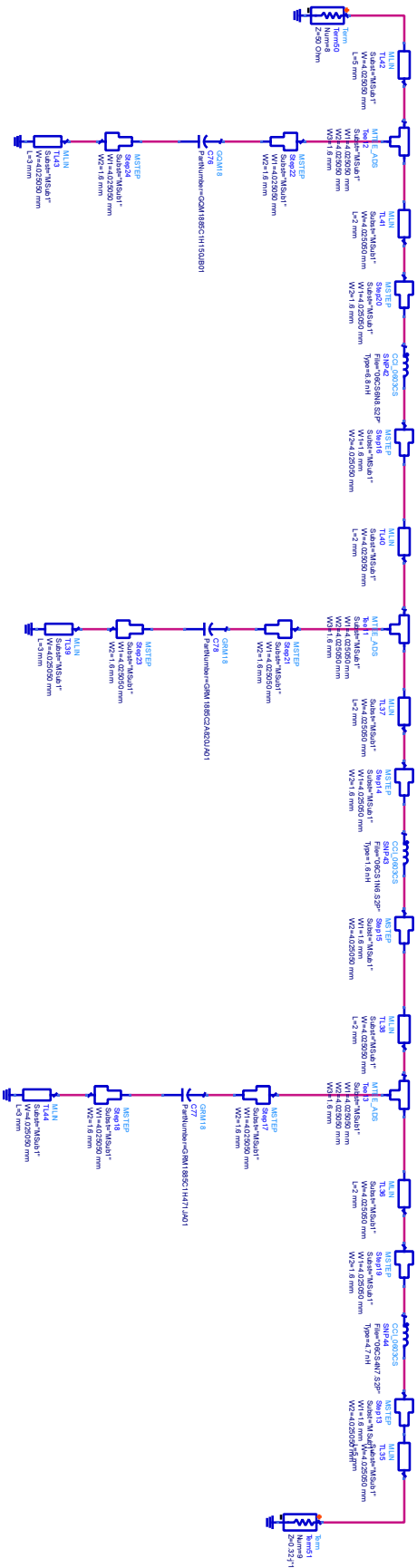

FIGURE C.11: Simulation layout for matching network with realistic feed tracks and S-parameter based components.

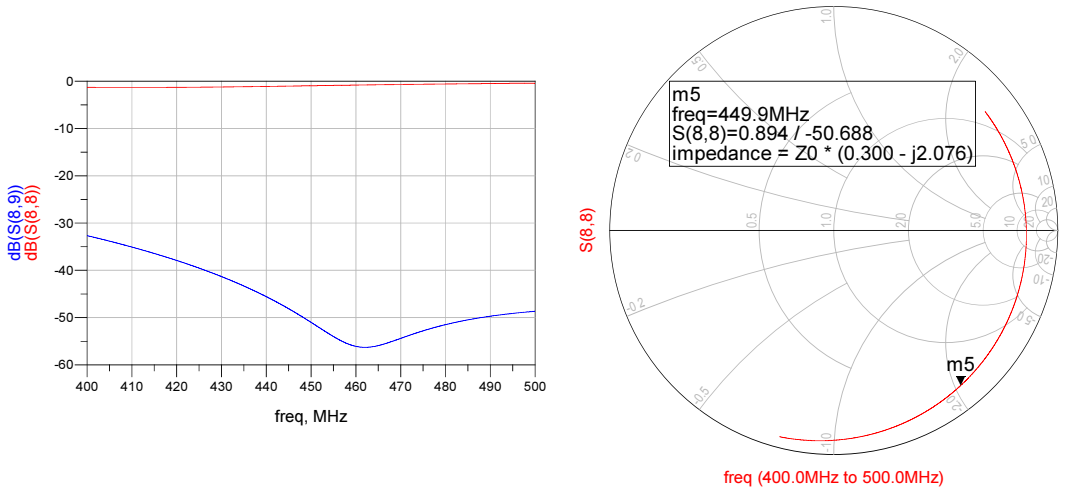

FIGURE C.12: Matching network performance for realistic simulation including feed tracks and parasitic effects of components.

Appendix D

Code listing for optimal impedance matching

This appendix provides a code listing for the MATLAB script used to select the optimal values of impedance matching components of a network of N stages, first described in Han and Perreault [157] and applied to an electrically small antenna in Appendix C.

The code is written on the assumption that the source resistance is higher than the load resistance, and as such the parallel elements are all in parallel with the source resistance, while the series elements occur in series with the load resistance of each stage.

```
function [ void ] = OptMatch( freq,n,Q_ind,Rp,Rs )
%OPTMATCH Optimal narrowband matching script
%   For a given match between a source resistance and a load resistance,
%   the optimally _efficient_ matching solution can contain multiple
%   stages driven by the Q of any inductor used to obtain the match. This
%   function takes frequency, Q_inductor, the source and load resistances
%   as arguments. In version 1, the user specifies the number of stages
%   required. The script prints the optimal Q at each stage, the expected
%   optimal efficiency, and L/C values for low-pass / high-pass
%   configurations. The background to this function is described in Han and
%   Perreault, "Analysis and Design of High Efficiency Matching Network,"
%   IEEE Transactions on Power Electronics, Vol 21 No. 5, Sept 2006.
%
% Oliver N. James, 16/11/2017

%% 0. Set up variables.

omega = 2*pi*freq;

disp('Source resistance = ');
disp(Rp);
disp('Load resistance = ')
disp(Rs);
```

```
disp('Number of stages = ');
disp(n);
disp('Matching frequency = ');
disp(freq);
disp('Q for inductor = ')
disp(Q_ind);

%% 1. Calculate optimal number of stages

% Version 1 just use n = 3

%% 2. Calculate efficiency given by this number of stages

eff = 1 - n/Q_ind * sqrt( (Rp/Rs)^(1/n)  - 1);

disp('Efficiency upper limit = ');
disp(eff);

%% 3. Calculate Q_i, the optimal value of Q for each matching stage.

Q_i = sqrt((Rp/Rs)^(1/n) - 1);
disp('Q_i, Q of each matching stage:');
disp(Q_i);

%% 4. Determine intermediate resistances
% Each stage matches its source resistance (Rp) to a load resistance. These
% are only known in advance for first and last stages, for intermediate
% stages, they need to be calculated from Q_i.

    for stage = 1:n

        % Calculate source resistance
        if stage == 1
            R_source(stage) = Rp;
        else
            R_source(stage) = R_load(stage-1); % The source resistance is the
    load
                                        % resistance of the previous stage.
        end

        % Calculated load resistance
        if stage == n
            R_load(stage) = Rs;
        else
            R_load(stage) = 1/((Q_i^2 + 1)/R_source(stage)); % May want to read
    this
                                                    % out into file later.
        end
    end % End of intermediate resistance calculation

%% 5. Calculate series and shunt reactances of each stage.
% Note that Q_series and Q_shunt both need to be equal to Q_i.

for stage = 1:n
```

```
    X_series(stage) = Q_i * R_load(stage);
    X_shunt(stage) = R_source(stage)/Q_i;

end

%% 6. Calculate network values

% Low pass (all series L, shunt C)
for stage = 1:n

    L_lowpass(stage) = X_series(stage)/omega;
    C_lowpass(stage) = 1/(omega*X_shunt(stage));

end

% High pass (all series C, shunt L)
for stage = 1:n

    L_hipass(stage) = X_shunt(stage)/omega;
    C_hipass(stage) = 1/(omega*X_series(stage));

end

%% 7. Done calculating. Output L and C in a format useful to designer

% Display output by network type, then by stage

disp('Low pass network values:');
disp('Series L values, nH:');
disp(L_lowpass./1e-9);
disp('Shunt C values, pF');
disp(C_lowpass./1e-12);
disp('');
disp('High pass network values:');
disp('Series C values, pF:');
disp(C_hipass./1e-12);
disp('Shunt L values, nH:');
disp(L_hipass./1e-9);
disp('');
disp('Done. Try above values in a simulator.');

end
```

Appendix E

Achievable tuning envelope in small loop antenna

In Chapter 5, tuneable loop electrically small antennas (ESAs) were designed, fabricated and characterised. These antennas all shared geometrically identical layouts in terms of the dimensions of the feed loop and main tuneable radiating loop. However, their accessible tuning ranges (in integrated impedance bandwidth terms) all had different values due to the use of different substrates and lumped components.

Here, the simulated maximum achiveable tuning range for the loop structure is shown for RT5880 and FR-4 substrates, using both the trimmer- and varactor-tuned loop layouts described in Chapter 5. To test what is possible in terms of tuning range given only the limitation of the conductor layout and lumped component values, the allowable tuning capacitance C_{var} (Figure 5.2) has been relaxed to unrealistic limits. Tuning sweeps depicted in Figure E.1 are given for capacitance values ranging from 0.01 pF (unrealistically low) to 10 pF (realistic but so high that the realised operating frequency is very low compared to the intended UHF band limit). In Table E.1, the realised -3 dB tuning bandwidth can be seen to be much lower than that potentially achiveable given the loop dimensions and unrealistically low tuning capacitances.

TABLE E.1: Maximum -3 dB tuning range of ESA loops given with relaxed tuneable C_{var} limits.

Substrate	Capacitor type	Freq. range (max. achievable, sim., MHz)	Freq. range (meas., MHz)	-3 dB imp. BW (max. achievable, %)	-3 dB imp. BW. (meas., %)
RT5880	Trimmer	338–890	330–616	99.8	30.2
RT5880	Varactor	367–860	212–522	68.4	42.2
FR-4	Trimmer	265–793	324–564	89.9	27.0
FR-4	Varactor	272–758	201–496	80.4	42.3

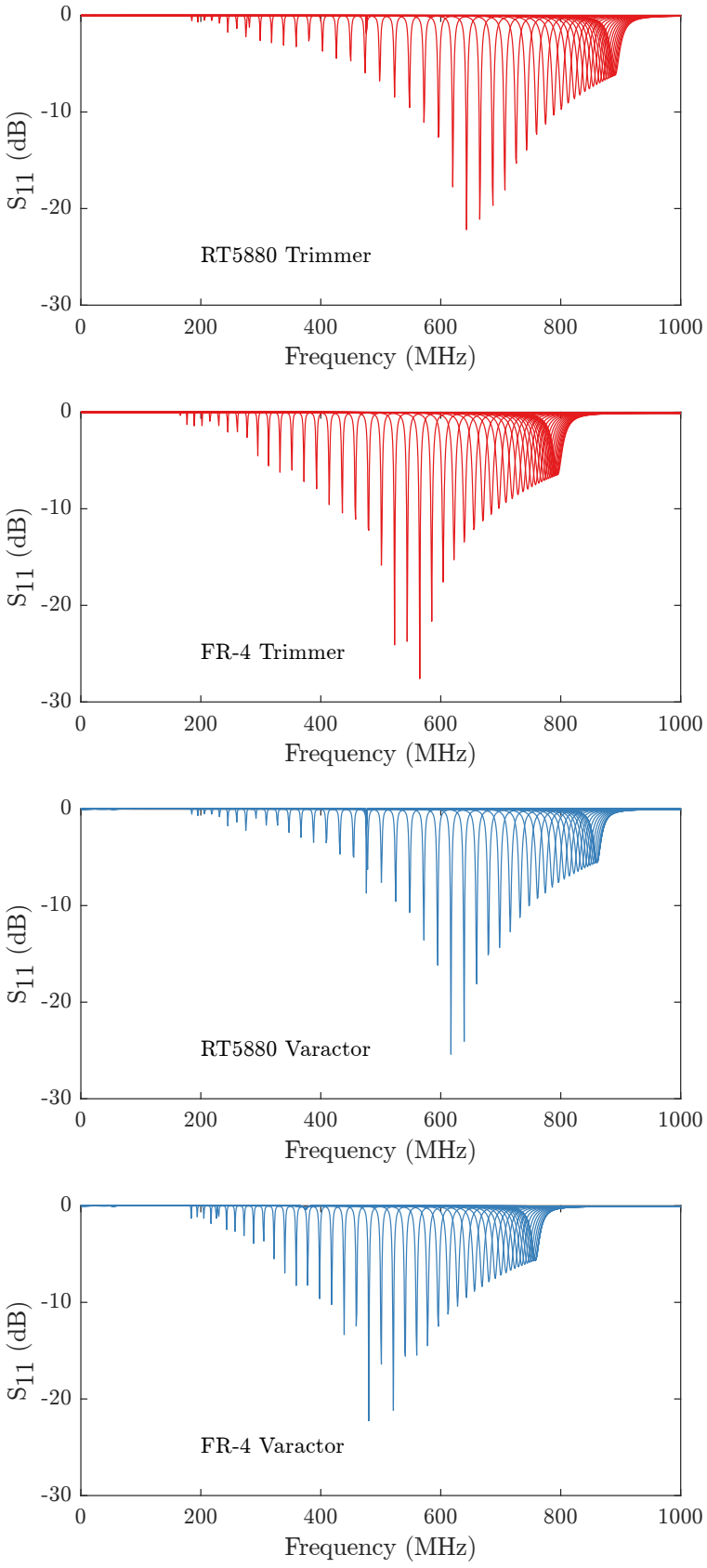

FIGURE E.1: Simulated maximum impedance tuning range for loop ESAs, permitting unrealistic/unhelpful values of tuning capacitance. Low frequency given by C_{var} = 10 pF, high frequency given by C_{var} = 0.01 pF.

Appendix F

Anechoic chamber images

To help the reader better visualise the anechoic chamber testing set up, photographs taken inside the chamber are presented in Figure F.1. The chamber measures approximately $8 \times 5 \times 4$ metres, with transmission and reception antenna separation of 5.4 metres.

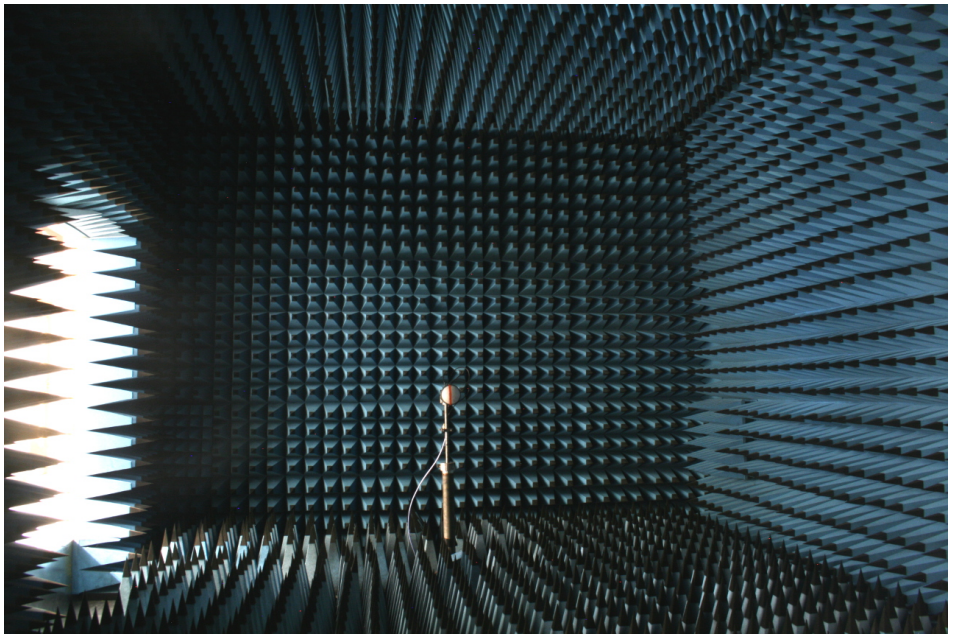

View towards transmitter end. Antenna statically mounted is a Flann DP240 horn antenna.

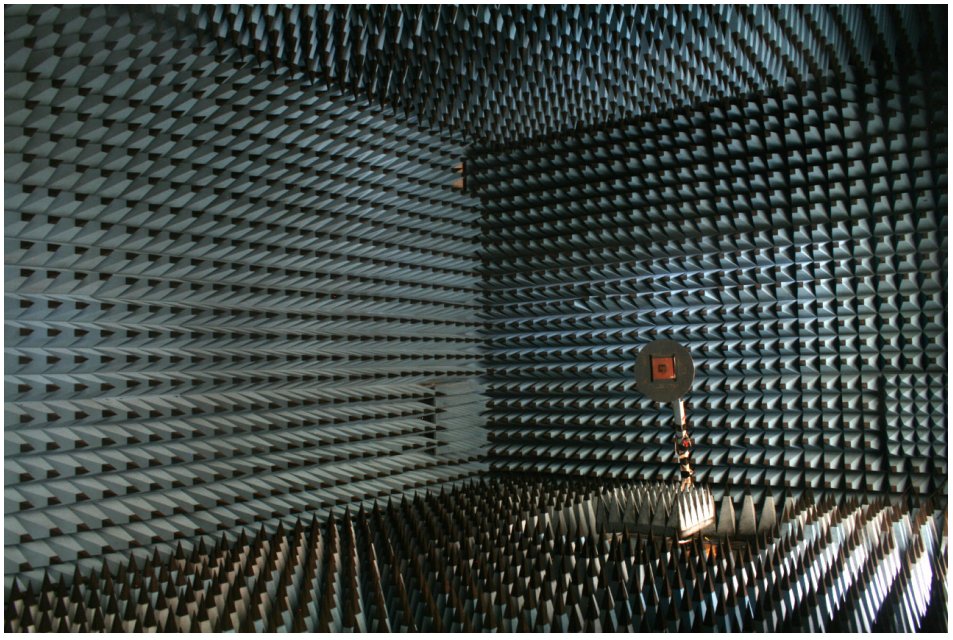

View towards receiver end. Antenna-under-test is shown mounted on 3D rotating positioner.

FIGURE F.1: Photographs of anechoic chamber general set up.

References

[1] Ofcom. (2008) The Communications Market Report (UK, 2008). [Online]. Available: http://webarchive.nationalarchives.gov.uk/20160703014921/http://stakeholders.ofcom.org.uk/market-data-research/market-data/communications-market-reports/cmr08/

[2] ——. (2014) The Communications Market Report (UK, 2014). [Online]. Available: https://www.ofcom.org.uk/__data/assets/pdf_file/0031/19498/2014_uk_cmr.pdf

[3] ——. (2018) The Communications Market Report (UK, 2018). [Online]. Available: https://www.ofcom.org.uk/research-and-data/multi-sector-research/cmr/cmr-2018/report

[4] Office for National Statistics. (2018) Population estimates time series dataset (UKPOP). [Online]. Available: https://www.ons.gov.uk/peoplepopulationandcommunity/populationandmigration/populationestimates/timeseries/ukpop/pop

[5] A. Tanenbaum and D. Wetherall, *Computer Networks*, 5th ed. Prentice Hall, 2011.

[6] A. Zanella, N. Bui, A. Castellani, L. Vangelista, and M. Zorzi, "Internet of Things for smart cities," *IEEE Internet of Things Journal*, vol. 1, no. 1, pp. 22–32, Feb 2014.

[7] University College London, London Wildlife Trust and the Bat Conservation Trust. (2017) Nature-Smart Cities: Urban Bat Life. [Online]. Available: http://naturesmartcities.com

[8] Intel. (2018) A Guide to the Internet of Things. [Online]. Available: https://www.intel.co.uk/content/www/uk/en/internet-of-things/infographics/guide-to-iot

[9] GrowthEnabler. (2017) Market Pulse Report, Internet of Things (IoT). [Online]. Available: https://growthenabler.com/reports/IOT

[10] Statista. (2016) Internet of Things (IoT) connected devices installed base worldwide from 2015 to 2025. [Online]. Available: https://www.statista.com/statistics/471264/iot-number-of-connected-devices-worldwide

[11] "Radio transmission and reception, rev. 8.20.0," *3GPP Technical Specification TS05.05*, Nov 2005.

[12] "Evolved universal terrestrial access (E-UTRA); user equipment (UE) radio transmission and reception, rev. 14.2.0," *3GPP Technical Specification TS36.101*, Jan 2017.

[13] International Telecommunication Union. (2012) Radio Regulations: Volume I, Article 2.1. [Online]. Available: http://www.itu.int/pub/R-REG-RR-2012

[14] Microsoft. (2015) Project Belgrade [provision of Internet to low-income households in Cambridge]. [Online]. Available: https://www.microsoft.com/en-us/research/project/project-belgrade

[15] Ofcom. (2017) UK Frequency Allocation Table 2017. [Online]. Available: https://www.ofcom.org.uk/__data/assets/pdf_file/0016/103309/uk-fat-2017.pdf

[16] Federal Communications Commission, "Unlicensed Operation in the TV Broadcast Bands/Additional Spectrum for Unlicensed Devices Below 900 MHz and in the 3 GHz Band," FCC (USA), Tech. Rep. FCC 12-36, Apr. 2012.

[17] J. Cook, D. Nuccitelli, S. A. Green, M. Richardson, B. Winkler, R. Painting, R. Way, P. Jacobs, and A. Skuce, "Quantifying the consensus on anthropogenic global warming in the scientific literature," *Environmental Research Letters*, vol. 8, no. 2, p. 024024, 2013. [Online]. Available: http://stacks.iop.org/1748-9326/8/i=2/a=024024

[18] J. Cook, N. Oreskes, P. T. Doran, W. R. L. Anderegg, B. Verheggen, E. W. Maibach, J. S. Carlton, S. Lewandowsky, A. G. Skuce, S. A. Green, D. Nuccitelli, P. Jacobs, M. Richardson, B. Winkler, R. Painting, and K. Rice, "Consensus on consensus: a synthesis of consensus estimates on human-caused global warming," *Environmental Research Letters*, vol. 11, no. 4, p. 048002, 2016. [Online]. Available: http://stacks.iop.org/1748-9326/11/i=4/a=048002

[19] H. A. Wheeler, "Fundamental limitations of small antennas," *Proceedings of the IRE*, pp. 1479–1484, Dec 1947.

[20] Oliver James and Geoff Hilton and Mark Beach, "Efficiency-based approach to quantifying 'tuneability' performance in frequency-agile narrowband antennas," *accepted for publication in IET Microwaves, Antennas & Propgation Journal*, 2019.

[21] O. J. Norman, G. Hilton, and M. Beach, "Measurement of efficiency degradation due to external detuning of a tunable patch antenna," in *2016 IEEE International Symposium on Antennas and Propagation (APSURSI)*, June 2016, pp. 2145–2146.

[22] O. N. James, G. Hilton, and M. Beach, "Hexaferrite substrate versus impedance matching for tuneable patch antenna miniaturisation," in *2018 12th European Conference on Antennas and Propagation (EuCAP 2018)*, London, United Kingdom (Great Britain), April 2018.

[23] O. James, G. Hilton, and M. Beach, "Radiation efficiency analysis of balanced-impedance hexaferrite substrate for antenna miniaturisation," in *The Loughborough Antennas & Propagation Conference 2017 (LAPC)*, November 2017, pp. 1–5.

[24] C. Balanis, *Antenna Theory: Analysis and Design*, 3rd ed. Wiley, 2003.

[25] J. H. Poynting, "On the transfer of energy in the electromagnetic field," *Philosophical Transactions of the Royal Society of London*, vol. 175, pp. 343–361, 1884. [Online]. Available: http://rstl.royalsocietypublishing.org/content/175/343.short

[26] D. M. Pozar, *Microwave Engineering*, 4th ed. Wiley, 2012.

[27] S. C. D. Barrio, A. Morris, and G. F. Pedersen, "MEMS Tunable antennas to address LTE 600 MHz-bands," in *2015 9th European Conference on Antennas and Propagation (EuCAP)*, May 2015, pp. 1–4.

[28] L. J. Chu, "Physical limitations of omni-directional antennas," *Journal of Applied Physics*, vol. 19, pp. 1163–1175, Dec 1948.

[29] J. S. McLean, "A re-examination of the fundamental limits on the radiation Q of electrically small antennas," *IEEE Transactions on Antennas and Propagation*, vol. 44, no. 5, pp. 672–676, May 1996.

[30] H. L. Thal, "New radiation Q limits for spherical wire antennas," *IEEE Transactions on Antennas and Propagation*, vol. 54, no. 10, pp. 2757–2763, Oct 2006.

[31] S. R. Best, "Electrically small resonant planar antennas: Optimizing the quality factor and bandwidth," *IEEE Antennas and Propagation Magazine*, vol. 57, no. 3, pp. 38–47, Jun 2015.

[32] P. Bhartia and I. Bahl, "A frequency agile microstrip antenna," in *1982 Antennas and Propagation Society International Symposium*, vol. 20, May 1982, pp. 304–307.

[33] N. Haider, M. S. O. Alink, D. Caratelli, E. A. M. Klumperink, and A. G. Yarovoy, "Frequency-tunable antenna by input-impedance-tunable CMOS RF-frontend," in *2013 European Microwave Integrated Circuit Conference*, Oct 2013, pp. 308–311.

[34] S. Yao, K. Bao, X. Liu, and S. V. Georgakopoulos, "Tunable UHF origami spring antenna with actuation system," in *2017 IEEE International Symposium on Antennas and Propagation USNC/URSI National Radio Science Meeting*, July 2017, pp. 325–326.

[35] F. Wang and T. Arslan, "Microfluidic frequency tunable three-dimensional printed antenna," in *2017 IEEE MTT-S International Microwave Workshop Series on Advanced Materials and Processes for RF and THz Applications (IMWS-AMP)*, Sept 2017, pp. 1–3.

[36] A. Dey, R. Guldiken, and G. Mumcu, "Microfluidically reconfigured wideband frequency-tunable liquid-metal monopole antenna," *IEEE Transactions on Antennas and Propagation*, vol. 64, no. 6, pp. 2572–2576, June 2016.

[37] W. Su, B. Cook, M. Tentzeris, C. Mariotti, and L. Roselli, "A novel inkjet-printed microfluidic tunable coplanar patch antenna," in *2014 IEEE Antennas and Propagation Society International Symposium (APSURSI)*, July 2014, pp. 858–859.

[38] Q. Gu, J. R. D. Luis, A. S. Morris, and J. Hilbert, "An analytical algorithm for pi-network impedance tuners," *IEEE Transactions on Circuits and Systems I: Regular Papers*, vol. 58, no. 12, pp. 2894–2905, Dec 2011.

[39] W.-W. Lee and B. Jang, "A DVC switchable antenna technique for the hand effect in mobile terminals," *Microwave and Optical Technology Letters*, vol. 57, no. 11, pp. 2614–2617, 2015. [Online]. Available: http://dx.doi.org/10.1002/mop.29390

[40] S. Ershadi, A. H. Abdelrahman, M. Liang, X. Yu, H. Xin, and S. Ershadi, "A novel reconfigurable broadband antenna for cognitive radio systems," in *2016 IEEE International Symposium on Antennas and Propagation (APSURSI)*, June 2016, pp. 1799–1800.

[41] I. Vasilev, E. Foroozanfard, and B. K. Lau, "Adaptive impedance matching performance of MIMO terminals with different bandwidth and isolation properties in realistic user scenarios," in *2013 7th European Conference on Antennas and Propagation (EuCAP)*, April 2013, pp. 2590–2594.

[42] G. Mankaruse and R. R. Mansour, "Practical approach - tunable antennas and tunable matching networks," in *2015 IEEE International Symposium on Antennas and Propagation USNC/URSI National Radio Science Meeting*, July 2015, pp. 2383–2384.

[43] S. Kishimoto and M. Higaki, "Evaluation of bandwidth for tunable antennas with physical limitations on small antennas," in *2016 International Symposium on Antennas and Propagation (ISAP)*, Oct 2016, pp. 974–975.

[44] L. Huang and P. Russer, "Electrically tunable antenna design procedure for mobile applications," *IEEE Transactions on Microwave Theory and Techniques*, vol. 56, no. 12, pp. 2789–2797, Dec 2008.

[45] P. R. Rogers, G. S. Hilton, and I. J. Craddock, "Performance metrics for UWB antennas," in *11th International Symposium on Antenna Technology and Applied Electromagnetics [ANTEM 2005]*, June 2005, pp. 1–4.

[46] W. Thompson, R. Cepeda, G. Hilton, M. A. Beach, and S. Armour, "An improved antenna mounting for ultra-wideband on-body communications and channel characterization,"

IEEE Transactions on Microwave Theory and Techniques, vol. 59, no. 4, pp. 1102–1108, April 2011.

[47] A. Morris, S. C. D. Barrio, J. Shin, V. Steel, and G. F. Pedersen, "Tunable antennas for mobile devices: Achieving high performance in compelling form factors," in *2014 IEEE MTT-S International Microwave Symposium (IMS2014)*, June 2014, pp. 1–4.

[48] WiSpry Inc., "WS1050 Digitally Tunable Capacitor Array," *Preliminary Data Sheet v1.7*, 2014.

[49] Infineon, "BB833 Varactor," *Data Sheet*, 2009. [Online]. Available: https://www.infineon.com/dgdl/Infineon-BB833SERIES-DS-v01_01-en.pdf?fileId=db3a304313d846880113d969a38b0112

[50] M. Pelosi, O. Franek, M. B. Knudsen, M. Christensen, and G. F. Pedersen, "A grip study for talk and data modes in mobile phones," *IEEE Transactions on Antennas and Propagation*, vol. 57, no. 4, pp. 856–865, April 2009.

[51] M. Pelosi, O. Franek, M. B. Knudsen, G. F. Pedersen, and J. B. Andersen, "Antenna proximity effects for talk and data modes in mobile phones," *IEEE Antennas and Propagation Magazine*, vol. 52, no. 3, pp. 15–27, June 2010.

[52] P. Bahramzy and G. Pedersen, "Detuning effect study of high-Q mobile phone antennas," in *Antennas and Propagation (EuCAP), 2015 9th European Conference on*, April 2015, pp. 1–4.

[53] J. de Mingo, A. Valdovinos, A. Crespo, D. Navarro, and P. Garcia, "An RF electronically controlled impedance tuning network design and its application to an antenna input impedance automatic matching system," *IEEE Transactions on Microwave Theory and Techniques*, vol. 52, no. 2, pp. 489–497, Feb 2004.

[54] W. N. Allen and D. Peroulis, "Bandwidth-optimal single-tunable-element matching network for antenna tuning in mobile handsets," in *2011 IEEE MTT-S International Microwave Symposium*, June 2011, pp. 1–1.

[55] J. L. Buckley, K. G. McCarthy, D. Gaetano, L. Loizou, B. O'Flynn, and C. O'Mathuna, "Design of a compact, fully-autonomous 433 MHz tunable antenna for wearable wireless sensor applications," *IET Microwaves, Antennas Propagation*, vol. 11, no. 4, pp. 548–556, 2017.

[56] O. Rostbakken, G. S. Hilton, and C. J. Railton, "Adaptive feedback frequency tuning for microstrip patch antennas," in *Antennas and Propagation, 1995., Ninth International Conference on (Conf. Publ. No. 407)*, Apr 1995, pp. 166–170 vol.1.

[57] A. Baroni, P. Nepa, and H. Rogier, "Wearable self-tuning antenna for emergency rescue operations," *IET Microwaves, Antennas Propagation*, vol. 10, no. 2, pp. 173–183, 2016.

[58] R. Valkonen, C. Icheln, and P. Vainikainen, "Power dissipation in mobile antenna tuning circuits under varying impedance conditions," *IEEE Antennas and Wireless Propagation Letters*, vol. 11, pp. 37–40, 2012.

[59] S. E. Sussman-Fort and R. M. Rudish, "Non-Foster impedance matching of electrically-small antennas," *IEEE Transactions on Antennas and Propagation*, vol. 57, no. 8, pp. 2230–2241, Aug 2009.

[60] S. E. Sussman-Fort, "Non-Foster vs. active matching of an electrically-small receive antenna," in *2010 IEEE Antennas and Propagation Society International Symposium*, July 2010, pp. 1–4.

[61] K. Karlsson and J. Carlsson, "Non-Foster networks for improvement of radiation efficiency and effective diversity gain of a multi-port antenna," in *Proceedings of the Fourth European Conference on Antennas and Propagation*, April 2010, pp. 1–4.

[62] C. R. White and M. W. Yung, "An S-band negative-inductance integrated circuit," in *2015 IEEE MTT-S International Microwave Symposium*, May 2015, pp. 1–4.

[63] P. Jin and R. W. Ziolkowski, "Broadband, efficient, electrically small metamaterial-inspired antennas facilitated by active near-field resonant parasitic elements," *IEEE Transactions on Antennas and Propagation*, vol. 58, no. 2, pp. 318–327, Feb 2010.

[64] H. Mirzaei and G. V. Eleftheriades, "A wideband metamaterial-inspired compact antenna using embedded non-Foster matching," in *2011 IEEE International Symposium on Antennas and Propagation (APSURSI)*, July 2011, pp. 1950–1953.

[65] W. Wang, J. Geng, R. Jin, X. Liang, and R. W. Ziolkowski, "Design of a 600 MHz non-Foster dipole," in *2014 International Workshop on Antenna Technology: Small Antennas, Novel EM Structures and Materials, and Applications (iWAT)*, March 2014, pp. 351–354.

[66] H. Jaafar, D. Lemur, S. Collardey, and A. Sharaiha, "Wideband electrically small antenna internally loaded with non-Foster circuit," in *2018 18th International Symposium on Antenna Technology and Applied Electromagnetics (ANTEM)*, Aug 2018, pp. 1–2.

[67] T. Shi, M. Tang, Z. Wu, H. Xu, and R. W. Ziolkowski, "Improved signal-to-noise ratio, bandwidth-enhanced electrically small antenna augmented with internal non-Foster elements," *IEEE Transactions on Antennas and Propagation*, vol. 67, no. 4, pp. 2763–2768, April 2019.

[68] Q. Tang and H. Xin, "Non-Foster circuit for wideband matching of high frequency helical antenna," in *2017 IEEE MTT-S International Microwave Symposium (IMS)*, June 2017, pp. 352–355.

[69] M. A. Collett, C. D. Gamlath, and M. Cryan, "An optically tunable cavity-backed slot antenna," *IEEE Transactions on Antennas and Propagation*, vol. 65, no. 11, pp. 6134–6139, Nov 2017.

[70] Z. Zheng, H. Zhang, J. Q. Xiao, and F. Bai, "Low loss NiZn/Co_2Z composite ferrite with almost equal values of permeability and permittivity for antenna applications," *IEEE Transactions on Magnetics*, vol. 49, no. 7, pp. 4214–4217, July 2013.

[71] A. Tagantsev, V. Sherman, K. Astafiev, J. Venkatesh, and N. Setter, "Ferroelectric materials for microwave tunable applications," *Journal of Electroceramics*, vol. 11, no. 1, pp. 5–66, Sep 2003. [Online]. Available: https://doi.org/10.1023/B:JECR.0000015661.81386.e6

[72] P. Bao, T. J. Jackson, X. Wang, and M. J. Lancaster, "Barium strontium titanate thin film varactors for room-temperature microwave device applications," *Journal of Physics D: Applied Physics*, vol. 41, no. 6, p. 063001, March 2008.

[73] C. Christodoulou, Y. Tawk, S. Lane, and S. Erwin, "Reconfigurable antennas for wireless and space applications," *Proceedings of the IEEE*, vol. 100, no. 7, pp. 2250–2261, July 2012.

[74] L. Liu and R. J. Langley, "Liquid crystal tunable microstrip patch antenna," *Electronics Letters*, vol. 44, no. 20, pp. 1179–1180, September 2008.

[75] K. Buell, H. Mosallaei, and K. Sarabandi, "A substrate for small patch antennas providing tunable miniaturization factors," *IEEE Transactions on Microwave Theory and Techniques*, vol. 54, no. 1, pp. 135–146, Jan 2006.

[76] M. Fallahpour and R. Zoughi, "Antenna miniaturization techniques: A review of topology- and material-based methods," *IEEE Antennas and Propagation Magazine*, vol. 60, no. 1, pp. 38–50, Feb 2018.

[77] A. Alu, F. Bilotti, N. Engheta, and L. Vegni, "Subwavelength, compact, resonant patch antennas loaded with metamaterials," *IEEE Transactions on Antennas and Propagation*, vol. 55, no. 1, pp. 13–25, Jan 2007.

[78] F. Bilotti, A. Alu, and L. Vegni, "Design of miniaturized metamaterial patch antennas with μ-negative loading," *IEEE Transactions on Antennas and Propagation*, vol. 56, no. 6, pp. 1640–1647, June 2008.

[79] Rogers Corporation, "RT/Duroid 6006/6010LM High Frequency Laminates," *6006/6010 datasheet*, 2015.

[80] R. C. Pullar, Y. Zhang, L. Chen, S. Yang, J. R. Evans, P. K. Petrov, A. N. Salak, D. A. Kiselev, A. L. Kholkin, V. M. Ferreira, and N. M. Alford, "Manufacture and measurement of combinatorial libraries of dielectric ceramics Part II: Dielectric Measurements of $Ba_{1-x}Sr_xTiO_3$ Libraries," *Journal of the European Ceramic Society*, vol. 27, no. 16, pp. 4437 – 4443, 2007. [Online]. Available: http://www.sciencedirect.com/science/article/pii/S0955221907003408

[81] R. Hansen and M. Burke, "Antennas with magneto-dielectrics," *Microwave and Optical Technology Letters*, vol. 26, no. 2, pp. 75–78, Jul 2000.

[82] Z. Zheng, Q. Feng, Q. Xiang, Z. Di, and V. G. Harris, "Low-loss NiZnCo ferrite processed at low sintering temperature with matching permeability and permittivity for miniaturization of VHF-UHF antennas," *Journal of Applied Physics*, vol. 121, no. 6, p. 063901, 2017.

[83] Z. Su, Q. Li, X. Wang *et al.*, "Tunable permittivity and permeability of low loss Z + Y-type ferrite composites for ultra-high frequency applications," *Journal of Applied Physics*, vol. 117, no. 17, p. 17E506, 2015.

[84] P. M. T. Ikonen, K. N. Rozanov, A. V. Osipov, P. Alitalo, and S. A. Tretyakov, "Magnetodielectric substrates in antenna miniaturization: Potential and limitations," *IEEE Transactions on Antennas and Propagation*, vol. 54, no. 11, pp. 3391–3399, Nov 2006.

[85] R. C. Pullar, "Hexagonal ferrites: A review of the synthesis, properties and applications of hexaferrite ceramics," *Progress in Materials Science*, vol. 57, no. 7, pp. 1191 – 1334, 2012. [Online]. Available: http://www.sciencedirect.com/science/article/pii/S0079642512000369

[86] H. Mosallaei and K. Sarabandi, "Magneto-dielectrics in electromagnetics: concept and applications," *IEEE Transactions on Antennas and Propagation*, vol. 52, no. 6, pp. 1558–1567, June 2004.

[87] Z. Su, H. Chang, X. Wang, A. S. Sokolov, B. Hu, Y. Chen, and V. G. Harris, "Low loss factor Co_2Z ferrite composites with equivalent permittivity and permeability for ultra-high frequency applications," *Applied Physics Letters*, vol. 105, no. 6, p. 062402, 2014.

[88] A. P. Daigle, A. L. Geiler, E. DuPrél, Y. Chen, P. V. Parimi, C. Vittoria, and V. G. Harris, "Numeric simulations of a novel wideband electromagnetic band gap metamaterial utilizing oriented cobalt-substituted Z-type barium hexaferrites," *IEEE Magnetics Letters*, vol. 2, pp. 0 500 104–0 500 104, 2011.

[89] Z. Chen, J. Yu, X. Chen, C. Parini, X. Wang, H. Lin, Z. Zhou, T. Nan, and N. X. Sun, "UHF tunable compact antennas on Co_2Z hexaferrite substrate with 2.5/1 tunable frequency

range," in *2015 IEEE International Symposium on Antennas and Propagation USNC/URSI National Radio Science Meeting*, July 2015, pp. 2287–2288.

[90] S. Bae, Y. K. Hong, J. J. Lee, W. M. Seong, J. S. Kum, W. K. Ahn, S. H. Park, G. S. Abo, J. Jalli, and J. H. Park, "Miniaturized broadband ferrite t-dmb antenna for mobile-phone applications," *IEEE Transactions on Magnetics*, vol. 46, no. 6, pp. 2361–2364, June 2010.

[91] Q. Zhang, Z. Chen, Y. Gao *et al.*, "Miniaturized antenna array with Co_2Z hexaferrite substrate for massive MIMO," in *2014 IEEE Antennas and Propagation Society International Symposium (APSURSI)*, July 2014, pp. 1803–1804.

[92] W. Lee, Y. K. Hong, J. Park, M. Choi, J. Lee, I. S. Baek, N. P. Hur, and W. M. Seong, "Low-profile multiband ferrite antenna for telematics applications," *IEEE Transactions on Magnetics*, vol. 52, no. 7, pp. 1–4, July 2016.

[93] S. Fujii, K. Wakamatsu, H. Satoh *et al.*, "Wide bandwidth CuO-modified $Ba_2Co_2Fe_{12}O_{22}$ ferrite antenna," *IEEE Antennas and Wireless Propagation Letters*, vol. 15, pp. 1171–1174, 2016.

[94] A. Saini, A. Thakur, and P. Thakur, "Miniaturization and bandwidth enhancement of a microstrip patch antenna using magneto-dielectric materials for proximity fuze application," *Journal of Electronic Materials*, vol. 46, no. 3, pp. 1902–1907, 2017. [Online]. Available: http://dx.doi.org/10.1007/s11664-016-5256-0

[95] S.-E. Lee, H.-J. Kim, J.-H. Lee, K.-S. Oh, H. T. Hahn, and J.-W. Choi, "Magnetodielectric hexaferrite flake/polymer substrate for implantable antenna with an enhanced insensitivity to implant position," *Materials Letters*, vol. 187, pp. 94 – 97, 2017. [Online]. Available: http://www.sciencedirect.com/science/article/pii/S0167577X16313957

[96] N. Neveu, Y. K. Hong, J. Lee, J. Park, G. Abo, W. Lee, and D. Gillespie, "Miniature hexaferrite axial-mode helical antenna for unmanned aerial vehicle applications," *IEEE Transactions on Magnetics*, vol. 49, no. 7, pp. 4265–4268, July 2013.

[97] E. Andreou, T. Zervos, E. Varouti, M. Pissas, C. Christides, A. A. Alexandridis, and G. Fikioris, "Magneto-dielectric substrate influence on the efficiency of a reconfigurable patch antenna," in *2017 International Workshop on Antenna Technology: Small Antennas, Innovative Structures, and Applications (iWAT)*, March 2017, pp. 191–194.

[98] E. Andreou, T. Zervos, A. A. Alexandridis, and G. Fikioris, "Magnetodielectric materials in antenna design: Exploring the potentials for reconfigurability," *IEEE Antennas and Propagation Magazine*, vol. 61, no. 1, pp. 29–40, Feb 2019.

[99] Y. Y. Kyi, L. Guo, and J. Lu, "Miniaturization of a patch antenna using magneto-dielectric material," in *2012 International Symposium on Antennas and Propagation (ISAP)*, Oct 2012, pp. 1433–1436.

[100] Z. Zheng, "Flexible high magnetodielectric materials for antenna applications (invited)," in *2018 International Conference on Microwave and Millimeter Wave Technology (ICMMT)*, May 2018, pp. 1–3.

[101] Q. Li, S. Yan, X. Wang, Y. Nie, Z. Feng, Z. Su, Y. Chen, and V. G. Harris, "Dual-ion substitution induced high impedance of Co_2Z hexaferrites for ultra-high frequency applications," *Acta Materialia*, vol. 98, pp. 190 – 196, 2015. [Online]. Available: http://www.sciencedirect.com/science/article/pii/S1359645415005091

[102] L. Kempel, B. Shanker, and C. Vittoria, "Radiation properties of a rectangular patch antenna loaded with a magnetoelectric material," in *2016 IEEE International Symposium on Antennas and Propagation (APSURSI)*, June 2016, pp. 1731–1732.

[103] W. Lee, Y. K. Hong, J. Lee *et al.*, "Dual-polarized hexaferrite antenna for unmanned aerial vehicle (UAV) applications," *IEEE Antennas and Wireless Propagation Letters*, vol. 12, pp. 765–768, 2013.

[104] L. J. Martin, S. Ooi, and D. Staiculescu, "Effect of permittivity and permeability of a flexible magnetic composite material on the performance and miniaturization capability of planar antennas for RFID and wearable wireless applications," *IEEE Transactions on Components and Packaging Technologies*, vol. 32, no. 4, pp. 849–858, Dec 2009.

[105] R. Waterhouse, "Small microstrip patch antenna," *Electronics Letters*, vol. 31, no. 8, pp. 604–605, April 1995.

[106] H. Mopidevi, Y. Damgaci, D. Rodrigo, and et al., "A quad-band antenna for public safety applications," *IEEE Antennas and Wireless Propagation Letters*, vol. 13, pp. 1231–1234, 2014.

[107] N. Kogo, M. Nagasaka, S. Nakazawa, and et al., "Folded-type rectangular loop antenna with tunable circuit," *Electronics Letters*, vol. 46, no. 1, pp. 19–21, January 2010.

[108] S. M. Kumar and Y. K. Choukiker, "Tunable wideband and switching polarisation reconfiguration antenna for wireless applications," *IET Microw. Antennas Propag.*, vol. 12, no. 15, pp. 2364–2371, 2018.

[109] F. Ferrero, A. Chevalier, J. M. Ribero, and et al., "A new magneto-dielectric material loaded, tunable UHF antenna for handheld devices," *IEEE Antennas and Wireless Propagation Letters*, vol. 10, pp. 951–954, 2011.

[110] M. W. Young, S. Yong, and J. T. Bernhard, "A miniaturized frequency reconfigurable antenna with single bias, dual varactor tuning," *IEEE Transactions on Antennas and Propagation*, vol. 63, no. 3, pp. 946–951, March 2015.

[111] L. Xing, Y. Huang, Q. Xu, and et al., "A transparent dielectric-loaded reconfigurable antenna with a wide tuning range," *IEEE Antennas and Wireless Propagation Letters*, vol. 15, pp. 1630–1633, 2016.

[112] Q. Bai, R. Singh, K. L. Ford, R. J. Langley, and T. O'Farrell, "Tuneable dual-band antenna for sub 1 GHz cellular mobile radio applications," *2016 Loughborough Antennas Propagation Conference (LAPC)*, pp. 1–5, 2016.

[113] Q. Bai, R. Singh, K. L. Ford, T. O'Farrell, and R. J. Langley, "An independently tunable tri-band antenna design for concurrent multiband single chain radio receivers," *IEEE Transactions on Antennas and Propagation*, vol. 65, no. 12, pp. 6290–6297, Dec 2017.

[114] S. W. Cheung, Y. F. Cao, and T. I. Yuk, "Compact frequency reconfigurable slot antenna with continuous tuning range for cognitive radios," *2015 9th European Conference on Antennas and Propagation (EuCAP)*, pp. 1–4, April 2015.

[115] Y. Yu, J. Xiong, H. Li, and et al., "An electrically small frequency reconfigurable antenna with a wide tuning range," *IEEE Antennas and Wireless Propagation Letters*, vol. 10, pp. 103–106, 2011.

[116] H. J. Huang, C. H. Tsai, C. P. Lai, and et al., "Frequency-tunable miniaturized strip loop antenna fed by a coplanar strip," *IEEE Antennas and Wireless Propagation Letters*, vol. 15, pp. 1000–1003, 2016.

[117] S. C. del Barrio, A. Morris, and G. F. Pedersen, "Addressing carrier aggregation with narrow-band tunable antennas," *2016 10th European Conference on Antennas and Propagation (EuCAP)*, pp. 1–5, 2016.

[118] F. A. Asadallah, J. Costantine, Y. Tawk, L. Lizzi, F. Ferrero, and C. G. Christodoulou, "A digitally tuned reconfigurable patch antenna for IoT devices," *2017 IEEE International Symposium on Antennas and Propagation USNC/URSI National Radio Science Meeting*, pp. 917–918, July 2017.

[119] A. Mansoul, F. Ghanem, M. R. Hamid, and M. Trabelsi, "A selective frequency-reconfigurable antenna for cognitive radio applications," *IEEE Antennas and Wireless Propagation Letters*, vol. 13, pp. 515–518, 2014.

[120] R. Aigner, "Tunable filters? reality check foreseeable trends in system architecture for tunable rf filters," *IEEE Microwave Magazine*, vol. 16, no. 7, pp. 82–88, Aug 2015.

[121] Qualcomm. (2017) TruSignal Antenna Boost Technology. [Online]. Available: http://www.qualcomm.com/solutions/mobile-computing/features/trusignal

[122] F. Canneva, J. M. Ribero, and R. Staraj, "Tunable antenna for DVB-H band," in *Proceedings of the Fourth European Conference on Antennas and Propagation*, April 2010, pp. 1–3.

[123] J. D. Kraus and R. J. Marhefka, *Antennas for all Applications*, 3rd ed. McGraw-Hill, 2002.

[124] Z. Chen and M. Chia, *Broadband Planar Antennas: Design and Applications*, 1st ed. Wiley, 2006.

[125] Farnell, "CIF FR4," *FR4 Data Sheet*, 2015. [Online]. Available: https://www.farnell.com/datasheets/1644697.pdf

[126] Rogers Corporation, "RT/Duroid 5870/5880 High Frequency Laminates," *5870/5880 datasheet*, 2016.

[127] CST. (2015) CST Microwave Studio. [Online]. Available: https://www.cst.com/products/cstmws

[128] W. L. Stutzman and G. A. Thiele, *Antenna Theory and Design*, 1st ed. Wiley, 1981.

[129] J. D. Dunlavy, "Wide range tunable transmitting loop antenna," 1971, US Patent 3,588,905.

[130] P. L. Chi, R. Waterhouse, and T. Itoh, "Compact and tunable slot-loop antenna," *IEEE Transactions on Antennas and Propagation*, vol. 59, no. 4, pp. 1394–1397, April 2011.

[131] H. Y. Li, H. P. Chen, S. C. Chen, C. H. Tai, and J. S. Fu, "A tunable slot loop antenna using interdigitated ferroelectric varactors," in *Proceedings of the 2012 IEEE International Symposium on Antennas and Propagation*, July 2012, pp. 1–2.

[132] H. Y. Li, C. T. Yeh, J. J. Huang, C. W. Chang, C. T. Yu, and J. S. Fu, "CPW-fed frequency-reconfigurable slot-loop antenna with a tunable matching network based on ferroelectric varactors," *IEEE Antennas and Wireless Propagation Letters*, vol. 14, pp. 614–617, 2015.

[133] C. Parini, *Theory and Practice of Modern Antenna Range Measurements*, ser. Electromagnetic Waves. Institution of Engineering and Technology, 2013.

[134] S. Gregson, *Principles of Planar Near-Field Antenna Measurements*, ser. Electromagnetic Waves. Institution of Engineering and Technology, 2007.

[135] RFXpert. (2018) How to Measure All Types of Antennas Using Very-Near-Field Measurement. [Online]. Available: https://www.mdltechnologies.co.uk/technical-docs/RFxpert%20White%20Paper%201-A4.pdf

[136] A. Yaghjian, "An overview of near-field antenna measurements," *IEEE Transactions on Antennas and Propagation*, vol. 34, no. 1, pp. 30–45, January 1986.

[137] Satimo. (2019) SG 64 Antenna Measurement System. [Online]. Available: https://www.mvg-world.com/en/products/field_product_family/antenna-measurement-2/sg-64

[138] X. Chen, "Generalized statistics of antenna efficiency measurement in a reverberation chamber," *IEEE Transactions on Antennas and Propagation*, vol. 62, no. 3, pp. 1504–1507, March 2014.

[139] A. Lambourne. (2007) Reverberation Chambers. [Online]. Available: http://resource.npl.co.uk/docs/networks/electromagnetics/071129/cispr_alexander/lambourne.pdf

[140] R. H. Johnston and J. G. McRory, "An improved small antenna radiation-efficiency measurement method," *IEEE Antennas and Propagation Magazine*, vol. 40, no. 5, pp. 40–48, Oct 1998.

[141] Flann Microwave, "Dual Polarised Horns Series DP240," *Data Sheet*, 2018.

[142] ——, "Standard Gain Horns Series 240," *Data Sheet*, 2018.

[143] Teseq (formerly Chase), "UPA 6109 Log Periodic Antenna," *Data Sheet*, 2018.

[144] D. L. Paul, H. Giddens, M. G. Paterson *et al.*, "Impact of body and clothing on a wearable textile dual band antenna at digital television and wireless communications bands," *IEEE Transactions on Antennas and Propagation*, vol. 61, no. 4, pp. 2188–2194, April 2013.

[145] G. S. Hilton, P. R. Urwin-Wright, and I. J. Craddock, "Full radiation pattern measurements of antenna arrays to obtain accurate pattern correlation levels for use in MIMO system performance," in *2004 IEE Antenna Measurements and SAR, AMS 2004*, May 2004, pp. 83–86.

[146] E. Arabi, K. A. Morris, and M. A. Beach, "Analytical formulas for the coverage of tunable matching networks for reconfigurable applications," *IEEE Transactions on Microwave Theory and Techniques*, vol. 65, no. 9, pp. 3211–3220, Sept 2017.

[147] C. Bowick, *RF Circuit Design*, 2nd ed. Newnes, 2007.

[148] P. Liu and A. Springer, "Tunable antenna impedance matching for 4G mobile communications," in *2013 Proceedings of the International Symposium on Antennas Propagation*, vol. 02, Oct 2013, pp. 863–866.

[149] Coilcraft Inc., "0603CS Chip Inductor," *Datasheet 195-1*, 2016.

[150] Cavendish Kinetics. (2017) RF MEMS SmarTuners. [Online]. Available: https://www.cavendish-kinetics.com/rf-mems-products/rf-mems-smartuners/

[151] WiSpry. (2017) Tunable Digital Capacitor Arrays. [Online]. Available: http://wispry.com/solutions/tunable-digital-capacitor-arrays/

[152] Coilcraft Inc., "Mini air-core inductor," *Datasheet Document 107-1*, 2011.

[153] Y. Zheng, *Tunable Multiband Ferroelectric Devices for Reconfigurable RF-Frontends*, 1st ed. Springer, 2013.

[154] Cavendish Kinetics. (2015) Using ADS to Simulate Actively Tuned Antennas with High Performance RF MEMS. [Online]. Available: http://www.keysight.com/upload/cmc_upload/All/4_Simulation_of_antenna_tuning_w_RFMEMS.pdf

[155] A. D. Yaghjian and S. R. Best, "Impedance, bandwidth, and Q of antennas," *IEEE Transactions on Antennas and Propagation*, vol. 53, no. 4, pp. 1298–1324, April 2005.

[156] J. Rahola, "Effect of antenna Q to the radiation efficiency of tunable antennas," in *The 8th European Conference on Antennas and Propagation (EuCAP 2014)*, April 2014, pp. 3285–3288.

[157] Y. Han and D. J. Perreault, "Analysis and design of high efficiency matching networks," *IEEE Transactions on Power Electronics*, vol. 21, no. 5, pp. 1484–1491, Sept 2006.

[158] A. Petosa, "Frequency agile antennas for wireless communications: A survey," in *2010 14th International Symposium on Antenna Technology and Applied Electromagnetics the American Electromagnetics Conference*, July 2010, pp. 1–4.

[159] P. Tornatta, R. Gaddi, L. Morrell, V. Joshi, and B. Bishop, "Radiated efficiency of aperture tuned antennas: Comparison of MEMS digital variable capacitor and fixed ceramic capacitors," in *2014 IEEE MTT-S International Microwave Symposium (IMS2014)*, June 2014, pp. 1–4.

[160] L. Zhang, A. Puri, K. Sertel, J. L. Volakis, and H. Verweij, "Low Loss Z-Type $Ba_3Co_2Fe_{24}O_{41}$ Hexaferrites for Antennas and RF Devices," *IEEE Transactions on Magnetics*, vol. 47, no. 8, pp. 2149–2152, Aug 2011.

[161] A. P. Daigle, "Design of novel wideband electromagnetic band gap metamaterials and antenna elements utilizing oriented cobalt-substituted Z-type barium hexaferrites," Ph.D. dissertation, Northeastern University, 2011.

[162] Keysight Technologies. (2016) E4991B Impedance Analyzer, 1MHz to 500 MHz/1 GHz/3 GHz. [Online]. Available: http://www.keysight.com/en/pd-2405182-pn-E4991B

[163] W. Lee, Y.-K. Hong, J. Park, G. LaRochelle, and J. Lee, "Low-loss Z-type hexaferrite ($Ba_3Co_2Fe_{24}O_{41}$) for GHz antenna applications," *Journal of Magnetism and Magnetic Materials*, vol. 414, pp. 194 – 197, 2016. [Online]. Available: http://www.sciencedirect.com/science/article/pii/S0304885316304280

[164] P. R. Urwin-Wright, G. S. Hilton, I. J. Craddock, and P. N. Fletcher, "An electrically-small annular slot operating in the 'DC' mode," in *Twelfth International Conference on Antennas and Propagation, 2003 (ICAP 2003). (Conf. Publ. No. 491)*, vol. 2, March 2003, pp. 686–689 vol.2.

[165] P. R. Rogers, "An electrically-small tuneable annular slot antenna for future mobile terminals," Ph.D. dissertation, University of Bristol, 2004.

[166] Johanson Technology, "R14S Series 0603 Capacitor," *Datasheet*, 2017. [Online]. Available: http://www.johansontechnology.com/R14S

[167] R. C. Hansen and R. E. Collin, *Small Antenna Handbook*, 1st ed. Wiley, 2011.

[168] Eclipse Magnetics, "N800 Magnets," *Datasheet*, 2017. [Online]. Available: http://www.farnell.com/datasheets/612878.pdf

[169] M. G. S. Hossain and T. Yamagajo, "Reconfigurable printed antenna for a wideband tuning," in *Proceedings of the Fourth European Conference on Antennas and Propagation*, April 2010, pp. 1–4.

[170] M. M. Bilgic and K. Yegin, "Gain-bandwidth product for aperture-coupled antennas," in *Computational Electromagnetics Workshop (CEM), 2013*, Aug 2013, pp. 21–22.

[171] J. Friden, "Gain-bandwidth limitations evaluated for real user devices," in *2013 7th European Conference on Antennas and Propagation (EuCAP)*, April 2013, pp. 505–509.

[172] A. A. Baba, R. M. Hashmi, and K. P. Esselle, "Achieving a large gain-bandwidth product from a compact antenna," *IEEE Transactions on Antennas and Propagation*, vol. 65, no. 7, pp. 3437–3446, July 2017.

[173] MuRata, "TZW4Z1R5A001R00 Trimmer Capacitor," *Data Sheet*, 2015. [Online]. Available: http://uk.farnell.com/murata/tzw4z1r5a001r00/cap-trimmer-0-4-1-5pf-250v-top/dp/1115036

[174] Maxim Integrated, "Matching Maxim's 300 MHz to 450 MHz transmitters to small loop antennas," 2004, application Note 3401. [Online]. Available: http://pdfserv.maximintegrated.com/en/an/AN3401.pdf

[175] Keysight Technologies. (2014) Advanced Design System. [Online]. Available: http://www.keysight.com/find/eesof-ads-latest-downloads